

Ultra-wideband Small Scale Channel Modeling and its Application to Receiver Design

David R. McKinstry

Thesis submitted to the Faculty of the
Virginia Polytechnic Institute and State University
in partial fulfillment of the requirements for the degree of

Master of Science
in
Electrical Engineering

Committee:

R. Michael Buehrer (chair)
Jeffrey H. Reed
Dennis G. Sweeney

June 17, 2003
Blacksburg, VA

Keywords: ultra-wideband, UWB, channel model, Rake receiver,
energy detector, interference rejection

Copyright 2003, David R. McKinstry

Ultra-wideband Small Scale Channel Modeling and its Application to Receiver Design

David R. McKinstry
Thesis Abstract

Recently, ultra-wideband (UWB) technology based on the transmission of short duration pulses has gained much interest for its application to wireless communications. This thesis covers a range of topics related to the analysis of indoor UWB channels for communications and to system level design issues for UWB receivers. Measurement based UWB small scale modeling and characterization efforts as well as UWB communications system analysis and simulation are presented.

Relevant background material related to UWB communications and wireless channel modeling is presented. The details of the small scale channel modeling work, including statistical characterization and potential models, are discussed. A detailed analysis of the CLEAN algorithm, which was used to process all the measurement data, is also given, and some limitations of the algorithm are presented.

The significance, in terms of performance, of the channel impulse response model chosen for the simulation of UWB communications systems is also evaluated. Three traditional models are found to be useful for modeling NLOS UWB channels, but not LOS channels. A new model for LOS UWB channels is presented and shown to represent LOS channels much more accurately than the traditional models.

Receiver architectures for UWB systems are also discussed. The performance of correlation receivers and energy detector receivers are compared as well as Rake diversity forms of each of these types to show tradeoffs in system complexity with performance. Interference to and by UWB signals is considered. A narrowband rejection system for UWB receivers is shown to offer significant system improvement in the presence of strong interferers.

This research was funded by a Bradley Fellowship and by the DARPA NETEX program.

Acknowledgements

First and foremost, I would like to thank my Lord and Savior Jesus Christ. “He is the image of the invisible God, the firstborn over all creation. For by him all things were created: things in heaven and on earth, visible and invisible, whether thrones or powers or rulers or authorities; all things were created by him and for him. He is before all things, and in him all things hold together. And he is the head of the body, the church; he is the beginning and the firstborn from among the dead, so that in everything he might have the supremacy. For God was pleased to have all his fullness dwell in him, and through him to reconcile to himself all things, whether things on earth or things in heaven, by making peace through his blood, shed on the cross.” (Colossians 1:15-20) I pray that this work and all I do in my life would glorify God.

I would also like to thank my family for their constant love and support. I would not be the person I am without their influence and encouragement. I would also like to thank my many friends, here at Virginia Tech and elsewhere, for the many good times and for helping me keep perspective during the occasionally stressful times.

I owe much, in particular to the development and completion of this work, to my advisor, Dr. R. Michael Buehrer. I have learned a tremendous amount from him and I believe his guidance has well prepared me for the future. I also thank Dr. Jeffrey Reed and Dr. Dennis Sweeney for serving on my committee and reviewing my work. Many thanks go to everyone at MPRG. Thanks to all the staff for always keeping everything running smoothly and for willingly helping me whenever I needed it. Thanks also to the other students; I appreciate having had the chance to get to know many of them and learn more about the world and other cultures from them and that they were always there to listen to ideas or help work out problems. Many thanks also go to the faculty and students of the Time Domain Laboratory for providing the measurement data that much of this work is built upon. I would also like to thank the professors of Virginia Tech whom I learned a great deal from in the classroom.

Table of Contents

1	Ultra-wideband Communications	1
1.1	Background	1
1.2	Thesis Organization	17
2	Channel Measurement and Small Scale Channel Modeling Background	20
2.1	Traditional Measurement and Modeling	20
2.1.1	Narrowband/Wideband Channel Measurement	21
2.1.2	Linear Filter based Small Scale Channel Models	24
2.2	UWB Channel Measurement and Modeling	26
2.2.1	Previous Measurement Campaigns	26
2.2.2	UWB Small Scale Channel Modeling	32
2.2.3	Other Measurements and Characterization	34
3	UWB Small Scale Channel Modeling	37
3.1	Material Dependent Pulse Distortion	37
3.1.1	Distortion caused by Transmission through a Material	37
3.1.2	Significance of Distorted Reflections to Performance of Correlation Receiver	46
3.2	Small Scale Indoor Channel Modeling	53
3.2.1	Data Processing and Analysis Methodology	53
3.2.2	Channel Characteristics	69
3.2.3	Small Scale Channel Impulse Response Models	84
3.2.4	Comparison to Previous Results	93
3.3	Conclusions	93
4	Limitations of the CLEAN Algorithm	95
4.1	CLEAN Experiment: Sub-pulse-width Resolution	95
4.2	CLEAN Experiment: Pulse Distortion due to Material	103
4.3	Energy Capture from CLEAN	105
4.4	Conclusions	110
5	UWB Channel Models and Their Significance in Communications System Performance	111
5.1	Comparison between Traditional Channel Models	111
5.2	Comparison of Models to LOS Measurement Data	118
5.3	New Model for UWB LOS Channels	124
5.4	Comparison of Models to NLOS Measurement Data	131
5.5	Conclusions	137
6	Significance of Fractional Bandwidth	138
6.1	Comparison of Pulses with Different Fractional Bandwidths	138
6.2	Fading in Measured Channels	142
6.3	Conclusions	150
7	Receiver Architecture Analysis	151
7.1	Correlation Receiver	151
7.1.1	Probability of Bit Error for Correlation Receiver	152
7.1.2	Traditional Spread Spectrum Rake Receiver Performance	154
7.1.3	Semi-analytic Simulation of BER Performance in Multipath Channels	170
7.2	Energy Detector Receiver	179

7.2.1	Receiver Description and Theoretical Analysis.....	179
7.2.2	Probability of Bit Error for Energy Detector	184
7.2.3	Energy Detector Diversity Combining	189
7.2.4	Semi-analytic Simulation of BER Performance in Multipath Channels	190
7.3	Conclusions.....	197
8	Narrowband Interference Impact and Rejection for UWB Systems.....	199
8.1	Background.....	199
8.2	Impact of Narrowband Interference on a UWB signal	201
8.3	Impact of UWB Interference on a Narrowband Signal	204
8.4	LMS Analog and Digital Narrowband Rejection System.....	206
9	Conclusion	214
9.1	Summary and Future Work.....	214
9.2	Contributions.....	217
	References.....	218
	Vita.....	226

List of Figures

Figure 1-1.	Fractional bandwidth comparison	1
Figure 1-2.	Uniform pulse train (no modulation, no dithering).....	3
Figure 1-3.	Time hopping example, pulse has been shifted to hop position 4 in a frame with 8 possible hop positions.....	3
Figure 1-4.	Example of possible time shift for 4-ary time-hopping	4
Figure 1-5.	Example symbols for 4-ary PAM	5
Figure 1-6.	Example symbols for OOK.....	5
Figure 1-7.	Energy spectral density of antipodal modulated pulse train	7
Figure 1-8.	Energy spectral density of undithered, unmodulated pulse train	7
Figure 1-9.	Energy spectral density of time hopped pulse train	8
Figure 1-10.	Second derivative Gaussian (a) pulse and (b) energy spectral density	9
Figure 1-11.	Gaussian ‘doublet’ as defined by some researchers.....	10
Figure 1-12.	First derivative Gaussian (a) pulse and (b) energy spectral density.....	10
Figure 1-13.	Gaussian modulated sinusoidal (a) pulses and (b) energy spectral densities	12
Figure 2-1.	Traditional direct pulse measurement system	22
Figure 3-1.	2-6 GHz Gaussian-modulated sinusoidal pulses.....	39
Figure 3-2.	Spectrum of 2-6 GHz Gaussian-modulated sinusoidal pulse.....	39
Figure 3-3.	Insertion transfer function for bricks [48][50][51][52].....	40
Figure 3-4.	Spectrum of distorted 2-6 GHz Gaussian-modulated sinusoidal pulse.....	40
Figure 3-5.	2-6 GHz Gaussian-modulated sinusoidal pulse distorted by bricks.....	41
Figure 3-6.	1-7 GHz Gaussian-modulated sinusoidal pulses.....	42
Figure 3-7.	1-7 GHz Gaussian-modulated sinusoidal pulse distorted by bricks.....	42
Figure 3-8.	0.5-5.7 GHz Gaussian-monocycle pulse (with its derivative)	43
Figure 3-9.	0.5-5.7 GHz Gaussian-monocycle pulse distorted by bricks	44
Figure 3-10.	0.9-10.0 GHz Gaussian-monocycle pulse (with its derivative)	45
Figure 3-11.	0.9-10.0 GHz Gaussian-monocycle pulse distorted by bricks	45
Figure 3-12.	Correlation template for Gaussian filtered pulse source	47

Figure 3-13. Freespace and through concrete blocks measurements.....	51
Figure 3-14. Freespace and through office partition measurements.....	51
Figure 3-15. Freespace and through bricks measurements.....	52
Figure 3-16. Comparison of impulse responses generated by the CLEAN algorithm (blue), inverse filtering (red), and the Van-Cittert techniques with Bennia-Riad criteria (green) (Note: the latter 2 responses have been scaled by 10 to allow for easier visual comparison).....	60
Figure 3-17. Comparison of measured signal (black) with estimates of the received signal based on the impulse responses generated by the CLEAN algorithm (blue), inverse filtering (red), and the Van-Cittert techniques with Bennia-Riad criteria (green)....	61
Figure 3-18. Sample impulse responses calculated by the CLEAN algorithm using a -15 dB threshold cutoff. (a) TEM horns, LOS; (b) TEM horns, NLOS; (c) bicones, LOS; (d) bicones, NLOS	63
Figure 3-19. (a) Generated pulse (fed directly to antenna) and (b) its amplitude spectrum	65
Figure 3-20. (a) LOS reference pulse for TEM antennas and (b) its amplitude spectrum	66
Figure 3-21. (a) LOS reference pulse for bicone antennas and (b) its amplitude spectrum	67
Figure 3-22. Comparison of received pulses at different elevation angles of arrival for the bicone antennas.....	68
Figure 3-23. Mean excess delay vs. distance (a) TEM horns, LOS, (b) TEM horns, NLOS, (c) bicones, LOS, (d) bicones, NLOS	70
Figure 3-24. RMS delay spread vs. distance (a) TEM horns, LOS, (b) TEM horns, NLOS, (c) bicones, LOS, (d) bicones, NLOS	71
Figure 3-25 Maximum excess delay vs. distance (a) TEM horns, LOS, (b) TEM horns, NLOS, (c) bicones, LOS, (d) bicones, NLOS.....	72
Figure 3-26. RMS delay spread vs. mean excess delay, all channels.....	73
Figure 3-27. Histograms of the number of multipaths. (a) TEM horns, LOS, (b) TEM horns, NLOS, (c) bicones, LOS, (d) bicones, NLOS.....	75
Figure 3-28. Number of paths vs. RMS delay spread, all channels.....	76
Figure 3-29. Histograms of interarrival times. (a) TEM horns, LOS, (b) TEM horns, NLOS, (c) bicones, LOS, (d) bicones, NLOS.....	79
Figure 3-30. Histograms of estimated energy decay parameter. (a) TEM horns, LOS, (b) TEM horns, NLOS, (c) bicones, LOS, (d) bicones, NLOS	83
Figure 3-31. Simulated impulse response using single Poisson process arrival times. (a) TEM horns, LOS, (b) TEM horns, NLOS, (c) bicones, LOS, (d) bicones, NLOS...	92
Figure 4-1. 1 GHz bandwidth pulse with center frequency 4 GHz	96
Figure 4-2. Top: received signal (pulses destructively interfere), Bottom: two path channel impulse response and CLEAN estimate of channel impulse response.....	97
Figure 4-3. 1 GHz pulse with fractional bandwidth almost 2.....	98
Figure 4-4. Top: received signal, Bottom: two path channel impulse response and CLEAN estimate of channel impulse response	98
Figure 4-5. Received signal and estimate of received signal using CLEAN impulse response, correlation = 97.0%.....	99
Figure 4-6. Received signal and estimate, BW = 0.25 GHz, $f_c = 0.5$ GHz Correlation = 99.8%	100

Figure 4-7. Received signal and estimate, BW = 0.25 GHz, $f_c = 0.3$ GHz Correlation = 91.2%	101
Figure 4-8. Received signal and estimate, BW = 0.25 GHz, $f_c = 0.7$ GHz Correlation = 99.9%	101
Figure 4-9. Received signal and estimate, BW = 1 GHz, $f_c = 2$ GHz Correlation = 91.0%	102
Figure 4-10. Received signal and estimate, BW = 1 GHz, $f_c = 4$ GHz Correlation = 43.0%	102
Figure 4-11. Received signal and estimate, BW = 1.5 GHz, $f_c = 1$ GHz Correlation = 58.9%	103
Figure 4-12. CLEAN impulse response generated from single distorted pulse	104
Figure 4-13. Distorted pulse and estimate of distorted pulse using CLEAN impulse response.....	105
Figure 4-14. Samples of Energy Capture Ratio and Relative Error vs. CLEAN iterations	108
Figure 4-15. Energy Capture Ratio + Relative Error vs. CLEAN iterations	109
Figure 4-16. Energy Capture Ratio and Relative Error for ray tracing simulation data of TEM LOS scenarios.....	109
Figure 5-1. Histogram of $\log_{10}(\text{BER})$ for 5 finger Rake at $E_b/N_o = 14$ dB, 6-7 GHz pulses, set 4 impulse responses, all three models	113
Figure 5-2. Zoomed on extreme values, histogram of BER (linear) for 5 finger Rake at $E_b/N_o = 14$ dB, 6-7 GHz pulses, set 4 impulse responses, all three models.....	114
Figure 5-3. Comparison of average energy capture for a Rake receiver when using different channel models with the bicone pulse.....	114
Figure 5-4. Comparison of average BER for antipodal signaling and a Rake receiver when using different channel models with the bicone pulse (1, 2, 5, 10, and 20 finger cases, from right to left).....	115
Figure 5-5. Comparison of average BER for binary PPM and a Rake receiver when using different channel models with the bicone pulse (1, 2, 5, 10, and 20 finger cases, from right to left)	115
Figure 5-6. Comparison of average energy capture for a Rake receiver when using different channel models with the 6-7 GHz pulse	116
Figure 5-7. Comparison of average BER for antipodal signaling and a Rake receiver when using different channel models with the 6-7 GHz pulse (1, 2, and 5 finger cases, from right to left).....	116
Figure 5-8. Comparison of average BER for binary PPM and a Rake receiver when using different channel models with the 6-7 GHz pulse (1, 2, and 5 finger cases, from right to left).....	117
Figure 5-9. Average energy capture for a Rake receiver when using different channel models compared with the measured LOS channels for the bicone pulse.....	119
Figure 5-10. Average BER for antipodal signaling and a Rake receiver when using single Poisson model compared with the measured LOS channels for the bicone pulse (1, 2, 5, 10, and 20 finger cases, from right to left).....	119
Figure 5-11. Average BER for PPM and a Rake receiver when using single Poisson model compared with the measured LOS channels for the bicone pulse (1, 2, 5, 10, and 20 finger cases, from right to left).....	120

Figure 5-12. Average energy capture for a Rake receiver when using different channel models compared with the measured LOS channels for the 6-7 GHz pulse	120
Figure 5-13. Average BER for antipodal signaling and a Rake receiver when using single Poisson model compared with the measured LOS channels for the 6-7 GHz pulse (1, 2, and 5 finger cases, from right to left).....	121
Figure 5-14. Average BER for PPM and a Rake receiver when using single Poisson model compared with the measured LOS channels for the 6-7 GHz pulse (1, 2, and 5 finger cases, from right to left)	121
Figure 5-15. Average energy capture for each Rake finger when using different channel models compared with the measured LOS channels for the bicone pulse.....	123
Figure 5-16. Average energy capture for each Rake finger when using different channel models compared with the measured LOS channels for the 6-7 GHz pulse	124
Figure 5-17. Average energy capture for each Rake finger for new LOS channel model compared with the measured LOS channels for the bicone pulse	127
Figure 5-18. Average energy capture for a Rake receiver when using new LOS model compared with the measured LOS channels for the bicone pulse	127
Figure 5-19. Average BER for antipodal signaling and a Rake receiver when using new LOS model compared with the measured LOS channels for the bicone pulse (1, 2, 5, 10, and 20 finger cases, from right to left).....	128
Figure 5-20. Average BER for PPM and a Rake receiver when using new LOS model compared with the measured LOS channels for the bicone pulse (1, 2, 5, 10, and 20 finger cases, from right to left)	128
Figure 5-21. Average energy capture for each Rake finger for new LOS channel model compared with the measured LOS channels for the 6-7 GHz pulse.....	129
Figure 5-22. Average energy capture for a Rake receiver when using new LOS model compared with the measured LOS channels for the 6-7 GHz pulse	129
Figure 5-23. Average BER for antipodal signaling and a Rake receiver when using new LOS model compared with the measured LOS channels for the 6-7 GHz pulse (1, 2, and 5 finger cases, from right to left).....	130
Figure 5-24. Average BER for PPM and a Rake receiver when using new LOS model compared with the measured LOS channels for the 6-7 GHz pulse (1, 2, and 5 finger cases, from right to left)	130
Figure 5-25. Average energy capture for each Rake finger for single Poisson and Saleh-Valenzuela models compared with the measured NLOS channels for the bicone pulse	133
Figure 5-26. Average energy capture for a Rake receiver when using single Poisson and Saleh-Valenzuela models compared with the measured NLOS channels for the bicone pulse	134
Figure 5-27. Average BER for antipodal signaling and a Rake receiver when using single Poisson and Saleh-Valenzuela models compared with the measured NLOS channels for the bicone pulse (1, 2, 5, 10, 25, and 50 finger cases, from right to left).....	134
Figure 5-28. Average BER for PPM and a Rake receiver when using single Poisson and Saleh-Valenzuela models compared with the measured NLOS channels for the bicone pulse (1, 2, 5, 10, 25, and 50 finger cases, from right to left)	135

Figure 5-29. Average energy capture for each Rake finger for single Poisson and Saleh-Valenzuela models compared with the measured NLOS channels for the 6-7 GHz pulse	135
Figure 5-30. Average energy capture for a Rake receiver when using single Poisson and Saleh-Valenzuela models compared with the measured NLOS channels for the 6-7 GHz pulse.....	136
Figure 5-31. Average BER for antipodal signaling and a Rake receiver when using single Poisson and Saleh-Valenzuela models compared with the measured NLOS channels for the 6-7 GHz pulse (1, 2, 5, 10, and 25 finger cases, from right to left)	136
Figure 5-32. Average BER for PPM and a Rake receiver when using single Poisson and Saleh-Valenzuela models compared with the measured NLOS channels for the 6-7 GHz pulse (1, 2, 5, 10, and 25 finger cases, from right to left)	137
Figure 6-1. 1 GHz bandwidth pulses with different fractional bandwidths.....	139
Figure 6-2. Normalized correlation addition (or subtraction) due to delayed pulse.....	140
Figure 6-3. Pulses with different fractional bandwidth, center frequency = 5 GHz.....	141
Figure 6-4. Normalized correlation addition (or subtraction) due to delayed pulse.....	142
Figure 6-5. Fading of total received energy vs. fractional bandwidth (constant absolute bandwidth)	144
Figure 6-6. Variance and minimum of the total received energy vs. fractional bandwidth (constant absolute bandwidth)	144
Figure 6-7. Fading of energy in the strongest path vs. fractional bandwidth (constant absolute bandwidth).....	145
Figure 6-8. Variance and minimum of energy in the strongest path vs. fractional bandwidth (constant absolute bandwidth)	145
Figure 6-9. Fading of total received energy vs. fractional bandwidth (constant center frequency)	146
Figure 6-10. Variance and minimum of the total received energy vs. fractional bandwidth (constant center frequency).....	146
Figure 6-11. Fading of energy in the strongest path vs. fractional bandwidth (constant center frequency)	147
Figure 6-12. Variance and minimum of energy in the strongest path vs. fractional bandwidth (constant center frequency).....	147
Figure 6-13 Fading of power in CW tones at 10 MHz, 100 MHz, 1 GHz, and 10 GHz	149
Figure 7-1. Block diagram of correlation receiver.....	152
Figure 7-2. Comparison of MRC BER with perfect channel knowledge, simulated MRC with estimation error, and approximate expression for MRC Rake receiver SNR with estimation errors.....	162
Figure 7-3. Coherent MRC Rake correlation receiver, antipodal signaling, bicone pulse	172
Figure 7-4. Coherent MRC Rake correlation receiver, orthogonal modulations, bicone pulse	173
Figure 7-5. Coherent MRC Rake correlation receiver, antipodal signaling, 6-7 GHz pulse	173
Figure 7-6. Coherent MRC Rake correlation receiver, orthogonal modulations, 6-7 GHz pulse	174

Figure 7-7. Comparison of MRC and EGC for LOS model, antipodal signaling, bicone pulse	176
Figure 7-8. Comparison of MRC and EGC for LOS model, antipodal signaling, 6-7 GHz pulse	176
Figure 7-9. Comparison of MRC and EGC for NLOS model (single Poisson), antipodal signaling, bicone pulse	177
Figure 7-10. Comparison of MRC and EGC for NLOS model (single Poisson), antipodal signaling, 6-7 GHz pulse	177
Figure 7-11. Comparison of Rake receiver performance with alternate templates, antipodal signaling, 6-7 GHz pulse	179
Figure 7-12. Comparison of Rake receiver performance with alternate templates, PPM, 6-7 GHz pulse	179
Figure 7-13. Energy detector block diagram	180
Figure 7-14. T_{opt} values for Gaussian modulated sinusoidal pulse	183
Figure 7-15. Probability of bit error for transmitted ‘0’ or ‘1’ versus decision threshold value	186
Figure 7-16. Average overall probability of bit error versus decision threshold value ..	187
Figure 7-17. Probability of bit error calculated using different methods for $TW = 1$	188
Figure 7-18. Probability of bit error calculated using different methods for $TW = 10$...	188
Figure 7-19. Rake energy detector in LOS channel, $T_{finger} = 120$ and 240 ps, OOK, bicone pulse	192
Figure 7-20. Rake energy detector in LOS channel, $T_{finger} = 0.6$ and 1.2 ns, OOK, 6-7 GHz pulse	192
Figure 7-21. Rake energy detector in NLOS channel, $T_{finger} = 120$ and 240 ps, OOK, bicone pulse	193
Figure 7-22. Rake energy detector in NLOS channel, $T_{finger} = 0.6$ and 1.2 ns, OOK, 6-7 GHz pulse	193
Figure 7-23. Average BER for single integration energy detector vs. integration time, OOK, bicone pulse, LOS channels	194
Figure 7-24. Average BER for single integration energy detector vs. integration time, OOK, 6-7 GHz pulse, LOS channels	195
Figure 7-25. Comparison of correlation receivers and energy detectors, bicone pulse, LOS channels	196
Figure 7-26. Comparison of correlation receivers and energy detectors, 6-7 GHz pulse, LOS channels	196
Figure 7-27. Comparison of correlation receivers and energy detectors, bicone pulse, NLOS channels	197
Figure 7-28. Comparison of correlation receivers and energy detectors, 6-7 GHz pulse, NLOS channels	197
Figure 8-1. $v_{I,min}/A_I$, as a function of the narrowband interferer frequency	203
Figure 8-2. Comparison of distribution of lowpass filtered impulses and Gaussian PDF.	205
Figure 8-3. Block diagram of narrowband cancellation circuit	206
Figure 8-4. Mean narrowband interference rejection	209
Figure 8-5. Variance of the narrowband interference rejection	210
Figure 8-6. Optimal λ versus INR	211

Figure 8-7. Mean narrowband interference rejection versus λ for INR = (a) 0 dB, (b) 8 dB, (c) 20 dB, and (d) 40 dB.....	211
Figure 8-8. Optimum received signal delay for maximum narrowband cancellation	212
Figure 8-9. UWB BER improvement with using narrowband canceller	213

List of Tables

Table 2-1. Summary of previous UWB channel measurements.....	31
Table 3-1. Correlation loss from distortion caused by passing through bricks	46
Table 3-2. Ratios of correlations of direct vs. reflected pulses with template pulse	48
Table 3-3. Loss of receivers using the template pulse versus an ideal receiver	50
Table 3-4. Received energy for different angle of arrivals.....	69
Table 3-5. Averages of delay statistics (-15 dB threshold).....	72
Table 3-6. Averages of delay statistics (-20 dB threshold).....	72
Table 3-7. Average of number of multipath components.....	75
Table 3-8. Average of number of multipath components.....	75
Table 3-9. Number and significance of pulse inversions.....	76
Table 3-10. Number and significance of pulse inversions.....	77
Table 3-11. Mean interarrival times.....	79
Table 3-12. Averages of exponential energy decay parameter.....	83
Table 3-13. Comparison of statistics from different deconvolution techniques.....	84
Table 3-14. Fit to modified Saleh-Valenzuela model. Values in () indicate target value.	87
Table 3-15. Fit to modified Δ -K model. Values in () indicate target value	89
Table 3-16. Fit to Single Poisson arrival time model. Values in () indicate target value.	90
Table 3-17. Comparison of results with previous research.....	94
Table 4-1. Accuracy of simulated signals using CLEAN estimate of impulse response from 1 GHz bandwidth, $f_c = 0.5$ GHz system	103
Table 4-2. Percentage of energy captured by CLEAN estimate of channel	106
Table 4-3. Percentage of energy captured by CLEAN estimate of channel	107
Table 4-4. Number of multipaths from measurement sets and ray tracing simulation...	109
Table 5-1. Average of statistics for simulated channel model impulse responses.....	118
Table 5-2. Comparison of model system performance with channel statistics.....	118
Table 5-3. Fit of bicone LOS data to new LOS channel model. Values in () indicate target value.....	126
Table 5-4. Average statistics of NLOS channels with no dominant paths and model parameters to match these statistics	132
Table 6-1. Variance of fading and worst case fade for CW tones	149

List of Animations (linked external files)

[Example iteration of the CLEAN algorithm](#)

[CLEAN output: pulse with fractional BW = 2, two path channel with same polarity](#)

[CLEAN output: pulse with fractional BW = 0.5, two path channel with same polarity](#)

[CLEAN output: dispersive pulse, two path channel with same polarity](#)

[CLEAN output: pulse with fractional BW = 2, two path channel with opposite polarity](#)

[CLEAN output: pulse with fractional BW = 0.5, two path channel with opposite polarity](#)

[CLEAN output: dispersive pulse, two path channel with opposite polarity](#)

1 Ultra-wideband Communications

1.1 Background

Ultra-wideband (UWB) communications systems can be defined as wireless communications systems with very large fractional bandwidth. Fractional bandwidth is defined as the ratio of the bandwidth occupied by the signal to the center frequency of the signal: $(f_h - f_l) / f_c$. Traditional communications systems typically use signals having a fractional bandwidth less than 0.01. Wideband CDMA has a fractional bandwidth of approximately 0.02. Many in the radar and communications fields consider signals with 0.25 or greater fractional bandwidth measured at the -3 dB points to be ultra-wideband (see Figure 1-1 for a comparative illustration of fractional bandwidths). A DARPA report which coined the term “ultra-wideband” used a 0.25 fractional bandwidth definition [25]. In its First Report and Order allowing the commercial use of UWB systems [19], the FCC defined UWB signals as those which have a fractional bandwidth greater than 0.20 or a bandwidth greater than 500 MHz measured at the -10 dB points.

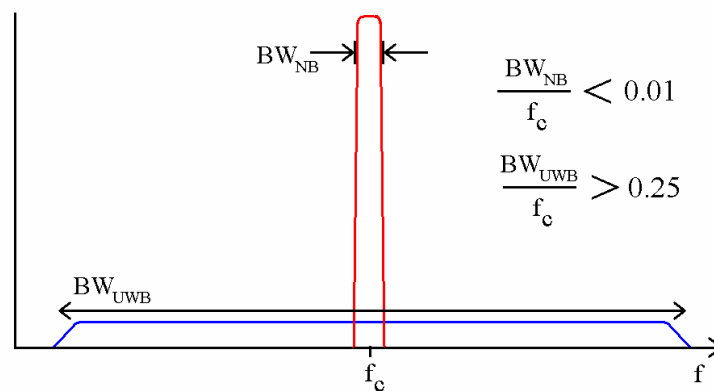


Figure 1-1. Fractional bandwidth comparison

While different methods could be employed to achieve these large bandwidths, typically the term UWB also refers to systems that use impulse radio. Impulse radio is

fundamentally different from traditional wireless communications in that short duration pulses are transmitted as opposed to sinusoidal based signals. In traditional communications systems, a sinusoidal signal is modulated by the data to be transmitted. In impulse radio, a train of pulses is modulated by the data. Throughout this work, unless stated otherwise, the use of the term UWB will also imply impulse radio.

Reference [68] introduced an impulsive UWB system that used pulse position modulation (PPM) and time hopping (TH). Several other authors have also used this system design for the basis of their UWB work and analysis. A general form of the received signal from the k -th user in this system can be represented by

$$s^{(k)}(t) = \sum_j A p\left(t - jT_f - c_j^{(k)}T_c - \delta d_{\lfloor j/N_s \rfloor}^{(k)}\right) \quad (1-1)$$

where

- A is the amplitude of the pulse, equal to $\sqrt{E_p}$ where E_p is the energy per pulse,
- N_s is the number of pulses used to represent one data symbol, i.e. the pulse repetition number
- $p(t)$ is the received pulse shape with normalized energy (this assumes all pulses received have experienced the same distortion due to the channel),
- T_f is the frame repetition time (a UWB frame is defined as the time interval in which one pulse is transmitted),
- $c_j^{(k)}$ is the time hopping sequence, often pseudorandom and/or repetitive,
- T_c is the granularity of the time hop delay (together $c_j^{(k)}$ and T_c determine the ‘coarse’ time dithering)
- δ is the PPM time delay parameter, and
- $d_{[\]}^{(k)}$ is a function of the data sequence
- (the $[\]$ notation represents the integer portion of the argument).

The total received signal is given by

$$r(t) = \sum_k s^{(k)}(t) * h^{(k)}(t) \quad (1-2)$$

where $h^{(k)}(t)$ is the channel impulse response between the k -th user and the receiver.

This scheme assumes a low duty cycle pulse train as the base waveform, shown in Figure 1-2, that is time modulated by the time hopping code and the data. For this system, a frame is defined as the time period within which one pulse is transmitted.



Figure 1-2. Uniform pulse train (no modulation, no dithering)

Within each frame, the pulse is pseudo-randomly positioned according to the value of the hopping code at that time. Time hopping can be used to smooth the spectrum of the signal or to allow for multiple access by assigning each transmitter a unique time hopping code. Without time hopping (or some other multiple access scheme), catastrophic collisions could occur if the frames from different transmitters aligned at the receiver. An example of a very simple time hopping scheme with eight possible hop positions is shown in Figure 1-3. The hopping codes could be based on pseudo-noise (PN) sequences or sequences designed to minimize interference between users.

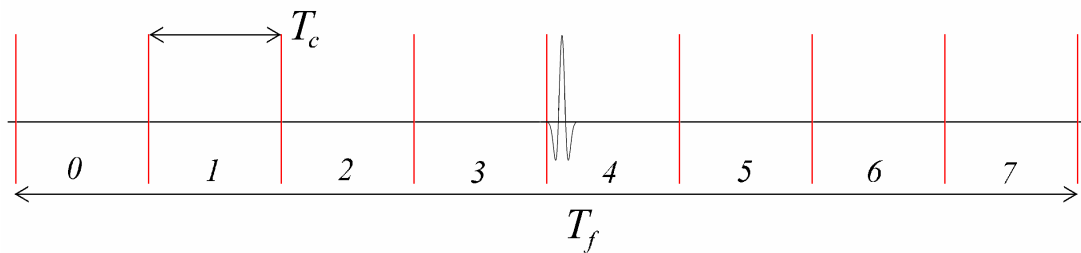


Figure 1-3. Time hopping example, pulse has been shifted to hop position 4 in a frame with 8 possible hop positions

Data modulation occurs in this system based on the fine time delay of each pulse. For a binary system, after time hopping, the pulse would either be transmitted at that time

(for a data ‘0’) or delayed an additional δ in time (for a data ‘1’), where $\delta < T_c$. M -ary PPM systems are also possible, but this may results in fewer time hopping positions for a given frame size and thus fewer multiple access codes. An example of 4-ary PPM is shown in Figure 1-4. The optimal value of δ is a function of the pulse shape used. If δ is greater than or equal to the pulse duration, orthogonal signaling is achieved.

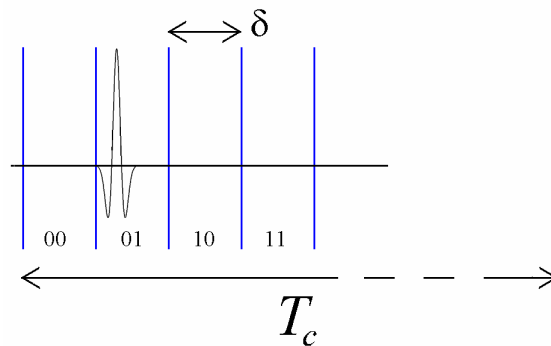


Figure 1-4. Example of possible time shift for 4-ary time-hopping

In general, the data symbol can be repeated over several pulses to attempt to use time diversity to improve the system performance. This scheme also allows for straightforward implementation of a rate adaptive system, where the frame size and power are held constant and N_s is software varied based on the signal to interference and noise ratio. This description of (1-1) also reduces to the case where each pulse represents one data symbol ($N_s = 1$).

Many variations of this system are also possible. Rather than using a fixed frame size, the coarse time delay between pulses could be pseudo-randomly varied (each pulse is transmitted at a pseudo-random delay relative to the time the last pulse was transmitted rather than relative to an imaginary frame beginning) [41]. For modulation, block waveforms with desired cross-correlation properties can be constructed [62][63][64]. In this case δ is no longer necessarily a constant.

Other modulation and multiple access schemes are also possible. Various forms of pulse amplitude modulation (PAM) could be employed (refer to Figure 1-5). On/off keying (OOK) is not very energy efficient, but its simplicity may be desirable for low cost systems (refer to Figure 1-6). Bipolar (antipodal) signaling can be attractive due to its energy efficiency; however coherent or differentially coherent reception is necessary in this case. M -ary PAM which is increasingly energy inefficient with increasing M , is somewhat less attractive since most UWB communications systems are power limited systems. Systems employing different pulse shapes to represent the different data symbols (orthogonal pulse shapes for example [28]) have also been proposed. Combinations of these modulation types are also possible. For example, bipolar signaling could be added to the previously described PPM system creating a system using a biorthogonal signal set.

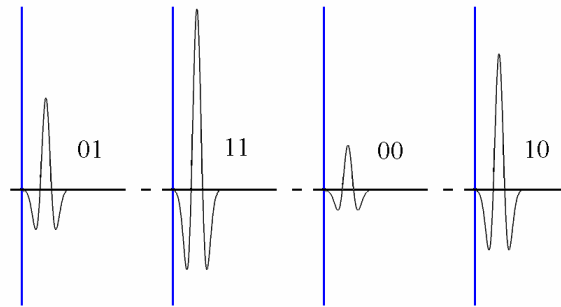


Figure 1-5. Example symbols for 4-ary PAM

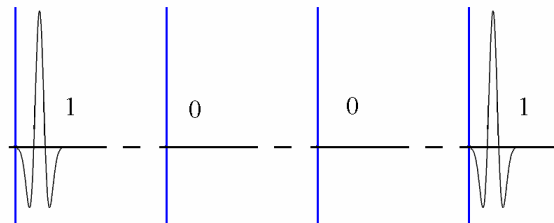


Figure 1-6. Example symbols for OOK

Another possibility for multiple access is to use a form of direct sequence (DS) similar to that used for many current spread spectrum (SS) systems [80][22][72]. A DS-UWB system where the pulses are transmitted successively such that the duty cycle approaches one, then becomes very similar to an extreme bandwidth version of direct sequence spread spectrum (DSSS) (with the main difference being that no sinusoidal carrier is present for the UWB system). For this type of system, the modulation and multiple access techniques developed for DSSS can be also be applied to the DS-UWB system.

The evaluation of the spectral characteristics of a UWB system are also important to be able determine potential interference to other systems and to assure that spectral masks and limits are met. The power density spectrum of a modulated data signal, $s(t)$, is given by [59]

$$\Phi_{ss}(f) = \frac{1}{T} |P(f)|^2 \Phi_{ii}(f) \quad (1-3)$$

where $P(f)$ is the Fourier transform of the pulse shape $p(t)$, $\Phi_{ii}(f)$ is the power spectral density (PSD) of the information sequence, and T is the interval between pulses. The overall spectrum is obviously largely influenced by the pulse shape. The power spectral density of the information sequence can have both continuous and discrete portions. If the information symbols are uncorrelated and have a mean of zero (as is the case with bipolar signaling and equally probable information symbols), the discrete component disappears. Figure 1-7 shows the energy spectral density (ESD) of a bipolar modulated pulse train (of Gaussian monocycles defined in (1-5)). However, for an unmodulated pulse train (such as the one in Figure 1-2), spectral components will be present at multiples of $1/T_f$ as shown in Figure 1-8. For the TH-PPM system, the pulse spacing T is

no longer a constant, but a PPM signal can be equivalently represented by an OOK signal with correlated information symbols that depend on the actual data sequence and time-hopping sequence [78]. Therefore it is clear that discrete spectral components will be present in the TH-PPM system. But, if the time hopping appears sufficiently random, the spectral components will be spread and the total spectrum will not have significant spikes. Figure 1-9 shows an example ESD of a time hopped pulse train.

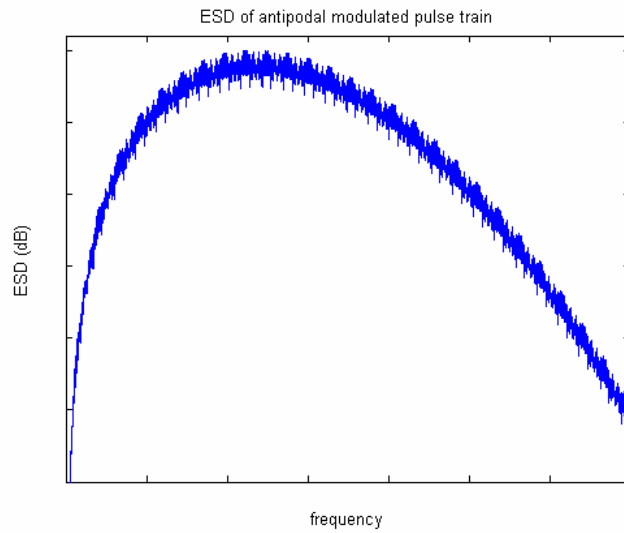


Figure 1-7. Energy spectral density of antipodal modulated pulse train

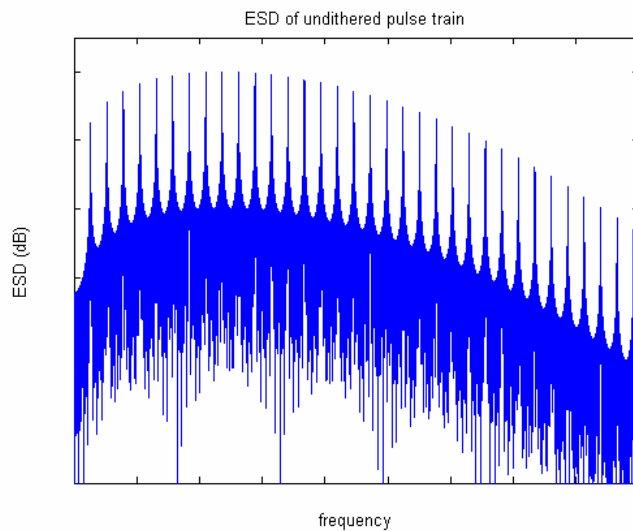


Figure 1-8. Energy spectral density of undithered, unmodulated pulse train

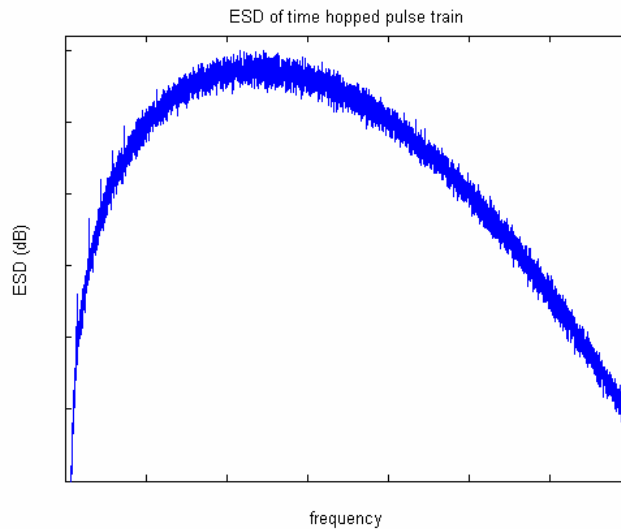


Figure 1-9. Energy spectral density of time hopped pulse train

The choice of pulse shape is crucial to the performance of a UWB system. As shown above, the spectrum of the signal, and thus the bandwidth, is largely dominated by the pulse shape. In general, shorter duration pulses lead to larger bandwidth. The pulse can be shaped intentionally by filters before it is transmitted, but the effect of the transmitting antenna (which can have differential or dispersive effects) must also be accounted for when predicting the emitted waveform to determine spectral characteristics. At the receiver these effects and the distortions caused by the channel and receiving antenna must be accounted for. To perform ideal correlation (i.e. achieve maximum signal to noise ratio) with the received pulses, a pulse of the same shape as the received pulse, including all distortions, must be generated at the receiver. The difficulty of generating an arbitrary analog waveform to match the distorted version of the transmitted pulse at the receiver is further complicated by the fact that different resolvable multipath components may experience different distortions due to the materials in the environment and multipath interference.

To model the received pulse some researchers [69] use the second derivative of a Gaussian pulse shown in Figure 1-10 and given by (normalized)

$$p(t) = \left(\frac{32k^2}{9\pi} \right)^{\frac{1}{4}} (1 - 2(kt)^2) e^{-(kt)^2} \quad (1-4)$$

This comes from assuming that a Gaussian filtered pulse is originally generated and both the transmitting and receiving antenna have a differential effect on the signal.

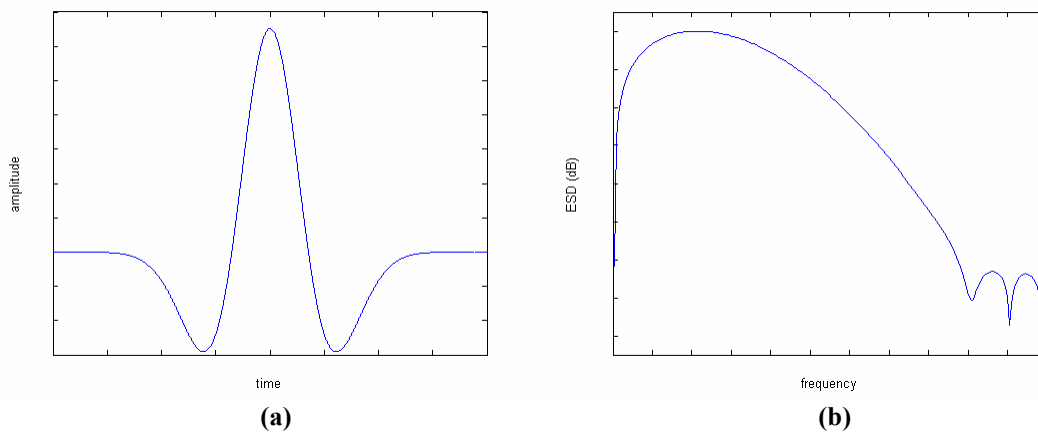


Figure 1-10. Second derivative Gaussian (a) pulse and (b) energy spectral density

Some (for example [83]) have referred to this as a Gaussian doublet since this pulse has two zero crossings. However, many in the radar community (for example [20]) and elsewhere define a doublet as the combination of a pulse and a delayed version of its inverse. Using the latter definition, an example Gaussian doublet is shown in Figure 1-11. The use of the term ‘doublet’ is not consistent in the UWB community and thus will be avoided here.

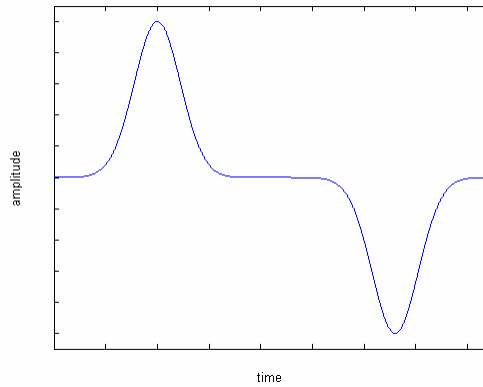


Figure 1-11. Gaussian ‘doublet’ as defined by some researchers

If the transmitting antenna is assumed to have a differential effect but not the receive antenna, the received pulse can be model as the first derivative of a Gaussian pulse shown in Figure 1-12 and given by (normalized)

$$p(t) = \left(\frac{32k^6}{\pi} \right)^{\frac{1}{4}} t e^{-(kt)^2} \quad (1-5)$$

Some researchers refer to this pulse specifically as a Gaussian monocycle, but most researchers use the term ‘monocycle’ generically to refer to any pulse. For each of the pulses of (1-4) and (1-5) k is a constant that determines the pulse width and thus also the spectral width.

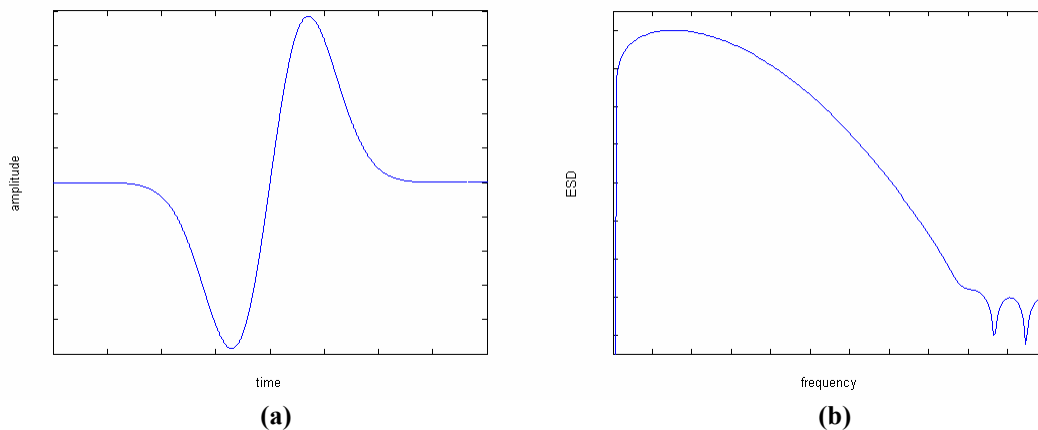


Figure 1-12. First derivative Gaussian (a) pulse and (b) energy spectral density

Reference [36] uses a received pulse model of

$$p(t) = \frac{E_o}{1-\alpha} \left(e^{-4\pi\left(\frac{t}{\Delta\tau}\right)^2} - \alpha e^{-4\pi\left(\alpha\frac{t}{\Delta\tau}\right)^2} \right) \quad (1-6)$$

which has a very similar shape to the second derivative Gaussian pulse.

Reference [28] has proposed using Hermite polynomials to model UWB received pulses, where the first ‘forms’ of the model yield the Gaussian pulse and its derivatives. However, [28] further suggests using the family of pulses generated from Hermite polynomials as an orthogonal signal set to be used for modulation, noting that even if the antennas have a differentiating effect, the pulses remain orthogonal to each other. A numerical method to generate orthogonal pulses with a specified frequency spectrum is described in [56].

The Gaussian modulated sinusoidal pulses are a set of pulses that are convenient for UWB simulation and analysis. These pulses are simply baseband Gaussian pulses multiplied by sinusoids. Gaussian pulses in time also have a Gaussian amplitude distribution in frequency so the bandwidth is simple to specify. The desired center frequency of the pulse is simply the frequency of the sinusoid. In-phase and quadrature versions can be formed by choosing either the sine or cosine function as the carrier. The normalized in-phase pulse is given by

$$p_I(t) = a_I e^{-kt^2} \cos(2\pi f_{c,UWB}t) \quad (1-7)$$

$$a_I = \left(\frac{8k}{\pi} \right)^{\frac{1}{4}} \frac{1}{\sqrt{1 + e^{-\frac{2\pi^2 f_{c,UWB}^2}{k}}}}$$

and the normalized quadrature pulse is given by

$$p_Q(t) = a_Q e^{-kt^2} \sin(2\pi f_{c,UWB} t) \quad (1-8)$$

$$a_Q = \left(\frac{8k}{\pi}\right)^{\frac{1}{4}} \frac{1}{\sqrt{1 - e^{-\frac{2\pi^2 f_{c,UWB}^2}{k}}}}$$

where

$$k = \frac{5\pi^2 W^2}{\ln(10) X_{dB}} \quad (1-9)$$

where $f_{c,UWB}$ is the center frequency of the pulse spectrum and W is the RF bandwidth measured at the $-X_{dB}$ dB points of the spectrum. In-phase and quadrature Gaussian modulated sinusoidal pulses are shown in Figure 1-13. As the bandwidth and center frequency are varied, the number of cycles in the pulse will change.

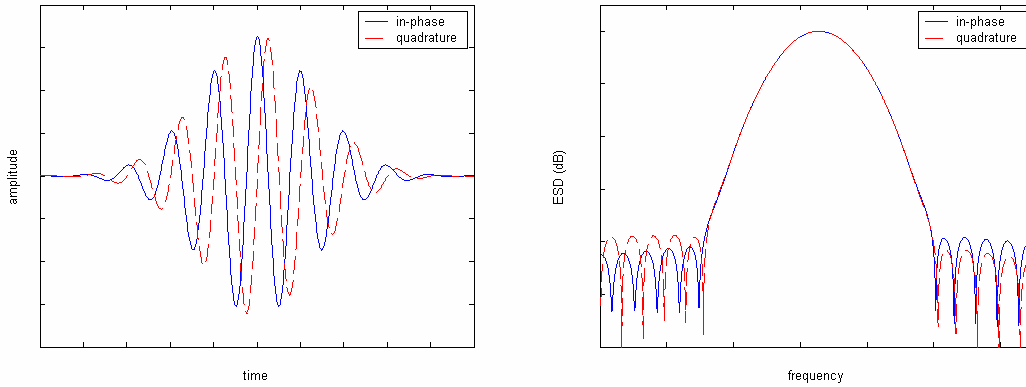


Figure 1-13. Gaussian modulated sinusoidal (a) pulses and (b) energy spectral densities

Accurate channel estimation of path amplitude strength and of the pulse distortion is a further challenge for UWB receivers. Since a large number of resolvable multipaths can exist in the UWB channel, the computational requirement for channel estimation can be high, especially since each path may experience different distortion. Also, UWB systems tend to operate in low power/low SNR modes making accurate channel estimation difficult.

Some of the potential advantages of UWB systems over narrowband and wideband systems are reduced system complexity (and thus cost), large information rates, support for a large number of users in a multiple access environment, low power spectral densities resulting in low interference to narrowband systems operating in overlapping frequency bands and low probability of detection (LPD) by hostile systems, immunity to multipath fading, large number of resolvable multipath components that can be exploited using a Rake receiver, and combined services such as communications, radar, and precision location.

One of the advantages claimed by some UWB proponents is that the transmitter and receiver hardware can be produced less expensively than traditional communications equipment. The generated pulses can be transmitted directly (or filtered and then transmitted) eliminating the need for oscillators, mixers, and other costly RF hardware. If the pulses are transmitted directly, a baseband system results where the signal occupies frequencies near DC to the highest frequency of the pulse (possibly in the gigahertz range). However, to transmit only in a higher frequency band or to more tightly control the spectral shape of the signal, the pulses can be filtered before they are radiated. This type of filtering can be used to meet specific spectrum masks such as those mandated by the FCC [19] or to intentionally avoid certain bands (such as GPS) to prevent interference to other systems. The antennas can also act as a filter or source of distortion for signals of such a large bandwidth and must be accounted for in determining the radiated spectrum. The pulses can also be modulated by a carrier to achieve a desired center frequency and frequency range, but then oscillators and mixers become necessary, increasing the complexity and thus the cost of the system.

From Shannon's theory of channel capacity

$$C = W \log_2 \left(1 + \frac{P_o}{N_o} \right) \quad (1-10)$$

where C is the channel capacity in bits/sec, W is the bandwidth in Hz, P_o is the signal power spectral density in W/Hz, and N_o is the noise power spectral density in W/Hz. For UWB the signal bandwidth is much larger than the information bandwidth and therefore, the system can operate at low signal to noise ratios ($\text{SNR} = P_o/N_o$) and relatively high data rates (compared to more narrowband systems). For these low SNR values, the capacity of the system increases almost linearly with power [78].

Since the energy is spread over such a large bandwidth in UWB, the power spectral density can be very low, often on the same order as the noise spectral density as discussed above. A narrowband system that operates in a band that overlaps a small portion of a band within which a UWB device is operating will experience some interference. However, the UWB interference will only raise the noise floor slightly (this assumes a Gaussian approximation for the UWB interference which results in $P_{inter} = P_o W \approx N_o W$). As more UWB devices are operating simultaneously, the interference power will be additive.

With a low power spectral density, the signal is also inherently more covert to hostile interceptors and detectors. It was shown that UWB signals are less detectable than wideband signals being detected by a wideband radiometer with some basic knowledge of the signal being detected [77]. The level of covertness was quantified using a metric that measures the probability of detection as a function of distance. However, while the radiometer is the optimum detector for CW signals, a modified

detector can improve the detection for impulse radio, exploiting the unique features of UWB signals such as high peak-to-average ratio and small duty cycle [9][44]. However the UWB signals detected by the improved system were still shown to be more covert than some wideband DSSS systems [44].

In traditional wideband DSSS systems, frequency diversity can be exploited through the use of a Rake receiver. Multipath components of the signal that are delayed in time by more than a chip duration are resolvable as they appear uncorrelated. The Rake receiver correlates with each of the delayed versions of the signal and combines them to increase the signal to noise ratio. This is possible because the delayed versions of the signal are close to orthogonal in code (delayed versions of the spreading code are nearly uncorrelated). For pulse based UWB systems, the multipath components that are delayed by more than the pulse duration are orthogonal in time (for low duty cycle signals) and can also be combined using a Rake receiver. Since the pulse duration is typically very short (on the order of the inverse of the bandwidth), a large number of resolvable multipath components may be present for many different channel types. For example, in outdoor channels, Rake receivers are often used to exploit multipath diversity in wideband CDMA systems where the delay between multipath components is large (relative to the chip duration), because the scatterers in the outdoor channel are spaced at large distances (mountains, buildings, etc.). However, in the indoor channel, the delay between multipaths is much less (indoor scatters, such as walls, furniture, etc. are spaced much closer) and therefore for traditional wideband systems, a Rake receiver is ineffective because the multipaths are not resolvable. But, if the UWB pulse duration is

less than the typical delay between multipath components, the time diversity can be exploited using a Rake receiver even in an indoor environment.

Since more of the multipath components are resolvable, it has been speculated that less paths contribute toward each resolvable component. In this case, some of the traditional models for multipath fading are not valid as they assume a large number of physical paths arrive at the same delay. Also, traditional fading models are based on CW signals that have a clearly defined phase term. UWB pulses do not have phase in the same sense that sinusoidal signals do. There has not been any research published that explores the theoretical basis for multipath fading in UWB. However, since many of the multipath components are expected to be resolvable, the fading variation of each component has been expected by some to be less severe than in more narrowband systems [79].

Radar Applications

UWB technology has been used in radar for many years. UWB pulses can be viewed as radar pulses, and therefore, multiple capabilities, such as communications and location finding, can be combined in one system. Some of the proposed applications for UWB include communications (indoor wireless networking, personal area networking, wireless multimedia distribution with a building, LPD tactical networks, roadside automotive information services), location services (inventory with wireless ID tags, precision distance measurements, smart highway automotive tracking), radar (ground penetrating radar for mining, wall/structure imaging for ‘stud finding’ and defect detection, through wall imaging for law enforcement/rescue workers, vehicular radar for collision avoidance and ride performance enhancement, improved resolution radar for

variety of civil and military applications), medical imaging, and intrusion/motion detection.

Some of the basic properties of UWB signals that make them desirable for use in non-communication applications (specifically radars) will only be briefly discussed here. In radar, the achievable resolution (and ranging accuracy) is inversely proportional to the bandwidth of the signal. Therefore, more detailed features of an object can be differentiated with a UWB radar than a more narrowband radar. As signals propagate through a given environment (or channel), they are reflected and absorbed between the transmitter and receiver. The effect of the channel can cause distortion to the signal. For sinusoidal signals this can be represented simply by an amplitude and a phase change. However, for UWB, the distortion of the pulse, which is a function of frequency that varies depending on the scatterers, can provide additional information about what types of materials the signals has interacted with. In conventional radar systems motion is calculated using information calculated about the Doppler effect, but with UWB radar, motion can be calculated without using the Doppler effect. UWB radars can require less post detection signal processing, especially for synthetic radar applications (SAR) over narrowband radars that require fast Fourier and inverse fast Fourier transforms, because of the time resolution of the UWB system. [37]

1.2 Thesis Organization

This thesis covers a range of topics related to the analysis of indoor ultra-wideband channels for communications and system level design issues for ultra-wideband receivers. The first chapters discuss measurement based UWB small scale

modeling and characterization efforts, while the latter chapters discuss UWB communications system analysis and simulation.

Chapter 2 presents background material related to the channel characterization work. Discussion of traditional communications channel measurement and modeling techniques are given as well as a summary of the work published to date on characterizing UWB channels.

Chapter 3 presents the details of the small scale channel modeling work based on indoor measurements taken at Virginia Tech. Data processing methodology is given as well as various statistical characteristics. Fits of the measurement data to some classic channel models are also evaluated and the various results are compared with the findings of other researchers.

More detailed analysis of the CLEAN algorithm, which is a deconvolution technique that was used to extract the channel impulse responses, is given in Chapter 4. This analysis is included since the majority of the work presented in Chapter 3 is based on data generated from the measurement data using the CLEAN algorithm. Possible limitations are discussed and the results of experiments showing cases where the CLEAN algorithm performs undesirably are presented.

The significance of the channel impulse response model chosen for the simulation of UWB communications systems is evaluated in Chapter 5. Pulses of different bandwidths and shapes are considered. The accuracies of traditional models are evaluated for their ability to reproduce UWB system performance for LOS and NLOS channels. A new UWB LOS channel model is presented and analyzed.

Chapter 6 discusses the significance of fractional bandwidth in the performance of UWB systems. Based on the measured impulse responses, the amount of fading as a function of the fractional bandwidth is also investigated.

Receiver architectures for UWB systems are discussed in Chapter 7. The performance of correlation receivers and energy detector receivers are considered as well as Rake diversity forms of each of these types. Bit error performance is the primary metric for comparison.

Chapter 8 discusses the impact of narrowband interference on UWB communications systems and inversely, the impact of UWB signals on narrowband systems. An analog and digital narrowband rejection system for UWB receivers is also presented and evaluated.

Finally, Chapter 9 provides an overall conclusion. Possibilities for future work and continuations of the work presented here are also given. The original contributions of this thesis are also summarized.

2 Channel Measurement and Small Scale Channel Modeling Background

2.1 Traditional Measurement and Modeling

Accurate channel models are extremely important for the design of communications systems. Knowledge of the features of the channel provides communications system designers with the ability to predict the performance of the system for specific modulation, channel coding, and signal processing. If an inaccurate channel model is used, the designed system may not perform as predicted and may not meet specifications. It can be very costly in time and resources to redesign systems or to implement changes to an already deployed system if even possible. Therefore, models that accurately describe the signal available to a receiver are crucial for a communications system designer. However, if the model is extremely complex and difficult to use in analysis or implement in simulation, the model is of limited use to a designer, who has finite time and resources (computational and otherwise) to evaluate potential system choices. While the complexity of simulation is relative and always changing, due to the ever-increasing availability of computer resources, useful channel models must balance detailed description of channel features with a simplicity that is still sufficient to predict system performance.

Small scale channel effects are those that can vary over a ‘local’ area or over a short time. For wideband systems, this is most often expressed in terms of the multipath structure. Understanding the distribution of the received energy allows for the designer to pick appropriate receiver techniques to balance performance and cost. While there can be significant variations between similar types of channels, most terrestrial channels can

be classified as indoor (relatively short range, highly cluttered), stationary outdoor (relatively long range, some clutter), and mobile outdoor (similar to stationary but with a dynamic channel). Here, the focus will be on stationary (non-mobile) indoor channels (even in ‘stationary’ channels, some changes are expected over time due to the movement of people and objects in the environment, but these changes are assumed to occur very slowly relative to the data rate).

2.1.1 Narrowband/Wideband Channel Measurement

Much work has been done work to characterize indoor and outdoor communications channels. The most useful and widely accepted models are grounded in reasonable theoretical explanation and are verified by extensive measurement campaigns. General agreement of results and conclusions from different measurement campaigns (especially those using different measurement systems and by different researchers) further confirm the validity and reliability of a model for general scenarios.

Wideband channel measurements can be made using different channel sounding techniques. The various techniques can typically be characterized as direct pulse measurements, spread spectrum sliding correlator measurements, and swept frequency measurements [65].

Traditionally in a direct pulse measurement system, an envelope detector is sampled by a digital sampling oscilloscope (DSO) which is used to detect the presence and strength of individual multipath components [65]. A block diagram of such a system is shown in Figure 2-1. The multipath components of the channel are resolvable if they arrive at a time difference greater than the duration of the pulse used. No phase information is available about the channel due to the envelope detection, but it is

reasonable to assume each path has a random phase. The rate of the DSO needs only be approximately the inverse of the pulse duration. An alternate method would be to use a sampling oscilloscope with a very high sampling rate (sampling rate \gg pulse duration). Using this method, information about the phase (or received pulse shape and more accurate path arrival time determination) can also be obtained where it is unavailable using an envelope detector. The modulation of the pulse onto a carrier is optional depending on the frequency band(s) of interest. The filter at the receiver must be very wideband so this type of system is subject to noise and interference. Noise can be mitigated somewhat using averaging on the oscilloscope to obtain the local average power delay profile. Proper and accurate triggering at the receiver can be difficult, especially if the first arriving pulse is blocked or significantly faded. For certain measurement scenarios, a wired trigger signal may be necessary to provide a reliable reference.

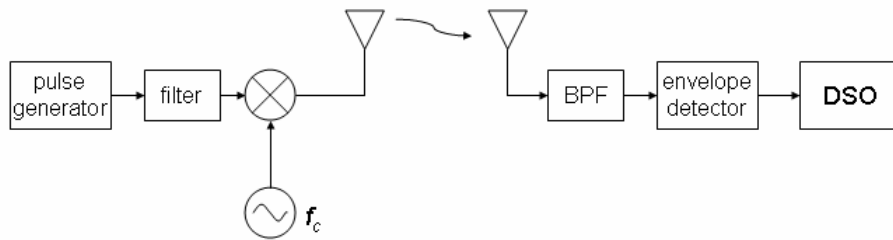


Figure 2-1. Traditional direct pulse measurement system

A block diagram of a spread spectrum sliding correlator channel measurement system can be found in [65] and the implementation of such a system is given in [2]. This system creates a wide bandwidth signal by multiplying a sinusoidal carrier signal with a binary pseudo-noise (PN) sequence. Therefore the transmitted signal has a null-to-null bandwidth of $2R_c$ (where R_c is the chip rate). At the receiver, the received signal is

filtered and then mixed with the same PN sequence as used at the transmitter, but the chip rate at the receiver is slightly slower than the chip rate at the transmitter. Thus, the receiver will have maximum correlation with each resolvable multipath component at different times (when the PN sequence of the multipath component aligns with the PN sequence of the receiver). Due to the different chip rates, the PN sequence of the receiver ‘slides’ past the PN sequences of the multipath components and provides a time expanded multipath profile of the channel. This type of measurement system has good noise rejection due to the processing gain capabilities of spread spectrum systems. The time resolution capability of this type of system is $\Delta\tau = 2/R_c$.

Channel measurements can also be performed using a vector network analyzer (VNA). A block diagram of an example setup to perform channel measurements using a VNA is also given in [65]. Antennas are connected to ports 1 and 2 of the VNA and the VNA performs a sweep of discrete frequency tones. The S-parameters of the ‘device under test’ (the wireless channel) are calculated at each of the frequencies in the sweep. The transmission from port 1 to port 2 is given by the measured S_{21} . $S_{21}(\omega)$ in this case also represents the frequency response, $H(\omega)$, of the channel. The VNA measures both amplitude and phase, so if the time domain response is desired, the inverse Fourier transform can be calculated for $H(\omega)$, yielding $h(t)$, the channel impulse response. This system requires a wired connection from each antenna back to the VNA, so only short range measurements are practical using this type of system. Also, since the VNA performs a frequency sweep, the measurement is not made in real time and thus is not useful for rapidly varying channels.

Many researchers have performed measurement campaigns to characterize particular indoor and outdoor channels. An excellent overview of the work done to characterize indoor channels is given in [29]. While many unique indoor environments exist, most researchers have focused on office environments (highly cluttered, with the signal often passing through several walls/partitions), factory environments (generally open, but with many scatterers at some locations), or residential environments (cluttered like an office, but typically containing different construction materials, such as wood rather than metal wall studs). An overview of measurements and models for the mobile radio channel is given in [65].

2.1.2 Linear Filter based Small Scale Channel Models

The small scale effects of the wireless channel are commonly described by a linear filter where the received signal is given by

$$r(t) = s(t) * h(t) + n(t) \quad (2-1)$$

where $s(t)$ is the transmitted signal, $h(t)$ is the channel impulse response, and $n(t)$ is complex-valued additive Gaussian noise. The impulse response can change as a function of time (or as a function of spatial variation) due to the motion of the transmitter or receiver and/or changes in the channel itself. The time-varying version of the channel model can be given as

$$h(t, \tau) = \sum_{k=0}^{N(\tau)-1} a_k(t) \delta[\tau - \tau_k(t)] e^{j\theta_k(t)} \quad (2-2)$$

If the channel is assumed to be static over the interval of interest, the time-invariant model of the channel can be used

$$h(\tau) = \sum_{k=0}^{N-1} a_k \delta(\tau - \tau_k) e^{j\theta_k} \quad (2-3)$$

The parameters of this model are as follows:

- δ is the Dirac delta function
- N is the number of resolvable multipaths
- t_k are the arrival times of the multipaths
 - o distributions used to describe arrival times are:
 - Standard Poisson Model
 - Modified 2-State Poisson Model (Δ -K Model)
 - Modified Poisson (Weibull Interarrivals)
 - Double Poisson (Saleh-Valenzuela /Neyman-Scott)
- a_k are the path amplitude values
 - o distributions used to describe amplitude values are:
 - Rayleigh
 - Rician
 - Nakagami (m-distribution)
 - Weibull
 - Suzuki
 - o The distribution used to model the relative average values of the successive multipath component powers is an exponential decay
- θ_k are the path phase values
 - o the initial phase is a uniformly distributed random variable from $[0, 2\pi)$
 - o phase value is incremented by:
 - random Gaussian variable
 - deterministic value calculated from environment

The channel can also be characterized by specific statistics such as mean excess delay, RMS delay spread, and maximum excess delay that describe the time dispersive properties of the channel. These are useful as single number descriptions of the channel to estimate the performance and potential for intersymbol interference (ISI). These values tend to increase with greater transmitter/receiver separation. The mean excess delay is defined as [65]

$$\bar{\tau} = \frac{\sum_k a_k^2 \tau_k}{\sum_k a_k^2} \quad (2-4)$$

and the RMS delay spread is defined as [65]

$$\sigma_{\tau} = \sqrt{\overline{\tau^2} - (\overline{\tau})^2} \quad (2-5)$$

where

$$\overline{\tau^2} = \frac{\sum_k a_k^2 \tau_k^2}{\sum_k a_k^2}$$

and the a_k are the multipath amplitudes, and the τ_k are the multipath delays relative to the first arriving multipath component. The maximum excess delay (X dB) is defined as the largest relative delay that a multipath component arrives with power greater than $-X$ dB of the strongest multipath component [65].

2.2 UWB Channel Measurement and Modeling

2.2.1 Previous Measurement Campaigns

A limited number of measurement campaigns and channel modeling efforts have been carried out to characterize the UWB channel. A few time domain, direct pulse measurement systems have been used for UWB channel sounding. Also, several researcher have performed frequency domain measurements using vector network analyzers. Most proposed UWB channel models are extensions of wideband channel models. Some proposed models are based on empirical UWB results while some are based on extrapolation from wideband measurements and models.

The results from the only known published measurement campaign taken in an outdoor environment are given in [81] by researchers originally at the University of Southern California and the Time Domain Corporation. The measurements were taken in a dense forest environment. The measurement system used a DSO as the receiver. The transmitter contains a pulse generator that creates UWB pulses with an approximate

bandwidth of 1.3 GHz every 500 nanoseconds. A probe antenna was placed close to the transmitting antenna to allow for receiver triggering and to allow all multipath profiles to have the same absolute delay reference. The sampling rate of the receiver was 20.48 GHz (48.828 ps time resolution). A pulse repetition time of 500 ns was deemed sufficiently long to ensure that the multipath response of the previous pulse had decayed. To reduce the effects of noise, 32 sequentially measured multipath profiles were averaged at each location. Power delay profiles for three cases are given as examples, but no small scale modeling is proposed. Values for the mean excess delay, RMS delay spread, path loss exponents, and forestation losses are given.

Indoor measurements in a modern office building (the Time Domain Headquarters) were also taken by the same researchers using basically the same measurement system [82][70]. Data was collected at 14 different rooms and hallways at 49 locations on a 7x7 square grid measuring 3 feet by 3 feet. The receive antenna was located 120 cm from the floor and 150 cm from the ceiling. Some initial analysis of basic parameters of the channel was presented along with the measurement results. The authors and others use these results to further analyze and propose more specific channel models in several subsequent publications. Several papers [13][14][15][11][12] have been published offering analysis of this measurement campaign. Researchers working at the time at AT&T Labs have used this data for analysis [11][12].

A TH-PPM based channel sounder developed by Time Domain Corporation is introduced in [84]. The instrument was intended to be used to create channel models that describe large scale $1/R^n$ attenuation, the number of time resolvable multipaths, their arrival times and amplitude statistics, and the variability of propagation paths as a

function of distance. The implementation described involves transmitting a 500 ps pulse (1.5 GHz bandwidth centered at 2 GHz) at a 10 MHz repetition frequency. 128 pulses are transmitted for each bit of data creating a 78.125 kbps link. The time hopping sequence repeats once per bit period and a test pattern of length 32,768 is transmitted when modulating the signal.

This receiver consists of two independently timed correlators. The tracking correlator is synchronized with the received pulse train for tracking. The scanning correlator is capable of sampling the received waveform at precise time delays relative to the tracking point of the other correlator. A complete sampled version of the waveform is captured by successively increasing the time delay. Samples of the tracking correlator are collected and represent integrated, demodulated data symbols prior to the decision logic. Samples from the tracking and sampling correlator are collected in pairs so that events in the waveform set are matched with events in the data symbol set. Time resolution as small as 3.052 ps is possible, but values around 60 ps are reported as typical. Therefore, this instrument can be used to measure the impulse response between any two points within the range of the system and can also provide a characterization of bit errors that occur. Reference [85] uses measurements taken with this system to calculate specific channel impulse responses, path loss values and RMS delay spread values. From their measurements, it was found that path loss and RMS delay spread both increase with distance and additionally that these two channel metrics are highly linearly correlated (RMS delay spread was found to be more linearly correlated to path loss than distance).

The CLEAN algorithm was used to process the data. NLOS measurements at distances of approximately 6 to 70 meters were taken in a modern office building (TDC

office). It is significant to note the building used was the Time Domain Headquarters (same location as the previously mentioned measurement campaign). Time Domain has additionally taken measurements in 11 home and office environments to collect 471 profiles [57]. Only 429 profiles were used due to duplication; 369 are from an office with metal studs, and 60 from homes with wood studs. Only office data is used for the presented statistics (there may also be some overlap with the measurements mentioned in [85]).

Intel researchers performed measurements from 2-8 GHz in residential environments. Reference [24] reveals some of the results of these measurements, but few details on exact scenarios due to submitted but not yet published work that contains such information. Some of Intel's measurement work (performed in a townhouse) is described in [58]. For calculation of the number of paths, a -10 dB threshold was used. Both a DSO measurement system and a frequency domain measurement system using a VNA were used. For time domain measurements, sub-nanosecond pulses were generated at the transmitter and the signal was measured simultaneously from two antennas using a 12.5 GHz DSO. Frequency domain measurements were taken using a 20 GHz VNA. Measurements were taken along 'baselines' moving the receive antenna over small spatial differences at each measurement location to extract information about the angle of arrival distributions for LOS and NLOS cases.

Other researchers have also performed measurements using a VNA to characterize the UWB channel. Researchers at IMST in Germany [42] measured office scenarios including corridor, in-office, and between offices using a VNA. The frequency sweep of the VNA was from 1 to 11 GHz. Biconical horn antennas at 1.5 m above the

floor were positioned on a 150x30 grid (with 1 cm separation between grid locations) at each measurement location. Researchers at CEA-LETI in France performed frequency domain measurements from 2-6 GHz in an office scenario for ranges up to 10 meters [39][40]. Omni-directional, conical monopole antennas were used, and the receive antenna was placed at locations on a 10x10 grid (with 10 cm separation between grid locations) for each measurement location. Other researchers at AT&T Labs [26] report the results of measurements taken in 23 different homes using a VNA yielding over 300,000 collected power delay profiles from 712 locations in 23 homes at distances from 1 to 15 meters. Identical conical monopole antennas were used over the frequency range 4.375–5.625 GHz. Researchers at University of Oulu in Finland [34] used a VNA to make channel measurements in a university building. Measurements were made over 2-8 GHz using conical antennas at 3 heights and 3 horizontal positions at each location.

The different measurement campaigns are summarized in Table 2-1.

Table 2-1. Summary of previous UWB channel measurements

researchers	measurement system	frequency range	environment	notes
USC/TDC [81]	DSO: 48.82 ps resolution	BW = 1.3 GHz	outdoor (forest)	<ul style="list-style-type: none"> • mean excess delay, RMS delay spread, path loss, and forestation loss are given
USC/TDC [82][70]	DSO: 48.82 ps resolution	BW = 1.3 GHz	Indoor (TDC office)	<ul style="list-style-type: none"> • 7x7 local area grid in 14 rooms • many publications based on these measurements
TDC [85][57]	Channel sounder: 3.052 ps resolution (60 ps typical)	1.25-2.75 GHz	indoor (TDC office and homes)	<ul style="list-style-type: none"> • 429 profiles collected • 6 to 70 m range in office • statistics on office data given
Intel [24][58]	DSO (12.5 GHz BW) VNA (20 GHz BW)	2-8 GHz	indoor (residential)	<ul style="list-style-type: none"> • 2 receive antennas used • measured along baselines to test AOA
IMST [42]	VNA	1-11 GHz	indoor (office)	<ul style="list-style-type: none"> • corridor, in office, inter-office scenarios • 150x30 (1 cm) spacing local area grid
CEA-LETI [39][40]	VNA	2-6 GHz	indoor (office)	<ul style="list-style-type: none"> • up to 10 m range • 10x10 (10 cm) spacing local area grid
AT&T Labs [26]	VNA	4.375–5.625 GHz	indoor (residential)	<ul style="list-style-type: none"> • 300,000 profiles at 712 locations in 23 homes from 1 to 15 m
Univ of Oulu [34]	VNA	2-8 GHz	indoor (university)	<ul style="list-style-type: none"> • 3 heights and 3 horizontal positions at each location

2.2.2 UWB Small Scale Channel Modeling

For indoor small scale channel modeling, most researchers have used the wideband model given in (2-3) but neglect the phase term. Values and discussion of the RMS delay spread are also given by several authors.

For the arrival time distribution, [43] suggests using the double Poisson model, while [21] and [87] both propose using the Δ -K model. These researchers all base their proposed models on extensions from wideband models rather than empirical UWB support.

For path amplitudes several different distributions have been proposed. [43] proposed using a Rayleigh distribution, but they do not have empirical UWB support for this. A Ricean distribution is assumed by [34] and they fit their data to this distribution. [42] claims that a Ricean distribution offers a good fit to data collected using a VNA with a short observation time. For larger observation intervals, [42] finds that a Nakagami distribution offers a good fit. [11][12] also suggest using a Nakagami distribution for path amplitudes based on the measurement campaign described in [82]. A lognormal distribution is suggested by [21] based on extrapolation from the wideband model given in [30]. In [86], a new distribution named POCA-NAZU is suggested for UWB path amplitudes. The POCA-NAZU distribution is similar to the Ricean distribution where a dominate path is assumed to be present, but unlike Ricean, only a small number of unresolvable paths contribute to each measured path.

Several researchers [11][87][21][42][39][34] propose using an exponential power decay model for the average power of successive multipath components. Some of the

researchers [11][42][39][34] base this on measurements while the rest simply extend wideband models to the UWB case.

References [13][14][69][85] propose using a variation of the CLEAN algorithm, originally developed for use in radio astronomy, to determine the angle of arrival (AOA) information of a channel and to differentiate multipath components that cover a large dynamic range.

Reference [42] proposes that a frequency dependent decay of the signal be added to the channel model. The use of a polynomial fit to the measured transfer function and a frequency power law model is suggested because they expect more attenuation at higher frequencies based on their measurements. Reference [75] proposes modeling the UWB channel in the frequency domain using a 2nd-order auto-regressive model that uses four complex parameters and one real parameter. This model accounts for frequency selectivity and can be implemented as an IIR filter.

A channel model based on the decomposition of the total field into scattering centers is proposed by [60][61]. This model uses numerical solutions of Maxwell's equations and considers the problem of channel model determination as analogous to radar target identification.

The IEEE 802.15 working group for wireless personal area networks is considering UWB systems for its physical layer standard. Based on the work of several of the previously mentioned research efforts (in section 2.2.1), a modified version of the Saleh-Valenzuela model has been adopted to allow fair performance comparisons for specific UWB implementation simulations [23]. It is noted that this is not a mature

model for UWB and more work must be done to better understand and characterize UWB propagation.

2.2.3 Other Measurements and Characterization

The NTIA also performed extensive UWB channel measurements, but with the primary purpose of observing and recording the temporal and spectral characteristics of UWB signals for use by the FCC and government agencies as an aid in making policies (based on the potential interference caused by UWB signals). Secondary purposes were to develop reliable and repeatable UWB measurement methods using COTS systems and to determine the effects of UWB signals on federal radar systems [41]. Experiments to determine the specific interference effects of UWB signals on GPS receivers were also analyzed [31][32]. While the goal of the NTIA in their measurements was different from channel modeling, they present UWB measurement techniques that could potentially be applied for other purposes.

In the NTIA effort to characterize UWB signals, five UWB devices were chosen out of an available twenty for testing. These were chosen so as to best represent a variety of pulse shapes and dithering types used by UWB systems currently available. The analysis was based on the measured waveforms and spectra only; no analysis was made of the device's ability to perform as the manufacturer intended (i.e. how well it communicated or how effective its imaging capabilities are). An electric drill conforming to FCC part 15 rules was also tested for comparison.

Two different types of measurements were made on the equipment being tested. 'Conducted' measurements were taken by connecting the output of the UWB device by coaxial cable through an attenuator to either a sampling oscilloscope or a single event

transient digitizer. The oscilloscope used has a bandwidth of 20 GHz and is capable of collecting 4096 samples per record. The single event transient digitizer was used for systems where the pulse repetition time varied and/or the pulse shape was not constant. The digitizer has a bandwidth of 4.5 GHz and is capable of collecting 1024 samples per shot. Total peak power and total average power were calculated from these measurements.

‘Radiated’ measurements performed in an anechoic chamber were also taken. A ridged horn antenna covering the frequency range from 1-4 GHz was used for some of the measurements and a NIST 30cm TEM horn antenna with frequency range from 0.2-4 GHz was used for the others. Various combinations of attenuators and amplifiers were used based on the signal strength of the UWB system tested.

In addition to these “full bandwidth” measurements, techniques and results from using bandlimited measurements of UWB are discussed. Bandlimited measurement techniques are useful particularly for interference modeling because they may closely match the bandlimited interference narrowband receivers experience. Also, bandlimited measurements may be useful, due to the difficulty of performing full bandwidth measurements and to the limited availability of such large bandwidth systems. Even using bandlimited measurements, several characterizations that may be derived are proposed, including: emission spectra as a function of IF measurement bandwidth; pulse width estimation; pulse shape as a function of IF measurement bandwidth; pulse repetition rate, sequence and gating; amplitude probability distributions; peak power; and average power.

Several measurable characteristics of the UWB signal become functions of the IF measurement bandwidth. As expected, the measured peak power decreases with decreasing measurement bandwidth. The amplitude probability distribution (APD) can be used as a description of how noise-like the UWB signal appears in the narrowband receiver. The ADP shows the percentage of time that emission exceeds a given power threshold. It was found that at relatively narrow measurement bandwidths, the noise appears almost Gaussian, but as the bandwidth increases, the noise appears more impulsive as the individual pulses become resolvable to the receiving system.

3 UWB Small Scale Channel Modeling

This chapter presents the results of the small scale characterization of the UWB indoor channel. These results are based on two different measurement efforts conducted by the Time Domain Laboratory of Virginia Tech. The first half of the chapter examines the significance of pulse distortion that may be caused when pulses pass through various materials in the environment. Since UWB systems are typically impulsive and have a much wider bandwidth than traditional communications systems, the impact of distortion must be considered to fully understand the effect of the channel on the UWB signal, while with narrowband signals, the impact of frequency dependent distortion is considered negligible. The second half of the chapter considers the overall indoor channel presenting several statistics, based on FIR impulse responses calculated using the CLEAN algorithm, which are useful for creating stochastic models. Knowledge gained from the findings presented in the first half are important toward validating some of the assumptions used in the second half. Some traditional stochastic small scale communications models are fit to the data and it is these type of models that are necessary for accurate analysis of UWB modulation schemes and receiver types.

3.1 Material Dependent Pulse Distortion

3.1.1 Distortion caused by Transmission through a Material

Due to the extremely wide bandwidth occupied by UWB pulses, it is expected that there would be some noticeable and possibly significant distortion due to dispersion and frequency dependent losses encountered from passing through or reflecting off various materials. Measurement data collected by the Time Domain Laboratory of

Virginia Tech to characterize the effect of different materials on UWB transmission is used here to analyze the effect different materials could potentially have on a communications receiver's performance. Details of the measurements are given in [48][50][51][52].

From the measurements, noticeable distortion was observed on pulses that had passed through a test brick wall setup, but not for most other materials. Therefore, here the focus is on the impact of the bricks. Therefore, the insertion transfer function (ITF) of the brick wall calculated from those measurements was used to predict the effect on a received pulse that passed through a similar brick wall at normal incidence and the effective loss due to correlating the distorted pulse with an undistorted pulse (one that had traveled through free space only). Two pulse types were analyzed: Gaussian-modulated sinusoidal pulses and Gaussian monocycles (first derivative of a Gaussian pulse).

Gaussian-modulated sinusoidal pulse (2-6 GHz)

In-phase and quadrature Gaussian-modulated sinusoidal pulses (refer to (1-7) and (1-8)) with 10 dB bandwidth from 2-6 GHz were created in simulation. These pulses were chosen because they allow simple creation of signals that span an arbitrary frequency band. The in-phase pulse was the 'transmitted' pulse for this simulation. These pulses are shown in Figure 3-1.

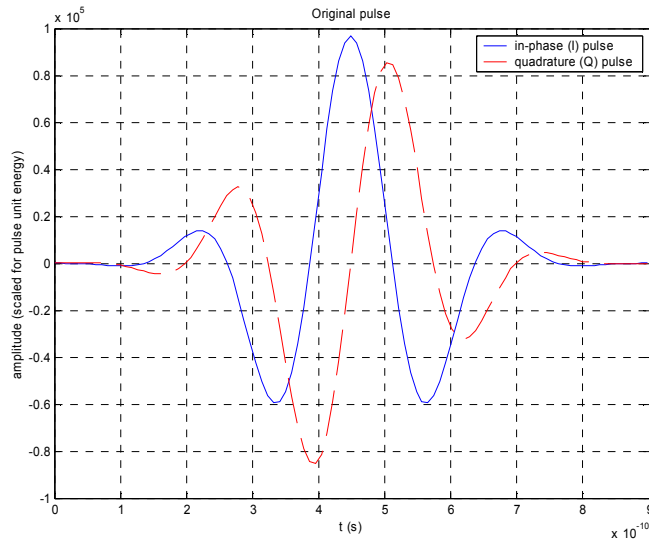


Figure 3-1. 2-6 GHz Gaussian-modulated sinusoidal pulses

The spectrum of the in-phase pulse was calculated using an FFT and is shown in Figure 3-2.

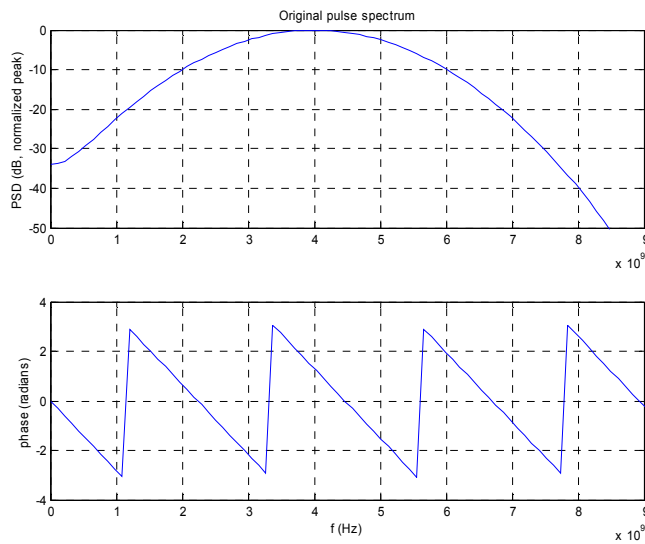


Figure 3-2. Spectrum of 2-6 GHz Gaussian-modulated sinusoidal pulse

The insertion transfer function of the material (bricks) was calculated from the data available (the magnitude of the ITF and the dielectric constant, ϵ_r') [48][50][51][52].

The data was linearly interpolated (and extrapolated outside the measurement range) to

match the frequency points of the pulse spectrum. The ITF of the bricks is shown in Figure 3-3.

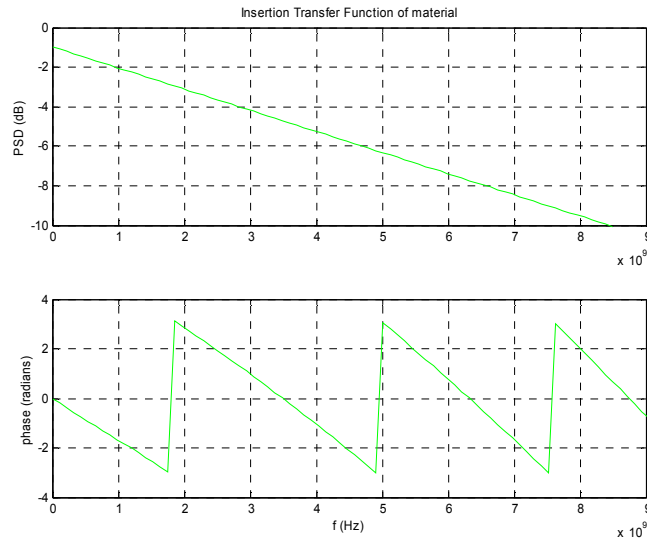


Figure 3-3. Insertion transfer function for bricks [48][50][51][52]

The pulse spectrum and the ITF were multiplied to give the spectrum of the distorted pulse, shown in Figure 3-4.

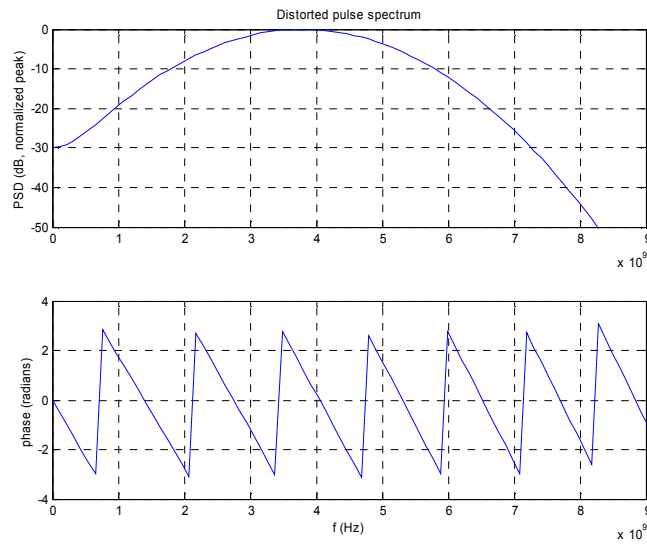


Figure 3-4. Spectrum of distorted 2-6 GHz Gaussian-modulated sinusoidal pulse

This spectrum was then inverse Fourier transformed (using an IFFT) and the resulting pulse is shown in Figure 3-5.

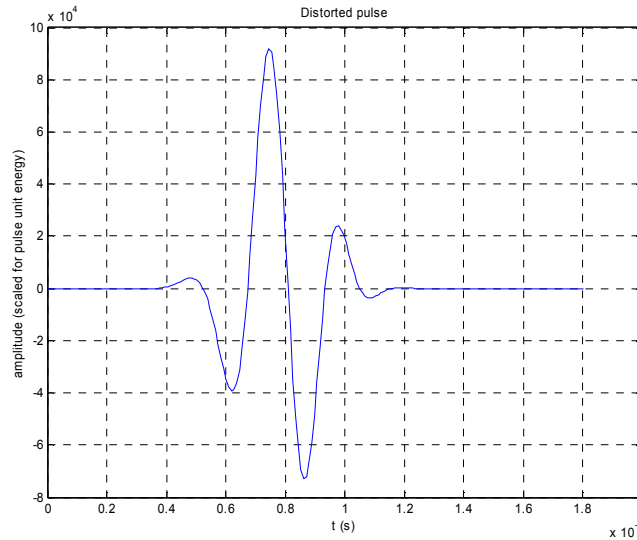


Figure 3-5. 2-6 GHz Gaussian-modulated sinusoidal pulse distorted by bricks

This pulse was then match filtered by each of the undistorted in-phase and the quadrature pulses. The pulses were all normalized to have unit energy so the correlation output is a measure of the correlator performance versus a perfectly matched correlator. The maximum correlation (positive or negative) with the in-phase pulse was 0.9667, which is a loss of 0.29 dB from an undistorted pulse, and the maximum correlation with the quadrature pulse was 0.9768, a loss of 0.20 dB.

Gaussian-modulated sinusoidal pulse (1-7 GHz)

The same procedure was carried out as before but with a pulse having 10 dB bandwidth from 1-7 GHz. The undistorted pulses are shown in Figure 3-6 and the distorted pulse is shown Figure 3-7. The maximum correlation (positive or negative) with the in-phase pulse was 0.9324, a loss of 0.61 dB, and the maximum correlation with the quadrature pulse was 0.9253, a loss of 0.67 dB.

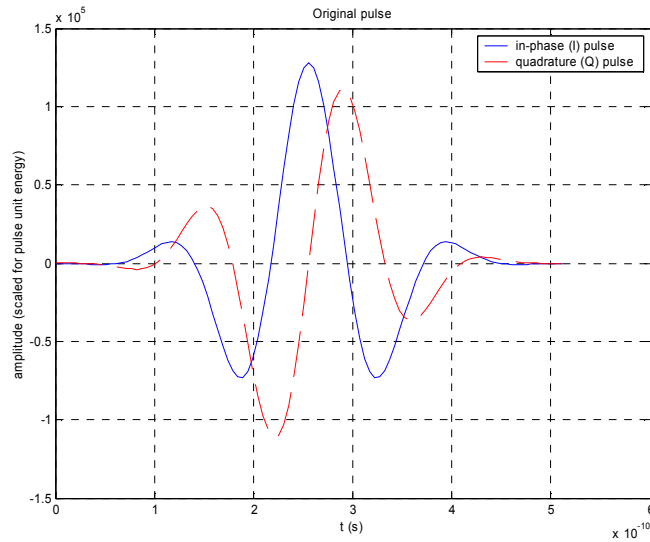


Figure 3-6. 1-7 GHz Gaussian-modulated sinusoidal pulses

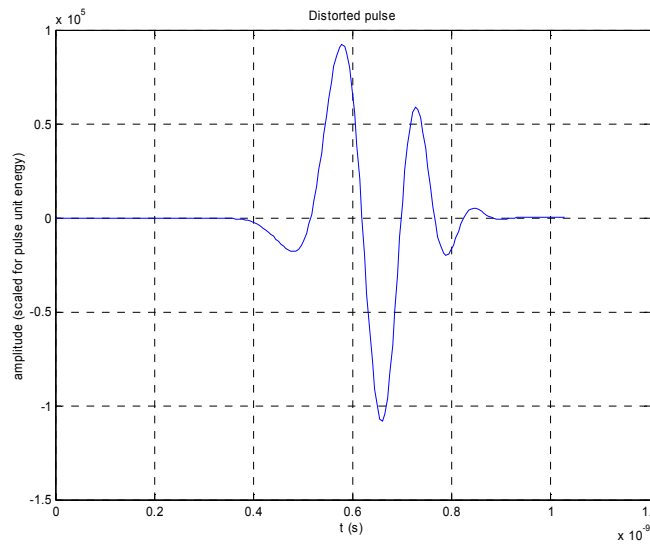


Figure 3-7. 1-7 GHz Gaussian-modulated sinusoidal pulse distorted by bricks

Gaussian monocycle pulse (0.5-5.7 GHz)

The same procedure was also carried out for two first derivative Gaussian pulses. The first derivative Gaussian monocycle, as defined in (1-5), considered has a 10 dB bandwidth from 0.5-5.7 GHz and is shown in Figure 3-8. The derivative of this monocycle, a second derivative Gaussian pulse, is also shown. The second derivative

pulse is considered as a possibility for correlation because the distorted monocycle pulse here and for other bandwidths begins to look somewhat similar to the second derivative pulse. The distorted monocycle is shown in Figure 3-9. The maximum correlation between the distorted pulse and the undistorted monocycle was 0.9641, a loss of 0.32 dB. The correlation between the distorted monocycle and the second derivative Gaussian pulse was 0.8065, a loss of 1.87 dB.

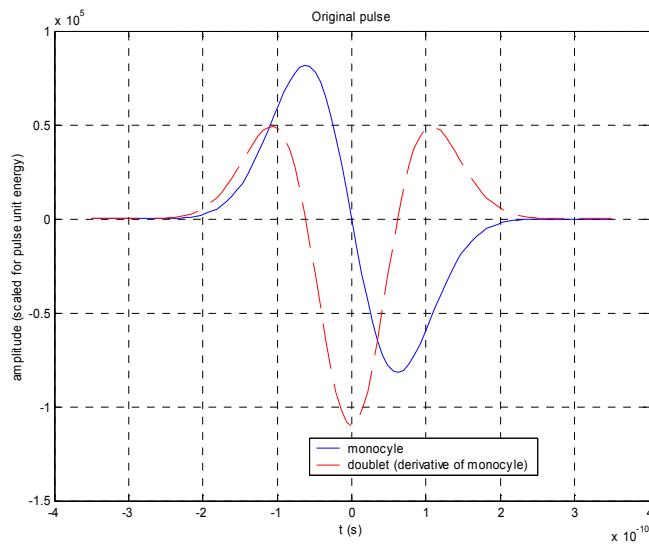


Figure 3-8. 0.5-5.7 GHz Gaussian-monocycle pulse (with its derivative)

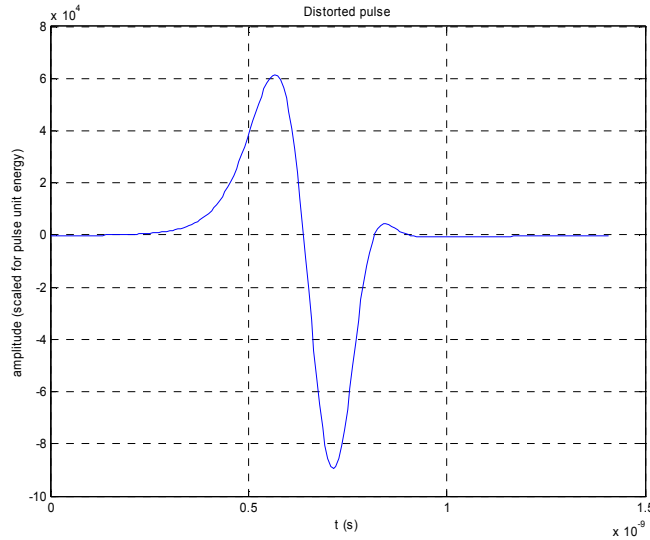


Figure 3-9. 0.5-5.7 GHz Gaussian-monocycle pulse distorted by bricks

Gaussian monocycle pulse (0.9-10.0 GHz)

The second monocycle had a 10 dB bandwidth from 0.9-10.0 GHz and is shown in Figure 3-10. The corresponding second derivative Gaussian pulse is also shown. The distorted monocycle is shown in Figure 3-11. The maximum correlation between the distorted pulse and the undistorted monocycle was 0.8037, a loss of 1.90 dB. The correlation between the distorted monocycle and the second derivative Gaussian pulse was 0.7394, a loss of 2.62 dB.

A summary of the correlation loss that a receiver would see when receiving a UWB signal distorted by transmission through a brick wall for the different pulses considered is shown in Table 3-1. For a pulse with a 10 dB bandwidth greater than 9 GHz, the correlation loss was shown to be less than 2 dB. Further, for the other materials measured (except the concrete blocks), the distortion caused was negligible compared to the bricks. It should be noted that the overall attenuation caused by the bricks was also much higher (2.06-8.48 dB over 1-7 GHz [48][50][52]) than for the other materials

(except the concrete blocks). For the concrete blocks, the distortion was much greater, but the attenuation was also extremely high compared to all other materials considered.

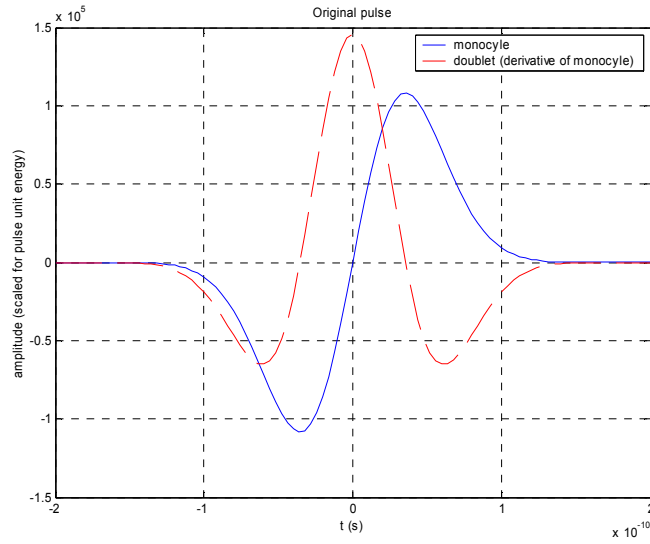


Figure 3-10. 0.9-10.0 GHz Gaussian-monocycle pulse (with its derivative)

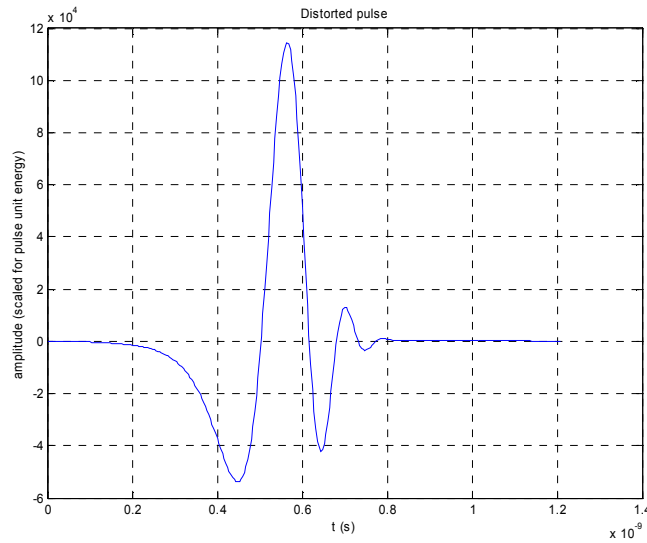


Figure 3-11. 0.9-10.0 GHz Gaussian-monocycle pulse distorted by bricks

Table 3-1. Correlation loss from distortion caused by passing through bricks

pulse	correlation loss (dB)	
	<i>correlated w/ undistorted pulse</i>	<i>correlated w/ quadrature pulse</i>
Gaussian modulated sinusoid, 2-6 GHz	0.29	0.20
Gaussian modulated sinusoid, 1-7 GHz	0.61	0.67
	<i>correlated w/ undistorted pulse</i>	<i>correlated w/ 2nd derivative pulse</i>
1st deriv Gaussian pulse, 0.5-5.7 GHz	0.32	1.87
1st deriv Gaussian pulse, 0.9-10 GHz	1.90	2.62

3.1.2 Significance of Distorted Reflections to Performance of Correlation Receiver

A Gaussian shaped pulse was used as the source to feed a TEM antenna used as the transmitter in the measurements used to calculate the following results. Typically, TEM horn transmitting antennas are considered to have a differentiation effect on the signal fed into it. The balun used appears to be acting as a bandpass filter on the pulse. These effects must be accurately accounted for to predict the transmitted (and then received) signal shape. If these effects are accounted for, a reasonable correlation template pulse can be constructed from the generated pulse (a property that would be desirable in a communications receiver, where the same type of pulse generator is likely to already be present due to its use in that user's transmitter). A bandpass filtered and then differentiated version of the Gaussian pulse was generated to be used as a correlation template pulse and is shown in Figure 3-12.

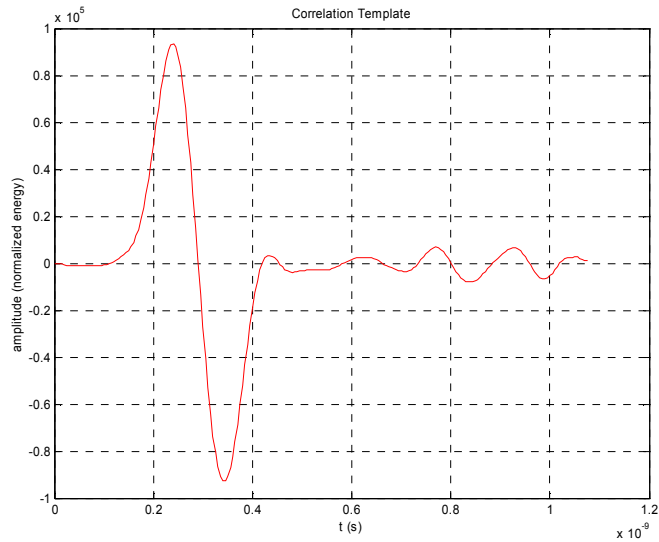


Figure 3-12. Correlation template for Gaussian filtered pulse source

Relative strength of the direct path to reflected path

The template pulse shown in Figure 3-12 was used as a matched filter on measurement data for the various tested scenarios. The measurements were taken at relatively short distances and the dominant elements in the received signal are due to the LOS path and a path that has reflected off the floor. The reflected pulse has noticeable distortion with reference to the LOS path. This distortion is primarily due to the angle of arrival at the receiving antenna. Pulse distortion caused by the angle of arrival for these TEM horn antennas is discussed in [48] and [3]. Other experiments performed by the Time Domain Laboratory confirm that the distortion is primarily due to the angle of arrival rather than the reflection off the floor.

The ratio of amplitudes of the correlation outputs of the direct path and the reflection off the floor were calculated. The template is a good match for the direct path pulse, but it is not nearly as good of a match for the reflection path. This ratio is thus a measure of the combination of the relative signal strength and the distortion experienced

by the reflected path (distortion being the change in shape of the signal that leads to a poor match with the template pulse). These calculated ratios are shown in Table 3-2.

Table 3-2. Ratios of correlations of direct vs. reflected pulses with template pulse

measurement test	material	energy captured direct/reflected (dB)
1	No material	16.19
	Drywall ('Wallboard')	15.81
2	No material	7.18
	Office partition	5.70
3	No material	16.39
	Particle board ('structure wood')	15.71
4	No material	8.19
	Wooden Door	7.73
5	No material	7.55
	Plywood	7.01
6	No material	16.38
	Glass	15.53
7	No material	7.68
	Styrofoam	7.44
8	No material	8.01
	Bricks	17.26
9	No material	7.57
	Concrete Blocks	8.93

The large variation in the calculated ratios for the various data sets where no material was present is at first somewhat unexpected. However, it is important to note that TEM horns were used in these measurements and signals that arrive off bore-sight can be significantly attenuated and also distorted. The different measurement scenarios listed quite likely had different transmitter-receiver distances and therefore the reflected pulses to and from the horns were at different angles to bore-sight, causing loss and distortion (which could result in poorer correlation, not capturing all of the available energy). Therefore, from this data, it is difficult to make any isolated conclusions about the loss and distortion on UWB pulses due only to reflections off objects in the operating

environment. This data does help provide some measure of the expected energy capture possible for a system using horn antennas and a single correlation template at the receiver.

Performance of correlation receiver and two finger Rake receiver

First, the energy of the measurement data was normalized so that each measurement set had unit energy so that the loss introduced by using a single correlation template (the one shown in Figure 3-12) for both paths of two finger Rake receiver could be evaluated. The correlation outputs corresponding to the direct and reflected components were used to compute the fraction of the total available energy that was captured using either one or two correlators (or Rake fingers). The loss of using this template as compared to using an ideal receiver (one that in some way optimally captures all the available energy) is shown in Table 3-3.

In general, the greater the loss from an ideal receiver indicates that the received pulses are more distorted with reference to the template pulse. This is especially pronounced in the case of the concrete blocks where the loss due to imperfect correlation is greatest of these sample cases and the received signal also appears more distorted (see Figure 3-13). However, this is not a perfect measure of the distortion as some cases that appear to have less distortion than others upon inspection of the received signals (for example the office partition versus the bricks) but have a higher correlation loss. This is influenced some by environmental factors and the measurement interval. For example, from inspecting the office partition data (Figure 3-14, bottom), it appears that a couple other weaker multipath components may also be present influencing the energy normalization calculation and thus reducing the fraction of the captured energy. Since the exact environment (primarily transmitter-receiver distance and also distance to other

reflectors such as walls) is potentially different for each measurement case, the influence of the changes in the environment may also be influencing these calculations. Again, the effect of the antennas (and their separation and orientation relative to the reflectors) likely had a large impact on the consistency of these calculations. Viewing, the free space measurements corresponding to the office partition (Figure 3-14, top) and the bricks (Figure 3-15, top), it appears that the reflected component of Figure 3-14, top, may be more distorted than the reflected component of Figure 3-15, top, which as discussed above is most likely due to the effects of the angle of arrival/departure relative to the horn antenna.

Table 3-3. Loss of receivers using the template pulse versus an ideal receiver

measurement test	Material	Loss of single correlation from ideal (dB)	Loss of two finger Rake from ideal (dB)
1	no material	0.98	0.88
	Drywall ('Wallboard')	1.05	0.93
2	no material	2.39	1.63
	Office partition	3.31	2.27
3	no material	0.92	0.82
	Particle board ('structure wood')	1.12	1.01
4	no material	1.94	1.33
	Wooden Door	2.28	1.60
5	no material	2.20	1.50
	Plywood	2.51	1.73
6	no material	0.89	0.79
	Glass	1.05	0.93
7	no material	2.20	1.52
	Styrofoam	2.26	1.54
8	no material	2.10	1.47
	Bricks	2.49	2.40
9	no material	2.33	1.63
	Concrete Blocks	6.42	5.89

For reference, example plots of the measurement data [48][50] are shown below so the direct (blue) versus reflected components (red) can be compared visually.

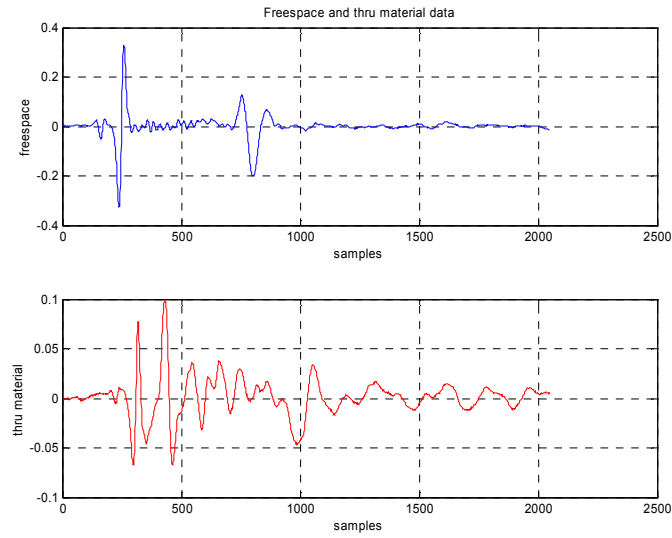


Figure 3-13. Freespace and through concrete blocks measurements

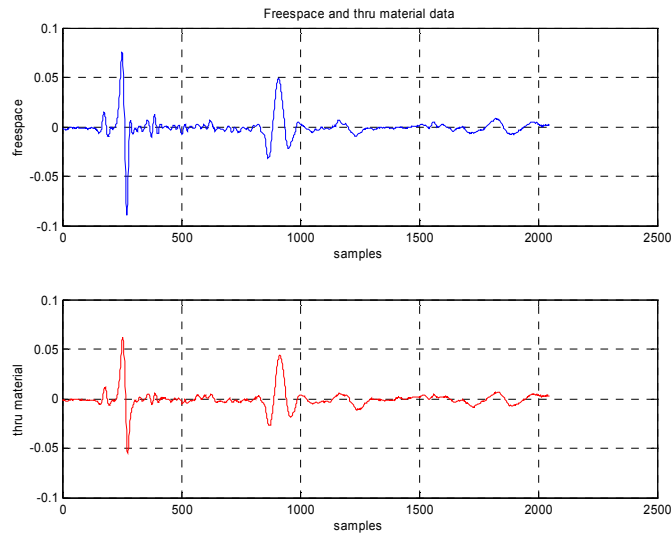


Figure 3-14. Freespace and through office partition measurements

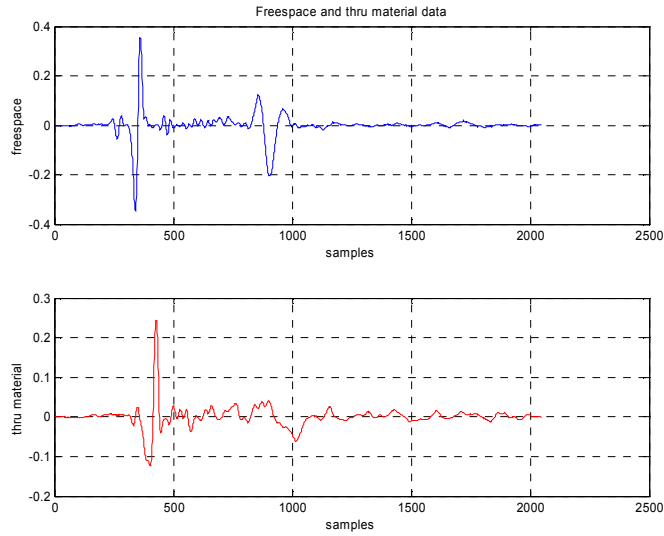


Figure 3-15. Freespace and through bricks measurements

This analysis of the material characterization measurements reveals that when UWB signals pass through many common materials found in indoor environments, the frequency dependent distortion is minimal. For the materials that cause significant distortion to UWB signals, the signal is also heavily attenuated. Therefore, in the cluttered indoor environment, such attenuated multipath components will likely not contribute significantly to the overall received signal, where less attenuated (and less distorted) multipath components will dominate. It has also been shown that multipath components that arrive off the bore-site of the receiving antenna will be distorted, but the loss in performance to a receiver that uses only a single correlations is in many cases is small. This also suggests that care must be taken when using directional antennas for short range UWB communications because off-boresite pulses do not match a LOS template. The overall indoor channel is dominated by multipath reflections as opposed to material dependent distortion. The distortion caused by reflections and diffraction off different materials still needs to be examined.

3.2 Small Scale Indoor Channel Modeling

Numerous indoor UWB measurements were taken by researchers of the Time Domain Laboratory of Virginia Tech. Both LOS and a limited number of NLOS measurements were taken. Measurements were taken using a pulse generator capable of generating pulses each with duration of less than 200 ps, a 20 GHz digital sampling oscilloscope (DSO), and either a set of TEM horn antennas or a set of biconical antennas. Details of the specific measurement scenarios and measurement system used are given in [48].

3.2.1 Data Processing and Analysis Methodology

The received signal from a measurement set can be represented in the frequency domain as

$$R(f) = \int_0^{\pi} \int_0^{2\pi} \int_0^{\pi} \int_0^{2\pi} P_{gen}(f) H_{tx,ant}(f, \theta_{tx}, \phi_{tx}) H_{chan}(f, \theta_{tx}, \phi_{tx}, \theta_{rx}, \phi_{rx}) H_{rx,ant}(f, \theta_{rx}, \phi_{rx}) d\theta_{tx} d\phi_{tx} d\theta_{rx} d\phi_{rx} \quad (3-1)$$

where $P_{gen}(f)$ is the Fourier transform of generated pulse, and the $H_{x,x}(f, \dots)$ are the transfer functions of the antennas and the channel, which are all functions of frequency and the three dimensional antenna structure or environment. However, this is an overly complicated expression and would be exceptionally difficult to evaluate and use for analysis. Therefore, the angular dependencies of the responses are subsumed into the channel impulse response. Therefore, the resulting channel impulse response from analysis will be somewhat antenna dependent, but will still offer general characterization of the channel as would be seen by similar antennas (similar in this case being most significantly the spatial pattern of the antenna). For the receiving antenna, some distortion is expected as a function angle of arrival (AOA). The significance of

neglecting AOA distortion at the receiving antenna is discussed below. Applying these assumptions, the received signal can be approximated by

$$R(f) \approx P_{gen}(f) H_{tx,ant}(f) H_{chan}(f) H_{rx,ant}(f) \quad (3-2)$$

or in the time domain

$$r(t) = p_{gen}(t) * h_{tx,ant}(t) * h_{chan}(t) * h_{rx,ant}(t) \quad (3-3)$$

It is desired to extract the channel impulse response, $h_{chan}(t)$, from the measured data, $r(t)$. Knowledge of $h_{chan}(t)$ allows a general analysis of UWB channels independent of the generated pulse, $p_{gen}(t)$, and largely independent of the antennas used. The convolution of both antenna responses with the generated pulse is what the received signal would be if the channel were not present (or equivalently, the impulse response were equal to an impulse). If the channel is freespace, the impulse response is simply an impulse at a delay equal to the propagation time

$$r_{freespace}(t) = p_{gen}(t) * h_{tx,ant}(t) * \delta(t - \tau) * h_{rx,ant}(t) \quad (3-4)$$

A direct unobstructed LOS path with no reflectors/diffractors in the environment is very nearly equivalent to freespace. Therefore, if a received pulse from only the LOS path can be isolated from pulses arriving along other paths through time gating, this pulse can be used to determine the channel impulse response.

$$p_{rx,LOS}(t) \approx p_{gen}(t) * h_{tx,ant}(t) * h_{rx,ant}(t) \approx r_{freespace}(t + \tau) \quad (3-5)$$

These combined effects will be removed from the received signal by deconvolving the LOS pulse from the received signal to estimate the channel impulse response where

$$r(t) = p_{rx,LOS}(t) * h_{chan}(t) \quad (3-6)$$

Deconvolution techniques are discussed below.

It must be noted that if the angular dependencies of the antennas are subsumed into the channel response, the directivity of the antennas still influence the calculated channel impulse response even when angular dependent pulse distortion is neglected. The channel impulse response for directional antennas (such as TEM horns) would not be influenced significantly by reflectors/diffractors behind the antennas. However, the channel impulse response for omnidirectional (in one plane only) antennas would be affected by more reflectors/diffractors in the environment than the directional antennas. Therefore, since the channel impulse response is affected by the directivity of the antennas used for the measurement, the characterizations of data for the TEM horns and the bicones are performed independently.

Deconvolution Techniques

Deconvolution is the process of separating two signals that have been combined by convolution. Several deconvolution techniques have been developed [66], often for specific types of signals or for use with a specific application. Deconvolution can be performed in the time domain or the frequency domain. Different techniques will emphasize different aspects of the deconvolved signal and can offer different advantages depending on what further analysis is desired.

In the frequency domain, the most straightforward deconvolution method is known as inverse filtering [76]. $x(t)$ and $y(t)$ are known and $h(t)$ is the signal to be determined where

$$y(t) = x(t) * h(t) \quad (3-7)$$

In the frequency domain, this can be represented equivalently as

$$Y(f) = X(f)H(f) \quad (3-8)$$

where $Y(f)$, $X(f)$, and $H(f)$ are the Fourier transforms of $y(t)$, $x(t)$, and $h(t)$, respectively. By dividing $Y(f)$ by $X(f)$, $H(f)$ can be determined. However if $Y(f)$ is noisy at frequencies where $X(f)$ is small, the estimate of $H(f)$ will be unreliable (and not defined where $X(f) = 0$). Therefore, $H(f)$ at these frequencies can be zeroed out to minimize the impact of noise on the impulse response. This approach effectively bandlimits the estimated signal $H(f)$ (and thus $h(t)$). Therefore

$$H(f) = \begin{cases} \frac{Y(f)}{X(f)}, & |X(f)| > \text{threshold} \\ 0, & |X(f)| < \text{threshold} \end{cases} \quad (3-9)$$

The impulse response, $h(t)$, is then simply the inverse Fourier transform of $H(f)$.

Another technique that has been widely used is the Van-Cittert deconvolution technique. This iterative method can be performed in either the time or frequency domain. Reference [7] proposes using this technique in the frequency domain and they also propose criteria to optimize the number of iterations to use. In the frequency domain, $H(f)$ is computed by

$$H_i(f) = H_{i-1}(f) + \tilde{Y}(f) - \tilde{X}(f)H_{i-1}(f) \quad (3-10)$$

$$H_0(f) = \tilde{Y}(f)$$

where

$$\begin{aligned} \tilde{Y}(f) &= \frac{AX^*(f)Y(f)}{\max[|X(f)|^2]} \\ \tilde{X}(f) &= \frac{AX^*(f)X(f)}{\max[|X(f)|^2]} = \frac{A|X(f)|^2}{\max[|X(f)|^2]} \end{aligned} \quad (3-11)$$

where A is a constant less than 1. $Y(f)$ and $X(f)$ are scaled and blurred to give $\tilde{Y}(f)$ and $\tilde{X}(f)$ to assure that the convergence conditions of this technique are satisfied [7].

This technique approaches inverse filtering (without any zeroing out of certain frequencies) as the number of iterations approaches infinity. At any stage of iteration, the response is effectively a low pass filtered version of the inverse filtered response. The bandwidth of the low pass filter increases with the number of iterations. Therefore, [7] suggests breaking the signals into a pass band (or information region where $X(f)$ has significant energy) and a stop band (or noise region where $X(f)$ is negligible). For each band, the standard deviation of the difference between $H_i(f)$ and $H_\infty(f)$ is calculated by

$$\sigma_{H_{diff}} = \sqrt{\frac{1}{f_h - f_l} \int_{f_l}^{f_h} |H_i(f) - H_\infty(f)|^2 df} \quad (3-12)$$

It is desirable to have the standard deviation near minimum in the pass band and near maximum in the stop band. This indicates that $H(f)$ is well matched in the desired frequency range and minimized in the noise dominated stop band. The standard deviation is normalized to a maximum of 1 for each band for analysis. Parameters can be specified (such as the pass and stop bands and the desired normalized standard deviations for these bands), but there is no guarantee that these criteria can be met. Therefore, this technique with optimization criteria can be difficult to automate for all possible signals.

The third deconvolution technique considered is the CLEAN algorithm which is a time domain technique. The CLEAN algorithm has been used by other researchers in UWB channel measurement analysis [85]. The CLEAN algorithm uses match filtering to find the strength and delay of individual multipath components. This algorithm assumes

the response to be determined is discrete in nature, while the previously described techniques assume the impulse response is a continuous, bandlimited function. Through the iterative nature of the CLEAN algorithm, discrete components in the impulse response (individual multipath components) that are separated by less than the duration of $x(t)$ (the pulse width) can be resolved. To use the CLEAN algorithm to estimate the impulse response of a channel, it is assumed that there is no significant pulse distortion caused to any of the paths. This assumption agrees with the findings of section 3.1.

To perform the CLEAN algorithm, the autocorrelation of $x(t)$ and the cross-correlation of $x(t)$ and $y(t)$ must be calculated.

$$c_{xx}(t) = \int_{-\infty}^{\infty} x(\tau)x(t+\tau)d\tau \quad (3-13)$$

$$c_{xy}(t) = \int_{-\infty}^{\infty} x(\tau)y(t+\tau)d\tau \quad (3-14)$$

Then peaks are found, recorded, and subtracted from the cross-correlation function as follows

$$h_i(t) = h_{i-1}(t) + A_i\delta(t - \tau_i) \quad (3-15)$$

$$h_0(t) = 0$$

$$d_i(t) = d_{i-1}(t) - A_i c_{xx}(t - \tau_i) \quad (3-16)$$

$$d_0(t) = c_{xy}(t)$$

where

$$|d_{i-1}(\tau_i)| = \arg \max_t |d_{i-1}(t)| \quad (3-17)$$

$$A_i = d_{i-1}(\tau_i)$$

Some stopping criteria must be established to stop iteration of the algorithm. A threshold, V , can be established such that if $|A_i| < V \max |c_{xy}(t)|$, the algorithm is ended. Some researchers [57] have suggested using an energy capture ratio as the stopping criteria (this characterization of the calculated impulse response is discussed in section 4.3). Discussion of the accuracy and limitations of the CLEAN algorithm are given in Chapter 4.

The CLEAN algorithm was chosen as the primary method for determining the channel impulse responses. The frequency domain techniques considered here treat the impulse response as bandlimited, while the indoor propagation channel is not expected to be bandlimited*. The frequency domain techniques examined may provide useful responses for use in fitting the data to models that characterize the channel in the frequency domain such as is proposed in [33][75]. However, this work focuses on time domain characterization of the channel and the discrete nature of this algorithm makes the resulting impulse responses more reasonable to characterize statistically in the time domain. The bandlimited impulse responses can be discretized by breaking the time axis into bins and calculating the energy contained in each bin. However, the time resolution would be limited to approximately the pulse duration (the inverse of the pulse bandwidth) and the arrival times would be limited to fixed delays based on the bin divisions, which does not agree well with the observed measurement results. Examples of the impulse responses generated by each deconvolution method for a specific measurement set are shown in Figure 3-16 for comparison. The inverse filtering impulse response and the Van-Cittert impulse response are nearly identical and the CLEAN impulse response

* The channel is not expected to be bandlimited relative to the bandwidth of the sounding pulse used.

shows the same primary features of the channel. Estimates of the received signal can be generated by convolving the impulse response with the LOS pulse used in the deconvolution. The measured signal is plotted with the estimates of this signal using the impulse responses from each of the three deconvolution techniques in Figure 3-17. Visually, the measured signal, the inverse filter reproduced signal, and the Van-Cittert reproduced signal are nearly identical. Noticeable differences are seen between the measured signal and the CLEAN reproduced signal, but the signals still agree reasonably well.

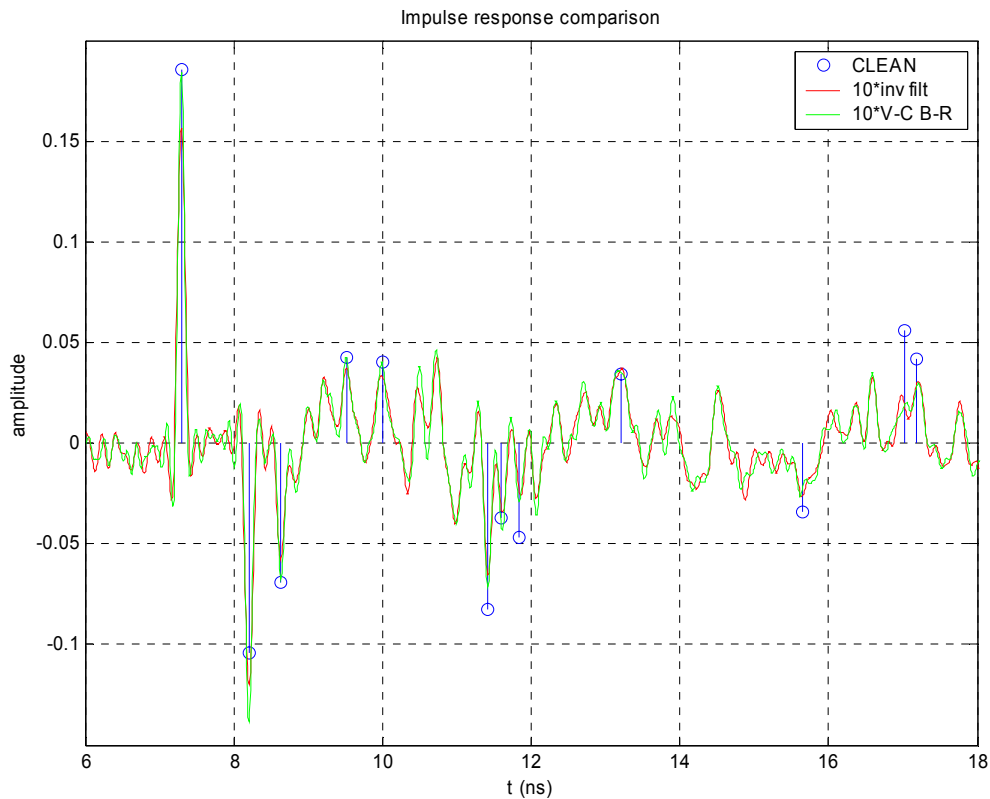


Figure 3-16. Comparison of impulse responses generated by the CLEAN algorithm (blue), inverse filtering (red), and the Van-Cittert techniques with Bennia-Riad criteria (green) (Note: the latter 2 responses have been scaled by 10 to allow for easier visual comparison)

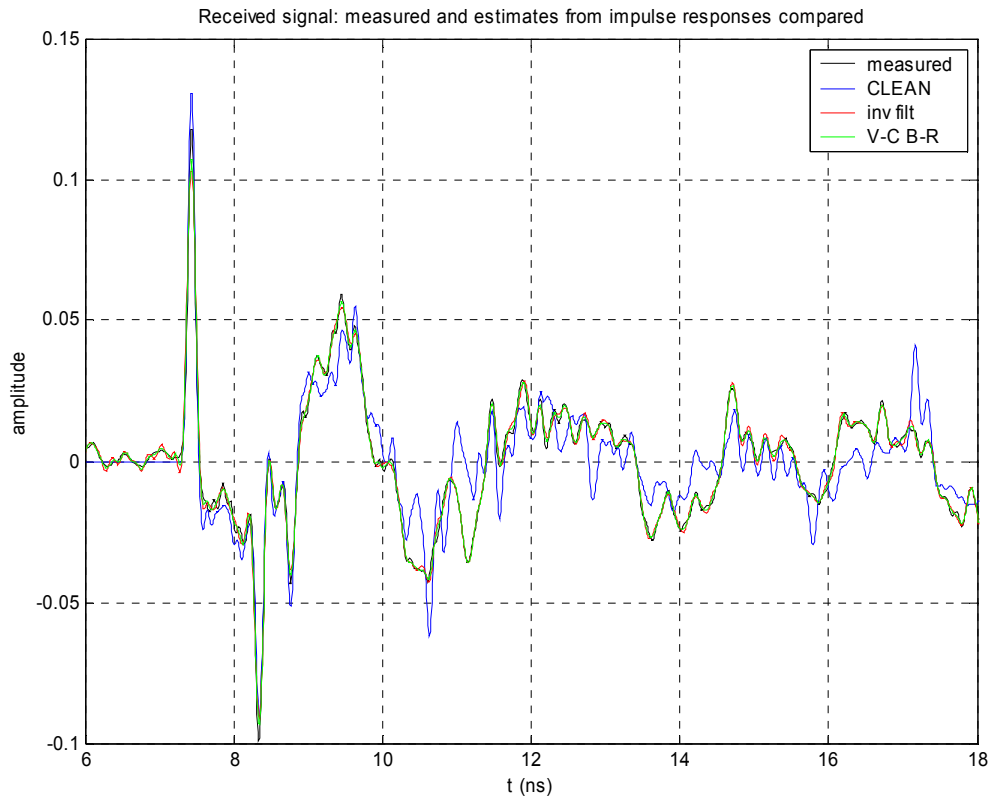
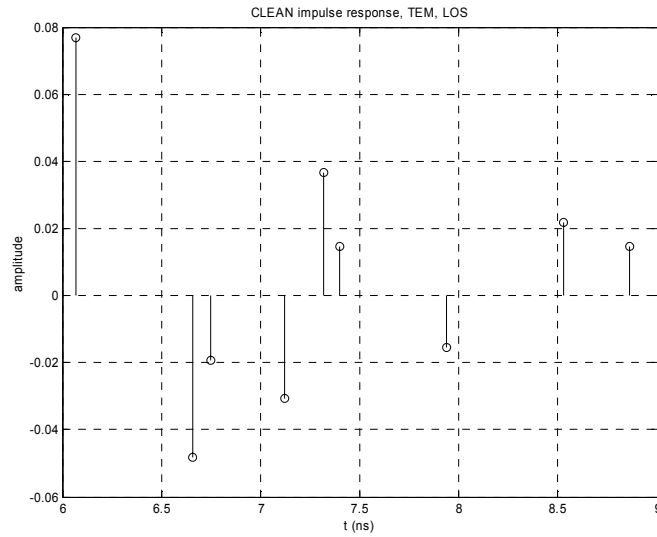


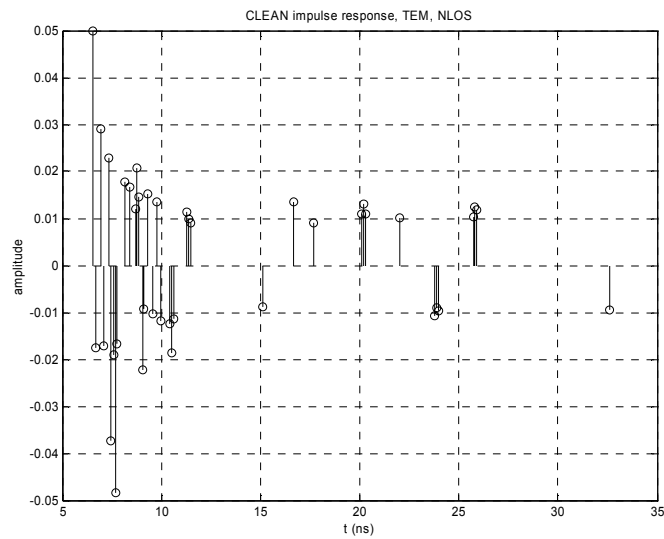
Figure 3-17. Comparison of measured signal (black) with estimates of the received signal based on the impulse responses generated by the CLEAN algorithm (blue), inverse filtering (red), and the Van-Cittert techniques with Bennia-Riad criteria (green)

The measured data was first filtered from 0.1-12 GHz to remove the effects of a 30 MHz spurious signal from the pulse generator output. The CLEAN algorithm [85] was performed on all the data signals to deconvolve the response of the antennas from the channel impulse response (a reference LOS pulse was deconvolved from each measurement set). The CLEAN algorithm was stopped after the remaining undetected paths were below -15 dB of the peak path strength. The data was separated into sets based on the antenna type, directional (TEM horns) or omnidirectional (biconical antennas), and environment (LOS or NLOS). Samples of impulse responses calculated from the CLEAN algorithm using the -15 dB threshold are shown in Figure 3-18.

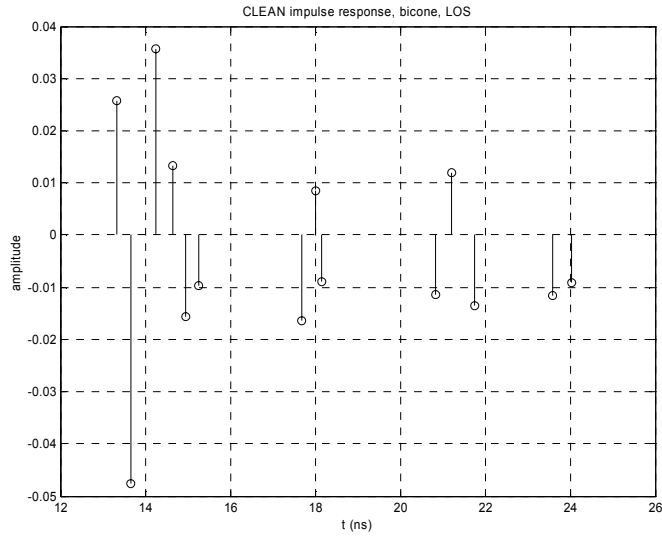
The same processing procedure was repeated with a -20 dB threshold level cutoff level and the basic channel statistics were calculated to determine the sensitivity of the measurements to the threshold level used.



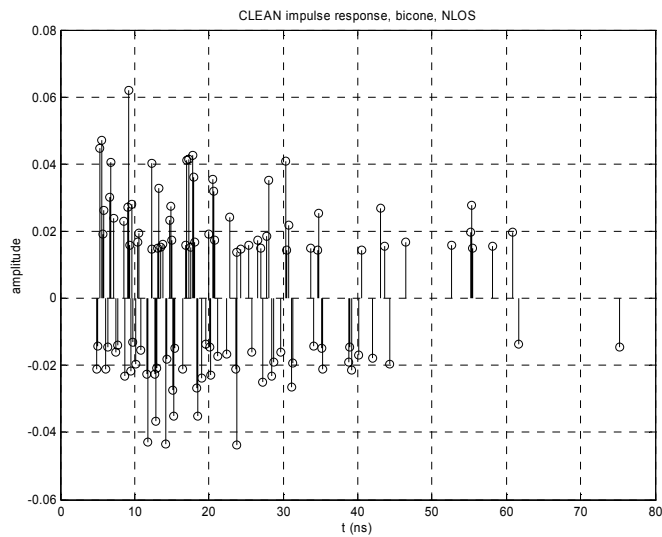
(a)



(b)



(c)



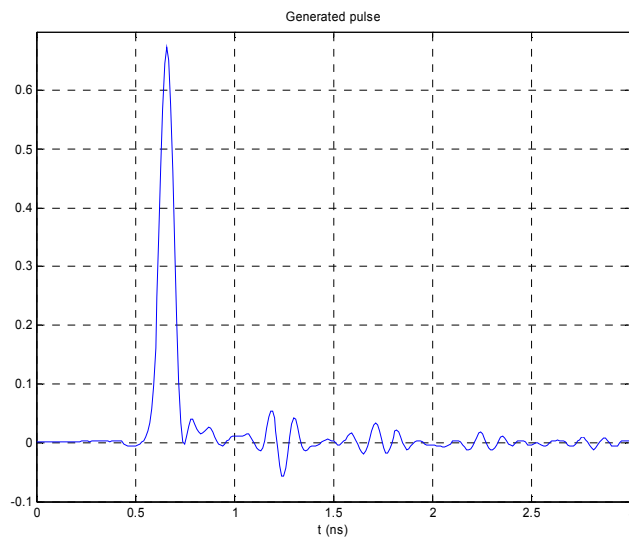
(d)

Figure 3-18. Sample impulse responses calculated by the CLEAN algorithm using a -15 dB threshold cutoff. (a) TEM horns, LOS; (b) TEM horns, NLOS; (c) bicones, LOS; (d) bicones, NLOS

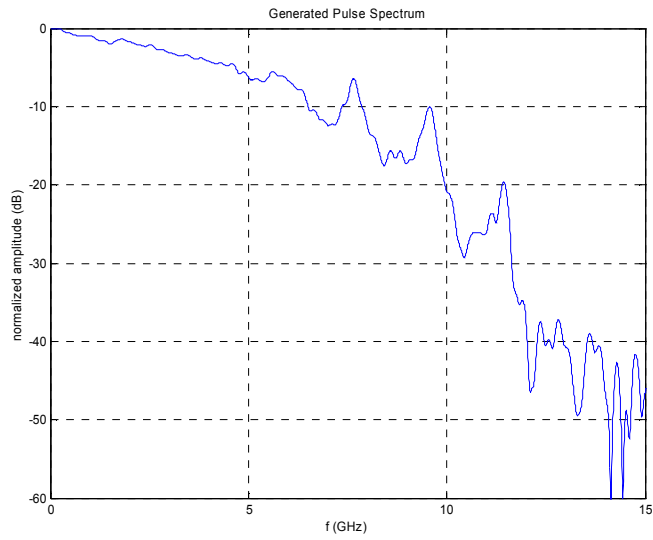
Reference Pulse

To determine an appropriate windowing interval to capture only the LOS pulse from a short range measurement set, the transient response of the antennas must be known (or at least approximately known).

The TEM horns are well designed for pulse radiation and the transient response of these antennas dies down very quickly. From a measurement set corresponding to the horns facing each other with a separation of 1.00 m, the relative arrival time of the second path (floor) is known. Therefore, when windowing the data to capture only the first path, the relative (to the peak value) instantaneous power level is above -25 dB for less than 0.93 ns. The significant transient response of the antenna is likely less, because the ‘ringing’ seen after the main pulse is also present in the generated pulse (shown in Figure 3-19). The reference LOS pulse used for deconvolution (where the instantaneous power has dropped below -25 dB) is shown in Figure 3-20.

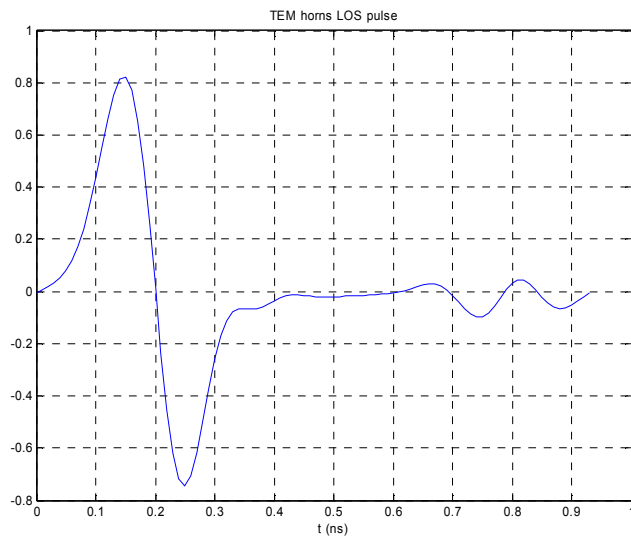


(a)

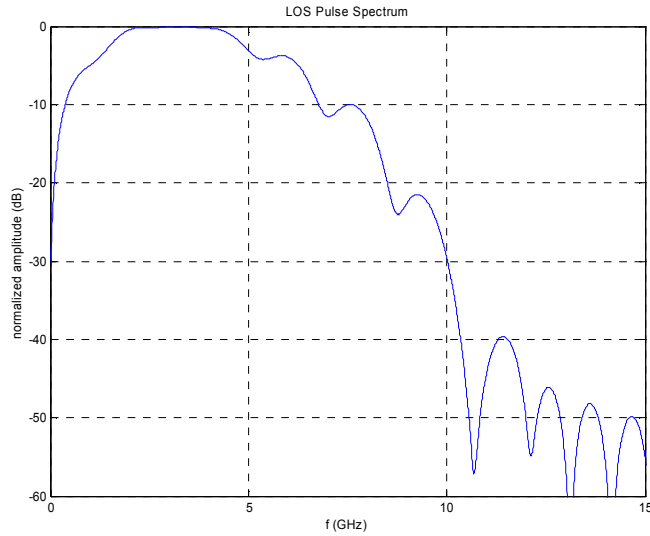


(b)

Figure 3-19. (a) Generated pulse (fed directly to antenna) and (b) its amplitude spectrum



(a)



(b)

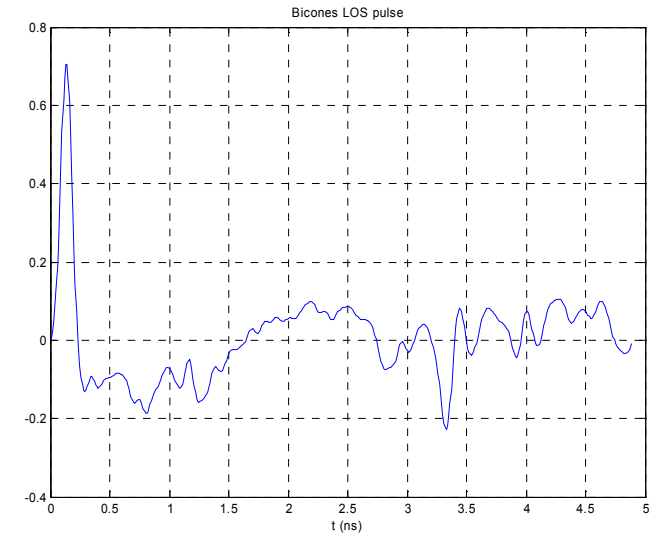
Figure 3-20. (a) LOS reference pulse for TEM antennas and (b) its amplitude spectrum

The angle of arrival at the receiving horn antenna also affects the received signal strength and pulse shape. Reference [49] illustrates this distortion and shows that in the specific measurement scenario presented, a significant amount of energy can be lost if only one template pulse is used for deconvolution*. However, it must be noted that [49] presents a modified form of deconvolution* and their aims are somewhat different than those here.

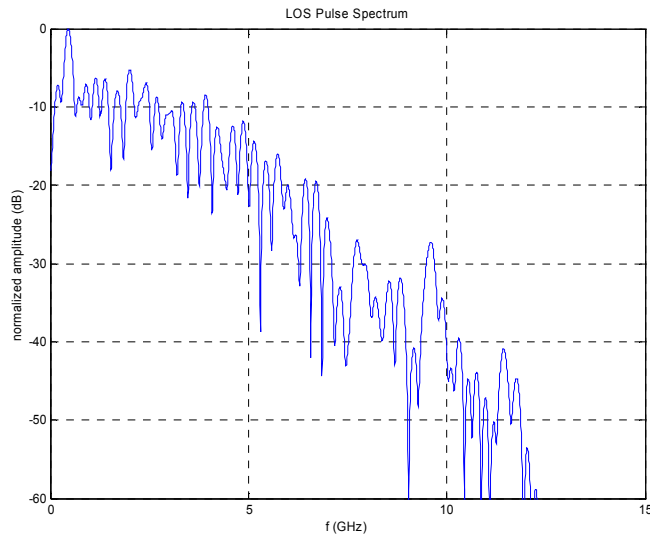
The biconical antennas are ‘wideband’ antennas but are not specifically designed for impulse radiation. These antennas were characterized in the Virginia Tech Antenna Group (VTAG) anechoic chamber at 0, 30, 60 and 90 degrees from vertical. To estimate the duration of the LOS pulse when using these antennas, the transient response was analyzed and determined to be above -20 dB (relative to the peak value) over a duration of 3.85 ns and above -23 dB over a duration of 4.90 ns. In the shortest range

* The deconvolution referred to in [49] is really a measure of the resolvable multipaths available to a Rake receiver and is not deconvolution in the traditional sense.

measurement distance, the floor reflection path was expected to arrive approximately 5.5 ns after the direct path. Therefore, the LOS template was chosen based on the -23 dB instantaneous power level and is shown Figure 3-21.



(a)



(b)

Figure 3-21. (a) LOS reference pulse for bicone antennas and (b) its amplitude spectrum

The significance of the distortion caused by the angle of arrival was evaluated based on the antenna characterization data. Each of the transient responses

corresponding to different elevation angles was convolved with the generated pulse (Figure 3-19) and they are all shown in Figure 3-22 for comparison. The energy of each resulting signal (normalized to the energy found at 0 degrees) was calculated and is shown in Table 3-4. As expected, the received energy decreases with increasing angle. The correlated energy of the signals with the signal received at 0 degrees was calculated and is also shown in Table 3-4 (note: the signals were not normalized to unit energy before correlation, so the correlation value represents the difference in the energy and the pulse shape). The use of a single template pulse to remove the antenna effects from the channel response is justified by the following: 1) The pulses arriving at angles off the main lobe of the antenna have significantly reduced energy and thus contribute far less to the effective channel response. 2) Most omnidirectional antennas are only omnidirectional in one plane (as is true with the bicones) and will have similar effects (i.e. reduction in signal strength and change in pulse shape) as the elevation angle of arrival increases.

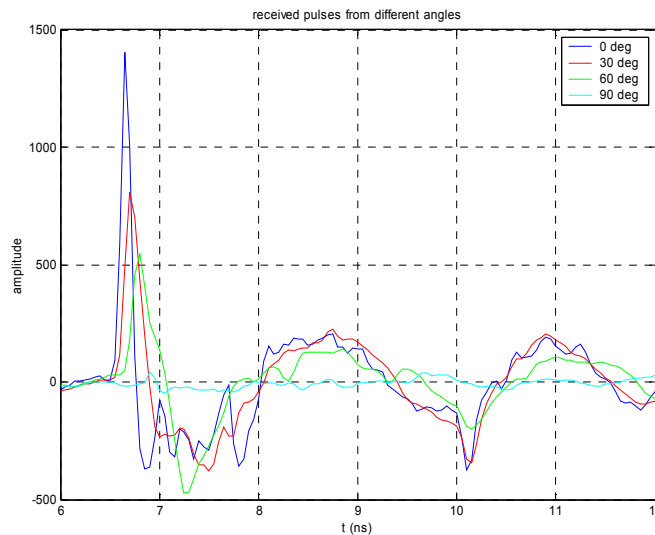


Figure 3-22. Comparison of received pulses at different elevation angles of arrival for the bicone antennas

Table 3-4. Received energy for different angle of arrivals

AOA	Energy	Correlated Energy
0 degrees	1	1
30 degrees	.717	.524
60 degrees	.465	.208
90 degrees	.086	.007

3.2.2 Channel Characteristics

Time Dispersion Statistics

It is useful to have some parameters that generally describe the multipath channel structure as a function of delay. The most commonly used time dispersion parameters are mean excess delay, RMS delay spread, and maximum excess delay as defined in (2-4), (2-5), and section 2.1.1.

Several power delay profiles (PDPs) (square of the impulse responses) corresponding to measurements taken over a local area (9 locations on a 0.9m x 0.9m grid in this case) are averaged before calculating these statistics. Since the impulse responses are discrete and the CLEAN algorithm inherently eliminates components below a threshold, the maximum excess delay is simply calculated as the delay of last arriving multipath component in the averaged PDP. The time dispersion parameters are plotted versus transmitter-receiver separation in Figure 3-23, Figure 3-24, and Figure 3-25. While some researchers [85][27] report a correlation between distance and delay spread, no such correlation is evident from these limited available data sets. Therefore, since these data sets represent a fairly diverse set of environments (different types of rooms with different scatterers and different types of materials), it is concluded that for the specific environments and distances considered the physical environment has a much

more significant impact on the time dispersive nature of the channel than the distance. The average values for these parameters are recorded in Table 3-5. The average values of these parameters calculated from impulse responses generated by the CLEAN algorithm with a -20 dB threshold are also recorded in Table 3-6 for comparison.

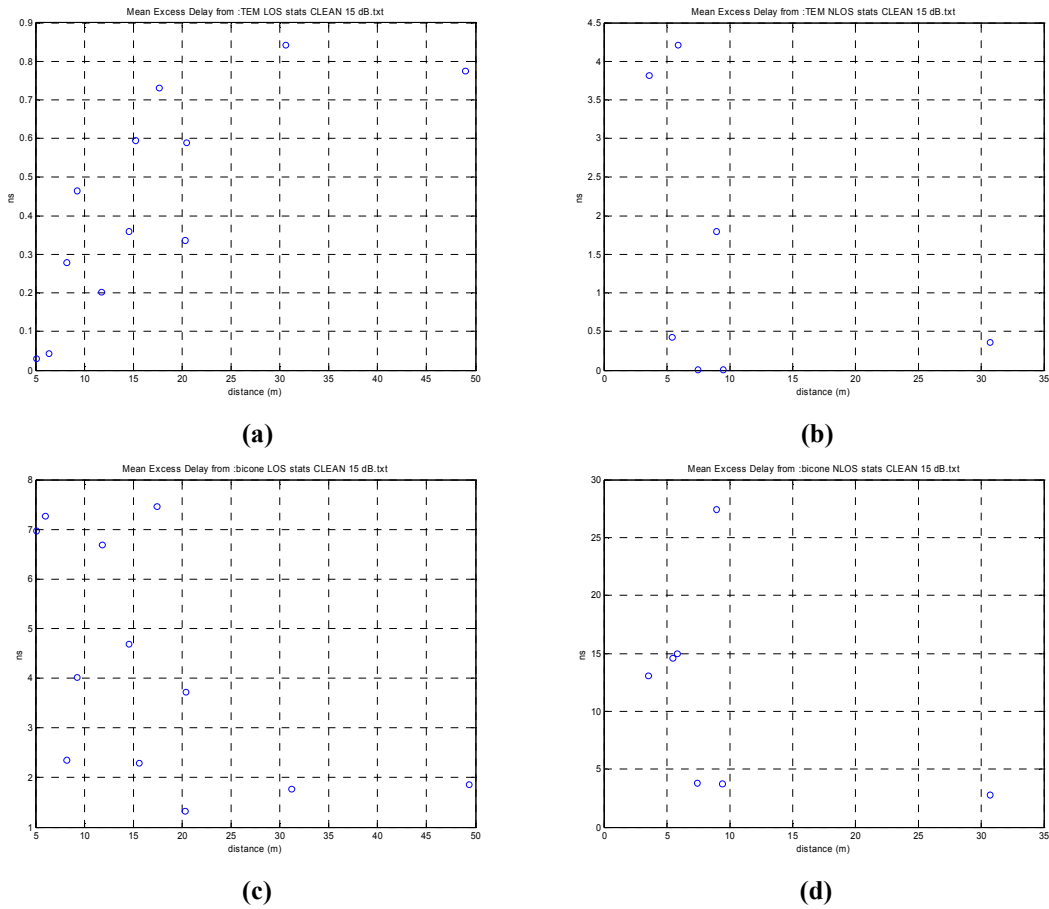
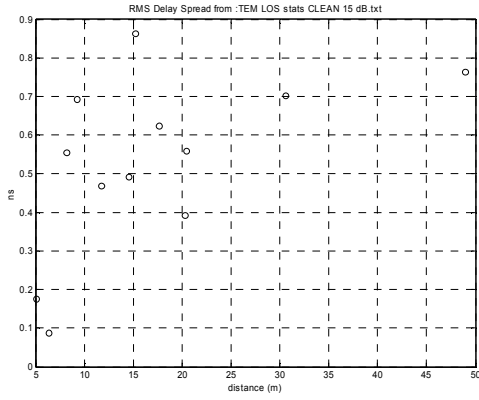
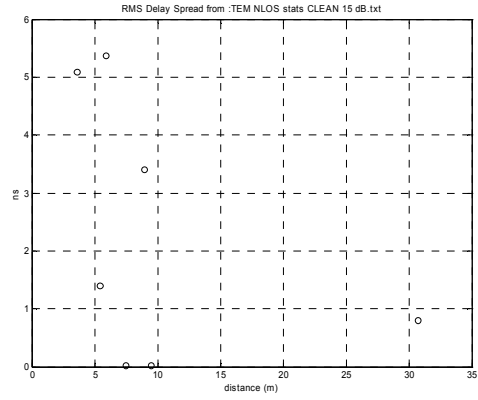


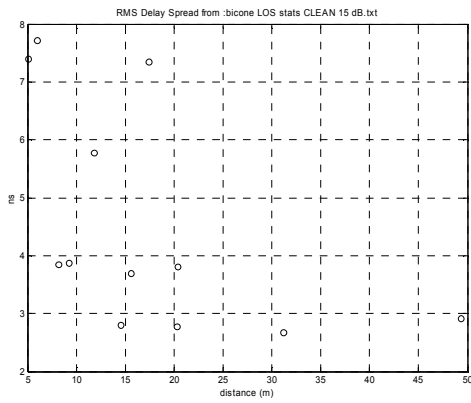
Figure 3-23. Mean excess delay vs. distance
(a) TEM horns, LOS, (b) TEM horns, NLOS, (c) bicones, LOS, (d) bicones, NLOS



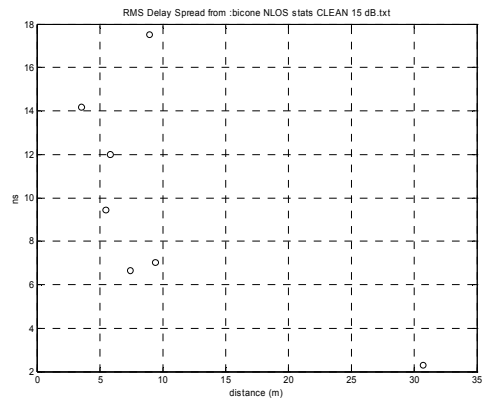
(a)



(b)

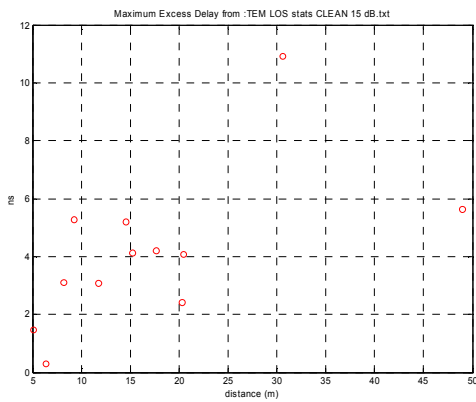


(c)

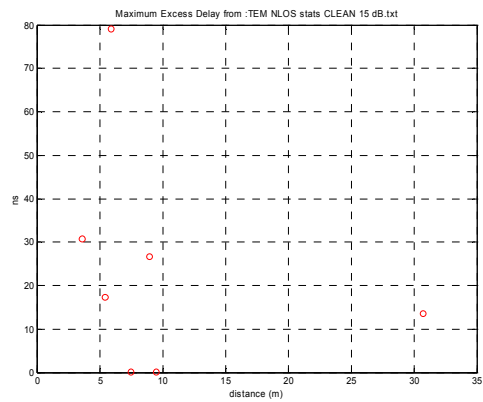


(d)

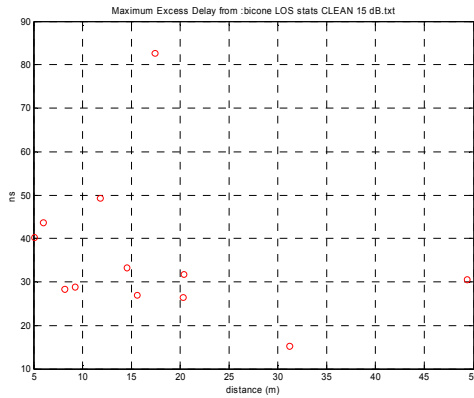
Figure 3-24. RMS delay spread vs. distance
(a) TEM horns, LOS, (b) TEM horns, NLOS, (c) bicones, LOS, (d) bicones, NLOS



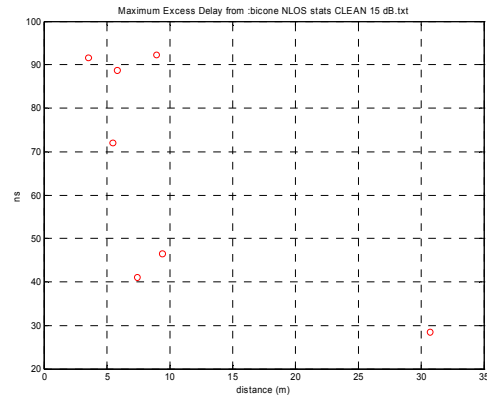
(a)



(b)



(c)



(d)

Figure 3-25 Maximum excess delay vs. distance
 (a) TEM horns, LOS, (b) TEM horns, NLOS, (c) bicones, LOS, (d) bicones, NLOS

Table 3-5. Averages of delay statistics (-15 dB threshold)

averages (in ns):		mean excess delay	RMS delay spread	max excess delay
TEM horns	LOS	0.44	0.53	4.15
	NLOS	1.52	2.30	23.90
Bicones	LOS	4.20	4.55	36.41
	NLOS	11.47	9.87	65.77

Table 3-6. Averages of delay statistics (-20 dB threshold)

averages (in ns):		mean excess delay	RMS delay spread	max excess delay
TEM horns	LOS	1.52	1.58	21.87
	NLOS	4.81	5.08	58.16
Bicones	LOS	9.48	7.35	71.83
	NLOS	16.36	13.18	88.43

The RMS delay spread values are plotted versus the corresponding mean excess delay values. As expected there is a large degree of correlation between these values that appears fairly linear.

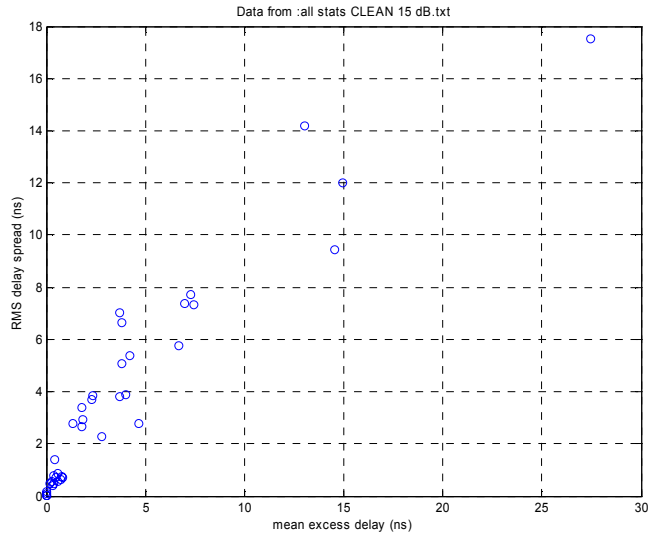
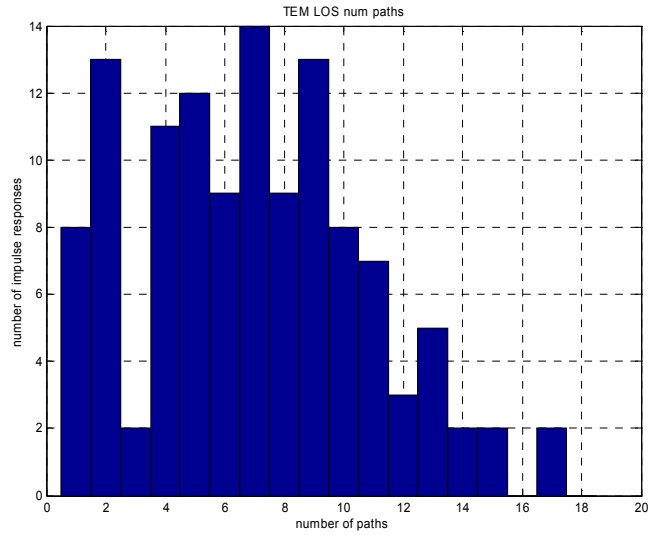


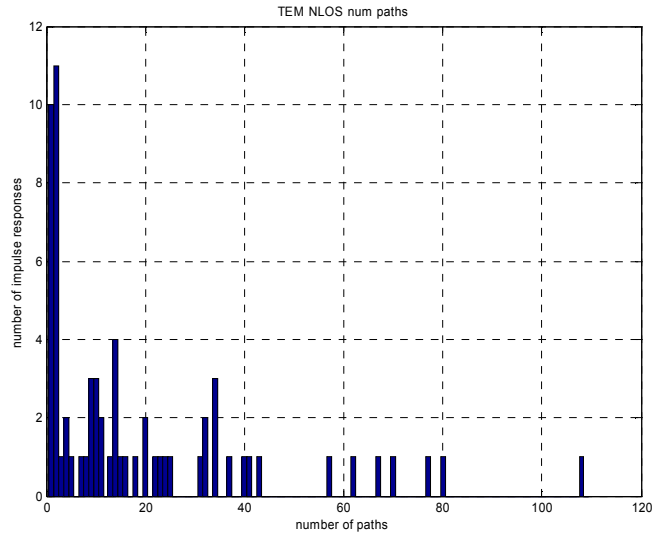
Figure 3-26. RMS delay spread vs. mean excess delay, all channels

Number of Multipath

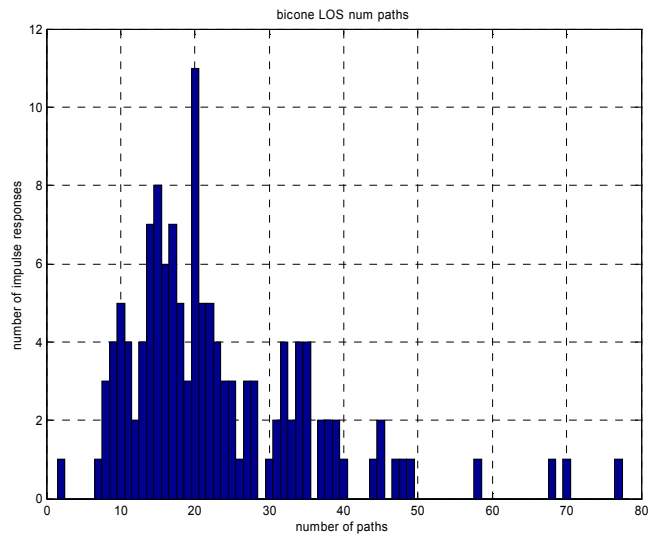
Histograms of the number of detected multipath components for the different measurement scenarios are shown in Figure 3-27. The average number of detected multipath is shown in Table 3-7. The average values for a -20 dB threshold are shown in Table 3-8.



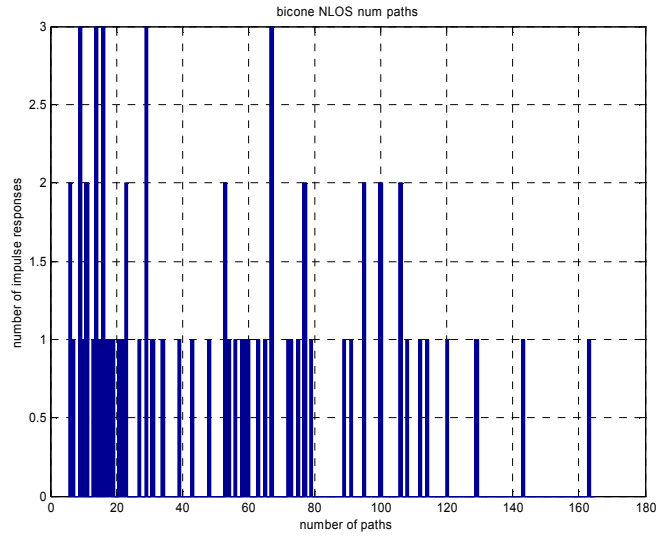
(a)



(b)



(c)



(d)

Figure 3-27. Histograms of the number of multipaths.
 (a) TEM horns, LOS, (b) TEM horns, NLOS, (c) bicones, LOS, (d) bicones, NLOS

Table 3-7. Average of number of multipath components

CLEAN w/ 15 dB threshold		average number of paths
TEM horns	LOS	7.0
	NLOS	19.3
Bicones	LOS	23.2
	NLOS	52.9

Table 3-8. Average of number of multipath components

CLEAN w/ 20 dB threshold		average number of paths
TEM horns	LOS	17.0
	NLOS	64.5
Bicones	LOS	61.7
	NLOS	129.4

It is expected that the number of detected multipath components may be related to the RMS delay, because if more paths are present then it seems likely that they will be spread over a longer duration of time. The number of multipath components detected is

plotted versus the RMS delay spread in Figure 3-28 and an approximately linear relationship between these parameters is observed.

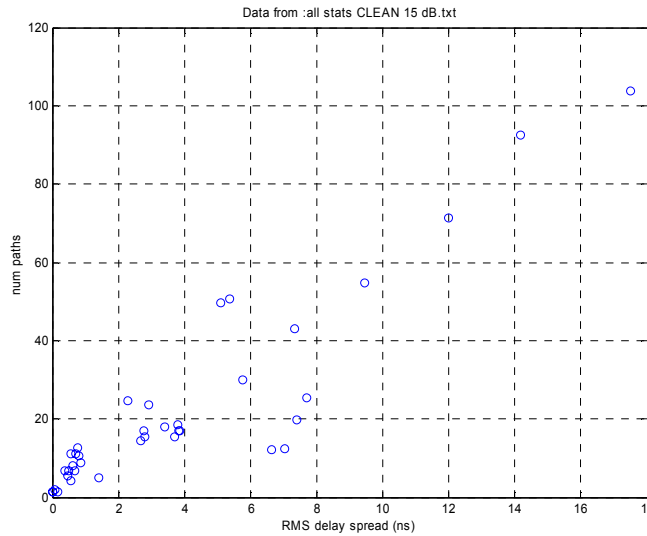


Figure 3-28. Number of paths vs. RMS delay spread, all channels

Pulse Inversions

In a pulse based coherent measurement system, it is more obvious when a multipath component has been inverted by the physical channel than when continuous wave signals are used. The percentage of the received multipath components that were inverted and the percentage of the total energy (of the impulse response) that these inverted pulses contain is shown in Table 3-9 and Table 3-10 for -15 dB and -20 dB thresholds respectively.

Table 3-9. Number and significance of pulse inversions

CLEAN w/ 15 dB threshold	% pulses inverted	% E in inverted pulses
TEM horns	LOS	46.0
	NLOS	36.9
Bicones	LOS	46.7
	NLOS	52.9

Table 3-10. Number and significance of pulse inversions

CLEAN w/ 20 dB threshold		% pulses inverted	% E in inverted pulses
TEM horns	LOS	49.3	31.9
	NLOS	39.5	28.1
Bicones	LOS	48.1	49.3
	NLOS	50.0	43.3

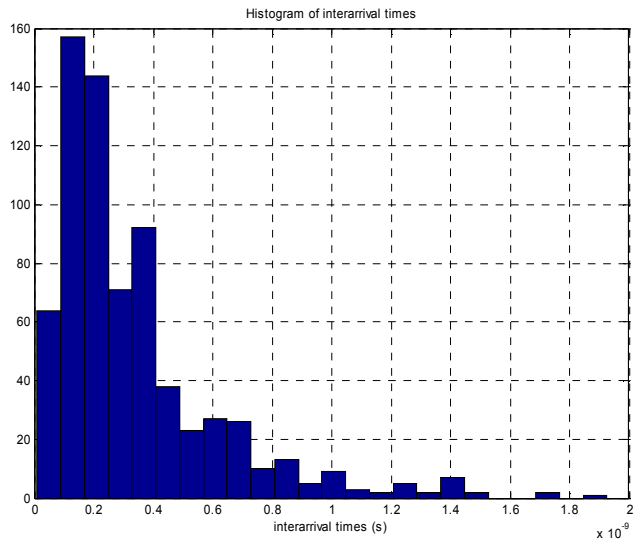
Arrival Times

Many researchers have used a Poisson process or some modification of a Poisson process to describe the arrival times of multipath components in an indoor channel [29]. A Poisson distribution would be an accurate description if the objects which cause the reflections were located with complete randomness throughout the physical environment [29]. While in a realistic indoor environment, the arrangement of the physical objects that cause reflectors is likely to have some structure or groupings, a Poisson process is an appropriate starting point to analyze the arrival times of multipath components. If the arrival times are described by a Poisson process, then the interarrival times are described by an exponential distribution.

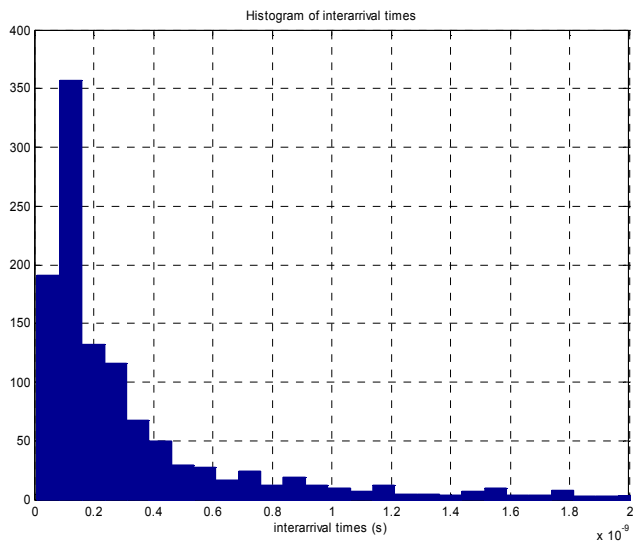
$$p(\tau_k | \tau_{k-1}) = \lambda \exp[-\lambda(\tau_k - \tau_{k-1})], \quad k > 0 \quad (3-18)$$

where λ is the mean arrival rate.

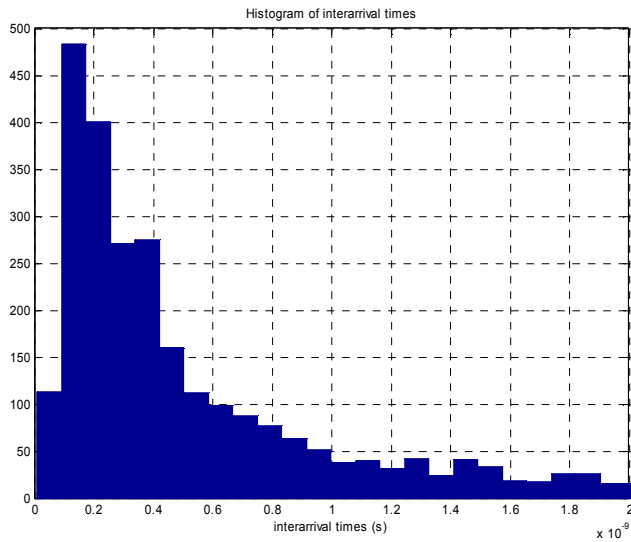
The interarrival times of the paths in the CLEAN impulse responses, were calculated and histograms of these interarrival times are shown in Figure 3-29. The distributions appear to be roughly exponential, verifying that a Poisson process is a reasonable approximation to the arrival time. The mean interarrival times are given in Table 3-11.



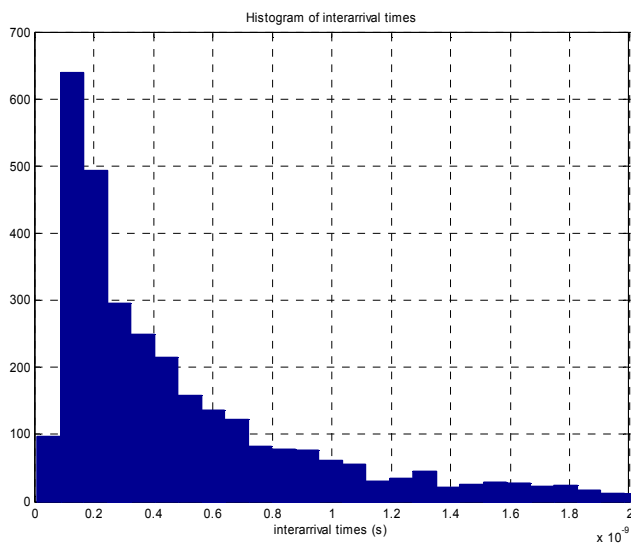
(a)



(b)



(c)



(d)

Figure 3-29. Histograms of interarrival times.
(a) TEM horns, LOS, (b) TEM horns, NLOS, (c) bicones, LOS, (d) bicones, NLOS

Table 3-11. Mean interarrival times

		$1/\lambda$ (ns)
TEM horns	LOS	0.39
	NLOS	0.58
Bicones	LOS	1.12
	NLOS	0.93

Energy Decay

Multipath components arriving at later delays are expected in general to have less energy than the components arriving earlier within a power delay profile. Many researchers have assumed that the mean energy decay follows an exponential decay of the form

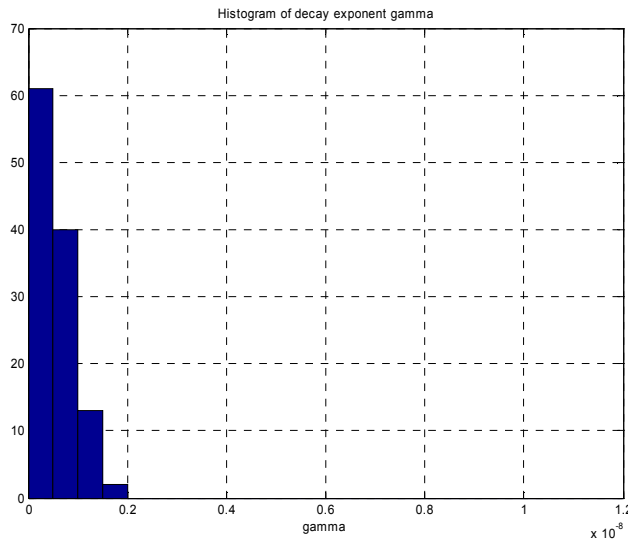
$$\overline{\beta_k^2} = \overline{\beta_0^2} e^{-\tau_k/\gamma} \quad (3-19)$$

where $\overline{\beta_k^2}$ is the expected value of the energy in the k -th multipath, τ_k is the delay of the k -th multipath such that the first multipath, $k = 0$, arrives at $\tau_0 = 0$, and γ is the energy decay exponent. This description has some validity from a physical standpoint [67]. As a wave bounces off more objects on its path to the receiver, it will arrive at later delays due to the additional distance traveled and also suffer more attenuation in decibels depending on the materials of the reflectors in the environment. Thus, on average the received energy can be expected to decrease exponentially with delay.

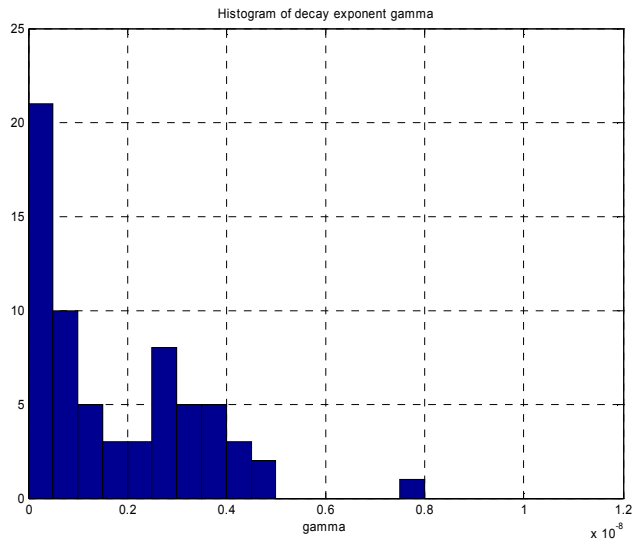
Assuming the measurement data followed a single exponential decay, a minimum mean square error (MMSE) linear fit of the power versus delay in the (natural) log domain was performed. This MMSE calculation attempts to find the value of γ (slope of the MMSE linear fit), which determines the expected value of a path at that delay.

At greater delays in a CLEAN impulse response, there tends to be a few components slightly above the threshold value (and of course, no components below the threshold). However, based on an exponential decay model, the true average energy of paths arriving at these delays is likely below the threshold. The calculated impulse responses do not reflect this trend, since the delayed paths at or below the average were not detected. So using the CLEAN values at these later delays in the MMSE calculation

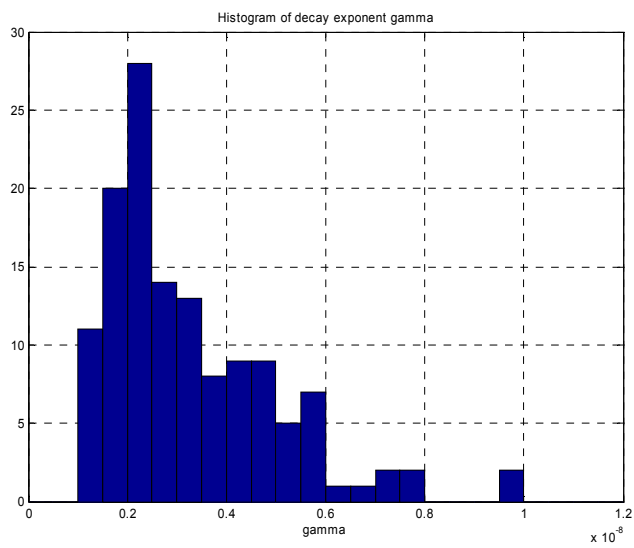
could result in artificially high values of gamma. Therefore to reduce this effect, the linear fit is only computed out to a maximum excess delay that is 3 dB above the threshold value used in the calculation of the impulse response. Since, the sensitivity of the measurement data is noise limited, for all the statistics considered above, the impulse responses calculated using a -15 dB threshold is considered reliable to quantify the channel. However, for this MMSE fit, impulse responses calculated using a -20 dB threshold are used to allow more data points and over a longer delay. The first arriving path is considered to be the first path that is within 3 dB of the strongest path. This assumption, while not perfectly accurate, is necessary because when the CLEAN algorithm is run with a -20 dB threshold, noise is occasionally identified as paths and weak false paths well before the true first arriving path can severely skew the estimate of γ and in some cases even cause negative values for the estimate of γ . Histograms of the calculated γ values are plotted in Figure 3-30. The average values of γ are given in Table 3-12.



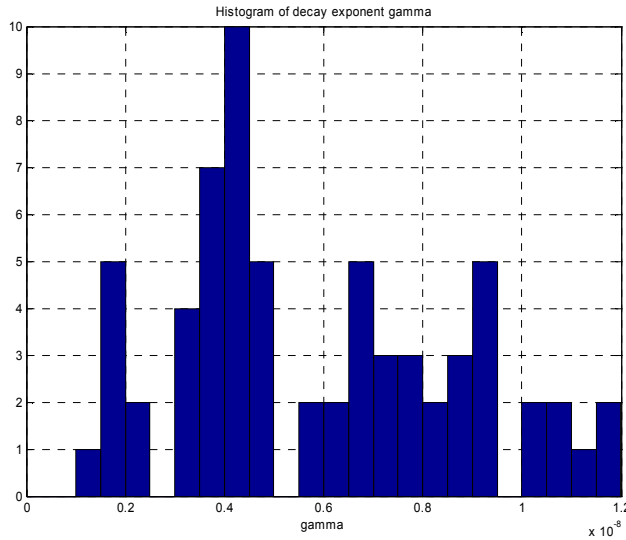
(a)



(b)



(c)



(d)

Figure 3-30. Histograms of estimated energy decay parameter.
 (a) TEM horns, LOS, (b) TEM horns, NLOS, (c) bicones, LOS, (d) bicones, NLOS

Table 3-12. Averages of exponential energy decay parameter

		γ (ns)
TEM horns	LOS	0.57
	NLOS	1.72
Bicones	LOS	3.25
	NLOS	5.88

Statistics from CLEAN vs. Inverse Filtering

To evaluate the reliability of the statistics computed from the CLEAN generated impulse responses, a sub-set of statistics was computed from the inverse filter generated impulse responses. Impulse responses were created using inverse filtering using the LOS bicone data sets and a -20 dB zeroing threshold in the frequency domain. The impulse response was discretized by calculating the square root of the energy in 250 ps bins (the approximate width of the received pulse main lobe). Bins below -15 dB of the peak were discarded. Thus, the polarity information is lost with this method, but the time dispersion parameters and number of paths can still be computed. The average mean excess delay,

RMS delay spread, and number of paths are shown in Table 3-13 with the values found with the corresponding values found using the CLEAN impulse responses. The number of paths found is noticeably higher, but reasonable agreement is found between the two deconvolution methods. The higher number of paths may be due to the time domain sidelobes generated from windowing the data in the frequency domain.

Table 3-13. Comparison of statistics from different deconvolution techniques

LOS, bicones	CLEAN	Inverse Filtering
$\bar{\tau}$ (ns)	4.20	6.60
σ_{τ} (ns)	4.55	5.06
number paths	23.2	31.4

3.2.3 Small Scale Channel Impulse Response Models

Saleh-Valenzuela Model

From observing the impulse responses, it appears that there may be some clustering of the multipath components. Also, clearly from the impulse responses, it is seen that the arrival times are random and would not be well modeled by a fixed arrival time model. As expected, the PDP decays with delay. It appears that there may be an exponential decay in some scenarios as is assumed in most traditional wideband channel models. However, much of the data sets considered here are from LOS situations down a hallway. In these cases, the hallway can act as a waveguide and thus an exponential decay might not be the most accurate model.

In general, these observed properties share many of the characteristics of the Saleh-Valenzuela model for wideband channels [67]. Therefore, the data is fitted to a modified version of the Saleh-Valenzuela model which is similar to model proposed in

[23]. It should be noted that the Saleh-Valenzuela model was developed for NLOS channels (and measurements taken down hallways were specifically discarded).

The Saleh-Valenzuela model is a tapped delay line given by

$$h(t) = \sum_{l=0}^{L_c} \sum_{k=0}^{K} \beta_{k,l} \delta(t - T_l - \tau_{k,l}) \quad (3-20)$$

Note that while the original model of [67] is a complex baseband model, this UWB model is a direct baseband model. It is assumed that the multipath components arrive in clusters. The cluster arrival rate is described by a Poisson process, and thus, the cluster interarrival times are described by exponential random variables

$$p(T_l | T_{l-1}) = \Lambda \exp[-\Lambda(T_l - T_{l-1})], \quad l > 0 \quad (3-21)$$

where Λ is the mean cluster arrival rate. Within a cluster, the ray arrival times are also described by a Poisson process, so the distribution of the interarrival times is variable

$$p(\tau_{k,l} | \tau_{(k-1),l}) = \lambda \exp[-\lambda(\tau_{k,l} - \tau_{(k-1),l})], \quad k > 0 \quad (3-22)$$

where λ is the mean ray arrival rate. The average power of both the clusters and the rays within the clusters are assumed to decay exponentially, such that the average power of a multipath component at a given delay, $T_l + \tau_{k,l}$, is given by

$$\overline{\beta_{k,l}^2} = \overline{\beta_{0,0}^2} e^{-T_l/\Gamma} e^{-\tau_{k,l}/\gamma} \quad (3-23)$$

where $\overline{\beta_{0,0}^2}$ is the expected value of the power of the first arriving multipath component, Γ is the decay exponent of the clusters and γ is the decay exponent of the rays within a cluster.

In the original model [67], the $\beta_{k,l}$ were all positive and distributed according to a Rayleigh distribution and the tapped delay line model of (3-20) also had a random phase

term. However, since this model is a baseband model, there is no phase term, but multipath components can be inverted by the physical environment. The Rayleigh distributed amplitudes and random phase model comes from the assumption that several paths arrive at delays that are not resolvable to the measurement system used. Here, the pulse bandwidth and the measurement resolution are much greater than in most previous pulsed channel sounding experiments [67][71]. Also, no envelope detection was used as was typically used in wideband pulsed measurements (where phase information was lost). Rather, the received signal was sampled directly, so no signal information was lost. The magnitudes of the path amplitudes are assumed to follow a lognormal distribution about the expected value given above in (3-23). Reference [23] suggests two independent lognormal variables to represent the amplitude variations of the clusters and rays. However, in the way the model of [23] is presented, these random variables can be combined as a single lognormal random variable. The polarity of the path is represented as an equiprobable binary random variable, $p_{k,l}$, taking on the values ± 1 . Thus, the path amplitudes are given by

$$\beta_{k,l} = p_{k,l} 10^{(\mu_{k,l} + X_{\sigma,k,l})/20} \quad (3-24)$$

where

$$\mu_{k,l} = \frac{20 \ln \left(\overline{|\beta_{0,0}|} \right) - 10T_l / \Gamma - 10\tau_k / \gamma}{\ln(10)} - \frac{\sigma^2 \ln(10)}{20}$$

and

$$X_{\sigma,k,l} = N(0, \sigma^2) \quad (\sigma \text{ is in dB})$$

To summarize, this model is described by 5 parameters:

- Λ is the mean cluster arrival rate
- λ is the mean ray arrival rate
- Γ is the cluster exponential decay factor
- γ is the ray exponential decay factor
- σ is the standard deviation of the lognormal distributed path powers

A search was performed to find appropriate parameters that generate impulse responses with the same characteristics as the measured impulse responses. The characteristics that determined the fit of the simulated responses to the measured responses were mean excess delay, RMS delay spread, and number of multipath components above the -15 dB threshold. The parameter values that were found to match the channel statistics reasonable well are shown in Table 3-14 along with the average statistics of 100 simulated impulse responses generated using these parameters.

Table 3-14. Fit to modified Saleh-Valenzuela model.

Values in () indicate target value.

	TEM horns		Bicones	
	LOS	NLOS	LOS	NLOS
$1/\Lambda$	1.2e-9	1.5e-9	5.0e-9	5.2e-9
$1/\lambda$	0.6e-9	0.8e-9	0.7e-9	0.8e-9
Γ	0.95e-9	3.0e-9	7.1e-9	12.0e-9
γ	0.3e-9	1.0e-9	2.0e-9	5.0e-9
σ	2	2	5	5
$\bar{\tau}$ (ns)	0.43 (0.44)	2.09 (1.52)	5.19 (4.20)	10.52 (11.47)
σ_{τ} (ns)	0.57 (0.53)	2.12 (2.30)	4.84 (4.55)	8.71 (9.87)
number paths	7.3 (7.0)	23.7 (19.3)	23.3 (23.2)	53.3 (52.9)

Δ -K model

The Δ -K model has also been used to model mobile and indoor wideband channels [74][73]. This model also assumes that multipath components arrive in clusters. However, the probability that a path arrives at any given delay is higher by a factor of K

if a path has arrived within the past Δ seconds. Therefore the paths tend to arrive in clusters. The arrival times thus follow a modified, two state Poisson process and the interarrival times follow an exponential distribution where the arrival rate is based on the state. When in state 1, (S-1), the mean arrival rate is given by λ . Transition to state 2, (S-2), is triggered when a path occurs. In (S-2), the mean arrival rate is given by $K\lambda$. If after Δ seconds, a path has not arrived, transition back to (S-1) occurs.

A single exponential energy decay is assumed here to describe the expected value of the energy in a path at a given delay. The polarity is again assumed to be +/-1 with equal likelihood, and amplitude fading is again assumed to be lognormal such that the amplitude of a path is given by

$$\beta_k = p_k 10^{(\mu_k + X_{\sigma,k})/20} \quad (3-25)$$

where

$$\mu_k = \frac{20 \ln(|\beta_0|) - 10\tau_k / \gamma}{\ln(10)} - \frac{\sigma^2 \ln(10)}{20}$$

and

$$X_{\sigma,k} = N(0, \sigma^2) \quad (\sigma \text{ is in dB})$$

Typically, for computer simulation this model is implemented using a discrete form. The discrete version of the Δ -K model presented by [73] has been modified here, and this implementation is a mix between the continuous and discrete versions of the model. In the discrete version given by [73], the time axis is divided into bins, and the probability of a path arriving in a given bin is based on whether a path arrived in the previous bin (probability being higher by a factor of K if a path was present). However,

for this modeling, the time spacing between samples (or bins) is much finer than that assumed by [73] resulting in the possibility of overlapping pulses which is not possible in the original discrete model. Therefore, in this modified version, the probability that a path arrives at a given sample time is based on whether a path a path has arrived in the past d sample times rather than just the previous sample time, where d samples corresponds to Δ seconds.

To summarize, this model is described by 5 parameters:

- λ is the mean arrival rate for (S-1)
- K is the mean arrival scaling factor for (S-2)
- Δ is the time from the last arriving path to transition to (S-1)
- γ is the exponential decay factor
- σ is the standard deviation of the lognormal distributed path powers

Again, a search was performed to find an appropriate set of these parameters that generate simulated impulse responses with similar statistics as the measurement data.

The parameters found to match the chosen channel statistics are shown in Table 3-15.

Table 3-15. Fit to modified Δ -K model.

Values in () indicate target value

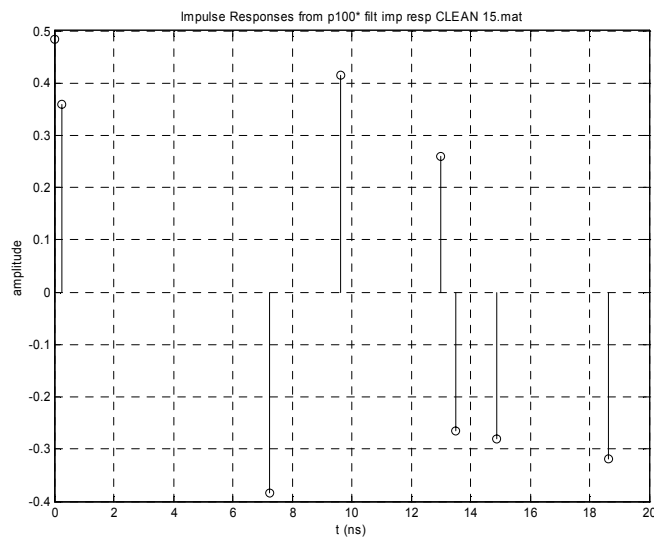
	TEM horns		Bicones	
	LOS	NLOS	LOS	NLOS
$1/\lambda$	0.7e-9	0.7e-9	1.2e-9	1.2e-9
Δ	0.7e-9	0.7e-9	0.5e-9	0.5e-9
K	2	2	2	2.3
γ	0.75e-9	2.35e-9	6.0e-9	14.0e-9
σ	2	2	2	2
$\bar{\tau}$ (ns)	0.41 (0.44)	1.69 (1.52)	4.33 (4.20)	11.21 (11.47)
σ_{τ} (ns)	0.50 (0.53)	1.75 (2.30)	4.36 (4.55)	10.19 (9.87)
number paths	7.3 (7.0)	19.1 (19.3)	22.9 (23.2)	53.6 (52.9)

Single Poisson process arrival time model

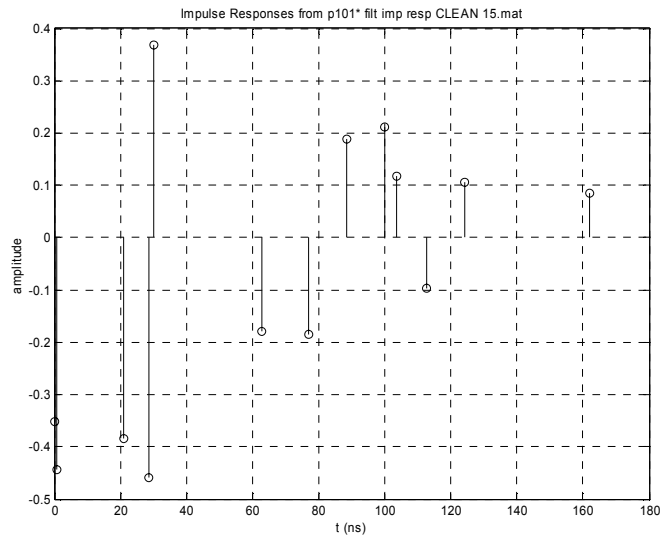
A simplified version of both of the previously introduced models assumes that only one cluster is present in the impulse response (or equivalently, no clustering of paths). A search was also performed to find appropriate values for this simplified single cluster model that match the channel statistics. These parameter values and the statistics of the simulated impulse responses are shown in Table 3-16. Some sample simulated impulse responses using the single cluster model are shown in Figure 3-31.

Table 3-16. Fit to Single Poisson arrival time model.
Values in () indicate target value

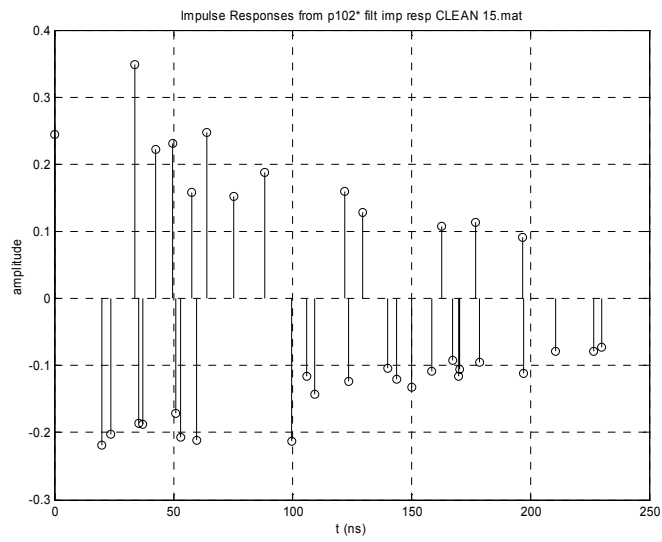
	TEM horns		Bicones	
	LOS	NLOS	LOS	NLOS
$1/\lambda$	0.38e-9	0.57e-9	0.84e-9	0.82e-9
γ	0.73e-9	3.4e-9	6.3e-9	15.0e-9
σ	2	2	2	2
$\bar{\tau}$ (ns)	0.41 (0.44)	2.50 (1.52)	4.94 (4.20)	10.52 (11.47)
σ_{τ} (ns)	0.54 (0.53)	2.54 (2.30)	4.77 (4.55)	10.90 (9.87)
number paths	7.3 (7.0)	19.8 (19.3)	23.8 (23.2)	52.9 (52.9)



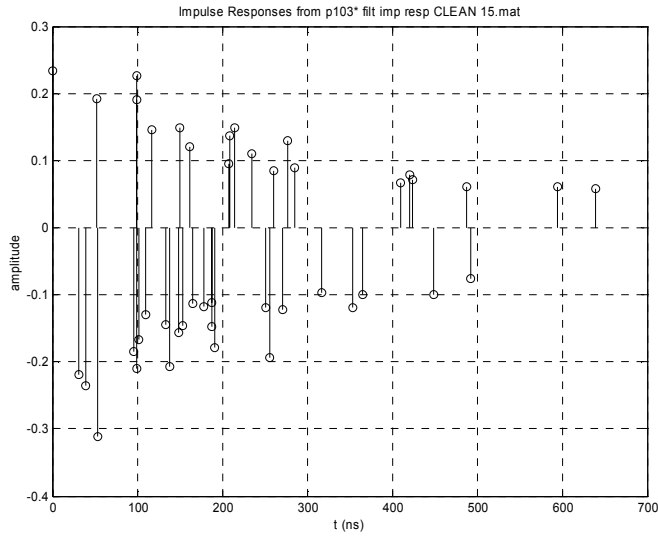
(a)



(b)



(c)



(d)

Figure 3-31. Simulated impulse response using single Poisson process arrival times. (a) TEM horns, LOS, (b) TEM horns, NLOS, (c) bicones, LOS, (d) bicones, NLOS

It is important to note that the model parameter values found and listed above do not represent a unique set of parameters to generate the desired channel statistics. But rather the desired statistical parameters (mean excess delay, RMS delay spread, and number of multipath) were chosen as parameters that are likely to have a significant impact on communications system performance. In particular, the variance of the amplitude fading (or even the exact distribution used) did not have a very significant impact on the chosen statistics. In Chapter 5, the sensitivity of communication system performance to the exact model used for simulation is evaluated, with the aim of determining which characteristics of the channel (such as time dispersiveness, arrival time distribution, etc.) have the greatest impact on performance.

3.2.4 Comparison to Previous Results

Channel Statistics

Several researchers have published statistical parameters based on UWB channel measurement efforts. No researchers are known to have examined channels for highly directional antennas such as the TEM horn antennas used for some of the measurement considered here. Comparisons of the finding of other researchers with the findings presented here for the results corresponding to the measurements taken with omnidirectional (bicone) antennas is shown in Table 3-17. An overview of the measurement campaigns referenced in Table 3-17 is given in section 2.2.1.

3.3 Conclusions

In this chapter, the distortion of UWB signals due to transmission through materials has been investigated and it was found that often this distortion is negligible. Therefore, the superposition of the multipath components is the dominant effect in the UWB channel. Further, the multipath characteristics have been statistically analyzed for UWB pulses and two types of antennas. As expected, the results showed that LOS channels are less dispersive and had less multipath components than NLOS channels, and channels calculated for TEM horns (highly directional) are less dispersive and had less multipath components than channels calculated for biconical antennas (omnidirectional).

Table 3-17. Comparison of results with previous research

Researchers	$\bar{\tau}$ (ns)	σ_{τ} (ns)	num paths	γ (ns)	$1/\lambda$ (ns)
LOS					
VT bicones	4.20	4.55	23.2	3.25	1.12
TDC [85][57]	4.95 (0-4m)	5.27 (0-4m)	24.0		
CEA-LETI [39]	4-9	14-18		29-35	
CEA-LETI [40]	6.53 (home) 6.42 (office)	11.45 (home) 10.07 (office)	3.4 (home) 2 (office)		
AT&T [27]		1.6			
AT&T [26]		1.1-16.6, mean 4.7			
Intel [58][24]	4	9	7		
802.15 model [23]	5.1	5.3	24	0.4 (43)*	4.3 (7.1)*
NLOS					
VT bicones	11.47	9.87	52.9	5.88	0.93
USC [13][14][15]	~59-126	~45-74		84.1 (27.9)*	2.3 (45.5)*
AT&T (USC/TDL data) [11][12]				16.1	
TDC [85][57]	10.04 (0-4m) 14.24 (4-10m)	8.78 (0-4m) 14.59 (4-10m)	36.1 (0-4m) 61.6 (4-10m)		
CEA-LETI [39]	17-23	14-18		41-55	
CEA [40]	16.01 (4-10m) 18.85 (10-20m)	14.78 (4-10m) 17.64 (10-20m)	46.8 (4-10m) 75.8 (10-20m)		
AT&T [27]		2.7			
AT&T [26]		0.75-21, mean 8.5			
Intel [58][24]	17	15	35		
802.15 model [23]	10.4/14.2	8/14.3	36/62	2/2.1 (2.5/15)*	6.7/7.9 (5.5/14)*
Hashemi [29] (survey paper of various non-UWB indoor results)		20-50, 25 (small/med office) <120,200 (large office) 70-90,<80 (office) <100 (university) 8.3 (LOS), 8.3, 14.1 (NLOS) (office)			

* these values assumed a Saleh Valenzuela model, first value is ray value, value in () is cluster value

4 Limitations of the CLEAN Algorithm

This chapter discusses some scenarios in which the CLEAN algorithm has been found to produce inaccurate and undesirable results. The intention is not to discredit the usefulness of the algorithm for use in determining channel impulse responses, but rather to point out specific situations where the output of the algorithm should be examined in more detail to determine if the results are sufficiently accurate. If the true impulse response of the channel were known, it could be generally applied to simulate systems of all bandwidths and center frequencies. Therefore, ideally the CLEAN estimate of the impulse response could also be applied to all bandwidths and frequencies, but there are some limitations to the generality of CLEAN generated impulse responses.

4.1 CLEAN Experiment: Sub-pulse-width Resolution

The CLEAN algorithm uses a match filtered signal to determine the arrival times and strengths of multipath components. If the multipath components are all resolvable, the CLEAN algorithm would produce a perfect estimate of the channel. However, if the paths are not resolvable, the match filter output is affected and the CLEAN algorithm does not necessarily produce the true channel response. However, through iteration, the impulse response estimate will improve in the sense that

$$\hat{y}(t) = \hat{h}_i(t) * x(t) \quad (4-1)$$

will be a better estimate of $y(t)$. However, even in a noise-free signal the CLEAN algorithm is not likely to converge to the true impulse response when unresolvable paths are present. Unresolvable pulses will sum creating constructive and destructive interference and thus the peaks in the match filtered signal will shift away from the

locations of the true path arrival times. As an example, consider the scenario shown in Figure 4-2 where the received signal shown in the top plot is due to a two path channel. The LOS pulse is a 1 GHz pulse with a center frequency of 4 GHz shown in Figure 4-1. The two path channel and the CLEAN estimate of the channel are shown in the lower graph of Figure 4-2. Due to the destructive interference, the largest correlation value is actually negative at a delay in between the two actual path delays. The algorithm continues from this incorrect 'path' to find other 'paths' that further minimize the updated matched filter output. The iteration of the CLEAN algorithm for this case is shown in an attached [animation](#).

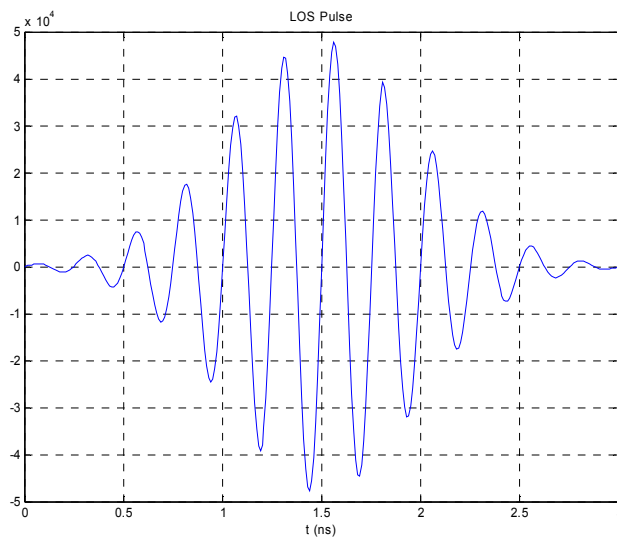


Figure 4-1. 1 GHz bandwidth pulse with center frequency 4 GHz

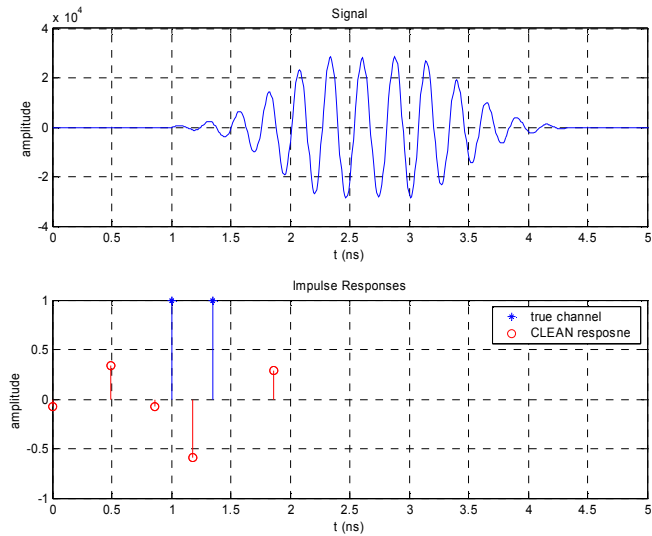


Figure 4-2. Top: received signal (pulses destructively interfere), Bottom: two path channel impulse response and CLEAN estimate of channel impulse response

The calculated CLEAN responses for two path channels similar to the one shown in Figure 4-2 were calculated for three different pulses (fractional bandwidths of 2 and 0.5 and a pulse that has experienced dispersion) for channels with same polarity path and also with an opposite polarity second path at different delays. These responses, as a function of increasing second path delay, are shown in attached animations: [fractional BW = 2, same polarity](#), [fractional BW = 0.5, same polarity](#), [dispersive pulse, same polarity](#), [fractional BW = 2, opposite polarity](#), [fractional BW = 0.5, opposite polarity](#), [dispersive pulse, opposite polarity](#).

While the CLEAN impulse response is not necessarily an accurate representation of the actual physical channel, it is still useful to create fairly accurate representation of the received signal. For a 1 GHz pulse with fractional bandwidth approximately equal to 2 (shown in Figure 4-3), and a two path channel (shown in Figure 4-4), the CLEAN generated impulse response has significant differences compared to the true channel as seen in Figure 4-4. The estimate of the received signal using the CLEAN impulse

response and the LOS pulse is compared to the actual received signal in Figure 4-5. While noticeable differences are present, the correlation between the two signals is still greater than 97%.

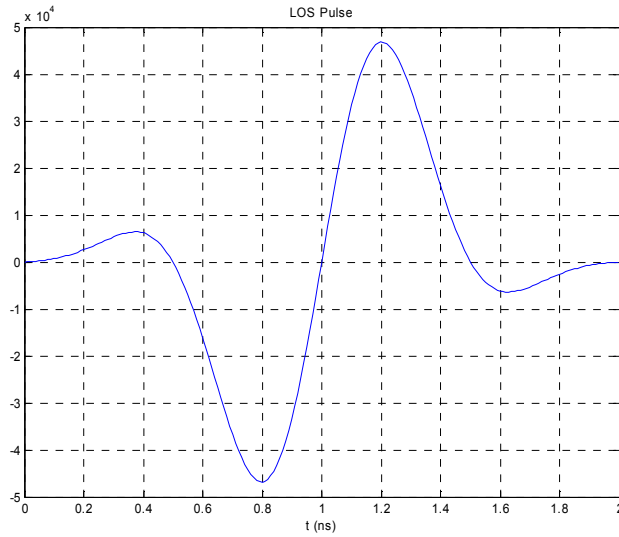


Figure 4-3. 1 GHz pulse with fractional bandwidth almost 2

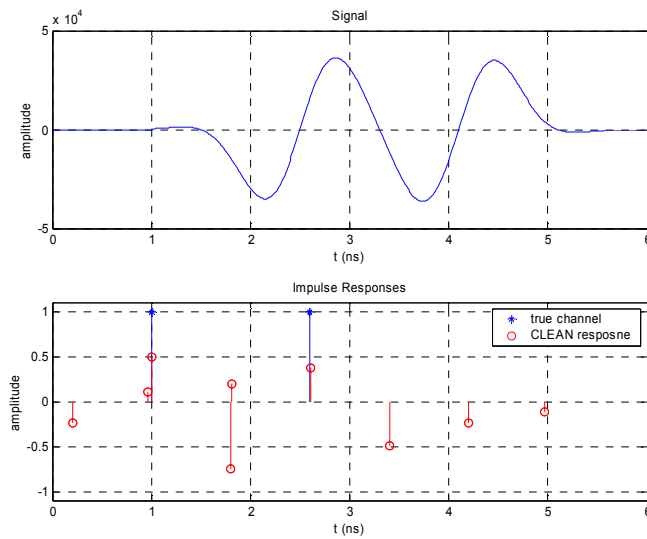


Figure 4-4. Top: received signal, Bottom: two path channel impulse response and CLEAN estimate of channel impulse response

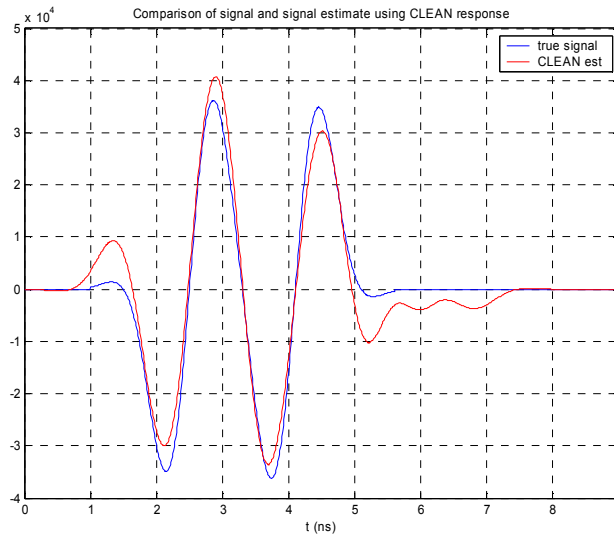
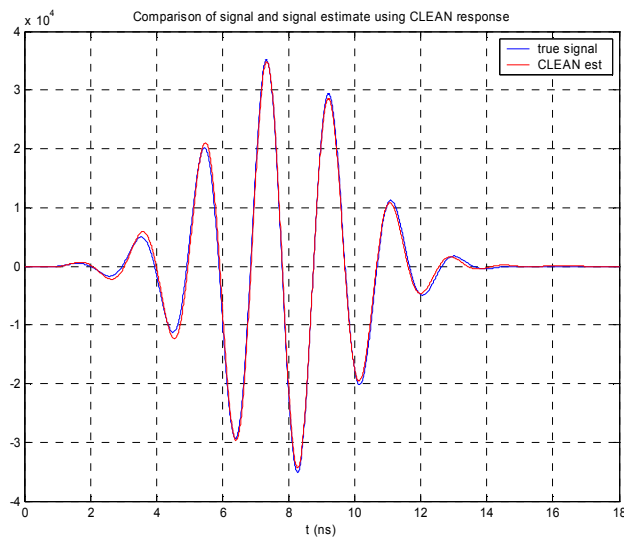


Figure 4-5. Received signal and estimate of received signal using CLEAN impulse response, correlation = 97.0%

But it is important to know if this CLEAN impulse response, calculated using the 1 GHz bandwidth pulse of Figure 4-3, can be extended to accurately estimate the received signal for systems employing different pulses other than the pulse used in the CLEAN algorithm. This CLEAN impulse response was chosen as an example because it is significantly different from the true impulse response. So, several example pulses of different bandwidths and center frequencies were considered. The true corresponding received signal assuming the two path model (shown in the bottom graph of Figure 4-4) was generated. Then the estimate of that signal was constructed using the CLEAN impulse response shown in Figure 4-4. The resulting signals and their correlation are given in Figure 4-6 to Figure 4-11. For pulses at the same center frequency and lower bandwidth than the original signal, the CLEAN response can be used to very accurately recreate the received signal (and actually does better in this case than with the original pulse). However, at other center frequencies, the CLEAN response does quite poorly at recreating the received signal. A summary of the accuracy of the simulated received

signals, using pulses of different bandwidths and frequencies, generated with the CLEAN impulse response calculated for the 1 GHz bandwidth pulse with fractional bandwidth of 2 is given in Table 4-1. These results do not discredit the usefulness of the CLEAN algorithm for determining the impulse responses of UWB channels. For the bicone pulse, the number of situations that produce undesirable outputs appear to be greatly reduced. This is because the bicone pulse has a large portion of its energy concentrated in a single lobe with no significant lobe of opposite polarity. The pulses with multiple cycles (or even one cycle) where the positive and negative lobes are roughly equal tend to experience more of the situations where the CLEAN algorithm generates the inaccurate impulse responses.



**Figure 4-6. Received signal and estimate, BW = 0.25 GHz, $f_c = 0.5$ GHz
Correlation = 99.8%**

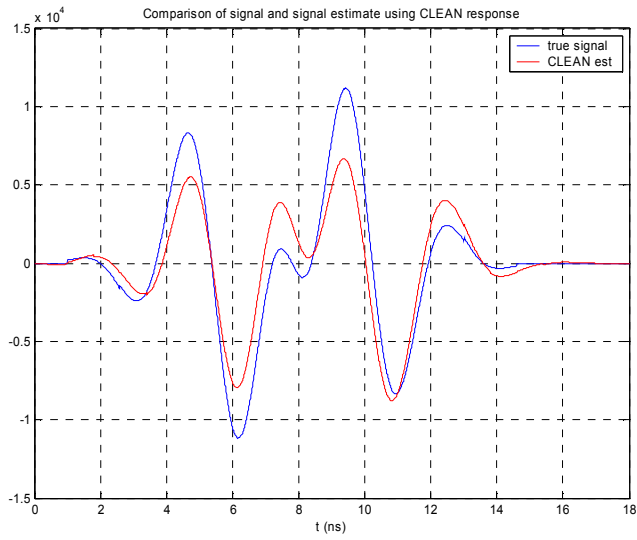


**Figure 4-7. Received signal and estimate, BW = 0.25 GHz, $f_c = 0.3$ GHz
Correlation = 91.2%**

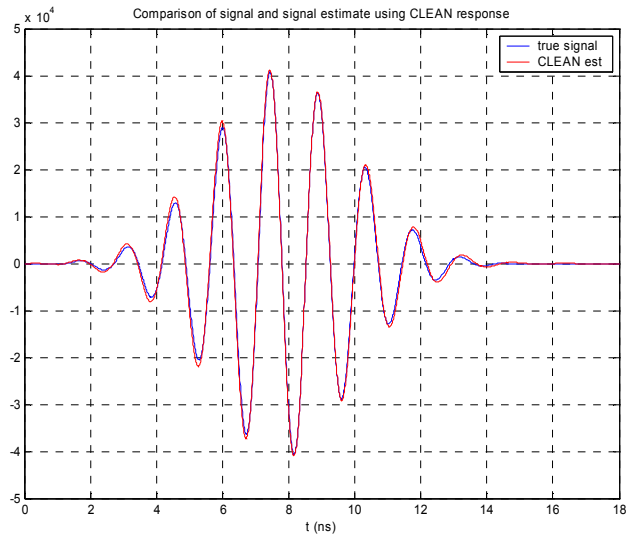


**Figure 4-8. Received signal and estimate, BW = 0.25 GHz, $f_c = 0.7$ GHz
Correlation = 99.9%**

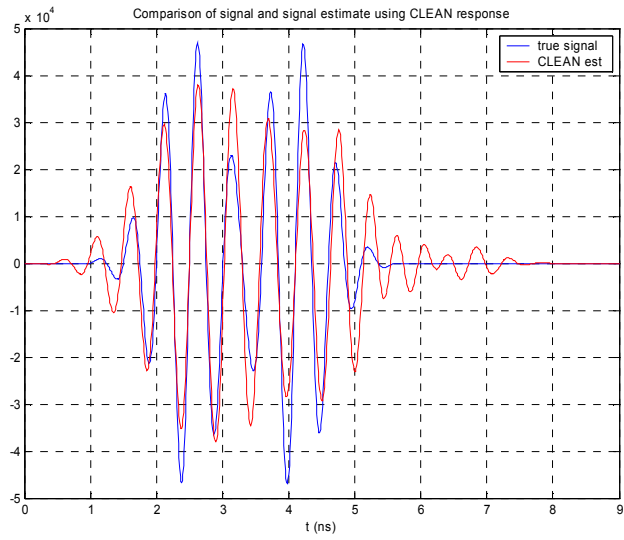


**Figure 4-9. Received signal and estimate, BW = 1 GHz, $f_c = 2$ GHz
Correlation = 91.0%**

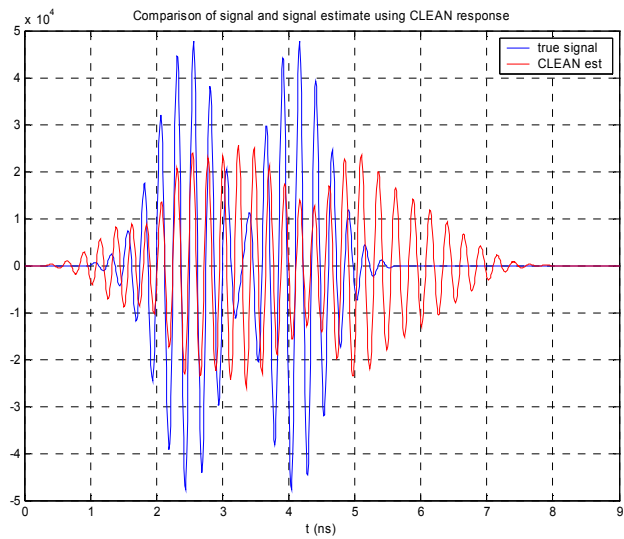


**Figure 4-10. Received signal and estimate, BW = 1 GHz, $f_c = 4$ GHz
Correlation = 43.0%**

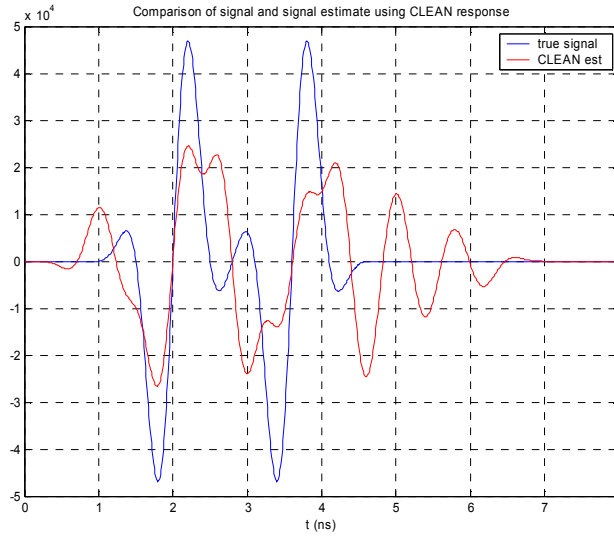


**Figure 4-11. Received signal and estimate, BW = 1.5 GHz, $f_c = 1$ GHz
Correlation = 58.9%**

Table 4-1. Accuracy of simulated signals using CLEAN estimate of impulse response from 1 GHz bandwidth, $f_c = 0.5$ GHz system

pulse	accuracy of the CLEAN simulated signal	
	correlation of simulated signal with true signal (%)	correlation loss (dB)
BW = 1 GHz, $f_c = 0.5$ GHz	97.0	0.26
BW = 0.25 GHz, $f_c = 0.5$ GHz	99.8	0.02
BW = 0.25 GHz, $f_c = 0.3$ GHz	91.2	0.80
BW = 0.25 GHz, $f_c = 0.7$ GHz	99.9	0.01
BW = 1 GHz, $f_c = 2$ GHz	91.0	0.82
BW = 1 GHz, $f_c = 4$ GHz	43.0	7.33
BW = 1.5 GHz, $f_c = 1$ GHz	58.9	4.60

4.2 CLEAN Experiment: Pulse Distortion due to Material

Using the frequency response from the material characterization work corresponding to transmission through bricks, a simulated distorted pulse was created. This pulse represents a single pulse, launched and received by TEM horns, that has passed through a brick wall. The CLEAN algorithm with a -15 dB threshold was run on the distorted pulse to illustrate how the algorithm models distorted pulses. The calculated

CLEAN response is shown in Figure 4-12. For this particular pulse, distortion, and threshold level, the CLEAN algorithm generates three taps to model the distorted pulse. Therefore, if pulses arriving at the receiver have experienced significant frequency dependent distortion, the CLEAN algorithm may generate extra taps that represent distortion rather than additional multipath components. The estimate of the distorted pulse using the CLEAN response is shown in Figure 4-13 with the actual distorted pulse. The correlation between these two pulses is 98.7 % and the loss due to the imperfect correlation is 0.11 dB. The CLEAN response is an FIR representation of the frequency distortion.

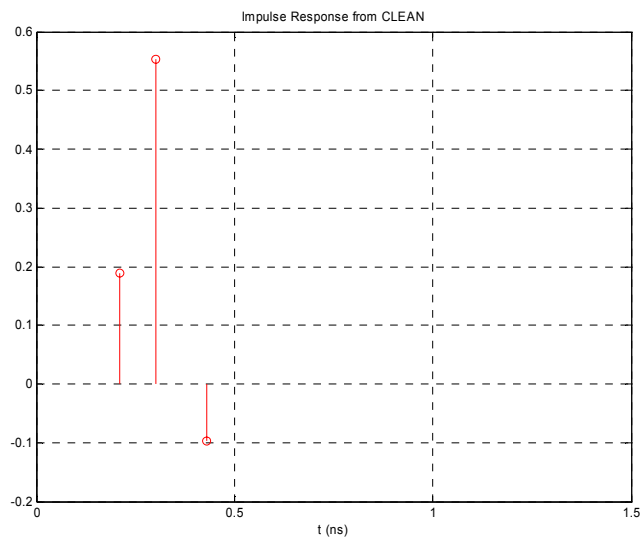


Figure 4-12. CLEAN impulse response generated from single distorted pulse

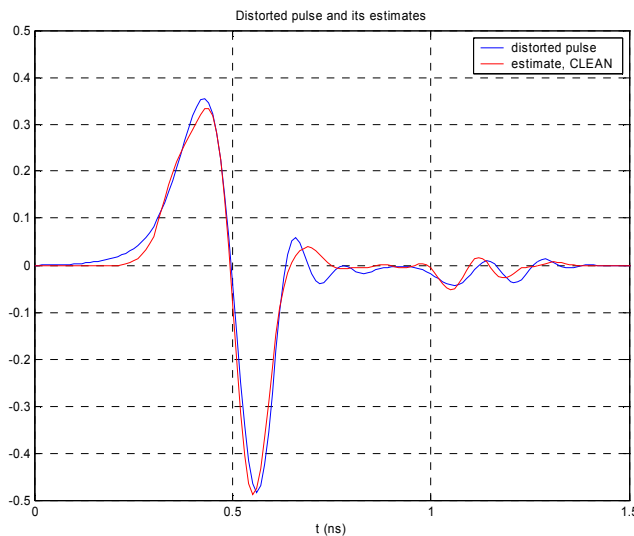


Figure 4-13. Distorted pulse and estimate of distorted pulse using CLEAN impulse response

4.3 Energy Capture from CLEAN

One measure of how accurately the impulse response generated by the CLEAN algorithm models the true channel impulse response is to evaluate how much of the energy measured in a particular data set can be represented by the calculated impulse response. To calculate this, the calculated impulse response is convolved with the template LOS pulse to create an estimate of the received signal. The energy of this estimate is then divided by the energy in the received signal to compute the energy capture ratio [57]

$$\text{Energy Capture Ratio} = \frac{\|r_{est}\|^2}{\|r_{meas}\|^2} \quad (4-2)$$

The relative error is a measure of the difference between the estimated and the measured signals and is defined as [57]

$$\text{Relative Error} = \frac{\|r_{meas} - r_{est}\|^2}{\|r_{meas}\|^2} \quad (4-3)$$

If the Energy Capture Ratio and the Relative Error sum to 1, then the noise and distortion represented by $r_{meas} - r_{est}$ is orthogonal to the signal estimate and this would represent a least squares error condition [57]

$$\text{Least Square Error Condition} \quad \frac{\|r_{est}\|^2}{\|r_{meas}\|^2} + \frac{\|r_{meas} - r_{est}\|^2}{\|r_{meas}\|^2} = 1 \quad (4-4)$$

Another characterization of the distortion is the fraction of the correlated energy in the estimated signal compared to the measured signal.

$$\text{Correlated Energy} = \left[\frac{\int r_{meas}(t)r_{est}(t)dt}{\|r_{meas}\|^2} \right] \quad (4-5)$$

All of these values calculated for the measurement data are shown in Table 4-2.

Table 4-2. Percentage of energy captured by CLEAN estimate of channel

CLEAN w/ 15 dB threshold		% Energy Capture	% Relative Error	% Correlated Energy
TEM horns	LOS	73.6	27.1	54.1
	NLOS	54.9	42.4	33.0
Bicones	LOS	61.5	37.3	39.6
	NLOS	60.4	37.9	38.7

These same values corresponding to impulse responses calculated by the CLEAN algorithm with a -20 dB threshold were also calculated and are shown in Table 4-3. While it may appear from these numbers, that a -20 dB threshold would seem a better choice as it appears to minimize the error term as defined above, inspection of the calculated impulse responses reveals that in several cases (in particular NLOS and other lower SNR cases) that the CLEAN algorithm detected paths above the -20 dB threshold that arrived well before the expected time for a LOS pulse.

Table 4-3. Percentage of energy captured by CLEAN estimate of channel

CLEAN w/ 20 dB threshold		% Energy Capture	% Relative Error	% Correlated Energy
TEM horns	LOS	78.4	20.8	62.4
	NLOS	62.9	31.1	43.9
Bicones	LOS	72.5	25.0	55.2
	NLOS	74.1	23.6	57.3

A trend of the noise being correlated with the template pulse used for deconvolution was observed in the measurement sets being analyzed. This may be due to the post-processing filtering that is performed on the measurement sets. The filtering was employed to remove the effects of a 30 MHz signal that was found to be a spurious output of the pulse generator. This filtering and the filtering effects of the hardware used in the measurements may have caused the shape of the noise to appear similar to the shape of the received pulses, and thus, there may be some correlation of the noise with the signal introduced.

Finally, a fixed energy threshold level was used as the stopping criteria for the CLEAN algorithm. Reference [57] proposes using the energy capture ratio as the stopping criteria. In their processing, they claim to see a minimization of the error term of (4-4), and that this minimization happened on average at an approximately 85% energy capture ratio. To evaluate the performance of the CLEAN algorithm on the measurement data sets as a function of the energy capture ratio, the algorithm was allowed to run for 10,000 iterations. Similar to the results reported in [57], the energy capture ratio of (4-2) did continue to increase asymptotically to unity as the number of iterations increased. However, no minimum of the error term of (4-3) was observed as in [57]. Example plots of the energy capture ratio and relative error versus the number of CLEAN algorithm iterations is shown in Figure 4-14. How nearly the least square error criteria was met (the

sum of the energy capture ratio and relative error) is shown Figure 4-15. Reference [57] indicates that they found this sum to equal 1 when the error was minimized. These trends were not found to be true in this analysis.

Therefore, this same energy capture and relative error analysis was performed on some noiseless signals generated from a ray tracing simulation created by Dr. Ahmed Attiya, currently a researcher with the Time Domain Laboratory of Virginia Tech. The simulations modeled some of the measurement scenarios in Whittemore hallways with the TEM horn antennas. The CLEAN algorithm was run on these simulated signals for numerous iterations and the resulting energy capture and relative error are shown in Figure 4-16. Similar to the measurement sets, no minimum of the relative error is seen.

Using the CLEAN algorithm with a -15 dB threshold, the number of paths found from the measurement sets and the signal generated by the ray tracing simulation are shown in Table 4-4 for comparison. There is good agreement between the sets, indicating the usefulness of the ray tracing simulations to model the true physical channel.

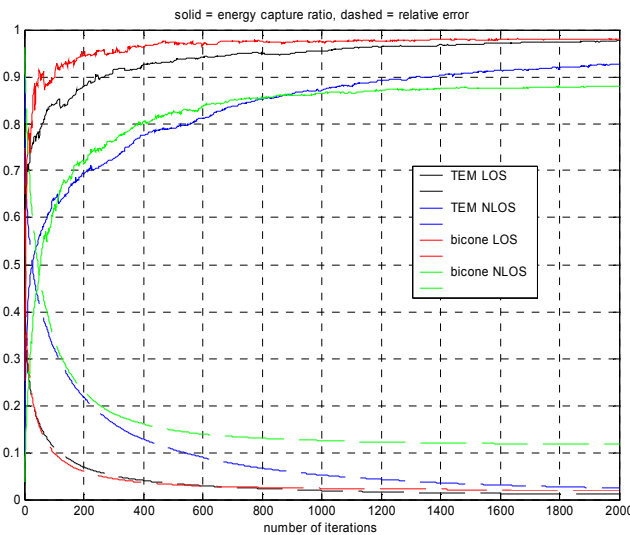


Figure 4-14. Samples of Energy Capture Ratio and Relative Error vs. CLEAN iterations

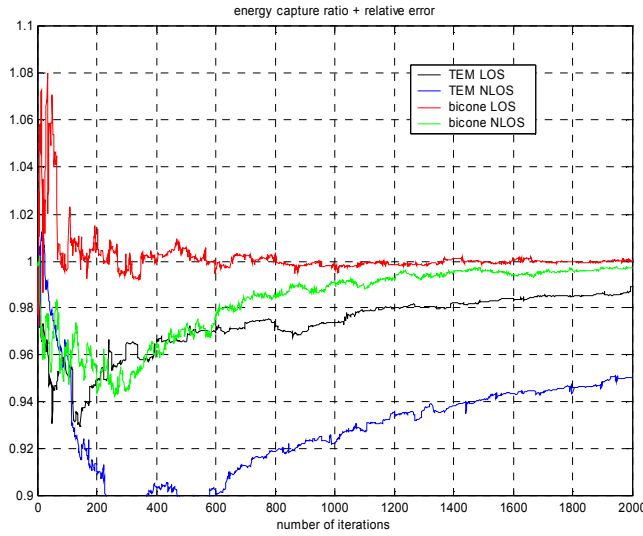


Figure 4-15. Energy Capture Ratio + Relative Error vs. CLEAN iterations

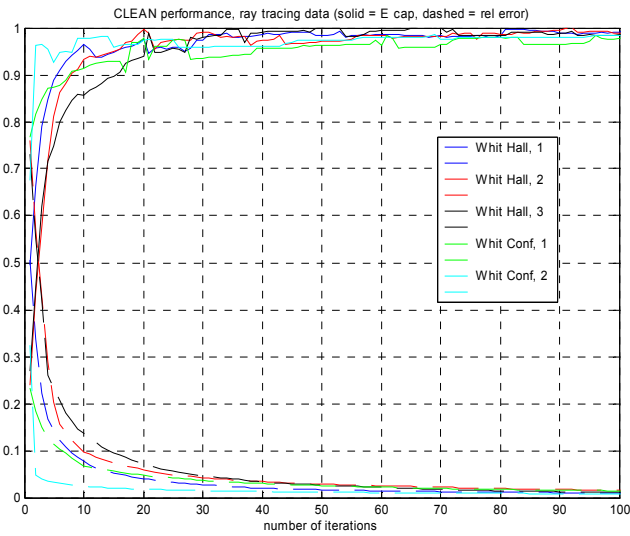


Figure 4-16. Energy Capture Ratio and Relative Error for ray tracing simulation data of TEM LOS scenarios

Table 4-4. Number of multipaths from measurement sets and ray tracing simulation

(all TEM, LOS, Whittemore)	Number of Paths (-15 dB threshold)	
	Measurement Data	Simulated Data
2nd floor Hall, position 1_41	9	7
2nd floor Hall, position 2_41	12	10
2nd floor Hall, position 3_41	15	13
Conference Room, position 1_41	1	3
Conference Room, position 2_41	2	2

4.4 Conclusions

Several specific cases have been presented illustrating limitations in the accuracy of the CLEAN algorithm. Here, trends of the CLEAN algorithm's accuracy were found to be different from the claims of other researchers [57]. Thus, further more analytic investigation into the performance of the CLEAN is necessary.

5 UWB Channel Models and Their Significance in Communications System Performance

One of the primary goals in developing channel models is to allow simple, efficient, and accurate simulation of communications systems. Therefore, it is not necessarily sufficient that the models share certain key statistics with the true channels (known through measurements). A communications system designer is concerned with the system performance (measured by such things as receiver energy capture, signal to noise ratio and bit error rate (BER)) and thus the model must be able to faithfully recreate the performance. This chapter analyzes the accuracy of different models in representing the performance of the true (measured) channels.

5.1 Comparison between Traditional Channel Models

Using the model parameters found and listed in Table 3-14, Table 3-15, and Table 3-16 corresponding to the LOS bicone cases, 100,000 impulse responses for each of the single Poisson arrival time model, the modified Saleh-Valenzuela model, and the modified Δ -K model are generated. Two pulses are considered: the received baseband pulse from the measurements using the bicone antennas and a 6-7 GHz (3 dB bandwidth) Gaussian modulated sinusoid pulse.

The (unit energy) pulse is convolved with the impulse response to create a simulated received signal. Each impulse response is normalized to have unit energy (such that the sum of the square the taps is equal to 1). The energy capture of a Rake receiver is calculated using the matched filter output of the received signal. For the simulated bicone signal, the template used for matched filtering is only the main lobe of

the bicone pulse rather than the entire pulse, since most of the energy is contained in this lobe that is less than 250 ps in duration while the entire pulse response is nearly 5 ns. The peaks in the matched filter output are chosen such that the first finger is the strongest correlation, the second finger is the next strongest correlation, and so on. The finger delays are chosen such that they are separated by at least the duration of the template.

The energy capture for different number of Rake fingers is calculated for each individual simulated signal. The average energy capture as a function of the number of fingers for each model considered is then calculated. The BER of a UWB system using antipodal signaling and binary PPM were also calculated at different SNR values for each simulated received signal.

100,000 impulse responses were generated because it was found that for sets with fewer sample impulse responses (1000 for example) there were not enough samples to accurately characterize the mean BER values. To determine an accurate approximation of the mean BER, a large number of samples are necessary (as compared to the mean energy capture) because the mean BER is dominated by the few unlikely channels that generate very strong signal fades (or cause interference in the time delayed or advanced correlation for PPM), and BER values tend to be spread over a log scale for energy capture values spread over a linear scale. When BER values are averaged, one or a few extreme values can dominate the average. Thus, to accurately represent the effect of these outlying extreme cases large sample sets are needed.

As an example, consider the case of a 5 finger Rake at $E_b/N_o = 14$ dB for the 6-7 GHz pulse system for each of the three models with the BER calculated from a set of 1000 impulse responses. The Saleh-Valenzuela model average BER is found to diverge

significantly toward higher BER rates compared with the other two models. A histogram of the \log_{10} of BER values for antipodal signaling at $E_b/N_o = 14$ dB for each of the three models is shown in Figure 5-1. Each of the models gives a similar distribution of BER values. However, one outlying high value of BER can be seen in the Saleh Valenzuela case. This outlier is even more obvious when the histogram of the BER in linear is viewed as in Figure 5-2. The extreme value that is causing the average BER of the Saleh-Valenzuela case to deviate is clearly seen here. This particular case corresponds to an impulse response that causes a severe fade for the 6-7 GHz pulse system. The total energy in the simulated received signal is only 0.27 (compared to energy of 1 if all impulse response taps corresponded to resolvable paths). The energy capture of the Rake is also observed to be very low for this particular impulse response.

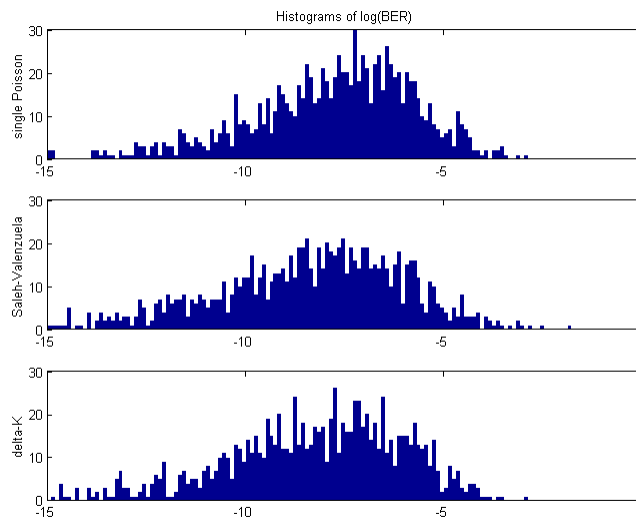


Figure 5-1. Histogram of $\log_{10}(\text{BER})$ for 5 finger Rake at $E_b/N_o = 14$ dB, 6-7 GHz pulses, set 4 impulse responses, all three models

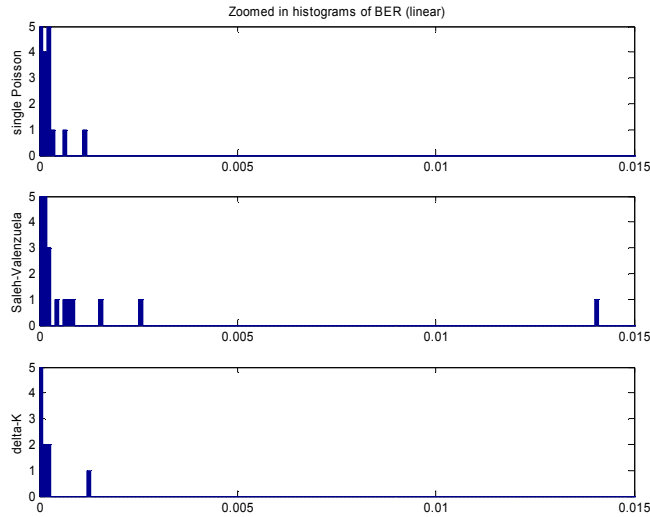


Figure 5-2. Zoomed on extreme values, histogram of BER (linear) for 5 finger Rake at $E_b/N_o = 14$ dB, 6-7 GHz pulses, set 4 impulse responses, all three models

The average energy capture for the baseband bicone pulse is shown in Figure 5-3 and the average energy capture for the 6-7 GHz pulse is shown in Figure 5-6. The average BER for the baseband bicone pulse signal with antipodal signal and PPM are shown in Figure 5-4 and Figure 5-5 respectively and the BER for the 6-7 GHz pulse signal with antipodal signal and PPM are shown in Figure 5-7 and Figure 5-8 respectively.

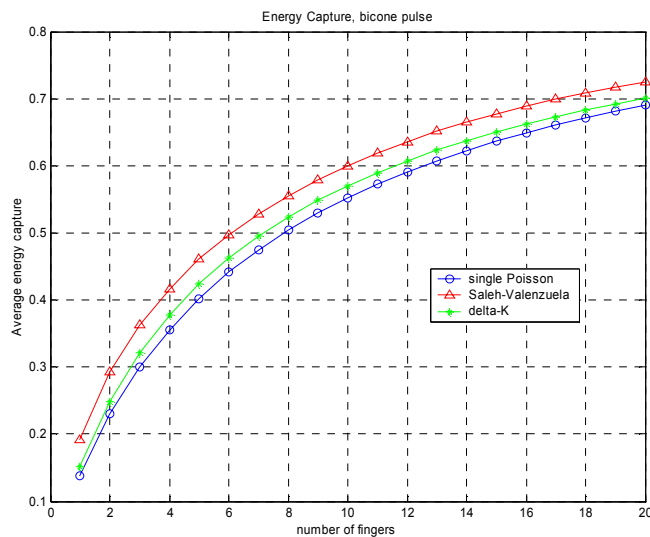


Figure 5-3. Comparison of average energy capture for a Rake receiver when using different channel models with the bicone pulse

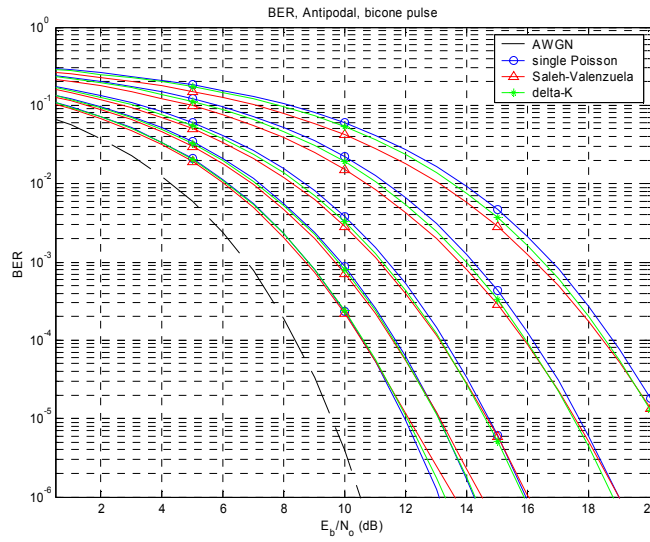


Figure 5-4. Comparison of average BER for antipodal signaling and a Rake receiver when using different channel models with the bicone pulse (1, 2, 5, 10, and 20 finger cases, from right to left)

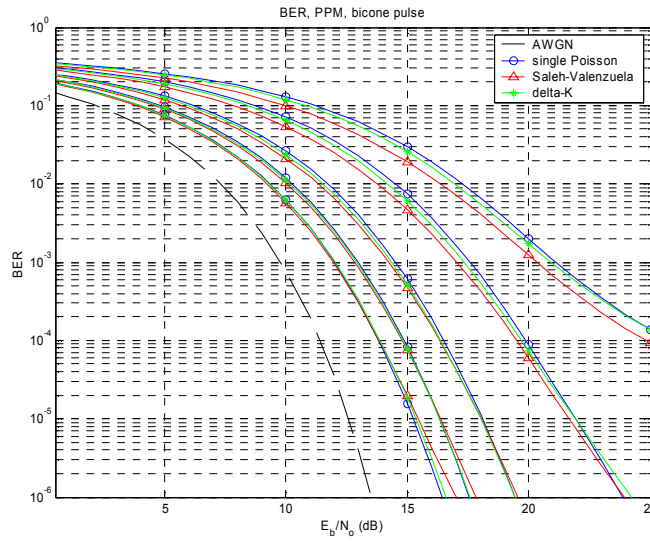


Figure 5-5. Comparison of average BER for binary PPM and a Rake receiver when using different channel models with the bicone pulse (1, 2, 5, 10, and 20 finger cases, from right to left)

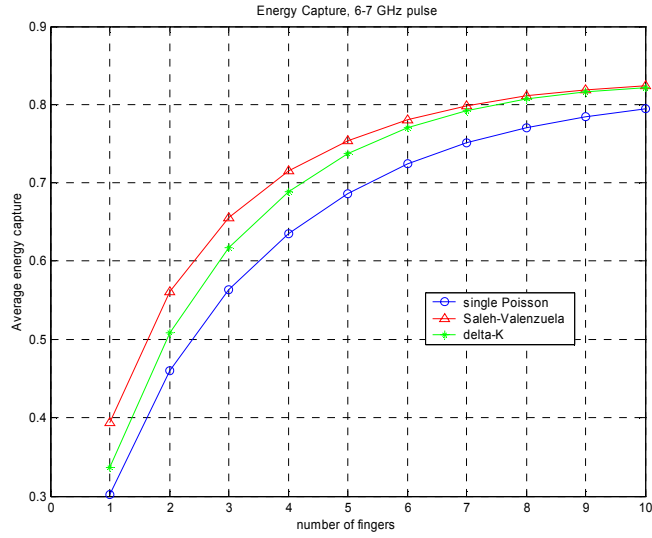


Figure 5-6. Comparison of average energy capture for a Rake receiver when using different channel models with the 6-7 GHz pulse

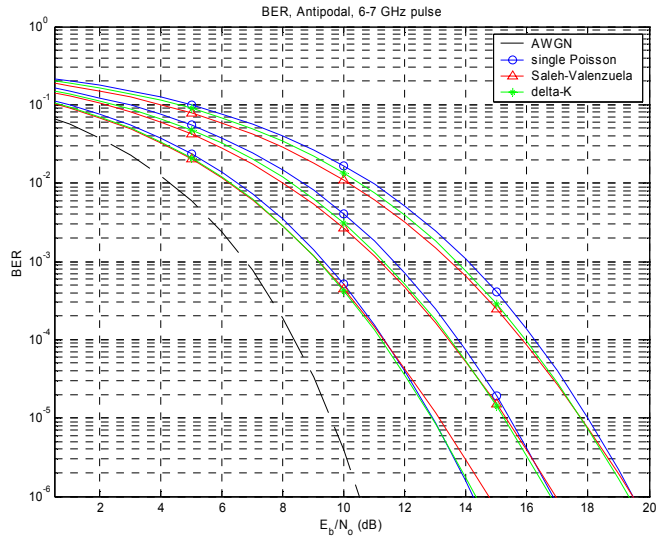


Figure 5-7. Comparison of average BER for antipodal signaling and a Rake receiver when using different channel models with the 6-7 GHz pulse (1, 2, and 5 finger cases, from right to left)

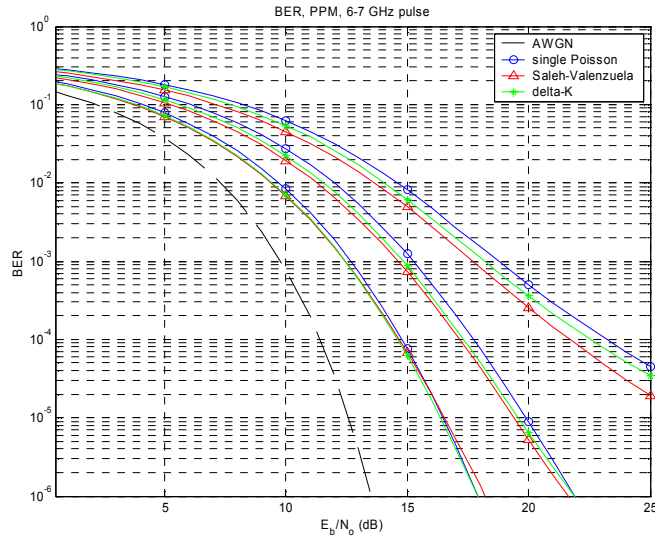


Figure 5-8. Comparison of average BER for binary PPM and a Rake receiver when using different channel models with the 6-7 GHz pulse (1, 2, and 5 finger cases, from right to left)

It should be noted that there are also some small differences in the statistics of the simulated impulse responses, shown in Table 5-1, that were used as metrics to allow a fair comparison between models. The ordering of these statistics is not entirely the same as the ordering of the performance, therefore there does appear to be some difference in the simulated performance levels when using different channel models. Table 5-2 compares the average BER performance/energy capture rankings with the ranking of the average channel statistics. The slight performance differences may be due to the slight difference in the channel delay statistics. The Saleh-Valenzuela model cases do appear to deviate slightly from the other two indicating that this model may need more samples to accurately characterize the mean. This would be true if the Saleh-Valenzuela model can create a larger variation of possible impulse responses because of the greater number of random variables that this model uses. The overall difference in the simulated system performance between these models is relatively small and is even further decreased for

higher order Rake receivers. Therefore, from a communications system simulation perspective, the choice between these three channel models appears to make little difference.

Table 5-1. Average of statistics for simulated channel model impulse responses

		$\bar{\tau}$ (ns)	σ_{τ} (ns)	num paths
set 3	single Poisson	4.96	4.74	23.6
	Saleh-Valenzuela	4.81	4.61	23.4
	Δ -K	4.58	4.44	22.2
set 4	single Poisson	4.96	4.72	24.1
	Saleh-Valenzuela	4.75	4.70	23.4
	Δ -K	4.75	4.48	22.6

Table 5-2. Comparison of model system performance with channel statistics

	BER/Energy Capture (best-worst)	number of paths (most-fewest)	delay statistics (largest-smallest)
Saleh-Valenzuela	1	2	1
Δ -K	2	3	2
single Poisson	3	1	3

5.2 Comparison of Models to LOS Measurement Data

The same procedure to determine energy capture and BER performance was performed on the 132 measurement sets corresponding to the LOS bicone scenarios. The mean value performance curves for the measurement sets are plotted with the mean value performance curves of the model generated impulse responses and are shown in Figure 5-9 to Figure 5-14. For the BER plots, the Saleh-Valenzuela and Δ -K models are not shown to make the plots more viewable.

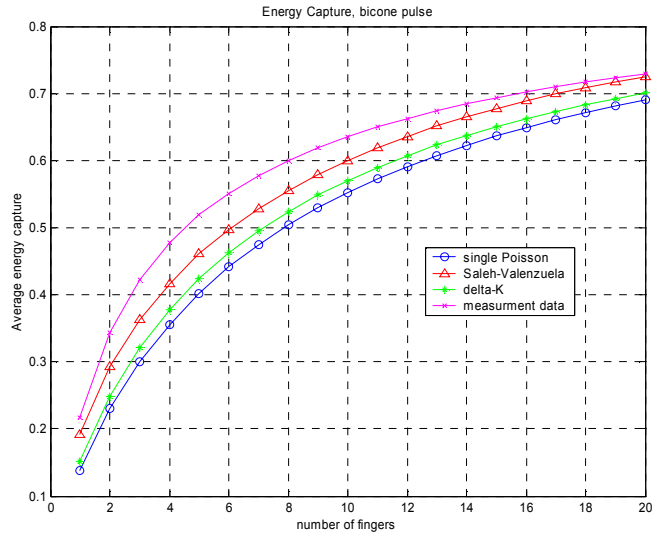


Figure 5-9. Average energy capture for a Rake receiver when using different channel models compared with the measured LOS channels for the bicone pulse

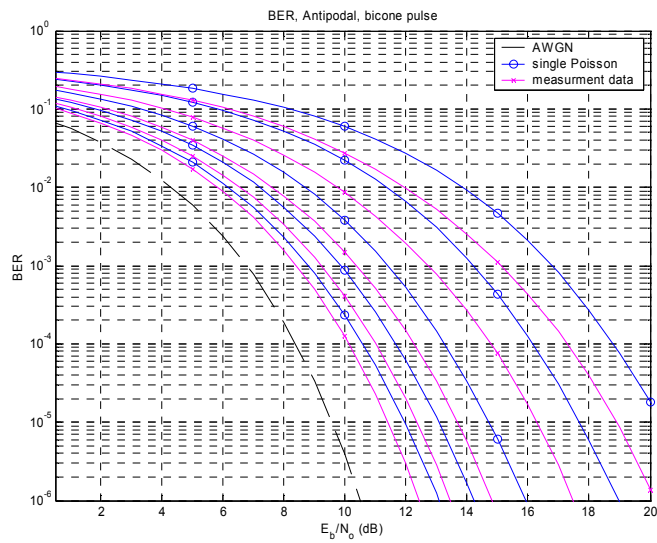


Figure 5-10. Average BER for antipodal signaling and a Rake receiver when using single Poisson model compared with the measured LOS channels for the bicone pulse (1, 2, 5, 10, and 20 finger cases, from right to left)

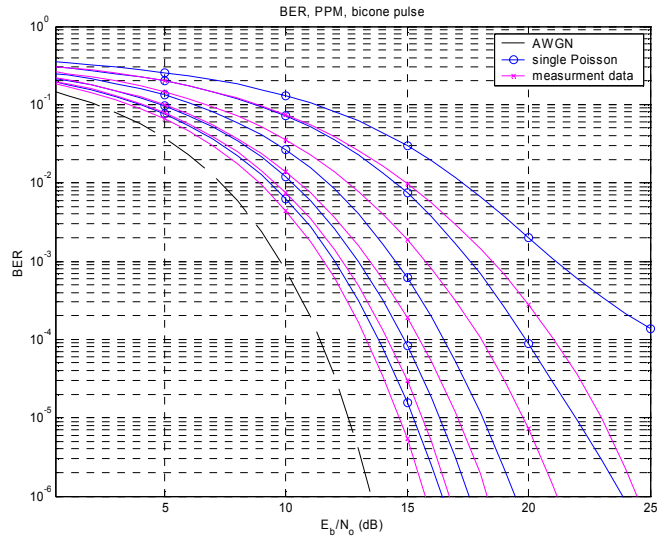


Figure 5-11. Average BER for PPM and a Rake receiver when using single Poisson model compared with the measured LOS channels for the bicone pulse (1, 2, 5, 10, and 20 finger cases, from right to left)

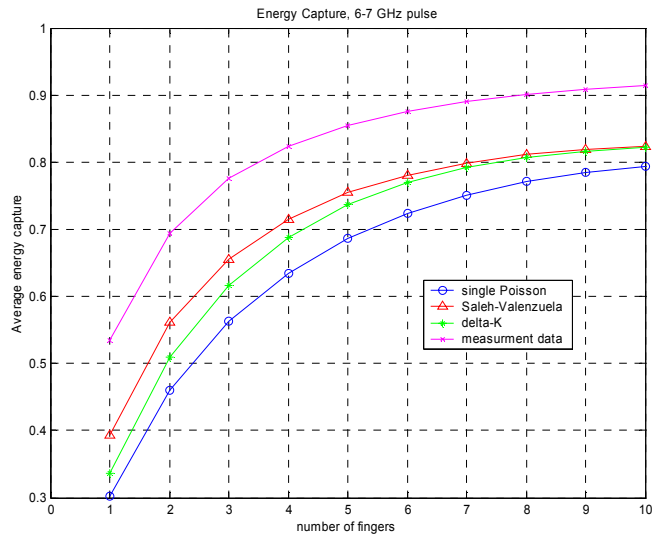


Figure 5-12. Average energy capture for a Rake receiver when using different channel models compared with the measured LOS channels for the 6-7 GHz pulse

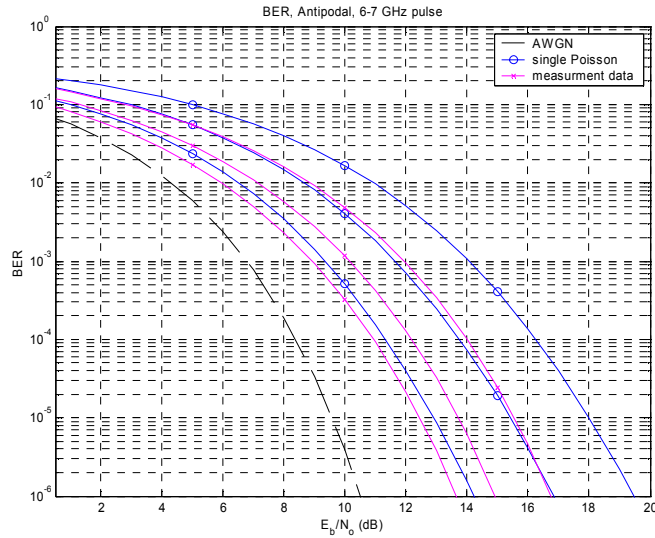


Figure 5-13. Average BER for antipodal signaling and a Rake receiver when using single Poisson model compared with the measured LOS channels for the 6-7 GHz pulse (1, 2, and 5 finger cases, from right to left)

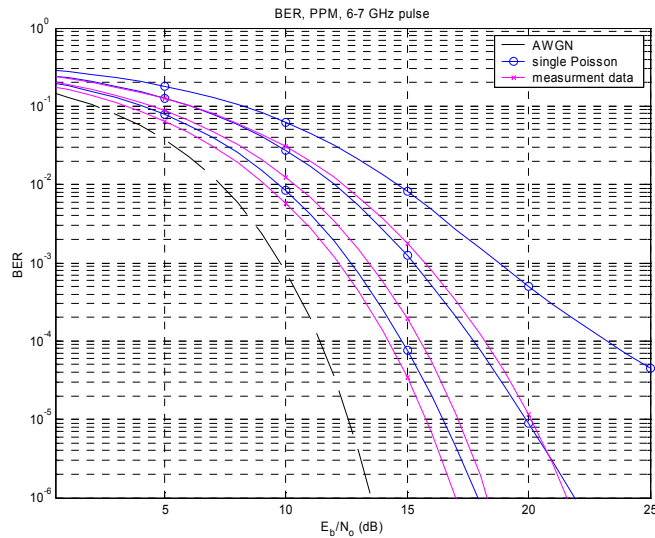


Figure 5-14. Average BER for PPM and a Rake receiver when using single Poisson model compared with the measured LOS channels for the 6-7 GHz pulse (1, 2, and 5 finger cases, from right to left)

There is a significant difference between the performances determined when using the LOS measurement channels versus the channels generated from the models, despite the similar statistics (mean excess delay, RMS delay spread, and number of

multipath components). This difference is likely due to the fact that the measurement sets correspond to LOS conditions and the LOS component is much stronger than any later arriving paths. The models considered assume an exponential power decay, but the LOS component (and perhaps other strong reflections such as are seen in hallway scenarios) likely do not fit the exponential decay that the later paths are expected to follow. It must be remembered that the models considered have previously been primarily suggested for NLOS channels. Figure 5-15 and Figure 5-16 show bar graphs of the energy captured by different fingers of the Rake receiver for the model and measurement impulse responses for the bicone pulse system and 6-7 GHz pulse system respectively. The finger numbers shown correspond to the ordering of greatest to least energy capture within each profile regardless of the temporal ordering. As expected, because of the LOS component and other strong reflections, the averages of the strongest three paths in the measurement data for the bicone pulse case are larger than the corresponding paths for the models. While these bar graphs do not indicate what relative time the strongest path arrived, from observation of the impulse responses, it is clear that these dominant paths arrive very early in the profile (and the LOS path always arrives first). Thus, for the same delay statistics, the measurement data has more relatively weak paths at greater delays, while for the model impulse responses, the energy is distributed more evenly over time (compared to the measurement data).

Interestingly, the Saleh-Valenzuela model on average produces a significantly greater strongest component than the other two models, followed by the Δ -K model and finally by the single Poisson model. This also generally follows the performance trends seen between the models. This may be due to the clustering inherent in the Saleh-

Valenzuela model. Clustering can produce groups of paths at different energy levels, which is more similar to the effects seen in the LOS data than a model that assumes a single exponential decay. However, the difference in BER performance between the measurement data and the Saleh-Valenzuela model is greater than might be expected from comparing the relative energy in the strongest few paths (while the difference in the energy in the strongest path between the Saleh-Valenzuela model and the other models appears significant, but the BER performance for all models is fairly similar).

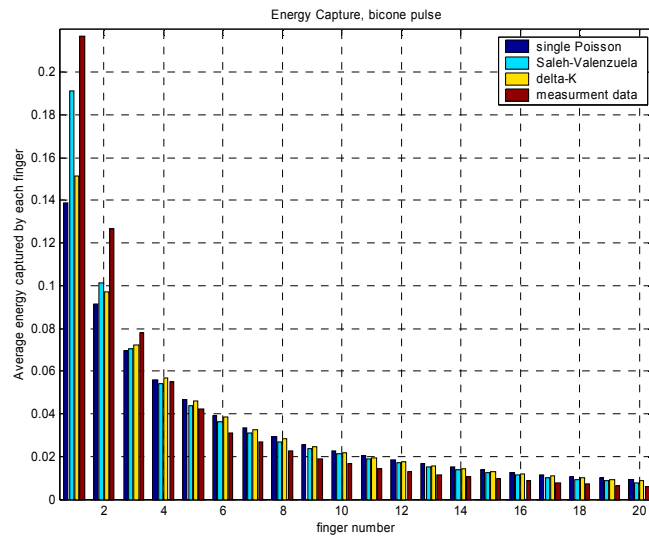


Figure 5-15. Average energy capture for each Rake finger when using different channel models compared with the measured LOS channels for the bicone pulse

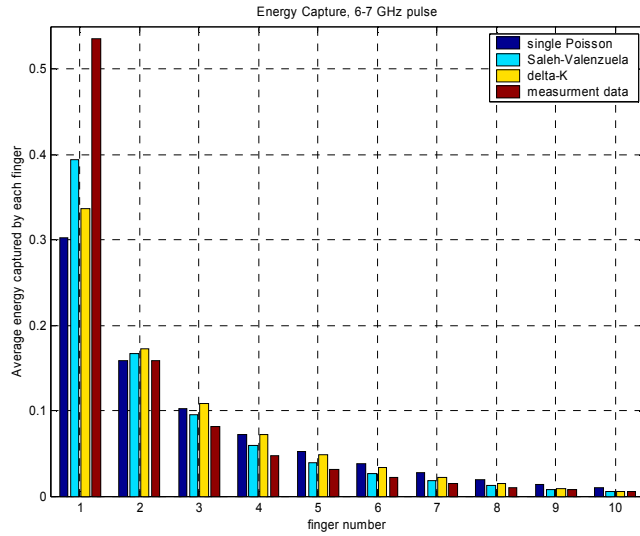


Figure 5-16. Average energy capture for each Rake finger when using different channel models compared with the measured LOS channels for the 6-7 GHz pulse

It is concluded that the models do not match the data because they are more appropriate for NLOS channels. However, it has been clearly shown that between the three models considered, the difference to UWB communications system performance is small.

5.3 New Model for UWB LOS Channels

Due to the discrepancy in the BER performance between the measurement channels and the model channels for LOS scenarios, a modified version of the single Poisson arrival time model with dominant early multipath components was developed to more accurately represent LOS channels. The model is based on the characteristics observed in the measurement data.

The first multipath components have significantly more energy than the later arriving components. The number of dominant components, M , is randomly chosen to be two, three, or four (each has equal likelihood). This agrees with the trends seen in the

measurement data. The majority of the available measurement data is from hallways, so to accurately represent different LOS scenarios, it may be necessary to reduce the number of dominant components. The interarrival times of the dominant components are exponentially distributed and given by

$$p(\tau_k | \tau_{k-1}) = \lambda_1 \exp[-\lambda_1 (\tau_k - \tau_{k-1})], \quad 0 < k < M \quad (5-1)$$

where λ_1 is the mean arrival rate of the dominant components. The amplitude of each dominant component is given by a lognormal random variable with unit mean energy and fading parameter σ_1

$$\beta_k = p_k 10^{(\mu_k + X_{\sigma,k})/20} \quad (5-2)$$

where

$$\mu_k = -\frac{\sigma_1^2 \ln(10)}{20}, \quad 0 < k < M$$

and

$$X_{\sigma,k} = N(0, \sigma_1^2) \quad (\sigma_1 \text{ is in dB}), \quad 0 < k < M$$

The first component arrives at zero delay ($\tau_0 = 0$) and has positive polarity ($p_0 = +1$) because this is assumed to be the LOS component which will not be inverted. All other paths have an equiprobable positive or negative polarity.

The interarrival times of the weaker components also follow an exponential interarrival, but with a different mean arrival rate λ_2

$$p(\tau_k | \tau_{k-1}) = \lambda_2 \exp[-\lambda_2 (\tau_k - \tau_{k-1})], \quad k \geq M \quad (5-3)$$

The mean energies of the weaker components follow a traditional exponential decay. The first component from this group has mean energy W dB less than the mean of the

dominant components and the means of the later components are taken relative to this first weak path. The weak path amplitudes are also lognormal variables with a different fading parameter, σ_2 , such that

$$\mu_k = -W - \frac{10(\tau_k - \tau_M)/\gamma}{\ln(10)} - \frac{\sigma_2^2 \ln(10)}{20}, \quad k \geq M$$

and

$$X_{\sigma,k} = N(0, \sigma_2^2) \quad (\sigma_2 \text{ is in dB}), \quad k \geq M$$

The parameters that were found to best match the desired average mean excess delay, average RMS delay spread, average number of multipaths, average energy capture and average BER performance are shown in Table 5-3. These parameters were used to generate 1000 sample impulse responses, where only the paths within 15 of the strongest path were kept. Then received signals were simulated for the bicone and 6-7 GHz pulses.

Table 5-3. Fit of bicone LOS data to new LOS channel model.

Values in () indicate target value.

$1/\lambda_1$	2e-9
σ_1	0.7
$1/\lambda_2$	0.7e-9
W	12
γ	23e-9
σ_2	0.5
$\bar{\tau}$ (ns)	4.15 (4.20)
σ_τ (ns)	4.72 (4.55)
number paths	22.4 (23.2)

The average energy captures for each finger of a Rake receiver are shown in Figure 5-17 and Figure 5-21 compared with the impulse responses from the measurement

data for the bicone pulse and 6-7 GHz pulse respective. Figure 5-18 and Figure 5-22 show the average energy captures of Rake receivers and Figure 5-19, Figure 5-20, Figure 5-23, and Figure 5-24 show the corresponding BER curves for antipodal signaling and PPM.

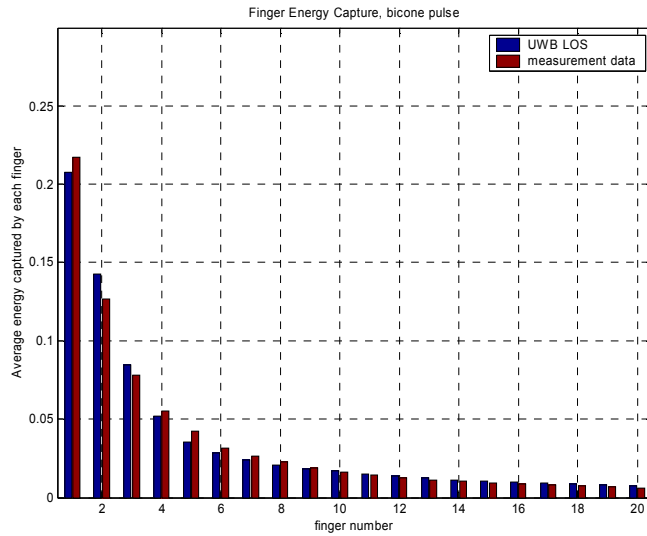


Figure 5-17. Average energy capture for each Rake finger for new LOS channel model compared with the measured LOS channels for the bicone pulse

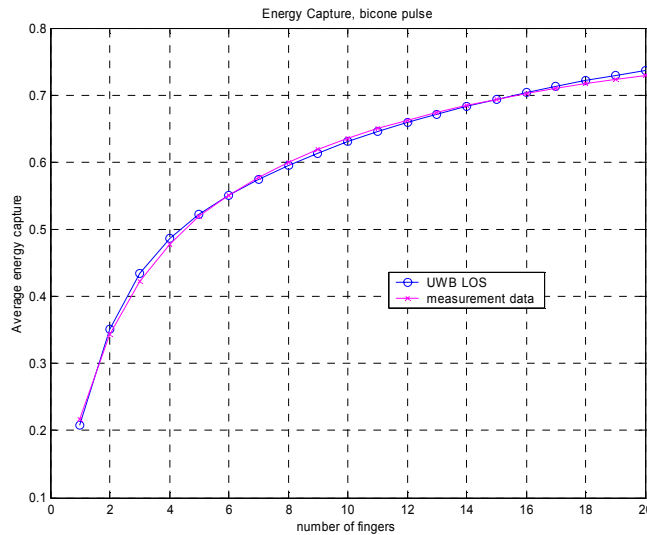


Figure 5-18. Average energy capture for a Rake receiver when using new LOS model compared with the measured LOS channels for the bicone pulse

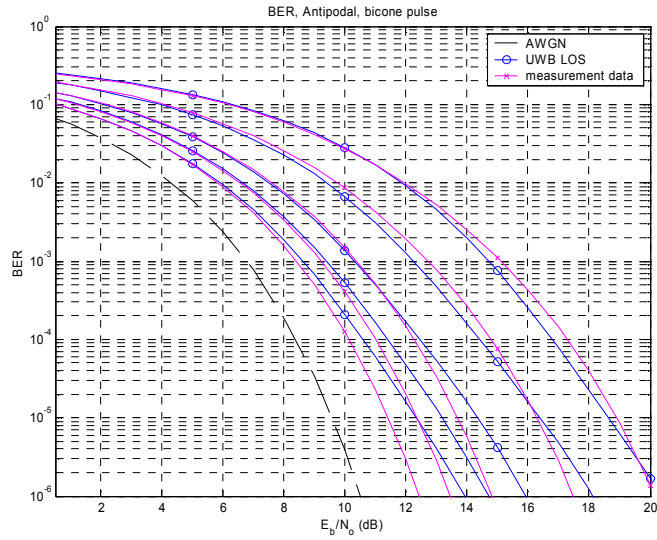


Figure 5-19. Average BER for antipodal signaling and a Rake receiver when using new LOS model compared with the measured LOS channels for the bicone pulse (1, 2, 5, 10, and 20 finger cases, from right to left)

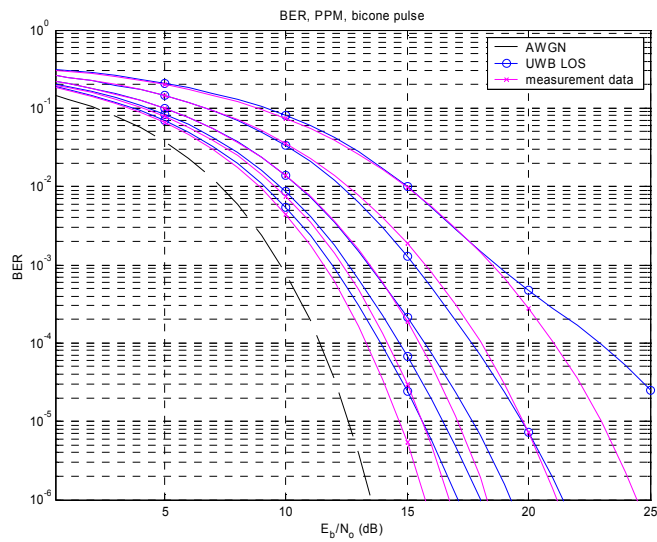


Figure 5-20. Average BER for PPM and a Rake receiver when using new LOS model compared with the measured LOS channels for the bicone pulse (1, 2, 5, 10, and 20 finger cases, from right to left)

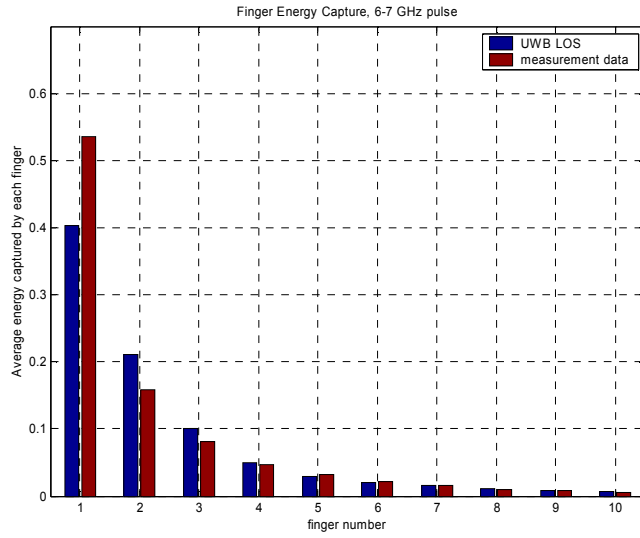


Figure 5-21. Average energy capture for each Rake finger for new LOS channel model compared with the measured LOS channels for the 6-7 GHz pulse

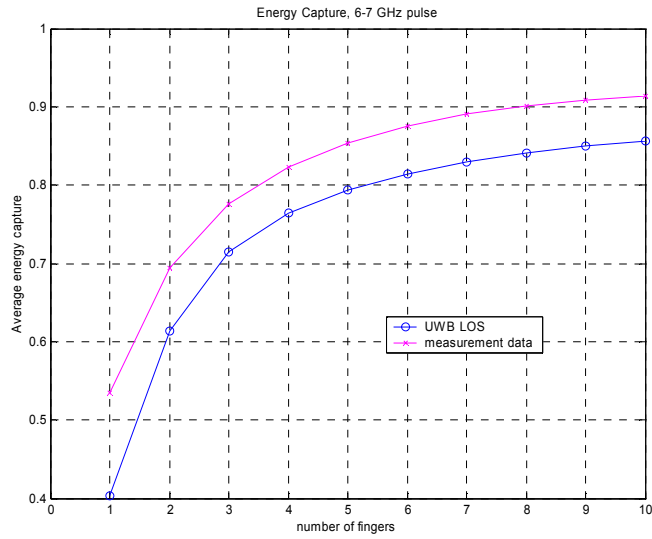


Figure 5-22. Average energy capture for a Rake receiver when using new LOS model compared with the measured LOS channels for the 6-7 GHz pulse

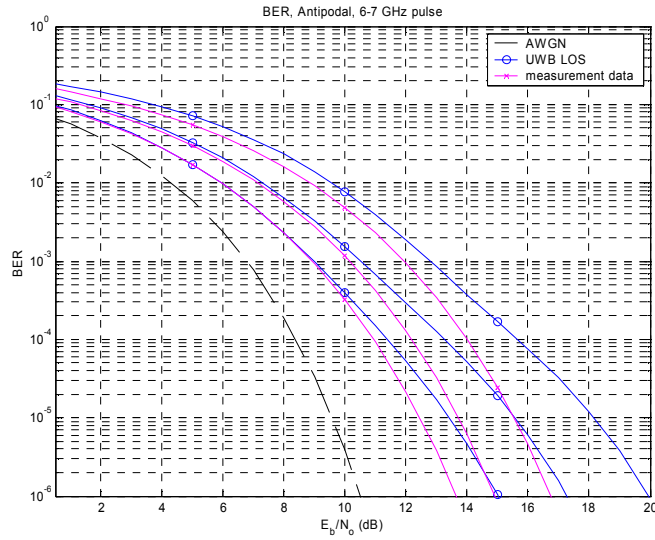


Figure 5-23. Average BER for antipodal signaling and a Rake receiver when using new LOS model compared with the measured LOS channels for the 6-7 GHz pulse (1, 2, and 5 finger cases, from right to left)

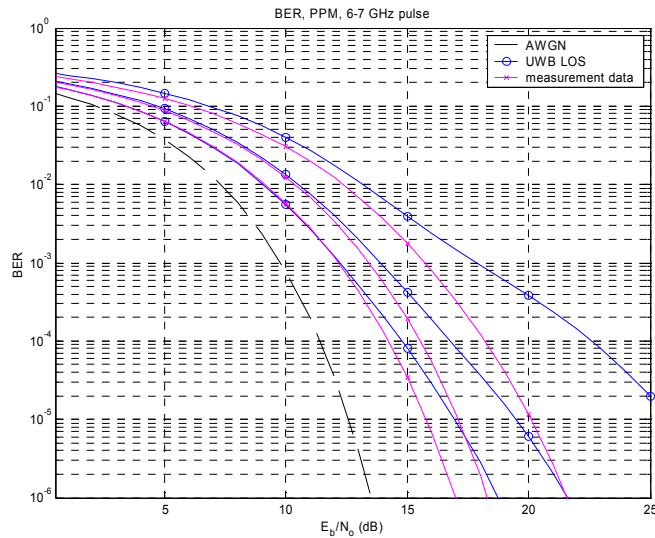


Figure 5-24. Average BER for PPM and a Rake receiver when using new LOS model compared with the measured LOS channels for the 6-7 GHz pulse (1, 2, and 5 finger cases, from right to left)

In searching for appropriate parameters, it was found that to match only the mean excess delay, RMS delay spread, and number of paths, the key parameters to adjust were the interarrival rates and exponential decays (for any model). The amplitude fading

variables were less important toward matching these components. To match the average energy capture, the W parameter, which creates dominant early paths, was crucial. The amplitude fading variables were also significant but not as much as W . But to achieve the best possible average BER match, the amplitude fading variables and W were both crucial. If the average energy capture is reasonably well matched, the mean BER may not be, because if the amplitude fading is too high, the worst case fades will be more severe and the corresponding high BER cases will affect the mean BER more than the low energy captures will affect the mean energy capture.

As seen from the above figures, the mean BER curves achieved using the new models do not agree exactly with the measurement data, but the agreement is far better than for any of the previously considered models (single Poisson, Saleh-Valenzuela, or Δ -K), especially at lower SNR levels. The agreement between the new model and the measurement data is better for the bicone pulse than for the 6-7 GHz pulse, particularly for the average energy captures. The reason for the difference may be due to the more complex interactions that occur when the 6-7 GHz pulses interfere. The 6-7 GHz pulse contain multiple cycles so the exact delays cause can more significant signal variations than for the simpler bicone pulses.

5.4 Comparison of Models to NLOS Measurement Data

The number of available NLOS measurement profiles is limited and the profiles used for analysis in section 3.2 are a mixture of different types of NLOS data. Some represent scenarios where the transmitter and receiver are located in different rooms separated by a wall, some represent a scenario where the transmitter and receiver are separated by untreated glass, and some represent situations where the LOS path is

blocked or partially blocked by a corner. The scenarios through glass have very dominant early paths (due to the minimal attenuation and distortion of the glass and other unique features of that specific measurement site) and do not share many general characteristics with the other NLOS scenarios. Since the traditional models considered here are based on NLOS channels with no dominant paths, for analysis in this section, only the measurements corresponding to separation by a wall or corner are considered leaving 39 profiles. The averages of the mean excess delay, RMS delay spread, and number of multipath components were recalculated for this NLOS subset and are shown in Table 5-4. Appropriate parameters for the single Poisson model and Saleh-Valenzuela model were found to match these NLOS subset statistics and are also shown in Table 5-4.

Table 5-4. Average statistics of NLOS channels with no dominant paths and model parameters to match these statistics

	measurements	single Poisson	Saleh-Valenzuela
$1/\Lambda$	---	---	10e-9
$1/\lambda$	---	0.7e-9	1.4e-9
Γ	---	---	21e-9
γ	---	20e-9	8e-9
σ	---	2	2
$\bar{\tau}$ (ns)	17.50	15.30	16.11
σ_{τ} (ns)	13.29	14.30	13.76
number paths	80.7	80.3	78.6

The energy capture and BER performance using the measured channels were compared with the performance using 1000 impulse responses from each of the single Poisson and Saleh-Valenzuela models generated using the parameters given in Table 5-4. Figure 5-25 through Figure 5-32 show the energy capture and BER performance for both the baseband bicone pulse and the 6-7 GHz Gaussian modulated sinusoid pulse. These

models are found to match the BER performance of the measured channels reasonably well. The match is better for the bicone pulse than the 6-7 GHz which is similar to what was seen above with the new LOS model. This may be because the measured channels correspond to bicone pulses and the models are thus biased to matching this case. As was shown in section 4.1, CLEAN impulses responses are not necessarily as applicable to pulses at different frequencies from that of the measurement pulse. The Saleh-Valenzuela model in general offers a slightly better match than the simpler single Poisson model, but the difference for either model is still small (less than 1 dB in most cases).

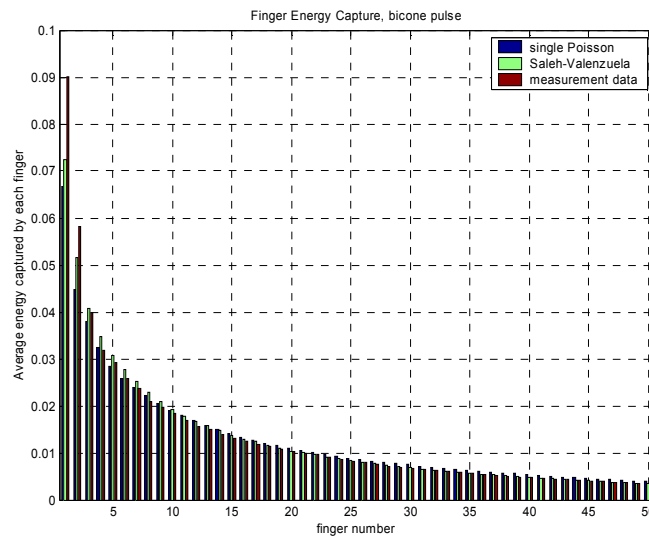


Figure 5-25. Average energy capture for each Rake finger for single Poisson and Saleh-Valenzuela models compared with the measured NLOS channels for the bicone pulse

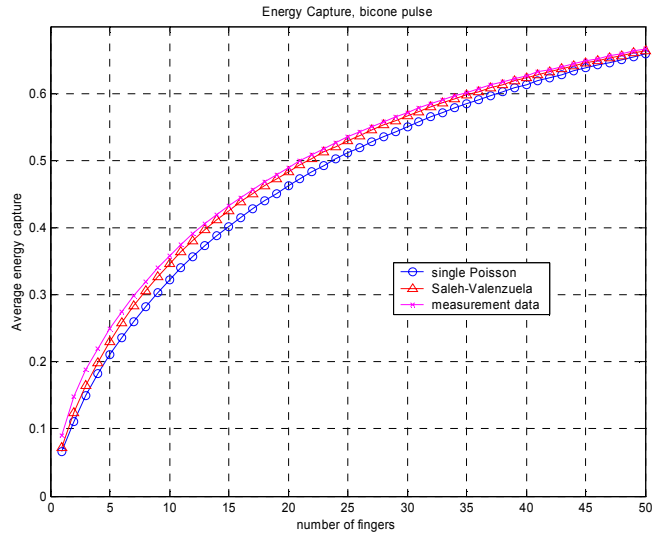


Figure 5-26. Average energy capture for a Rake receiver when using single Poisson and Saleh-Valenzuela models compared with the measured NLOS channels for the bicone pulse

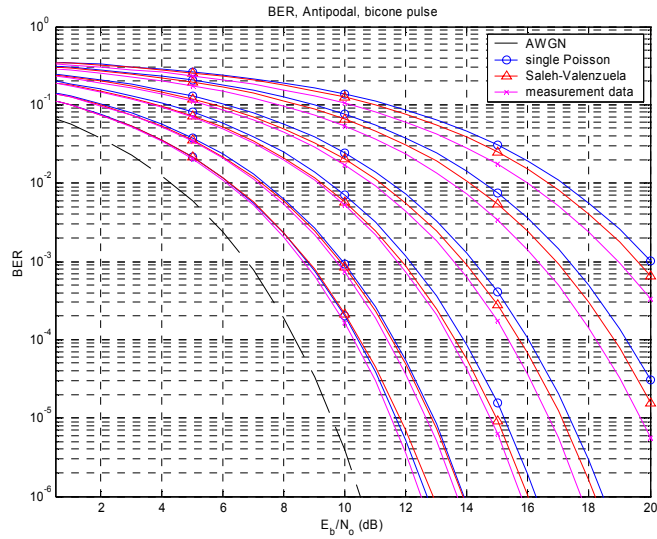


Figure 5-27. Average BER for antipodal signaling and a Rake receiver when using single Poisson and Saleh-Valenzuela models compared with the measured NLOS channels for the bicone pulse (1, 2, 5, 10, 25, and 50 finger cases, from right to left)

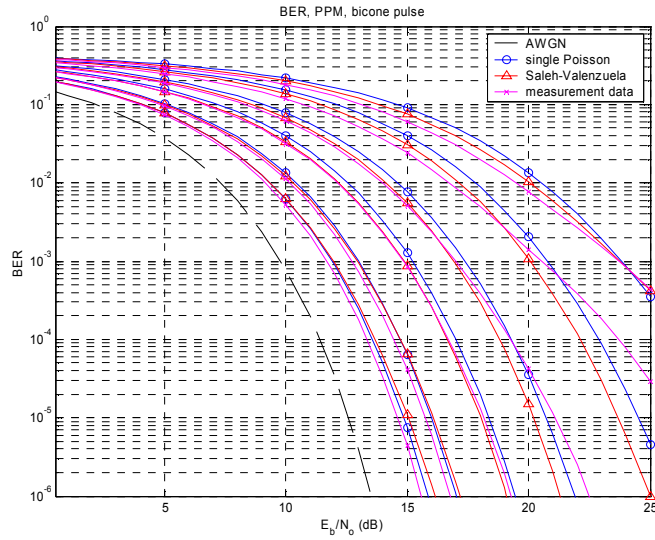


Figure 5-28. Average BER for PPM and a Rake receiver when using single Poisson and Saleh-Valenzuela models compared with the measured NLOS channels for the bicone pulse (1, 2, 5, 10, 25, and 50 finger cases, from right to left)

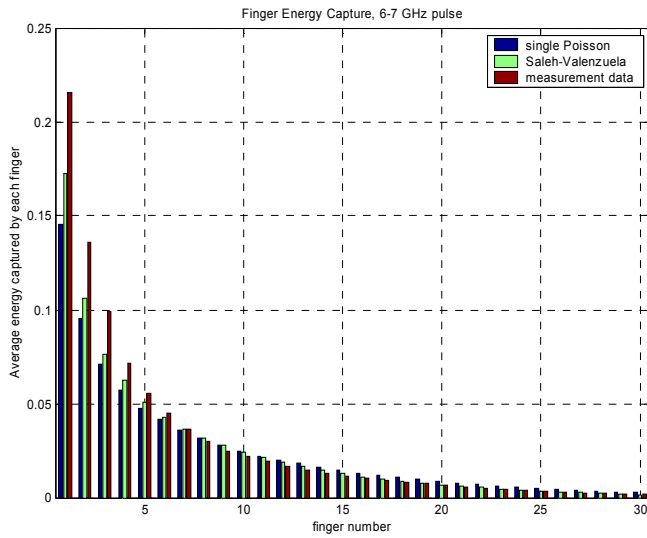


Figure 5-29. Average energy capture for each Rake finger for single Poisson and Saleh-Valenzuela models compared with the measured NLOS channels for the 6-7 GHz pulse

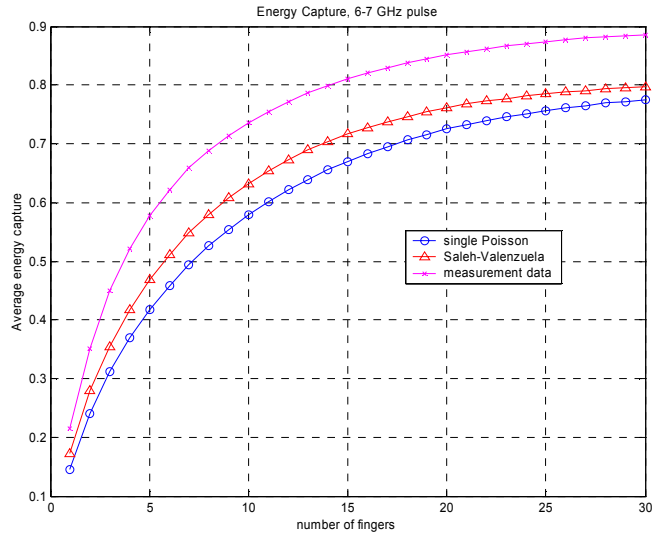


Figure 5-30. Average energy capture for a Rake receiver when using single Poisson and Saleh-Valenzuela models compared with the measured NLOS channels for the 6-7 GHz pulse

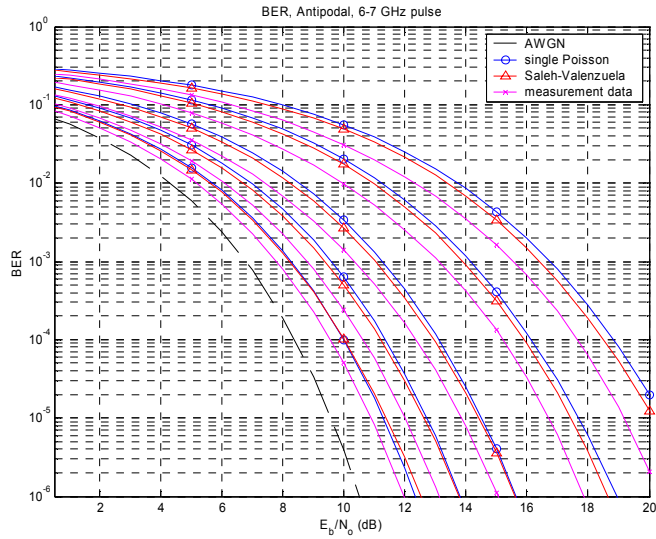


Figure 5-31. Average BER for antipodal signaling and a Rake receiver when using single Poisson and Saleh-Valenzuela models compared with the measured NLOS channels for the 6-7 GHz pulse (1, 2, 5, 10, and 25 finger cases, from right to left)

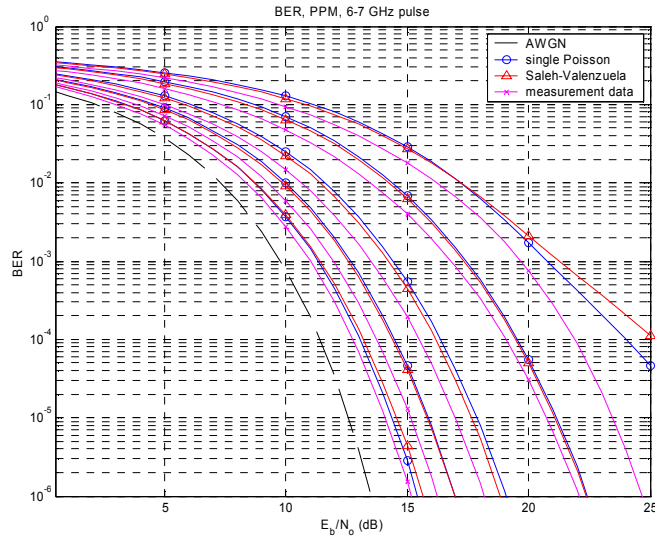


Figure 5-32. Average BER for PPM and a Rake receiver when using single Poisson and Saleh-Valenzuela models compared with the measured NLOS channels for the 6-7 GHz pulse (1, 2, 5, 10, and 25 finger cases, from right to left)

5.5 Conclusions

It has been shown that there is little difference in the simulated performance of UWB systems when any of the traditional channel models (the single Poisson arrival time model, the Saleh-Valenzuela model, and the Δ -K model) are used. These models are useful and appropriate to model NLOS channels, but not LOS channels. It was shown that the traditional models can be made to fit the statistics of LOS channels, but they predict very pessimistic energy capture and BER performance. These models were originally developed for NLOS channels and therefore do not have the dominant early arriving paths that are present in LOS channels. A new model for LOS channels was presented and shown to more accurately represent LOS channels than the traditional models.

6 Significance of Fractional Bandwidth

This chapter compares the impact of fractional bandwidth on UWB system performance. Specifically, the fading experienced by systems of different fractional bandwidths are compared. Fading has a significant impact on communications systems performance because if the received signal experiences large amounts of fading, the system design must compensate somehow (for example by requiring larger margins in the link budget). Thus, fractional bandwidth is tied to the system design and the required receiver complexity.

6.1 Comparison of Pulses with Different Fractional Bandwidths

It has been argued by some researchers [79] that UWB systems using larger fractional bandwidth can offer superior performance through reduced fading. Fractional bandwidth is a unitless quantity defined as

$$BW_{frac} = \frac{BW_{abs}}{f_c} \quad (6-1)$$

where BW_{abs} is the absolute bandwidth (typically just referred to as bandwidth and measured in Hz, rad/s or some similar units) and f_c is the center frequency. Therefore, to change the fractional bandwidth, the absolute bandwidth or the center frequency must be changed.

In order to evaluate the significance of different fractional bandwidths, first, the center frequency is varied while holding the absolute bandwidth constant to vary the fractional bandwidth. The pulses used here are Gaussian modulated sinusoids, given by (1-8), since the frequency content of these pulses are easily known from the time domain

expression. For a constant absolute bandwidth these pulses correspond to a single Gaussian envelope modulating sinusoids of different frequencies. Pulses with an absolute bandwidth of 1 GHz and fractional bandwidths of 0.25, 0.5, 1, and 2 are considered. These pulses are shown in Figure 6-1.

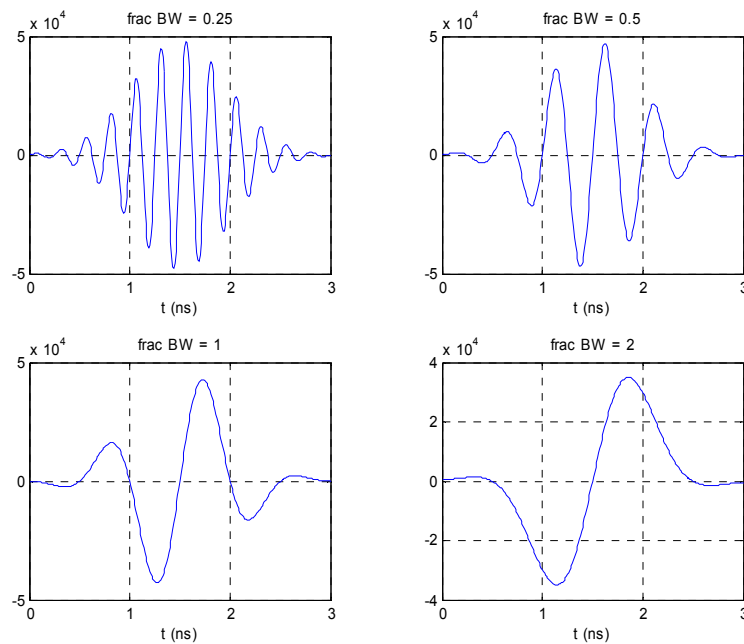


Figure 6-1. 1 GHz bandwidth pulses with different fractional bandwidths

To evaluate the severity of fading, the autocorrelation function for each of these pulses is calculated. The autocorrelation represents the addition to (or subtraction from) the correlation output on a given path when a multipath component partially overlaps in time with the given pulse. The normalized addition to (or subtraction from) the correlator output due to a delayed pulse is shown in Figure 6-2. For example, if two paths arrive at the same time (0 delay), have the same amplitude and the same polarity, the correlator output will be twice as large as if only one path were present. However, if there are equal energy 1 GHz pulses with the same polarity, fractional bandwidth of 0.25, and relative delay of 0.12 ns, the delayed pulse will destructively interfere and cancel out almost 98%

of the correlation of the first arriving pulse (a very severe fade). However, for pulses with higher fractional bandwidth, the worst case fade for equal energy pulses is reduced as seen in Figure 6-2. If the delayed pulse has opposite polarity to the first arriving pulse, the effect on the correlation output will be a subtraction of the corresponding values in Figure 6-2 where the worst case will always be a delay of 0 and have a normalized value of 1. The fading rate will also be reduced for larger fractional bandwidths for a mobile receiver as it moves at a given speed through the environment. This is expected since the fractional bandwidth increases with decreasing center frequency, and fading rates are directly proportional to the center (or carrier) frequency in narrowband as well as UWB systems. These pulses are all completely resolvable at delays of approximately 2 ns. This is due to the equivalent absolute bandwidth which defines the envelope that is common to all of these pulses.

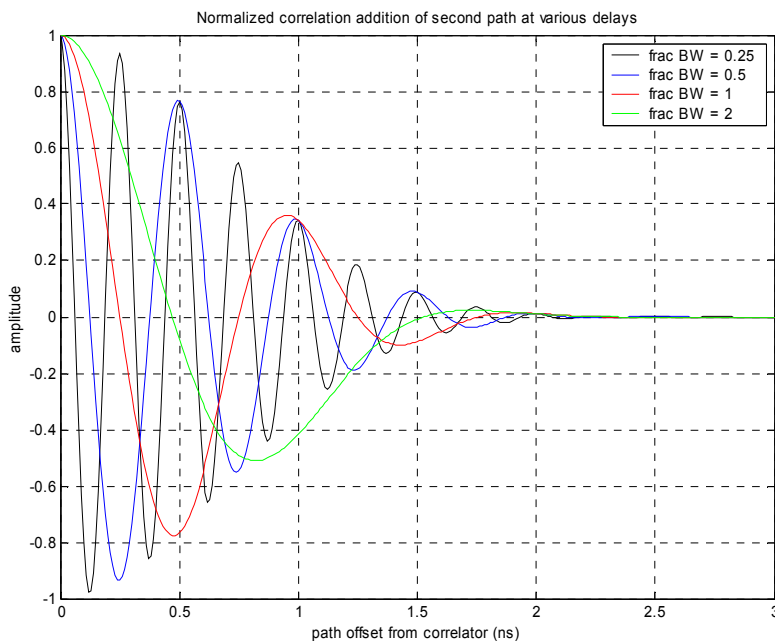


Figure 6-2. Normalized correlation addition (or subtraction) due to delayed pulse

Also, it is of interest to compare bandwidths about a common center frequency (if for example a given frequency band has been opened for UWB usage and the tradeoffs of different pulses are to be evaluated). Pulses with a common center frequency of 5 GHz and fractional bandwidths of 0.25, 0.5, 1, and 2 are shown in Figure 6-3.

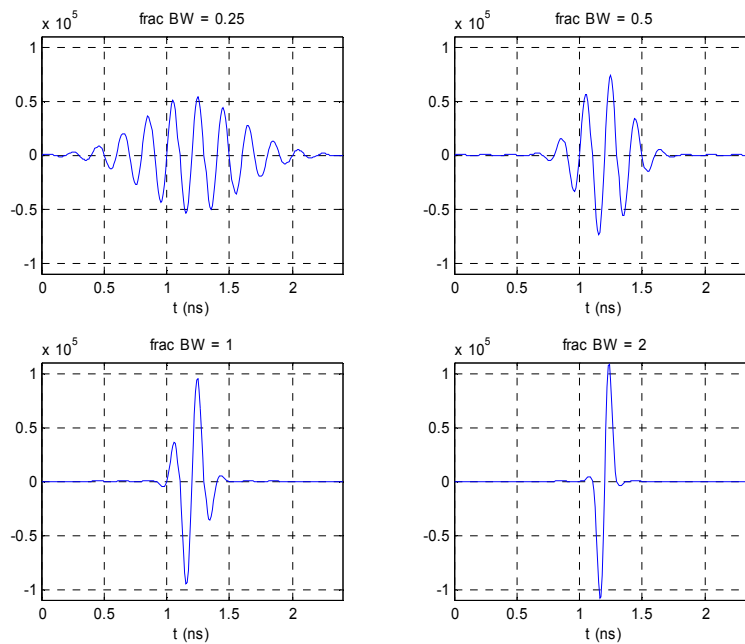


Figure 6-3. Pulses with different fractional bandwidth, center frequency = 5 GHz

The autocorrelation for these pulses is also calculated and is shown in Figure 6-4. Again, for equal polarity pulses, the worst case fade is reduced for pulses with larger fractional bandwidth. Most obvious from Figure 6-4 is that the pulses with higher fractional bandwidth can be completely resolved for much shorter delays. This is expected, because in this case, the absolute bandwidth and fractional bandwidth are directly related and systems (narrowband or UWB) with larger bandwidths offer greater time resolution.

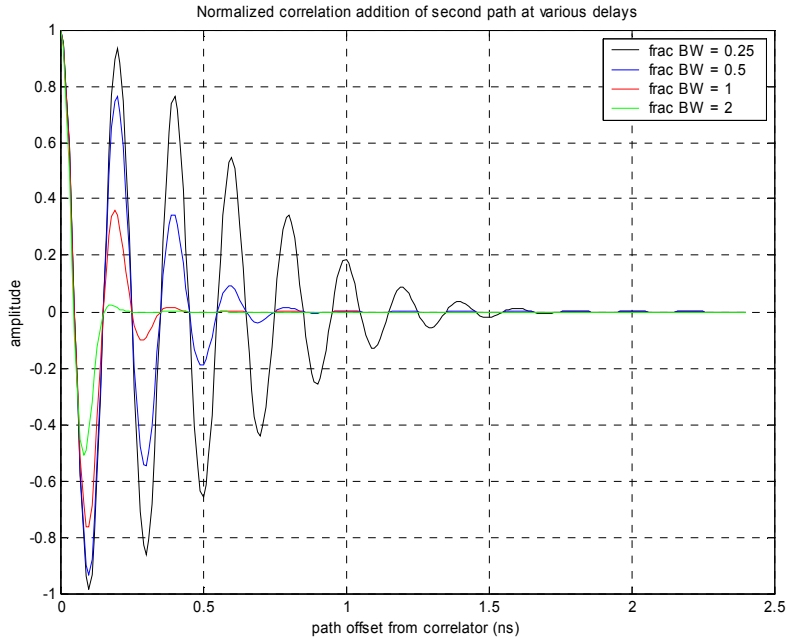


Figure 6-4. Normalized correlation addition (or subtraction) due to delayed pulse

6.2 Fading in Measured Channels

To evaluate the validity of the above analysis, indicating that fading is reduced for systems using larger fractional bandwidth, the channel impulse responses calculated from the measurement data corresponding to the LOS bicone scenarios are used to simulate received signals for UWB systems. To evaluate the severity of the fading that different fractional bandwidth pulses experience, the following procedure is iterated for all available impulse responses:

- 1) The impulse response is normalized to have unit gain (the sum of the square of the taps set equal to one)
- 2) The normalized impulse response is convolved with pulses of varying fractional bandwidths to simulate a received noise-free signal (pulses were all normalized to have unit energy)
- 3) The total energy in each of the received signals are calculated and recorded (this is a measure of the total fading the signal experiences)

- 4) The energy of the strongest correlation value for each generated signal is recorded as a measure of the available energy using a single path correlator.

This procedure was performed using a set of pulses representing fractional bandwidths from 0.2 to 2 with a 1 GHz constant absolute bandwidth and a set of pulses representing fractional bandwidths from 0.2 to 2 with a 1 GHz constant center frequency.

A scatter plot of the total energy in the simulated signals as a function of the fractional bandwidth is shown in Figure 6-5 for the constant absolute bandwidth pulses. The variance and minimum of the normalized fading (in dB) are plotted in Figure 6-6. The variance is a measure of the range of the fading of the received energy across similar channels. The minimum represents the worst case fade scenario. Also, a scatter plot is shown for the strongest single path in the simulated signal in Figure 6-7. The variance and minimum energy (in dB) for this strongest single path are plotted in Figure 6-8.

A scatter plot of the total energy in the simulated signals as a function of the fractional bandwidth is shown in Figure 6-9 for the constant center frequency pulses. The variance and minimum of the normalized fading (in dB) are plotted in Figure 6-10. Also, a scatter plot is shown for the strongest single path in the simulated signal for the constant center frequency pulses in Figure 6-11. The variance and minimum energy (in dB) for this strongest single path are plotted in Figure 6-12.

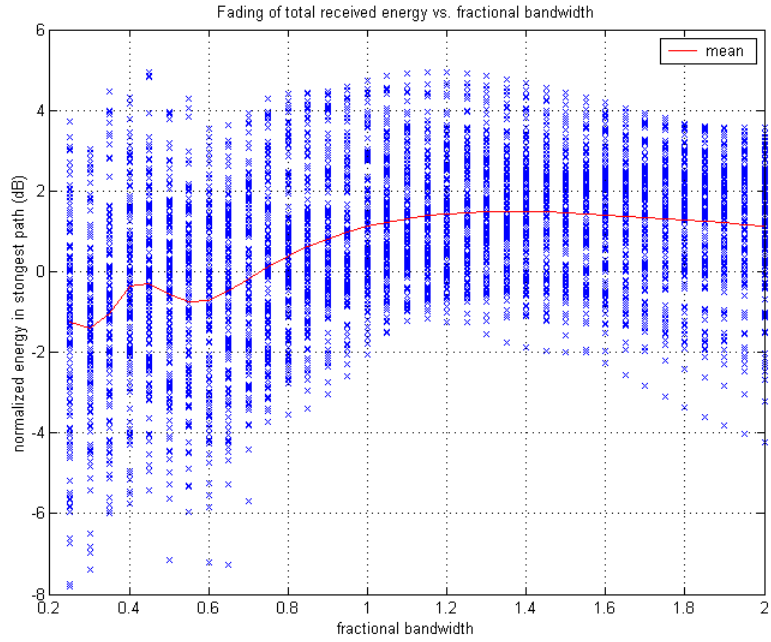


Figure 6-5. Fading of total received energy vs. fractional bandwidth (constant absolute bandwidth)

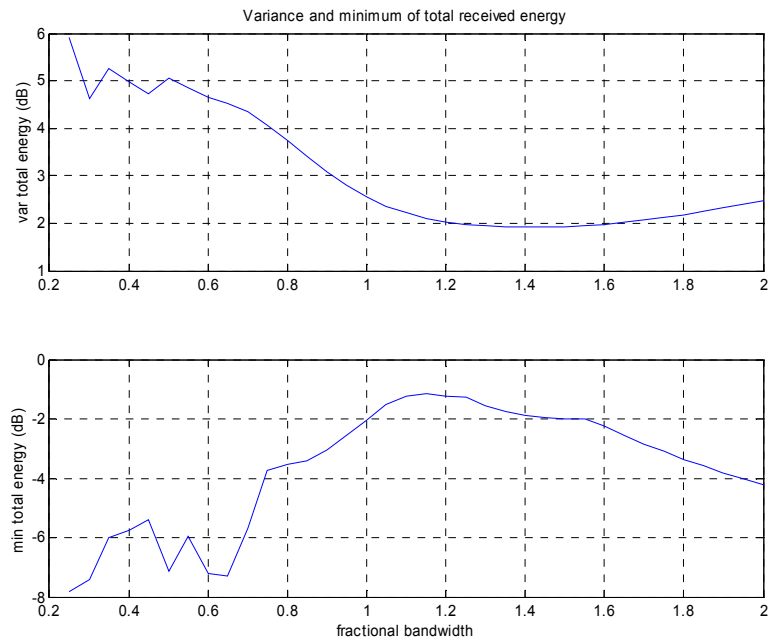


Figure 6-6. Variance and minimum of the total received energy vs. fractional bandwidth (constant absolute bandwidth)

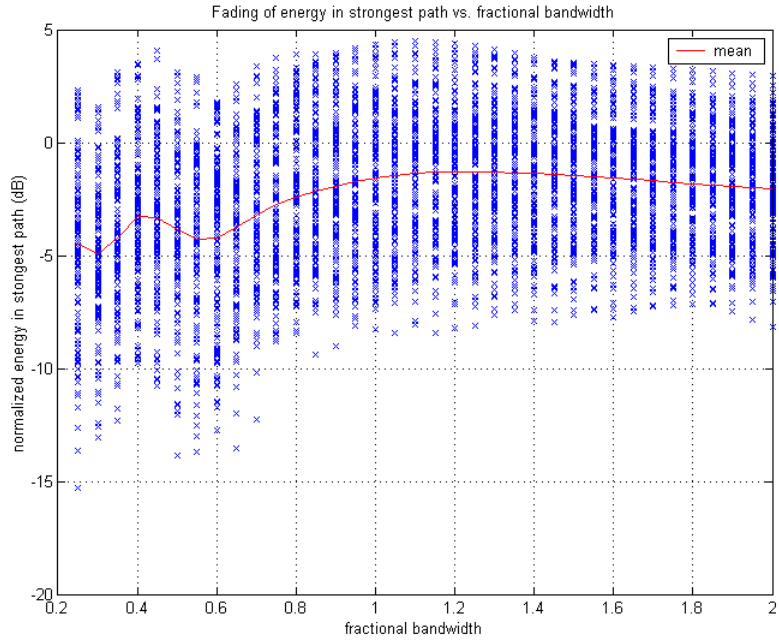


Figure 6-7. Fading of energy in the strongest path vs. fractional bandwidth (constant absolute bandwidth)

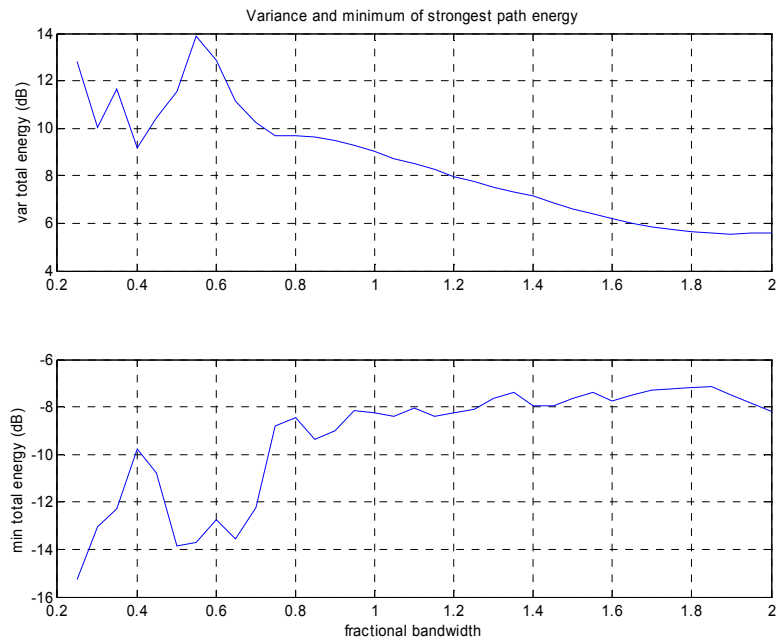


Figure 6-8. Variance and minimum of energy in the strongest path vs. fractional bandwidth (constant absolute bandwidth)

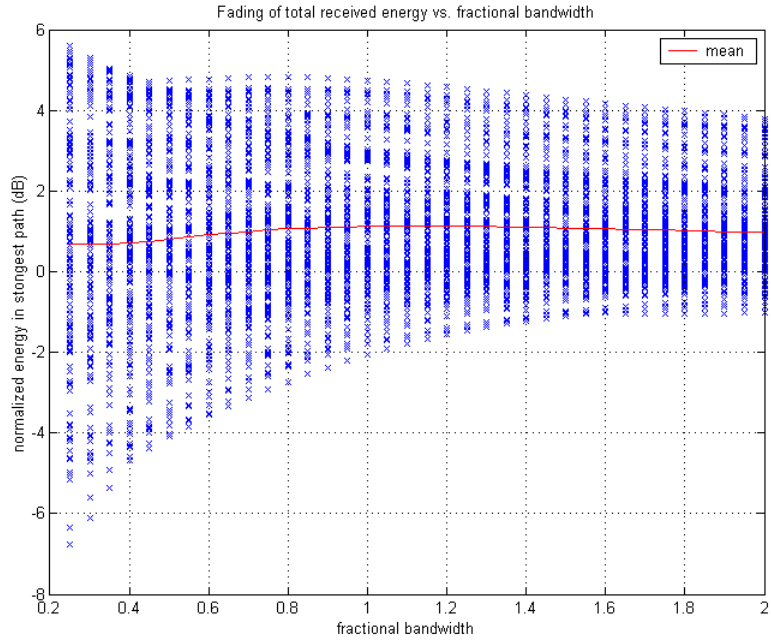


Figure 6-9. Fading of total received energy vs. fractional bandwidth (constant center frequency)

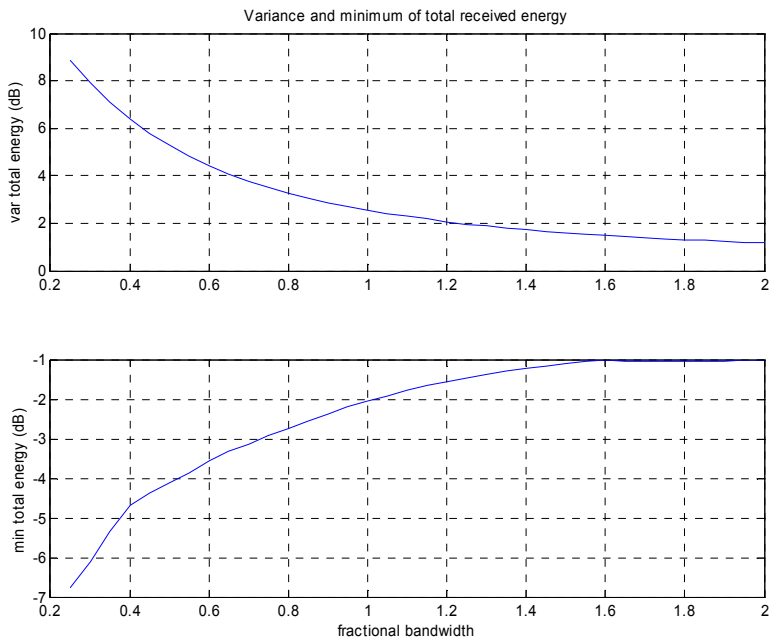


Figure 6-10. Variance and minimum of the total received energy vs. fractional bandwidth (constant center frequency)

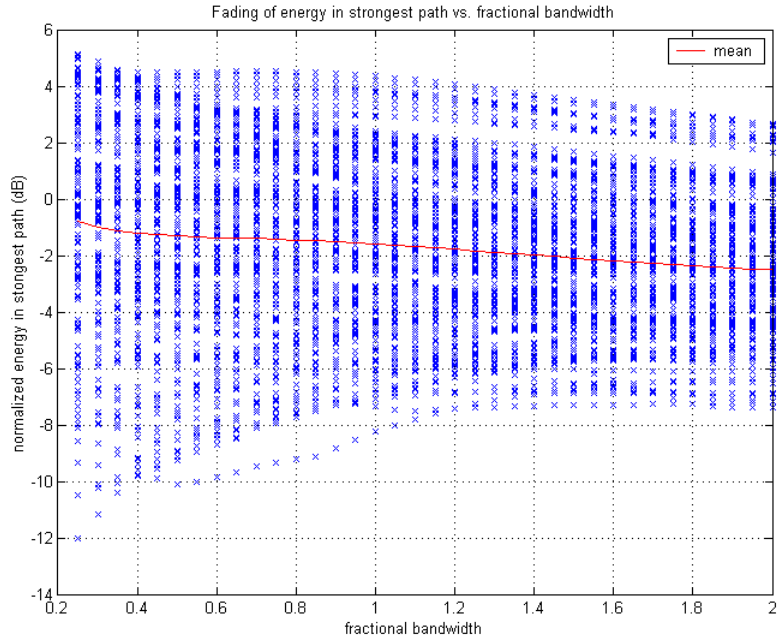


Figure 6-11. Fading of energy in the strongest path vs. fractional bandwidth (constant center frequency)

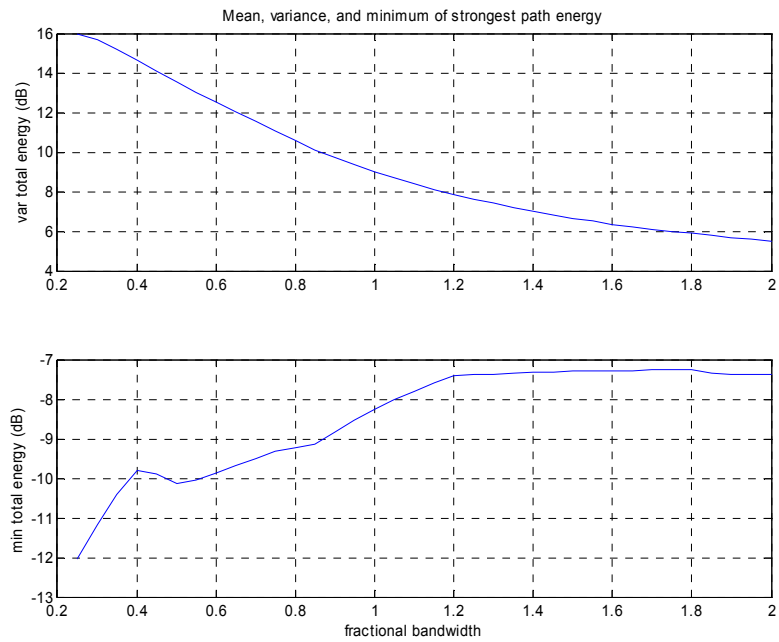


Figure 6-12. Variance and minimum of energy in the strongest path vs. fractional bandwidth (constant center frequency)

It was expected that the fading would be reduced for larger fractional bandwidths (i.e. the variance would decrease and the worst case fades would increase). Overall, these trends are observed. For the constant absolute bandwidth pulses, these trends are less consistent than for the constant center frequency pulses. The inconsistency with the expected results for the constant absolute bandwidth pulses may be due to the specific CLEAN generated impulse responses. It was shown in section 4.1 that CLEAN generated impulse responses are not necessarily applicable across different frequency bands. The highest frequency band considered here is 4.5-5.5 GHz (a 1 GHz bandwidth pulse with 0.2 fractional bandwidth) which is within the measurement bandwidth, but this may still be a factor.

For comparison, the fading experienced by continuous wave (CW) tones at various frequencies were calculated. Scatter plots of the fading seen by 10 MHz, 100 MHz, 1 GHz and 10 GHz sinusoids are shown in Figure 6-13. The variances of the fading and the worst case fades for these signals are listed in Table 6-1. The variances are considerably higher than for any of the UWB pulses considered. The worst case fades are also much worse for the CW tones than the UWB pulses.

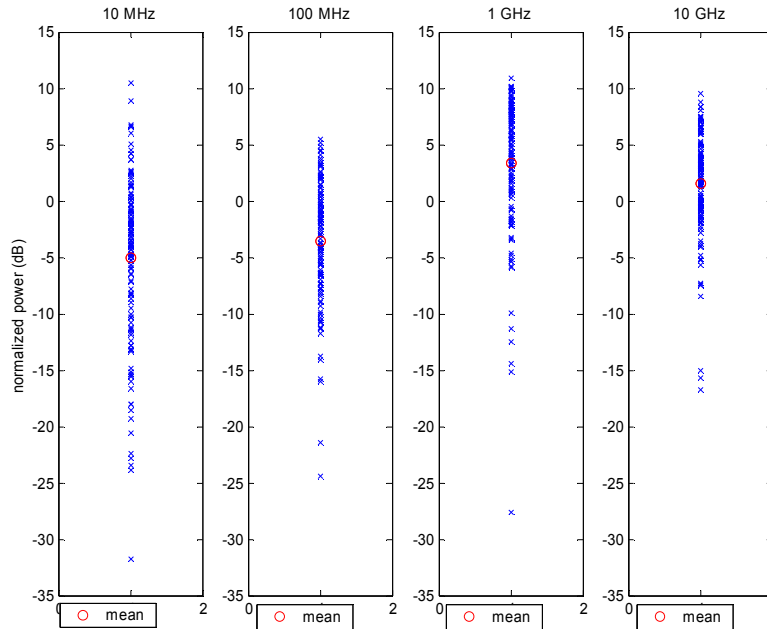


Figure 6-13 Fading of power in CW tones at 10 MHz, 100 MHz, 1 GHz, and 10 GHz

Table 6-1. Variance of fading and worst case fade for CW tones

	10 MHz	100 MHz	1 GHz	10 GHz
variance (dB)	55.8	28.4	36.4	21.9
minimum (dB)	-31.7	-24.5	-27.6	-16.8

The FCC has approved unlicensed operation of UWB communications devices from 3.1-10.6 GHz and its definition for UWB signals is any signal that has fractional bandwidth of at least 0.20 or absolute bandwidth of at least 500 MHz [19]. As a reference point for comparison of potential commercial UWB systems to this analysis: a 500 MHz pulse at the lowest end of the FCC band (pulse occupying 3.1-3.6 GHz) has a fractional bandwidth of approximately 0.15; a 500 MHz pulse at the highest end of the band (pulse occupying 10.1-10.6 GHz) has a fractional bandwidth of approximately 0.05; and a pulse that occupies the entire band (3.1-10.6 GHz) has a fractional bandwidth of approximately 1.09.

6.3 Conclusions

Larger fractional bandwidth systems tend to experience less severe fading. It is clear that increasing the absolute bandwidth is very significant to reduce the fading, although the fading improvement diminishes for higher fractional bandwidth (e.g. the variance of the received energy decreases by only about 1 dB when going from fractional bandwidths of 1 to 2 in Figure 6-10). In general, absolute bandwidth seems to have more influence on the fading than fractional bandwidth. Systems using any of the UWB pulses considered here would experience much less fading than a narrowband system in which the symbols are nearly CW relative to the time dispersion of the channel.

7 Receiver Architecture Analysis

This chapter presents theoretical analysis and semi-analytic simulations related to the performance of two types of receivers that can be used for UWB communications. Some of the different possible modulation schemes are compared. Comparisons are made to narrowband systems where the results are the same, and the unique aspects of UWB systems are highlighted where they differ from narrowband systems. Many researchers expect that UWB systems can offer an advantage in the large number of resolvable multipath components, so the performance of Rake receivers and diversity schemes are considered. Channel estimation will be important for Rake receivers using maximal ratio combining, so the impact of estimation error is also considered.

7.1 Correlation Receiver

It is well known that the optimal receiver for communications systems in AWGN is a correlation receiver (or equivalently a matched filter receiver) [59]. A block diagram of a simple correlation receiver is shown in Figure 7-1. For UWB systems operating in multipath rich environments, many of the multipaths will be resolvable (pulses not overlapping in time), so a Rake receiver can be used to exploit the frequency diversity. However, the pulses may experience distortion due to unresolvable multipath components or frequency dependent distortion due to the environment. The ideal receiver would use the received (distorted) pulse shape(s) as the correlation template. However, estimating the received pulse shape as well as generating arbitrary waveforms for correlation can be challenging. A reasonable choice for the correlation template is the pulse received from an undistorted LOS path only as discussed in section 3.2.1.

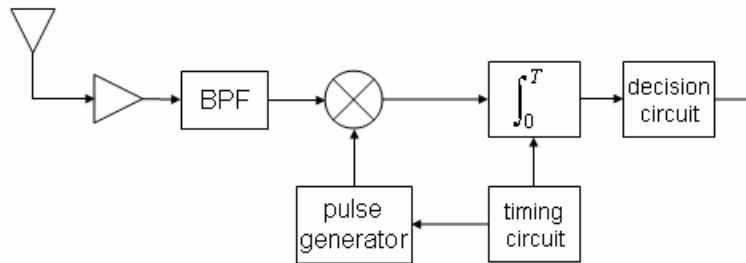


Figure 7-1. Block diagram of correlation receiver.

For traditional carrier based communications systems, correlation receivers can either be coherent or noncoherent. Coherent receivers track the phase of the received signal, while in general, noncoherent receivers sum the energy from in-phase and quadrature channels that have a random phase relative to the received signal. For non-carrier based UWB signals, the received signal has no ‘phase’ in this sense. However, the polarity of the signal may be reversed by the environment. Therefore for impulsive UWB, a coherent receiver must estimate the polarity of the signal (or multipath component in a Rake receiver combining), while a noncoherent receiver need not estimate the polarity of signal (or multipath) and uses the absolute value of the correlation for decisions.

7.1.1 Probability of Bit Error for Correlation Receiver

The bit error performance of UWB correlation receivers in AWGN is identical to any communications system employing a modulation scheme that has an equivalent signal space. The following notation is common when discussing modulation and receiver performance and will be used below

- M is the number of possible transmitted symbols
- k is the number of bits per symbol such that $2^k = M$
- E_s is the energy per received symbol

- E_b is the energy per received bit such that $E_s = kE_b$
- N_o is the noise power spectral density
- P_s is the probability of symbol error
- P_b is the probability of bit error

$$Q(x) = \frac{1}{\sqrt{2\pi}} \int_x^{\infty} e^{-\frac{t^2}{2}} dt = \frac{1}{2} \left[1 - \operatorname{erf} \left(\frac{x}{\sqrt{2}} \right) \right] \quad (7-1)$$

The following probability of bit error expressions are for AWGN channels (no multipath) and can be found in [59] or any good communications textbook. They can be used with additional analysis (such as that given in the next section) to determine performance in multipath channels where the noise is still Gaussian.

For a coherent receiver, antipodal signaling is possible and the probability of bit error is well known to be

$$P_b = Q \left(\sqrt{2 \frac{E_b}{N_o}} \right) \quad (7-2)$$

If the antipodal signal is differentially encoded and noncoherently detected, the probability of bit error is given by

$$P_b = \frac{1}{2} e^{-\frac{E_b}{N_o}} \quad (7-3)$$

Orthogonal signaling techniques are possible with UWB systems as well. These include on-off keying (OOK), pulse position modulation (PPM), or any scheme that employs orthogonal pulse shapes. For example, orthogonal pulse shapes have been proposed in UWB “multiband” which uses pulses separated in frequency. This type of pulse set could be used in a frequency shift keying (FSK) modulation scheme to give orthogonal modulation. Coherent binary orthogonal modulation schemes have a probability of bit error given by

$$P_b = Q\left(\sqrt{\frac{E_b}{N_o}}\right) \quad (7-4)$$

Expressions for the probability of bit error for coherent M -ary orthogonal modulation are given in both [59] and [88], but they cannot be expressed in closed form. An upper bound using the union bound can be found in a simpler form and is a very close approximation for larger values of E_b/N_o

$$P_b \leq 2^{k-1} Q\left(\sqrt{k \frac{E_b}{N_o}}\right) \quad (7-5)$$

For noncoherent binary orthogonal modulation, the probability of bit error is

$$P_b = \frac{1}{2} e^{-\frac{1 E_b}{2 N_o}} \quad (7-6)$$

More generally, for noncoherent M -ary orthogonal modulation, the probability of bit error is

$$P_b = \frac{2^{k-1}}{2^k - 1} \sum_{n=1}^{M-1} (-1)^{n+1} \binom{M-1}{n} \frac{1}{n+1} e^{-\frac{n}{n+1} k \frac{E_b}{N_o}} \quad (7-7)$$

Biorthogonal modulation schemes are also possible for UWB systems, for example by combining antipodal signaling with an orthogonal scheme such as PPM. Biorthogonal signaling must be coherently demodulated and the union bound for the probability of bit error is given by

$$P_b \leq \frac{2^{k-1} - 1}{1 - 2^{-k}} Q\left(\sqrt{k \frac{E_b}{N_o}}\right) \quad (7-8)$$

7.1.2 Traditional Spread Spectrum Rake Receiver Performance

Much research has been done to characterize the performance of Rake receivers for traditional spread spectrum systems. This work can be extended fairly easily to

evaluate the performance of UWB correlation Rake receivers. Immediately following is a discussion and overview of basic performance evaluations for Rake receivers. Some of the amplitude distributions traditionally used for spread spectrum models may not model UWB systems as well, but the principles of analysis are the same.

Assume there are L resolvable multipath components present. For a system employing equal energy transmit symbols the received signal from the i -th path can be represented as $r_i = \gamma_i d + n_i$ where γ_i is a complex number representing the faded amplitude and the phase shift (or polarity) of the path, d is the information symbol with normalized energy, n_i is additive white Gaussian noise with power (variance) = σ_N^2 . Throughout this analysis, the receiver is assumed to have perfect phase (or polarity) knowledge.

Distributions of Interest

Ricean Distributed Amplitudes

If $|\gamma_i|$ are **independent** Ricean distributed random variables, the PDF of $x_i = |\gamma_i|$ is

$$p_{x_i}(x_i) = \frac{x_i}{\sigma_i^2} e^{-\frac{(x_i^2 + s_i^2)}{2\sigma_i^2}} I_0\left(\frac{x_i s_i}{\sigma_i^2}\right), \quad x_i \geq 0 \quad (7-9)$$

The Rice distribution is often characterized by the Rice K factor defined as

$$K = \frac{s^2}{2\sigma^2} \quad (7-10)$$

Rayleigh Distributed Amplitudes

If $|\gamma_i|$ are **independent** Rayleigh distributed random variables, the PDF of $x_i = |\gamma_i|$ is

$$p_{x_i}(x_i) = \frac{x_i}{\sigma_i^2} e^{\frac{-x_i^2}{2\sigma_i^2}}, \quad x_i \geq 0 \quad (7-11)$$

which is a special case of the Ricean distribution with $s=0$ ($K=0$).

Average Energy per Multipath

For a fair comparison between combining techniques, the spatial average energy per bit per multipath compared to the noise power spectral density, $\overline{E_{b,i}} / N_o$ (the over-bar will be used throughout to indicate spatial average [average of variations caused by fading], while the subscript *ave* will denote time average [average of variations caused by non-constant envelope of transmitted signal]), will be used as the standard of comparison of performance between systems. The SNR here is defined as the ratio of the time average signal power (where time average power here refers to product of the symbol energy and the symbol rate since the duty cycle may be small and the power may not be constant over a over time for no fading) to the noise power at the receiver

$$SNR_i = \frac{P_{i,ave}}{P_{noise}} = \frac{|\gamma_i|^2}{\sigma_N^2} = \frac{2E_{s,i}}{N_o} = \frac{2kE_{b,i}}{N_o} = 2k\beta_i \quad (7-12)$$

where $E_{s,i}$ is the received energy per information symbol from path i , $E_{b,i}$ is the average received energy per bit from path i , k is the number of bits per symbol, N_o is the power spectral density of the noise, and β is defined here to be E_b/N_o . From (7-12) it can be seen that

$$\frac{|\gamma_i|}{\sigma_N} = \sqrt{2k\beta_i} \quad (7-13)$$

For the case with Ricean path amplitudes, the mean SNR (mean of a non-central chi-squared [59], see development in the next section) can be shown to be

$$E(SNR_i) = \frac{2\sigma_i^2 + s_i^2}{\sigma_N^2} = 2k\overline{\beta}_i \quad (7-14)$$

If the Rice K factor and $\overline{\beta}_i$ are specified, the appropriate σ_i and s_i of the distribution can be calculated by

$$\frac{s_i^2}{\sigma_N^2} = \frac{2K_i}{K_i + 1} k\overline{\beta}_i, \quad \frac{\sigma_i^2}{\sigma_N^2} = \frac{1}{K_i + 1} k\overline{\beta}_i \quad (7-15)$$

For the case with Rayleigh path amplitudes, the mean SNR (mean of a central chi-squared [59]) can be shown to be

$$E(SNR_i) = 2\frac{\sigma_i^2}{\sigma_N^2} = 2k\overline{\beta}_i \quad (7-16)$$

For a specific $\overline{\beta}_i$, the corresponding σ_i is

$$\frac{\sigma_i^2}{\sigma_N^2} = k\overline{\beta}_i \quad (7-17)$$

Maximal Ratio Combining (MRC) with perfect channel estimation

If MRC is used and all L available paths are used, assuming perfect channel estimation, the delayed and weighted path correlation summation is given by

$$z = \sum_{i=1}^L \gamma_i^* r_i = \sum_{i=1}^L |\gamma_i|^2 d + |\gamma_i| n_i \quad (7-18)$$

If $|\gamma_i|$ is assumed constant over a given period of time, z is a Gaussian random variable with mean

$$E[z] = \sum_{i=1}^L |\gamma_i|^2 \quad (7-19)$$

and variance

$$\text{var}[z] = \sum_i^L \text{var}[|\gamma_i|n_i] = \sum_i^L |\gamma_i|^2 \sigma_N^2 = \sigma_N^2 \sum_i^L |\gamma_i|^2 \quad (7-20)$$

Therefore, the total SNR per bit is

$$\Lambda = SNR_{tot} = \frac{(E[z])^2}{\text{var}[z]} = \frac{\left(\sum_{i=1}^L |\gamma_i|^2\right)^2}{2k\sigma_N^2 \sum_i^L |\gamma_i|^2} = \frac{\sum_{i=1}^L |\gamma_i|^2}{2k\sigma_N^2} = \sum_{i=1}^L \lambda_i \quad (7-21)$$

If $x_i = |\gamma_i|$, then $p_{x_i}(x_i)$ is the amplitude distribution of path i . In general the PDF of

$\lambda_i = \frac{|\gamma_i|^2}{2k\sigma_N^2}$ is given by

$$p_{\lambda_i}(\lambda_i) = \frac{1}{2} \sqrt{\frac{2k\sigma_N^2}{\lambda_i}} p_{x_i}(\sqrt{\lambda_i 2k\sigma_N^2}) \quad (7-22)$$

and thus, the PDF of Λ is given by

$$p_{\Lambda}(\Lambda) = p_{\lambda_1}(\lambda_1) * p_{\lambda_2}(\lambda_2) * \dots * p_{\lambda_L}(\lambda_L) \quad (7-23)$$

where $*$ is the convolution operation. If closed form solutions for these equations cannot be obtained, the PDF can be computed numerically using Matlab or a similar computer tool.

Ricean Distributed Amplitudes

If $|\gamma_i|$ are **independent** Ricean distributed random variables with PDF given by

(7-9), then $\lambda_i = \frac{|\gamma_i|^2}{2k\sigma_N^2}$ are distributed according to a non-central chi-squared distribution

with 2 degrees of freedom with PDF

$$p_{\lambda_i}(\lambda_i) = \frac{1}{2(\sigma_i')^2} e^{-\frac{(\lambda_i + (s_i')^2)}{2(\sigma_i')^2}} I_0\left(\frac{\sqrt{\lambda_i} (s_i')}{(\sigma_i')^2}\right), \quad \lambda_i \geq 0 \quad (7-24)$$

and characteristic function

$$\psi_{\lambda_i}(j\nu) = \frac{1}{1 - j\nu 2(\sigma_i')^2} e^{\frac{j\nu(s_i')^2}{1 - j\nu 2(\sigma_i')^2}} \quad (7-25)$$

where

$$(s_i')^2 = \frac{s_i^2}{2k\sigma_N^2} = \frac{K_i}{K_i + 1} \bar{\beta}_i \quad (\sigma_i')^2 = \frac{\sigma_i^2}{2k\sigma_N^2} = \frac{1}{2(K_i + 1)} \bar{\beta}_i \quad (7-26)$$

The characteristic function of the SNR, Λ , is then

$$\psi_{\Lambda}(j\nu) = \prod_{i=1}^L \psi_{\lambda_i}(j\nu) \quad (7-27)$$

If the paths are also **identically** distributed (i.e. $\sigma_i = \sigma$ and $s_i = s$, for all i), then

$$\psi_{\Lambda}(j\nu) = [\psi_{\lambda}(j\nu)]^L = \frac{1}{(1 - j\nu 2(\sigma')^2)^L} e^{\frac{j\nu L(s')^2}{1 - j\nu 2(\sigma')^2}} \quad (7-28)$$

which is a non-central chi-square distribution with $2L$ degrees of freedom and PDF

$$p_{\Lambda}(\Lambda) = \frac{1}{2(\sigma')^2} \left(\frac{\beta}{L(s')^2} \right)^{\frac{L-1}{2}} e^{-\frac{(\Lambda + L(s')^2)}{2(\sigma')^2}} I_{L-1} \left(\frac{\sqrt{\Lambda} \sqrt{L} (s')}{(\sigma')^2} \right), \quad \Lambda \geq 0 \quad (7-29)$$

This can be given in terms of $\bar{\beta}$ and K by substituting in (7-26) and (7-28) and rearranging

$$p_{\Lambda}(\Lambda) = \left(\frac{K+1}{\bar{\beta}} \right)^{\frac{L+1}{2}} \left(\frac{\Lambda}{LK} \right)^{\frac{L-1}{2}} e^{-\left[\frac{\Lambda(K+1)}{\bar{\beta}} + LK \right]} I_{L-1} \left(2\sqrt{\frac{\Lambda L K (K+1)}{\bar{\beta}}} \right), \quad \Lambda \geq 0 \quad (7-30)$$

Rayleigh Distributed Amplitudes

If $|\gamma_i|$ are **independent** Rayleigh distributed random variables with PDF given by (7-11) and if the paths are **identically** distributed, $s = 0$ can be plugged into (7-28) yielding

$$\psi_{\Lambda}(j\nu) = \frac{1}{\left(1 - j\nu 2(\sigma')^2\right)^L} \quad (7-31)$$

which is the central chi-squared distribution with $2L$ degrees of freedom and has a PDF

$$p_{\Lambda}(\Lambda) = \frac{1}{2^L (\sigma')^{2L} (L-1)!} (\Lambda)^{L-1} e^{\frac{-\Lambda}{2(\sigma')^2}}, \quad \Lambda \geq 0 \quad (7-32)$$

This can be given in terms of $\bar{\beta}$ by substituting (7-27) with $K = 0$ into (7-32) and rearranging

$$p_{\Lambda}(\Lambda) = \frac{\Lambda^{L-1}}{\bar{\beta}^L (L-1)!} e^{\frac{-\Lambda}{\bar{\beta}}}, \quad \Lambda \geq 0 \quad (7-33)$$

Maximal Ratio Combining (MRC) with channel estimation error

If MRC is used and all L available paths are used, but the channel estimates are imperfect (however, the phase, or polarity, is still assumed to be perfectly known), the delayed and weighted path correlation summation is given by

$$z = \sum_{i=1}^L \hat{\gamma}_i^* r_i = \sum_{i=1}^L \left| \hat{\gamma}_i \right| |\gamma_i| d + \left| \hat{\gamma}_i \right| n_i \quad (7-34)$$

where $\hat{\gamma}_i$ is the channel estimate with perfect phase (or polarity) but error in the amplitude. The channel estimate is assumed to be calculated using a pilot channel (or pilot symbols) by

$$|\hat{\gamma}_i| = \frac{|\gamma_i|}{|\gamma_{pilot,i}| q_{ch}} \sum_{j=1}^{q_{ch}} |\gamma_{pilot,i}| + n_j = |\gamma_i| + \sum_{j=1}^{q_{ch}} \frac{|\gamma_i|}{|\gamma_{pilot,i}| q_{ch}} n_j \sim N\left(|\gamma_i|, \frac{\sigma_N^2}{Jq_{ch}}\right) \quad (7-35)$$

which is a Gaussian distributed random variable where J is the ratio of the transmitted energy of a pilot symbol to the energy of a data symbol ($J = 1$ if these energies are the same) and q_{ch} is the number of symbols averaged to determine the channel estimate (the channel is assumed to be constant over these q_{ch} symbols).

Again, if the amplitude, $|\gamma_i|$, is assumed constant over the given period of interest, z is the sum random variables which are each the product of two Gaussian random variables (although z can be approximated as Gaussian) with mean

$$E[z] = \sum_{i=1}^L |\gamma_i|^2 \quad (7-36)$$

and variance

$$\begin{aligned} \text{var}[z] &= \sum_{i=1}^L \frac{|\gamma_i|^2 \sigma_N^2}{Jq_{ch}} + \left(|\gamma_i|^2 + \frac{\sigma_N^2}{Jq_{ch}}\right) \sigma_N^2 = \sum_{i=1}^L \left(\frac{|\gamma_i|^2 (1 + Jq_{ch}) + \sigma_N^2}{Jq_{ch}}\right) \sigma_N^2 \\ &= \frac{1 + Jq_{ch}}{Jq_{ch}} \sigma_N^2 \sum_{i=1}^L |\gamma_i|^2 + \frac{1}{Jq_{ch}} L \sigma_N^4 = \frac{\sigma_N^4}{Jq_{ch}} \left[L + (1 + Jq_{ch}) \sum_{i=1}^L \frac{|\gamma_i|^2}{\sigma_N^2} \right] \end{aligned} \quad (7-37)$$

Therefore, the total SNR per bit is approximately

$$\Lambda = SNR_{tot} = \frac{(E[z])^2}{2k \text{var}[z]} = \frac{\left(\sum_{i=1}^L |\gamma_i|^2\right)^2}{\frac{1}{Jq_{ch}} L 2k \sigma_N^4 + \frac{1 + Jq_{ch}}{Jq_{ch}} 2k \sigma_N^2 \sum_{i=1}^L |\gamma_i|^2} = \frac{\left(\sum_{i=1}^L \frac{|\gamma_i|^2}{2k \sigma_N^2}\right)^2}{\frac{L}{2kJq_{ch}} + \frac{1 + Jq_{ch}}{Jq_{ch}} \sum_{i=1}^L \frac{|\gamma_i|^2}{2k \sigma_N^2}} \quad (7-38)$$

which cannot be reduced as simply as when no channel estimation error is present. If

$w = \sum_{i=1}^L \frac{|\gamma_i|^2}{2k \sigma_N^2}$, then $p_w(w)$ can be used to find the distribution of Λ . To evaluate the

accuracy of this approximation, the BER performance of a Rake receiver with

channel estimation errors was simulated and compared with the BER derived when using this approximation. The BER calculated using the approximation is found to upper bound the true performance. The BER performances from simulation and from the approximation, when 10 equal energy paths are present and 10 symbols are used to estimate the amplitude of each path are plotted in Figure 7-2. The performance of MRC with perfect channel knowledge is also shown for comparison and will always lower bound the true MRC performance. As the number of symbols used in the amplitude estimation is increased, the approximation of (7-38) becomes a tighter bound.

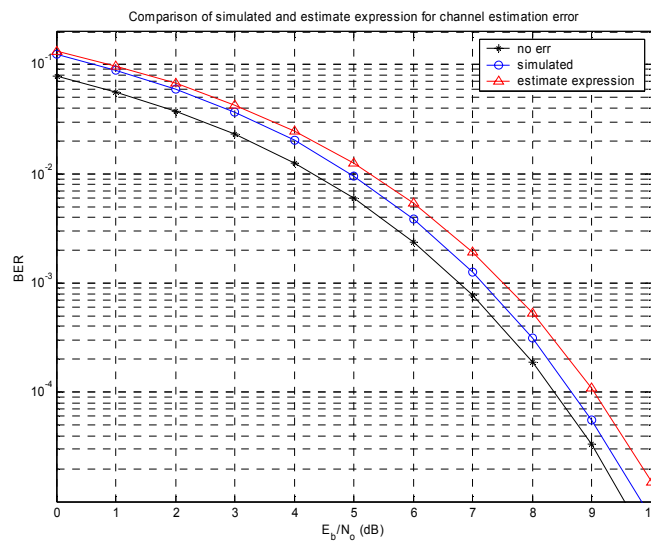


Figure 7-2. Comparison of MRC BER with perfect channel knowledge, simulated MRC with estimation error, and approximate expression for MRC Rake receiver SNR with estimation errors

It is important to note that w here is equal to the total SNR per bit for MRC with perfect channel estimation. The transformation to derive total SNR per bit for MRC with channel estimation errors is

$$\begin{aligned}
p_{\Lambda}(\Lambda) &= \frac{(a+bw)^2}{2aw-bw^2} p_w(w) & (7-39) \\
w &= \frac{b\Lambda + \sqrt{b^2\Lambda^2 + 4a\Lambda}}{2} = \frac{1}{2}b\Lambda \left(1 + \sqrt{1 + \frac{4a}{b^2\Lambda}} \right) \\
a &= \frac{L}{2kJq_{ch}} \\
b &= \frac{1+Jq_{ch}}{Jq_{ch}}
\end{aligned}$$

which although somewhat messy can be solved to give an approximation to $p_{\Lambda}(\Lambda)$ if $p_w(w)$ is known. It is interesting to note that here the SNR per bit is a function of k , where as before this variable canceled out completely. Note this representation is an approximation since z approximated as a Gaussian random variable.

Ricean Distributed Amplitudes

If $|\gamma_i|$ are **independent** Ricean distributed random variables with PDF given by (7-9), then $\lambda_i = \frac{|\gamma_i|^2}{\sigma_N^2}$ as before and w defined above has the same distribution as Λ with perfect channel estimation as given in (7-31). Therefore, using the transformation given in (7-39) on (7-31) with Λ replaced by w , the distribution of the SNR per bit can be found to be

$$\begin{aligned}
p_{\Lambda}(\Lambda) &= \frac{LK \left((L/k) + 2(1+Jq_{ch})w \right)^2 \left(\frac{K+1}{LK\beta} \right)^{\frac{L+1}{2}} w^{\frac{L-3}{2}} e^{-\left[\frac{w(K+1)}{\beta} + LK \right]} I_{L-1} \left(2\sqrt{\frac{wLK(K+1)}{\beta}} \right), \quad \Lambda > 0 & (7-40) \\
w &= \frac{1}{2Jq_{ch}} \left((1+Jq_{ch})\Lambda + \sqrt{(1+Jq_{ch})^2\Lambda^2 + 2(L/k)Jq_{ch}\Lambda} \right)
\end{aligned}$$

Rayleigh Distributed Amplitudes

If $|\gamma_i|$ are **independent** Rayleigh distributed random variables with PDF given by (7-11) and if the paths are **identically** distributed, the SNR per bit can be found by transforming (7-33) by (7-39) giving

$$p_{\Lambda}(\Lambda) = \frac{\left((L/k) + 2(1 + Jq_{ch})w\right)^2}{4Jq_{ch}\left((L/k) - (1 + Jq_{ch})w\right)} \frac{w^{L-2}}{\beta^L} e^{-\frac{w}{\beta}}, \quad \Lambda \geq 0 \quad (7-41)$$

$$w = \frac{1}{2Jq_{ch}} \left((1 + Jq_{ch})\Lambda + \sqrt{(1 + Jq_{ch})^2 \Lambda^2 + 2(L/k)Jq_{ch}\Lambda} \right)$$

Equal Gain Combining (EGC)

If EGC is used and all L available paths are used, the delayed path summation per bit is given by

$$z = \sum_{i=1}^L r_i = \sum_{i=1}^L |\gamma_i| d + n_i \quad (7-42)$$

If $|\gamma_i|$ is assumed constant over a given period of time, z is a Gaussian random variable with mean

$$E[z] = \sum_{i=1}^L |\gamma_i| \quad (7-43)$$

and variance

$$\text{var}[z] = \sum_{i=1}^L \text{var}[n_i] = \sum_{i=1}^L \sigma_N^2 = L\sigma_N^2 \quad (7-44)$$

Therefore, the total SNR per bit is

$$\Lambda = SNR_{tot} = \frac{(E[z])^2}{2k \text{var}[z]} = \frac{\left(\sum_{i=1}^L |\gamma_i|\right)^2}{2kL\sigma_N^2} = \left(\sum_{i=1}^L \frac{|\gamma_i|}{\sqrt{2kL}\sigma_N}\right)^2 = \left(\sum_{i=1}^L y_i\right)^2 \quad (7-45)$$

Again, if $x_i = |\gamma_i|$, then $p_{x_i}(x_i)$ is the amplitude distribution of path i . In general the PDF

of $y_i = \frac{|\gamma_i|}{\sqrt{2kL\sigma_N}}$ is given by

$$p_{y_i}(y_i) = \sqrt{2kL\sigma_N} p_{x_i}(\sqrt{2kL\sigma_N} y_i) \quad (7-46)$$

The PDF of $w = \sum_{i=1}^L y_i$ is

$$p_w(w) = p_{y_1}(y_1) * p_{y_2}(y_2) * \dots * p_{y_L}(y_L) \quad (7-47)$$

where $*$ is the convolution operation. The PDF of $\Lambda = w^2$ is thus

$$p_\Lambda(\Lambda) = \frac{1}{2\sqrt{\Lambda}} p_w(\sqrt{\Lambda}) \quad (7-48)$$

If a closed form solution cannot be obtained, the PDF can be computed numerically using Matlab or a similar computer tool.

Ricean Distributed Amplitudes

If $|\gamma_i|$ are Ricean distributed random variables, the PDF of $x_i = |\gamma_i|$ is given in (7-9).

The PDF of w and thus Λ cannot be found in closed form [38] but can be computed numerically using (7-47) and (7-48).

The distribution of y_i can given in terms of $\bar{\beta}$ and K using (7-15) and (7-46) giving

$$p_{y_i}(y_i) = \frac{2L(K_i+1)}{\bar{\beta}_i} y_i e^{-\left[\frac{y_i^2 L(K_i+1)}{\bar{\beta}_i} + K_i\right]} I_0\left(2y_i \sqrt{\frac{LK_i(K_i+1)}{\bar{\beta}_i}}\right), \quad y_i \geq 0 \quad (7-49)$$

Rayleigh Distributed Amplitudes

The PDF of $x_i = |\gamma_i|$ for Rayleigh distributed amplitudes is given in (7-11).

Similarly to the Ricean distributed case, the PDF of $y = \sum_{i=1}^L |\gamma_i|$ has not be found in closed form except for the case where $L=2$ [38].

The distribution of y can given in terms of $\bar{\beta}$ by setting $K_i = 0$ in (4-8)

$$p_{y_i}(y_i) = \frac{2L}{\beta_i} y_i e^{-\left[\frac{y_i^2 L}{\beta_i}\right]}, \quad y_i \geq 0 \quad (7-50)$$

For the case where $L = 2$, the closed form solution for the sum of two iid Rayleigh random variables is derived in [1] and elsewhere. It was also derived here and can be expressed as

$$p_q(q) = \frac{q}{2\sigma^2} e^{-\frac{q^2}{2\sigma^2}} + \left(\frac{q^2}{2\sigma^2} - 1\right) \frac{\sqrt{\pi}}{2\sigma} e^{-\frac{q^2}{4\sigma^2}} \operatorname{erf}\left(\frac{q}{2\sigma}\right), \quad q < 0 \quad (7-51)$$

Thus, this expression can be used to find a solution for (7-47) when $L=2$ by substituting

$\sigma = \frac{\sqrt{\beta}}{2}$ and $q = w$ giving

$$p_w(w) = \frac{2}{\beta} w e^{-\frac{2}{\beta} w^2} + \left(\frac{2}{\beta} w^2 - 1\right) \sqrt{\frac{\pi}{\beta}} e^{-\frac{1}{\beta} w^2} \operatorname{erf}\left(\sqrt{\frac{1}{\beta}} w\right), \quad w < 0, L = 2 \quad (7-52)$$

Transforming this by (7-48) gives

$$p_\Lambda(\Lambda) = \frac{1}{\beta} e^{-\frac{2}{\beta} \Lambda} + \left(\frac{\Lambda}{\beta} - \frac{1}{2}\right) \sqrt{\frac{\pi}{\Lambda\beta}} e^{-\frac{1}{\beta} \Lambda} \operatorname{erf}\left(\sqrt{\frac{\Lambda}{\beta}}\right), \quad \Lambda < 0, L = 2 \quad (7-53)$$

For $L > 2$, closed form solutions for the sum of Rayleigh random variables cannot be found. However, approximations can be found in usable forms. In [6], an infinite series representation is used to approximate the sum of independent random variables.

The sums of Rayleigh random variables are specifically shown and a closed form expression for the characteristic function of a Rayleigh random variable is also given. This same technique could be used for other distributions such as Ricean or Nakagami.

Selection Diversity

If selection diversity is used and all L available paths are compared, the chosen path correlation is given by

$$z = \max [r_i] = |\gamma_{\max}| d + n_{\max} \quad (7-54)$$

Therefore, the total SNR per bit is

$$\Lambda = SNR = \frac{(E[z])^2}{2k \text{var}[z]} = \frac{|\gamma_{\max}|^2}{2k\sigma_N^2} \quad (7-55)$$

If the paths are **independent** and **identically** distributed with the PDF of $x_i = |\gamma_i|$ given

by $p_{x_i}(x_i)$, then $\lambda_i = \frac{|\gamma_i|^2}{2k\sigma_N^2}$ has a PDF $p_{\lambda_i}(\lambda_i)$ which is the same as given in (7-22).

The CDF of λ_i is given by

$$P_{\lambda_i}(\lambda_i) = \int_{-\infty}^{\lambda_i} p_{\lambda_i}(u) du \quad (7-56)$$

From order statistics [16], the distribution of Λ can be found as

$$p_{\Lambda}(\Lambda) = \frac{1}{L} P_{\lambda_i}^{L-1}(\Lambda) p_{\lambda_i}(\Lambda) \quad (7-57)$$

Ricean Distributed Amplitudes

If $|\gamma_i|$ are Ricean distributed random variables, the PDF of $x_i = |\gamma_i|$ is given in (7-9).

Thus, $\lambda_i = \frac{|\gamma_i|^2}{2k\sigma_N^2}$ are distributed according to (7-24) following the previous development.

From [59], it is known that the CDF of λ_i is

$$P_{\lambda_i}(\lambda_i) = 1 - Q_1\left(\frac{s'}{\sigma'}, \sqrt{\lambda_i}\right) \quad (7-58)$$

where $Q_m(a, b)$ is the generalized Marcum's Q function with

$$Q_m(a, b) = \int_b^\infty x \left(\frac{x}{a}\right)^{m-1} e^{-(a^2+x^2)/2} I_{m-1}(ax) dx \quad (7-59)$$

$$Q_1(a, b) = e^{-(a^2+b^2)/2} \sum_{k=0}^{\infty} \left(\frac{a}{b}\right)^k I_k(ab), \quad b > a > 0$$

so,

$$P_{\lambda_i}(\lambda_i) = 1 - \int_{\frac{\sqrt{\lambda_i}}{\sigma'}}^\infty x e^{-\left(\frac{s'^2}{\sigma'^2} + x^2\right)/2} I_0\left(\frac{s'x}{\sigma'}\right) dx \quad (7-60)$$

(7-60) and (7-24) can be substituted into (7-57) yielding a complicated expression, but one that can be evaluated if desired.

Rayleigh Distributed Amplitudes

If $|\gamma_i|$ are Rayleigh distributed random variables, the PDF of $x_i = |\gamma_i|$ is given in

(7-11). Thus, $\lambda_i = \frac{|\gamma_i|^2}{2k\sigma_N^2}$ are central chi-square distributed according to

$$p_{\lambda_i}(\lambda_i) = \frac{1}{2(\sigma_i')^2} e^{-\frac{\lambda_i}{2(\sigma_i')^2}}, \quad \lambda_i \geq 0 \quad (7-61)$$

Since the n degrees of freedom here is even ($=2$), it is known that the CDF of λ_i can be given as [59]

$$P_{\lambda_i}(\lambda_i) = 1 - e^{-\frac{\lambda_i}{2(\sigma_i')^2}} \sum_{k=0}^1 \frac{1}{k!} \left(\frac{\lambda_i}{2(\sigma_i')^2} \right)^k = 1 - e^{-\frac{\lambda_i}{2(\sigma_i')^2}} \left[1 + \frac{\lambda_i}{2(\sigma_i')^2} \right], \quad \lambda_i \geq 0 \quad (7-62)$$

Substituting (7-61) and (7-62) into (7-57) yields

$$p_{\Lambda}(\Lambda) = \frac{1}{L} \left[1 - e^{-\frac{\Lambda}{2(\sigma_i')^2}} \left[1 + \frac{\Lambda}{2(\sigma_i')^2} \right] \right]^{L-1} \frac{1}{2(\sigma_i')^2} e^{-\frac{\Lambda}{2(\sigma_i')^2}} \quad (7-63)$$

Substituting (7-26) into (7-63) and rearranging gives

$$p_{\Lambda}(\Lambda) = \frac{1}{L\beta} e^{-\frac{\Lambda}{\beta}} \left[1 - e^{-\frac{\Lambda}{\beta}} \left[1 + \frac{\Lambda}{\beta} \right] \right]^{L-1} \quad (7-64)$$

Average Probability of Bit Error for Rake in Fading Environment

The probability of bit error P_b is a function of the available SNR. The distribution of P_b cannot be easily derived from the SNR distribution. However, the mean P_b for a given SNR distribution can be calculated by

$$\bar{P}_b = \int_0^{\infty} P_b(\Lambda) p_{\Lambda}(\Lambda) d\Lambda \quad (7-65)$$

where the function $P_b(\Lambda)$ depends on the modulation (also note that the above Rake combining techniques considered are coherent). The probability of error for several modulation schemes of interest was given in the previous section.

7.1.3 Semi-analytic Simulation of BER Performance in Multipath Channels

The new UWB LOS model channel model described in section 5.3 is chosen to simulate UWB signals and compute the performance of receivers for various modulation schemes of interest. The same set of 1000 channel impulse responses used in section 5.3 is used. The taps of in each impulse response are normalized to have unit energy. The number of multipath components and their amplitudes are random and based on the model and the parameters used (given in Table 5-3). Then the impulse response is convolved with the unit energy pulse being considered. As overlapping pulses interfere, the energy in the simulated received signal profile can be less than or greater than one. The same semi-analytic simulation methodology for the Rake receiver was used here as that described in section 5.1. The simulated signals were created using these randomly generated impulse responses. Then to evaluate BER performance, each simulated signal is multiplied by scalars to give the appropriate E_b/N_o (corresponding to the values shown in the plots) if the channel was only AWGN. Thus all profiles would have the same SNR if all the multipath components were all resolvable, but in actuality they will have a higher or lower SNR depending on the multipath interference. To calculate the BER of the Rake diversity combining techniques, the concepts and expressions of sections 7.1.1 and 7.1.2 were used to analytically derive the performance for each simulated signal. No additional path amplitude distributions such as Rayleigh and Ricean, as considered in the previous section, are assumed here. The path amplitudes are based only on the match filter output of the simulation signals.

Two different pulses are considered: the baseband bicone pulse from the measurement data and a 6-7 GHz Gaussian modulated sinusoid. These same pulses were

used for the evaluation of the different channel models in Chapter 5. For each channel impulse response, the BER of a Rake receiver with different numbers of fingers is computed. The BER values are then averaged and these averages are used for comparisons. For a coherent MRC Rake receiver (with perfect channel knowledge) using either the main positive lobe of the bicone pulse or the Gaussian modulated sinusoid pulse for the template as appropriate, the performance for antipodal signaling, OOK, and binary PPM is calculated.

The signal is assumed to have a low duty cycle and thus no intersymbol-interference (ISI) is present. As the pulse repetition rate increases, such that the decaying profile from one symbol overlaps with the next symbol, ISI will be introduced. The profiles for these indoor channels tend to extend over the duration of tens of nanoseconds, with the significant portion of response lasting longer for NLOS than LOS channels. Thus, for these simulations the performance of the antipodal signaling and OOK are based only on the energy captured by the fingers of the Rake. For PPM however, the time modulation parameter is assumed to be twice the time duration of the template signal. Therefore, multipath components can have an effect on the correlator output corresponding to the incorrect symbol (delayed or advanced in time from the correct symbol time). The BER curves for the bicone pulse are plotted in Figure 7-3 for antipodal signaling and in Figure 7-4 for OOK and PPM. There is slightly less than a 1 dB improvement in performance in going from 10 fingers to 20 fingers. There may not be 20 resolvable multipath components for all the channels, but since perfect channel knowledge is assumed for these plots, there is no performance degradation due to the

extra zero energy fingers. The PPM signal has degraded performance compared to the OOK signal due to the multipath interference.

For the 6-7 GHz pulse the BER curves are plotted in Figure 7-5 for antipodal signaling and in Figure 7-6 for OOK and PPM. Again, the PPM signal has degraded performance compared to the OOK signal due to the multipath interference. As expected, there are significantly less resolvable multipath components than with the bicone pulse, due to the longer pulse used. As a result, beyond five fingers, there is negligible gain for the 6-7 GHz pulse. However, performance for the 6-7 GHz pulse is only slightly degraded compared to the bicone pulse.

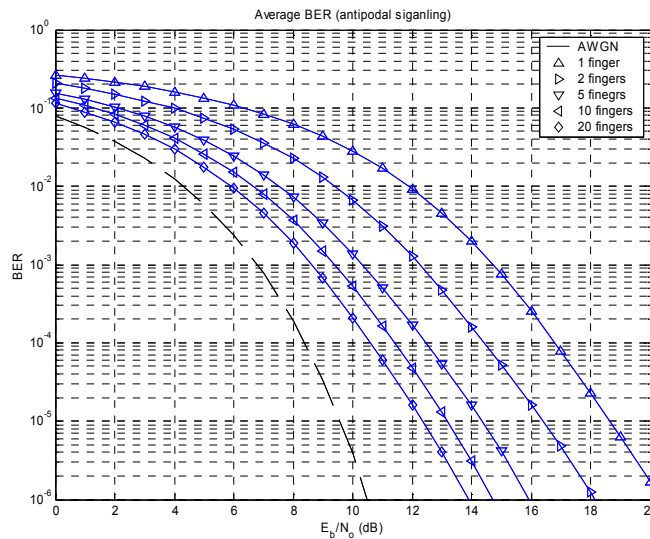


Figure 7-3. Coherent MRC Rake correlation receiver, antipodal signaling, bicone pulse

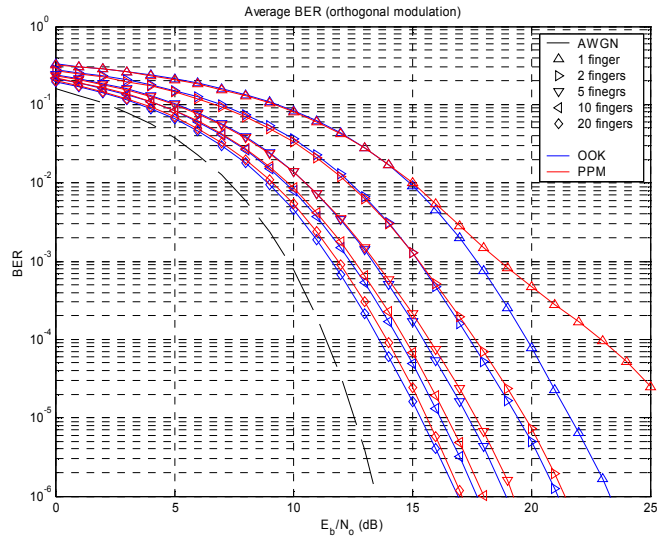


Figure 7-4. Coherent MRC Rake correlation receiver, orthogonal modulations, bicone pulse

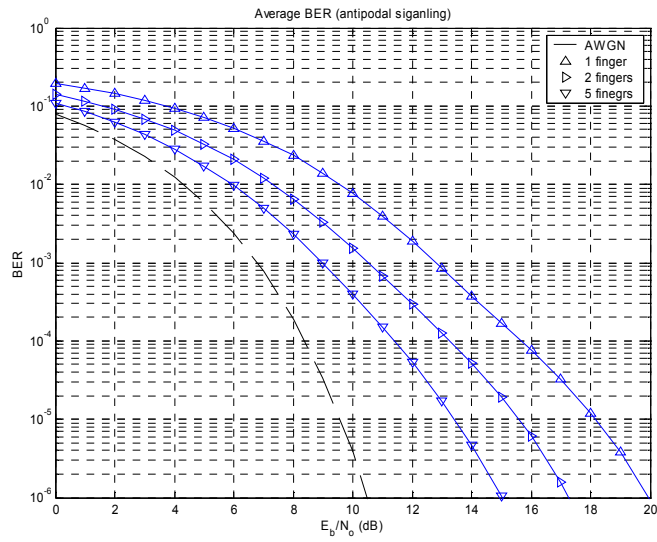


Figure 7-5. Coherent MRC Rake correlation receiver, antipodal signaling, 6-7 GHz pulse

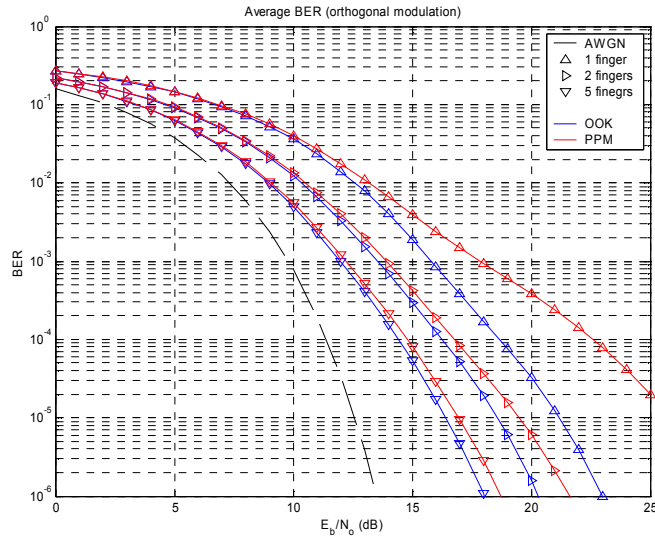


Figure 7-6. Coherent MRC Rake correlation receiver, orthogonal modulations, 6-7 GHz pulse

MRC with Channel Estimation Errors and EGC

The impact of channel estimation error is of concern for MRC Rake receivers where a relatively large number of paths are being combined. Also, the performance of EGC Rake receivers is of interest, because the added complexity of channel estimation, which is necessary for MRC, may not be worthwhile relative to the performance gains of using MRC over EGC. The average BER performances of Rake receivers, using antipodal signaling in the modeled LOS channels, for MRC with perfect channel knowledge, for an approximation of MRC with channels estimation errors using the expression of (7-38), and for EGC are shown in Figure 7-7 for the bicone pulse and in Figure 7-8 for the 6-7 GHz pulse. Similarly the average BER performances comparing MRC and EGC in the modeled NLOS channels (single Poisson model) are shown in Figure 7-9 for the bicone pulse and in Figure 7-10 for the 6-7 GHz pulse.

For the MRC case with channel estimation errors, it is assumed that 10 symbols are used for channel estimation. This could correspond to a situation where a frame of

data consists of 100 bits where the first 10 are pilot symbols used for the channel estimation. The channel is assumed to be static over the duration of the frame. The E_b/N_o is calculated neglecting the energy required for the pilot symbols, because either scheme, MRC or EGC will require some overhead.

From these plots, it appears that MRC with channel estimation errors will actually tend to perform worse than EGC. It should be noted that the approximate expression used to calculate the performance of MRC with estimation errors is somewhat pessimistic. However, the true MRC performance will be bounded by the approximate curve and the curve corresponding to no estimation error. For a two finger Rake, there is almost no gain for MRC with perfect channel estimation over EGC. In the LOS channels, the gain of perfect MRC over EGC increases to about 1 dB for Rake receivers with more fingers. For NLOS channels, the gain of perfect MRC over EGC is even smaller for Rake receivers with more fingers. Simulations must be performed to determine the exact MRC performance with estimation errors. It appears that the extra complexity necessary for channel estimation is not worthwhile for UWB systems and may actually degrade performance, especially in NLOS channels.

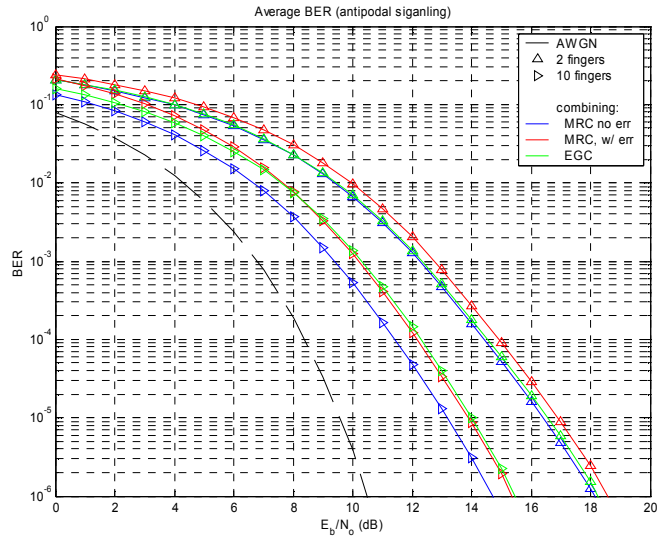


Figure 7-7. Comparison of MRC and EGC for LOS model, antipodal signaling, bicone pulse

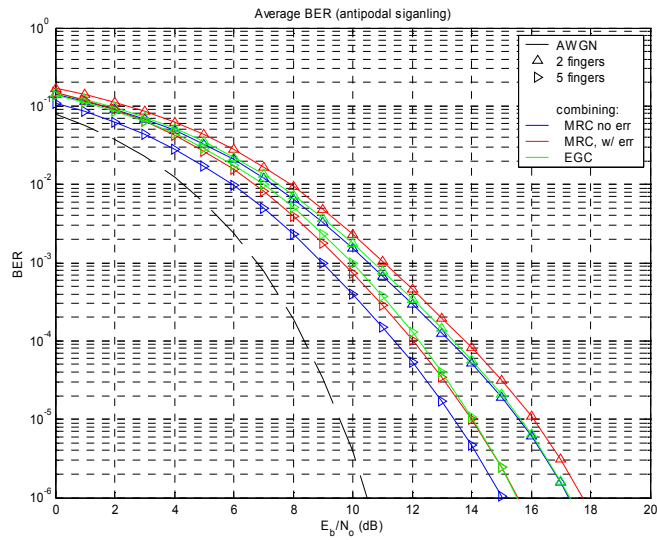


Figure 7-8. Comparison of MRC and EGC for LOS model, antipodal signaling, 6-7 GHz pulse

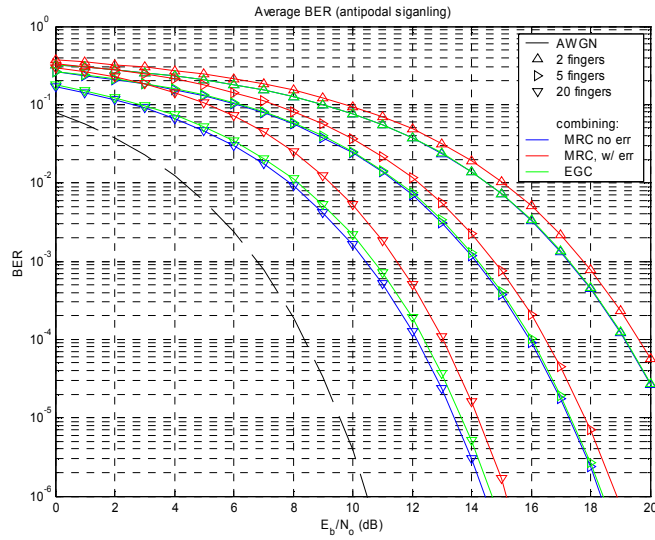


Figure 7-9. Comparison of MRC and EGC for NLOS model (single Poisson), antipodal signaling, bicone pulse

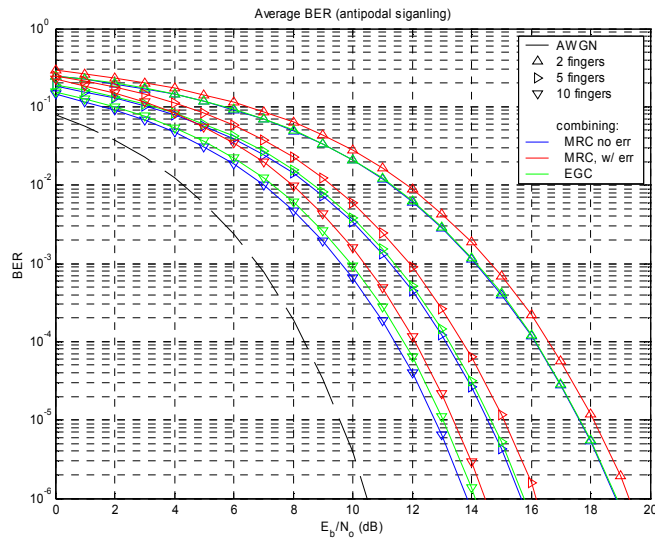


Figure 7-10. Comparison of MRC and EGC for NLOS model (single Poisson), antipodal signaling, 6-7 GHz pulse

Alternate Correlation Template

The received pulse shape may be difficult to regenerate at the receiver to use as a correlation template. For bandpass signals, such as the 6-7 GHz pulse considered here, a sinusoidal template at approximately the center frequency of the pulse may be a suitable

alternate template for the receiver. For the systems using the 6-7 GHz pulses, a 6.5 GHz sinusoid is considered for use as a correlation template. 1.2 ns and 0.6 ns are both evaluated as possible integration times for the correlation. For all match filtering simulations, the template signal has been normalized to have unit energy. This assures that the energy capture is consistent relative to the amount of noise captured by the template. The noise bandwidth will be different for different templates, but the normalization causes the simulated noise power at the output of the matched filter to be the same for all templates at a given noise power spectral density. The decision SNR is then just determined by the energy in the received signal that is correlated with the template signal.

Figure 7-11 and Figure 7-12 shows the performance of a Rake receiver (using MRC with perfect channel knowledge) with antipodal signaling and PPM respectively using these templates compared with the Rake receiver using the LOS pulse as a correlation template that was previously considered. Relatively small losses are seen for using these alternate templates. However, it must be noted that the Gaussian modulated sinusoidal pulse assumed here is likely to have higher correlation with a sinusoidal signal than an arbitrary pulse shape would.

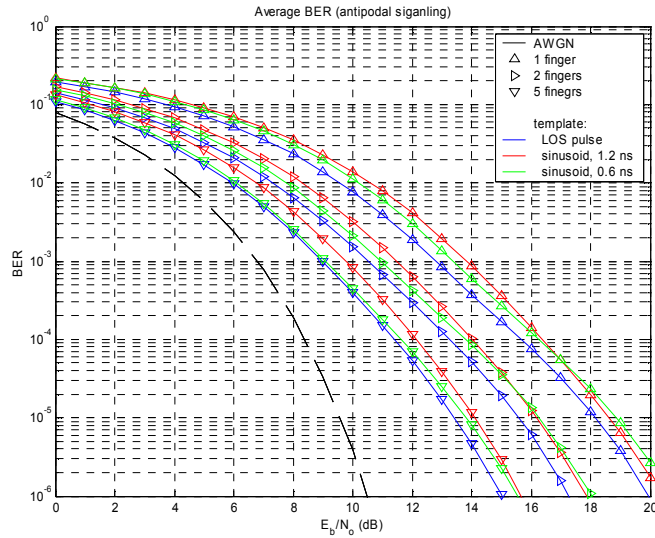


Figure 7-11. Comparison of Rake receiver performance with alternate templates, antipodal signaling, 6-7 GHz pulse

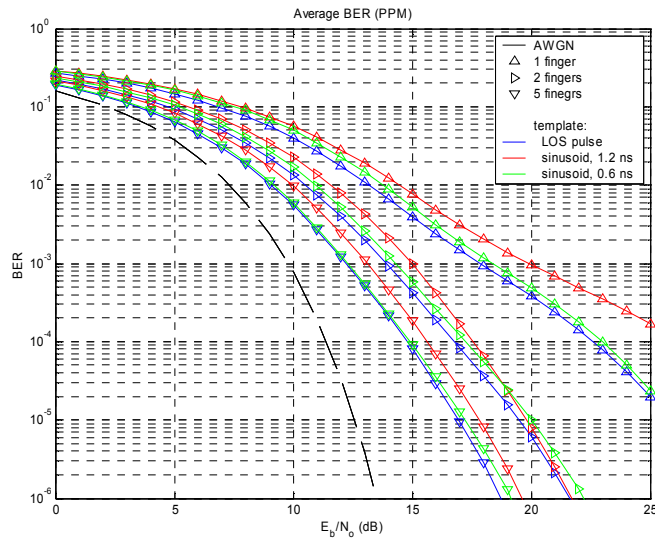


Figure 7-12. Comparison of Rake receiver performance with alternate templates, PPM, 6-7 GHz pulse

7.2 Energy Detector Receiver

7.2.1 Receiver Description and Theoretical Analysis

A block diagram of an energy detector, or radiometer, which could be used as a UWB receiver for certain modulation schemes (such as PPM or OOK) is shown in Figure

7-13. If the measured energy, z , is greater than the detection threshold, the output of the radiometer indicates that a signal is present.

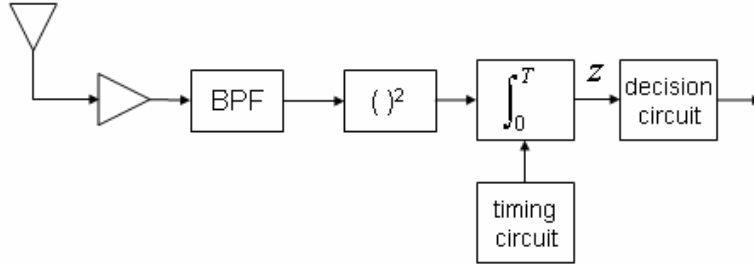


Figure 7-13. Energy detector block diagram

When the input is only additive white Gaussian noise with two sided power spectral density $N_o/2$, the normalized decision statistic, $y = 2z / N_o$, is known to be distributed according to a central chi-squared distribution with $2TW$ degrees of freedom (where T is the integration time and W is the noise equivalent bandwidth of the bandpass filter) [46]

$$p_n(y) = \frac{1}{2^{TW} \Gamma(TW)} y^{TW-1} e^{-\frac{y}{2}}, \quad y \geq 0 \quad (7-66)$$

If there is a signal present and the energy captured over the integration time is E , y is described by a noncentral chi-square distribution with noncentrality parameter $2E/N_o$ (due to the normalization) and again $2TW$ degrees of freedom

$$p_{s+n}(y) = \frac{1}{2} \left(\frac{y N_o}{2 E} \right)^{(TW-1)/2} e^{-\left(\frac{y+E}{2 N_o} \right)} I_{TW-1} \left(\sqrt{2y \frac{E}{N_o}} \right), \quad y \geq 0 \quad (7-67)$$

The probability that the output of the radiometer indicates a signal is present (detected) is the probability that the decision statistic, z , is greater than the threshold level, z_T . So the probability of false alarm is given by

$$P_{fa} = \int_{\frac{2z_T}{N_o}}^{\infty} p_n(y) dy \quad (7-68)$$

and the probability of detection (when a signal is actually present) is

$$P_d = \int_{\frac{2z_T}{N_o}}^{\infty} p_{s+n}(y) dy \quad (7-69)$$

These integrals cannot be found in closed form (except for TW equal to an integer). However, this type of detector has been modeled using numerical results using certain assumptions by various researchers depending on the application. Reference [46] provides several different detectability models for wideband radiometers. For radiometers with a large time-bandwidth product, TW , then y can be accurately approximated as a Gaussian random variable using the central limit theorem. This case is assumed in Edell's model [18]. The probability of detection, P_d , using this model is given by

$$P_d = Q\left(Q^{-1}(P_{fa}) - \sqrt{\frac{T}{W}} \frac{S}{N_o}\right), \quad TW \gg 1 \quad (7-70)$$

where P_{fa} is the probability of false alarm in noise alone, S is the signal power at the radiometer, and N_o is the noise power spectral density.

However, for a UWB system, the time-bandwidth product is not large and is likely to be on the order of one. In the past, some in the radar and spread spectrum communities have been concerned with detection of pulsed signals using a radiometer where the time-bandwidth product is not large. For these radiometers, Edell's model is no longer valid, but other models for a wide range of TW are also described in [46]. Park's [55] and Dillard's [17] models were chosen here since they are derived from

Barton's radar detector loss function [5] which is based on $TW = 1$. Probability of detection using Park's model can be expressed as

$$P_d \approx Q\left(Q^{-1}(P_{fa}) - \sqrt{2Y}\right) \quad (7-71)$$

and probability of detection for each channel using Dillard's model can similarly be expressed as

$$P_d \approx Q\left(\sqrt{-2\ln(P_{fa})} - \sqrt{Y + \sqrt{Y^2 + 9.2Y}}\right) \quad (7-72)$$

where

$$Y = \frac{TS^2}{2.3WN_o^2 + SN_o} \quad (7-73)$$

We assume here for this analysis that synchronization has already taken place and the receiver has perfect timing knowledge. Therefore, the integration time is aligned perfectly with the pulse occurrence. The instantaneous signal power is not a constant over this time. The average signal power S in the above equations is roughly equal to E_p/T , where E_p is the received energy per pulse. More precisely

$$S = \frac{E_p}{T} \int_{-T/2}^{T/2} [p(t)]^2 dt = \frac{E_p \mu(T)}{T} \quad (7-74)$$

where $p(t)$ is the normalized received pulse shape (centered about $t = 0$) and μ represents the fraction of the pulse energy captured in the integration (which is a function of the pulse shape and T). As the integration time is increased to capture the energy in the tails of the pulse, S (an average value) decreases. Therefore, the optimum value for T (that maximizes Y) will depend on the pulse shape and strength. Substituting in for S gives

$$Y = \frac{\left(\frac{E_p}{N_o} \mu(T)\right)^2}{2.3TW + \frac{E_p}{N_o} \mu(T)} = \frac{\left(\frac{E_p}{N_o} \frac{\mu(T)}{T}\right)^2}{2.3W + \frac{E_p}{N_o} \frac{\mu(T)}{T}} \quad (7-75)$$

Consider a system where the received pulse is Gaussian modulated sinusoidal pulse described by (1-8). For a pulse that occupies a -10 dB bandwidth from 3-10 GHz (pulse duration is approximately 400 ps), the optimal T value (based on the maximization of Y) is plotted as a function E_p/N_o in Figure 7-14. The step-like behavior is due to the pulse shape and the jumps correspond roughly to cycles within the pulse. As the signal to noise ratio increases, the energy captured by integrating over another half cycle is worthwhile compared to the extra noise also captured. However, as will be seen, the system performance is not very sensitive to the integration time as might be interfered from this plot.

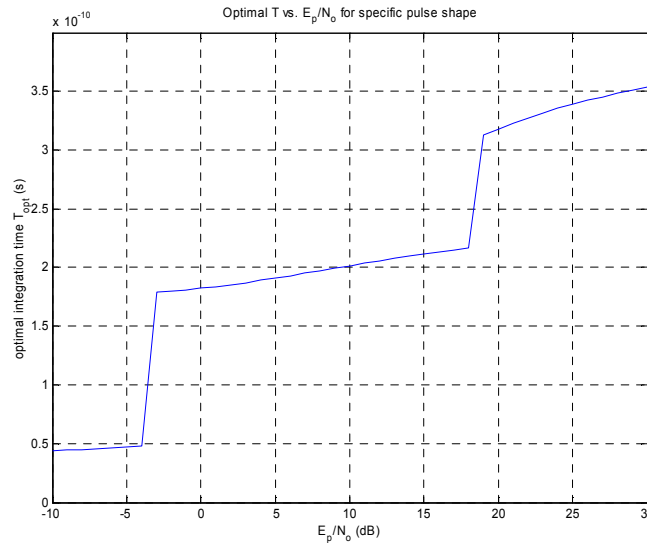


Figure 7-14. T_{opt} values for Gaussian modulated sinusoidal pulse

7.2.2 Probability of Bit Error for Energy Detector

OOK Modulation

If OOK is the modulation scheme and only one pulse is used per bit (no pulse sent, bit=0; pulse sent, bit=1), the probability of bit error can be found from the probability of detection equations. Therefore, as discussed above, the exact expression cannot be expressed in closed form, but will be based on the threshold value used for decisions.

$$P(\text{demod '1' | '0' sent}) = P_{fa} = \int_{\frac{2z_T}{N_o}}^{\infty} p_n(y) dy = 1 - F_n\left(\frac{2z_T}{N_o}\right) \quad (7-76)$$

$$P(\text{demod '0' | '1' sent}) = 1 - P_d = 1 - \int_{\frac{2z_T}{N_o}}^{\infty} p_{s+n}(y) dy = F_{s+n}\left(\frac{2z_T}{N_o}\right) \quad (7-77)$$

where $F(\)$ is the CDF of the respective chi-square random variables. For non-integer degrees of freedom, the CDFs of chi-square random variables cannot be expressed in closed form. They can however be computed numerically.

Park's model can be used here as an approximation to determine the system performance. It is chosen over Dillard's model because its form lends itself more easily to algebraic manipulation. Using Park's model, gives

$$P(\text{demod '1' | '0' sent}) = P_{fa} \quad (7-78)$$

$$P(\text{demod '0' | '1' sent}) = 1 - P_d = 1 - Q\left(Q^{-1}(P_{fa}) - \sqrt{2Y}\right) = Q\left(\sqrt{2Y} - Q^{-1}(P_{fa})\right) \quad (7-79)$$

Assuming equally likely symbols, P_{fa} (and thus the decision threshold) should be chosen such that the probability of error for either a 1 or 0 is equal. Therefore,

$$\begin{aligned}
P(\text{demod '1' | '0' sent}) &= P(\text{demod '0' | '1' sent}) \\
P_{fa} &= Q\left(\sqrt{2Y} - Q^{-1}(P_{fa})\right) \\
2Q^{-1}(P_{fa}) &= \sqrt{2Y} \\
P_{fa} &= Q\left(\sqrt{\frac{Y}{2}}\right)
\end{aligned} \tag{7-80}$$

Therefore, if the threshold value is optimally adjusted to achieve this optimal probability of false alarm, then the probability of false alarm becomes the overall probability of error.

$$P_{b,OOK} \approx Q\left(\sqrt{\frac{Y}{2}}\right) = Q\left(\frac{\frac{E_p}{N_o} \mu(T)}{\sqrt{4.6TW + 2\frac{E_p}{N_o} \mu(T)}}\right) \tag{7-81}$$

Written in terms of the average energy per bit

$$P_{b,OOK} \approx Q\left(\sqrt{\frac{Y}{2}}\right) = Q\left(\frac{2\frac{E_b}{N_o} \mu(T)}{\sqrt{4.6TW + 4\frac{E_b}{N_o} \mu(T)}}\right) \tag{7-82}$$

The choice of the threshold level as described above is not optimal from a bit error perspective, but very nearly optimal. As an illustration, the probability of bit error for a '0' being transmitted (i.e. nothing transmitted for OOK) and the probability of bit error for a '1' being transmitted are both plotted versus the threshold value in Figure 7-15. These curves are generated from the numerically calculated CDFs of chi-square random variables. The above discussion assumed that the threshold value was chosen based on where these two curves intersect (where the probability of error is the same for both possible transmitted symbols). However, the true optimal overall bit error performance will be achieved where the average of those two curves is a minimum. The average of

the curves shown in Figure 7-15 is shown in Figure 7-16. This threshold corresponding to the minimum of this curve is very close to threshold value corresponding to the intersection, but not exactly the same. For this example, the normalized threshold found from the intersection of curves is 16.87 and the corresponding probability of error is 7.73×10^{-2} . The threshold found from the minimum average probability of error is 17.19 and the corresponding probability of bit error is 7.71×10^{-2} . For this example, TW is equal to 5 and E_p/N_o is equal to 10 dB.

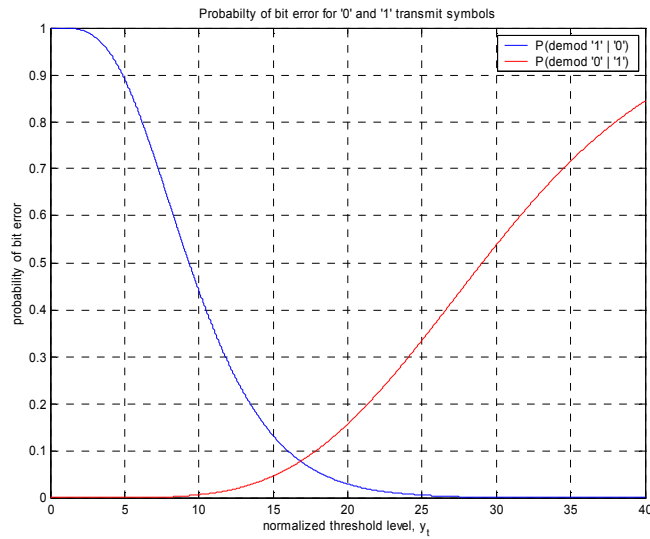


Figure 7-15. Probability of bit error for transmitted '0' or '1' versus decision threshold value

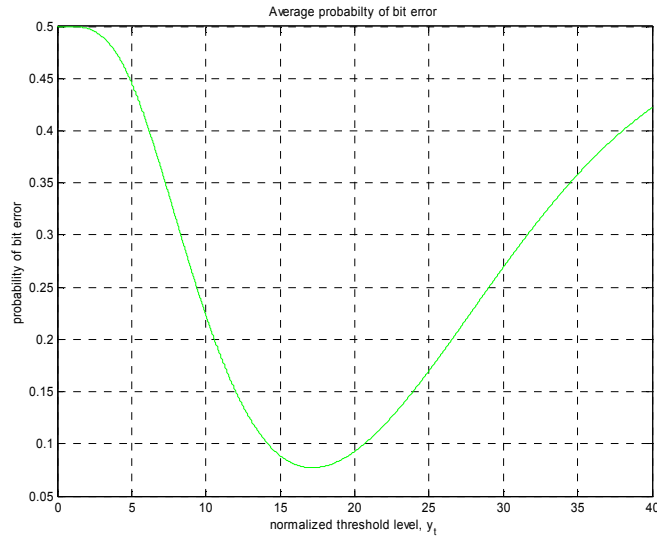


Figure 7-16. Average overall probability of bit error versus decision threshold value

Since bit error performance is typically the most significant measure for a communications system, the probability of bit error calculated using the numerical CDF method for the optimal and near-optimal threshold values are plotted in Figure 7-17 for a system with time bandwidth product equal to 1 and in Figure 7-18 for a system with time bandwidth product equal to 10. The estimate of the bit error based on Park's model as given in (7-82) is also plotted in these figures to evaluate the accuracy of this approximation. The curves corresponding to the intersection method of choosing the threshold is not visible in the plots because they are so nearly identical to the curves corresponding to the minimum average probability of error method of choosing the threshold. The approximation based on Park's model does differ some from the numerical CDF methods but by less than 0.7 dB for time-bandwidth products up to 10. Thus, the approximation of (7-82) may not give the best accuracy, but offers a simple method to quickly estimate performance.

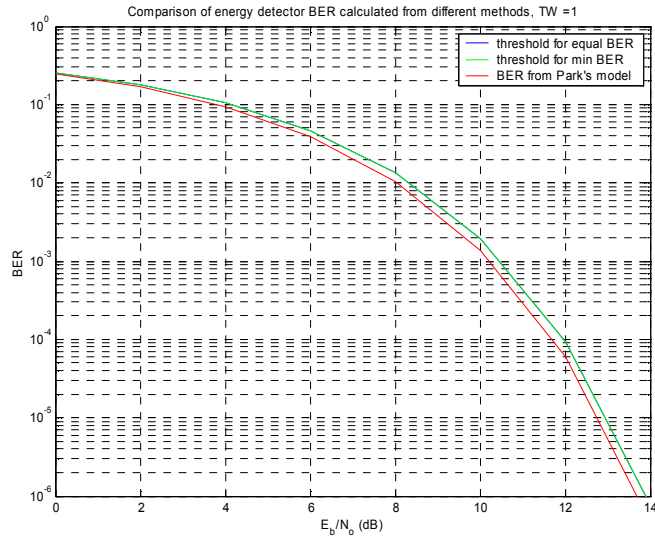


Figure 7-17. Probability of bit error calculated using different methods for $TW = 1$

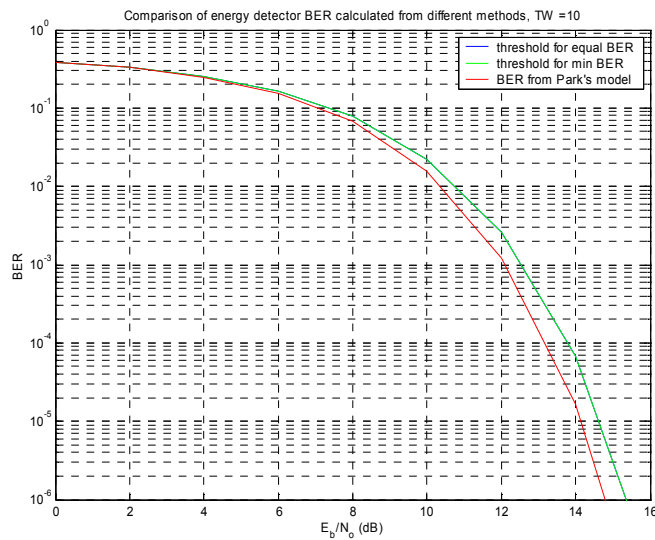


Figure 7-18. Probability of bit error calculated using different methods for $TW = 10$

M-ary Orthogonal Signaling

For M -ary orthogonal signaling in AWGN, the probability of symbol error of an energy detector receiver can be described by the probability that the decision output corresponding to the correct symbol (a noncentral chi-square random variable given by (7-67)) is greater than each of the outputs corresponding to the incorrect symbols (central

chi-square random variables given by (7-66)). Following a similar derivation as [59] for M -ary orthogonal signals using a correlation receiver

$$\begin{aligned} P_s &= 1 - \int_0^{\infty} P(z_1 > z_2, z_1 > z_3 \dots z_1 > z_M | z_1) p(z_1) dz_1 \\ &= 1 - \int_0^{\infty} P(y_1 > y_2, y_1 > y_3 \dots y_1 > y_M | y_1) p(y_1) dy_1 \end{aligned} \quad (7-83)$$

where

$$\begin{aligned} P(y_1 > y_m | y_1) &= \int_0^{y_1} p_{y_m}(x_m) dx_m = F_n(y_1) \\ &= \frac{1}{2^{TW} \Gamma(TW)} \int_0^{y_1} x_m^{TW-1} e^{-\frac{x_m}{2}} dx_m = \frac{1}{\Gamma(TW)} \gamma\left(TW, \frac{y_1}{2}\right) \end{aligned} \quad (7-84)$$

This expression using the incomplete gamma function, $\gamma(a,b)$, can only be further simplified if the a term (TW in this case) is equal to an integer. The probability of symbol error thus cannot be given in closed form, but could be numerically calculated by

$$\begin{aligned} P_s &= 1 - \int_0^{\infty} P(z_1 > z_2, z_1 > z_3 \dots z_1 > z_M | z_1) p(z_1) dz_1 \\ &= 1 - \int_0^{\infty} [F_n(y_1)]^{M-1} \frac{1}{2} \left(\frac{y_1}{2} \frac{N_o}{E}\right)^{(TW-1)/2} e^{-\left(\frac{y_1}{2} \frac{E}{N_o}\right)} I_{TW-1} \left(\sqrt{y_1 \frac{E}{N_o}}\right) dy_1 \end{aligned} \quad (7-85)$$

7.2.3 Energy Detector Diversity Combining

The above performance analysis can be very easily extended to a Rake type receiver that sums the outputs from several separate energy calculations to exploit the time diversity present due to the multipath. The normalized N -finger Rake decision output is given by

$$y_{\text{Rake}} = \sum_{n=0}^N y_{\text{finger},n} \quad (7-86)$$

This is a sum of noncentral chi-square random variables. In the general case, the integration times of the fingers need not be the equal. The characteristic function of a single finger output is given by

$$\psi_{y_{\text{finger},n}}(j\nu) = \frac{1}{(1-j2\nu)^{T_{\text{finger},n}W}} \exp\left(\frac{j\nu 2 \frac{E}{N_o}}{1-j2\nu}\right) \quad (7-87)$$

Therefore, the characteristic function of the Rake summation is

$$\psi_{y_{\text{Rake}}}(j\nu) = \prod_{n=1}^N \psi_{y_{\text{finger},n}}(j\nu) = \frac{1}{(1-j2\nu)^{W \sum_{n=1}^N T_{\text{finger},n}}} \exp\left(\frac{j\nu 2 \frac{\sum_{n=1}^N E}{N_o}}{1-j2\nu}\right) \quad (7-88)$$

The Rake output is also a non-central chi-square random variable and thus, the above derived performance equations can be used by plugging in the total captured energy and total integration time regardless of whether the integration times are continuous.

7.2.4 Semi-analytic Simulation of BER Performance in Multipath Channels

The performance of energy detector receivers is simulated using the same methodology as described above for correlation receivers. The set of 1000 channel impulse responses generated using the new UWB LOS model and the set of 1000 channel impulse responses generated using the NLOS single Poisson model are used with both the bicone pulse and the 6-7 GHz pulse.

It is well known that the optimal filter for maximum SNR is a matched filter. However, when discussing the use of energy detectors as receivers it is assumed that

matched filtering of the signal is too complex or not possible (potentially due to the necessity of an analog implementation) and thus more noise will be captured in generating the decision statistic(s). So, for the following analysis, it is assumed that the bandpass filter is a 6th order Butterworth bandpass filter. The filters that are chosen attenuate the energy in the pulse by only 5 %. The noise bandwidth of the filter for the bicone signal is 5.47 GHz and the noise bandwidth of the filter for the 6-7 GHz pulse is 1.97 GHz. The choice of bandpass filter will have a great impact on the system performance and it is likely that more optimal filters could be used.

To compute BER from the captured energy in the signals received signals, the approximation of (7-82) is used. The numerical CDF method proved to be too computationally intensive for use in calculating performance over such a large set of data (1000 impulse responses and at several E_b/N_o levels). The performance of Rake type receivers in LOS channels with single finger integration times of approximately 0.5 times and 1 times the pulse duration are simulated and are shown in Figure 7-19 and Figure 7-20 for the bicone pulse and the 6-7 GHz pulse respectively. Similarly, the performance of Rake type receivers in NLOS channels are shown in Figure 7-21 and Figure 7-22 for the bicone pulse and the 6-7 GHz pulse respectively. The performance of Rake receivers with only a few fingers (e.g. 1 or 2) in LOS channels is significantly better than in NLOS channels as expected because the LOS channels have a few dominant multipath components. In NLOS channels, the performance gain for more fingers is some larger than in LOS for the same reason.

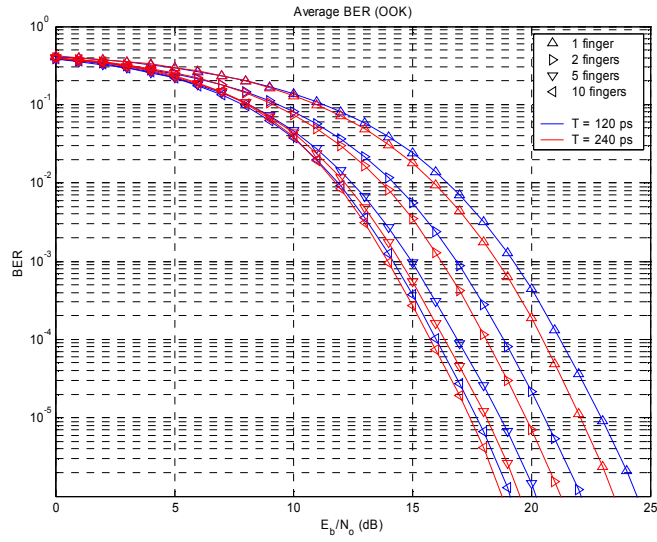


Figure 7-19. Rake energy detector in LOS channel, $T_{finger} = 120$ and 240 ps, OOK, bicone pulse

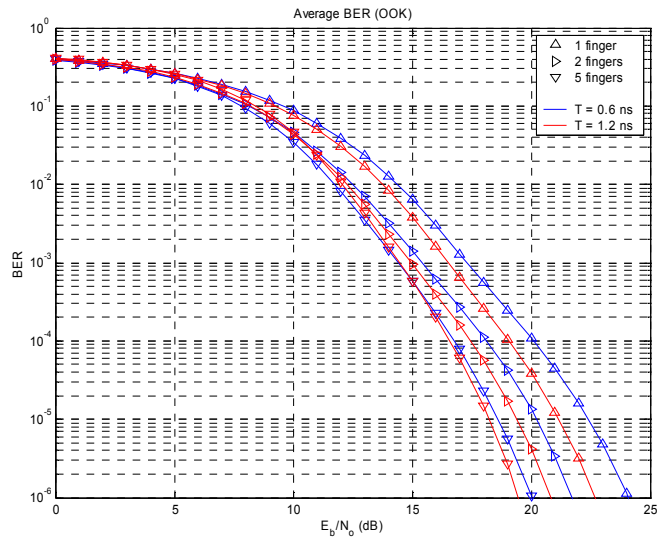


Figure 7-20. Rake energy detector in LOS channel, $T_{finger} = 0.6$ and 1.2 ns, OOK, 6-7 GHz pulse

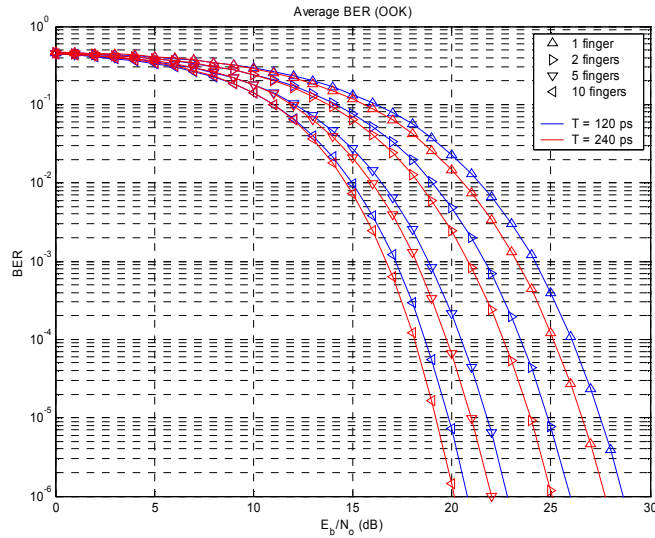


Figure 7-21. Rake energy detector in NLOS channel, $T_{finger} = 120$ and 240 ps, OOK, bicone pulse

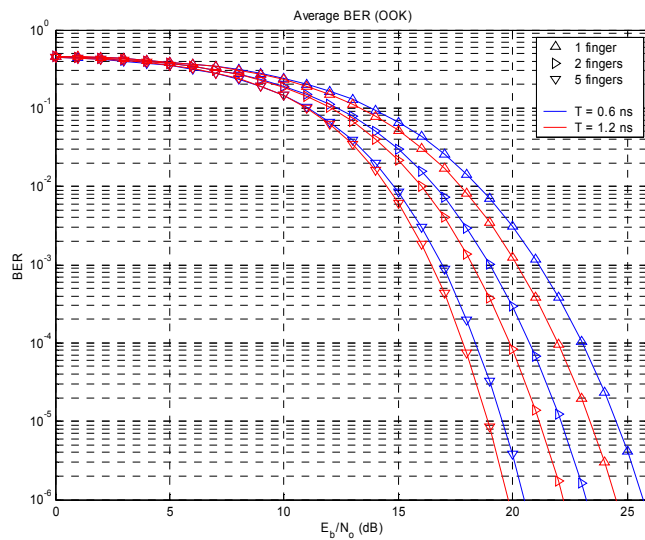


Figure 7-22. Rake energy detector in NLOS channel, $T_{finger} = 0.6$ and 1.2 ns, OOK, 6-7 GHz pulse

One of the potential advantages of an energy detector over a correlation receiver is simplified implementation. Thus adding the complexity of a Rake receiver may not be reasonable for an energy detector receiver. So simulations are performed to find the optimal T values for an energy detector receiver that uses a single continuous integration to estimate energy. Figure 7-23 and Figure 7-24 shows the average BER (using the same

set of 1000 impulse responses as before) for three different E_b/N_o levels as a function of the integration time for the bicone pulse and 6-7 GHz pulse respectively. As seen in the figures, the average BER performance varies slowly with changes in the integration time. Therefore, a range of T values will give near optimal BER performance, which simplifies choosing this value when designing a system that will operate in a random, unknown channel. It should be noted that using a long integration time would not work well for a system using PPM.

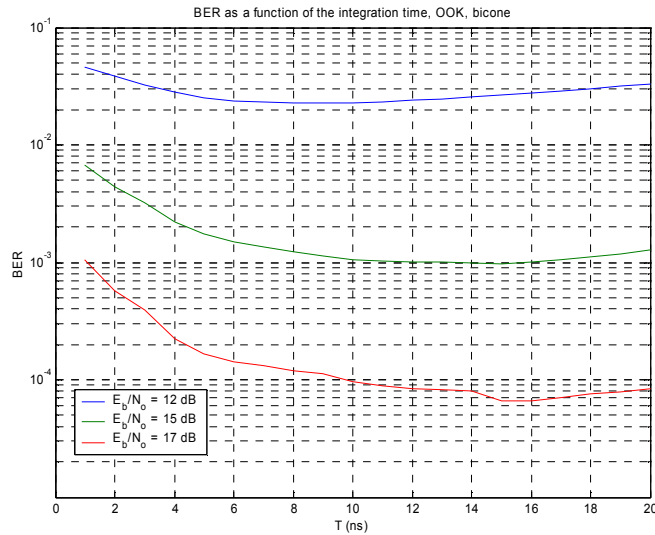


Figure 7-23. Average BER for single integration energy detector vs. integration time, OOK, bicone pulse, LOS channels

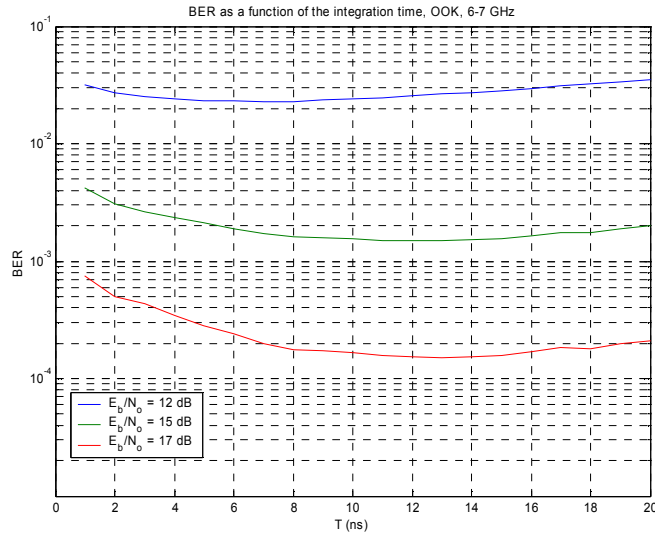


Figure 7-24. Average BER for single integration energy detector vs. integration time, OOK, 6-7 GHz pulse, LOS channels

For comparison, some of the energy detector BER curves are plotted with some correlation receiver BER curves. Figure 7-25 shows average BER curves (bicone pulse) for 1 and 10 finger correlation Rake receivers plotted with curves for 1 and 10 finger Rake energy detectors (with the finger integration time approximately equal to the pulse width) and a curve for a 14 ns single integration energy detector in LOS channels. It should be noted that these are all plotted for OOK. Antipodal signaling, which is 3 dB more energy efficient than OOK, could be employed with the correlation receiver, but not the energy detector. Figure 7-26 shows average BER curves (6-7 GHz pulse) for 1 and 5 finger correlation Rake receivers plotted with curves for 1 and 5 finger Rake energy detectors (with the finger integration time approximately equal to the pulse width) and a curve for a 14 ns single integration energy detector in LOS channels. Figure 7-27 shows average BER curves (bicone pulse) for 1 and 10 finger correlation Rake receivers plotted with curves for 1 and 10 finger Rake energy in NLOS channels. Figure 7-28 shows average BER curves (6-7 GHz pulse) for 1 and 5 finger correlation Rake receivers plotted

with curves for 1 and 5 finger Rake energy in NLOS channels. At higher values of SNR, the performance loss of an energy detector receiver is small compared to a correlation receiver for both LOS and NLOS channels.

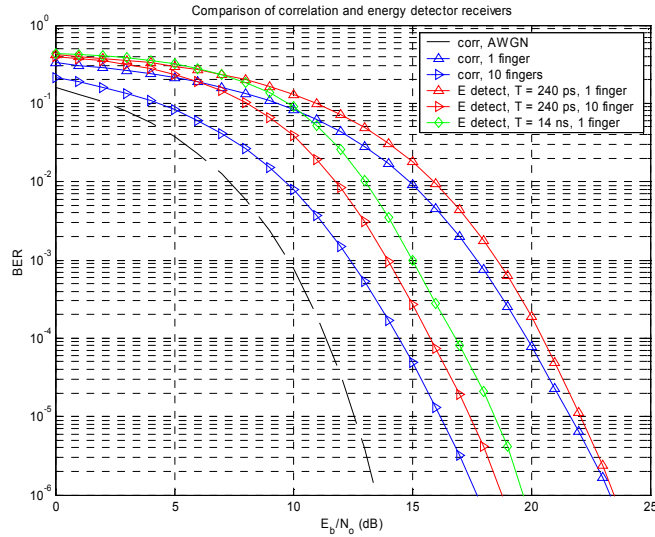


Figure 7-25. Comparison of correlation receivers and energy detectors, bicone pulse, LOS channels

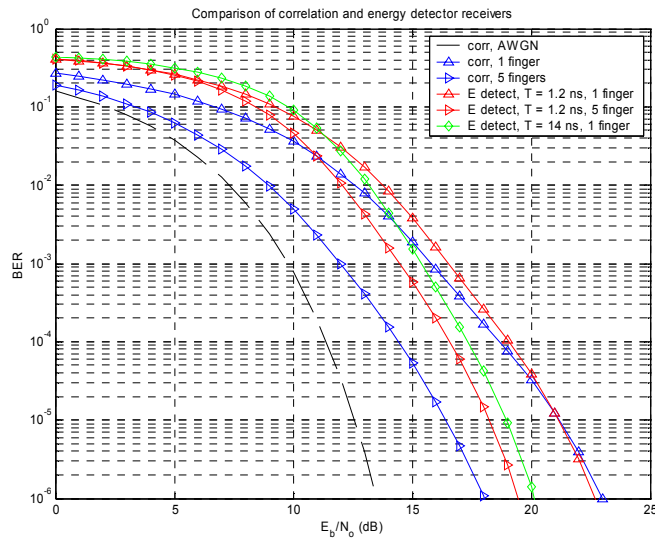


Figure 7-26. Comparison of correlation receivers and energy detectors, 6-7 GHz pulse, LOS channels

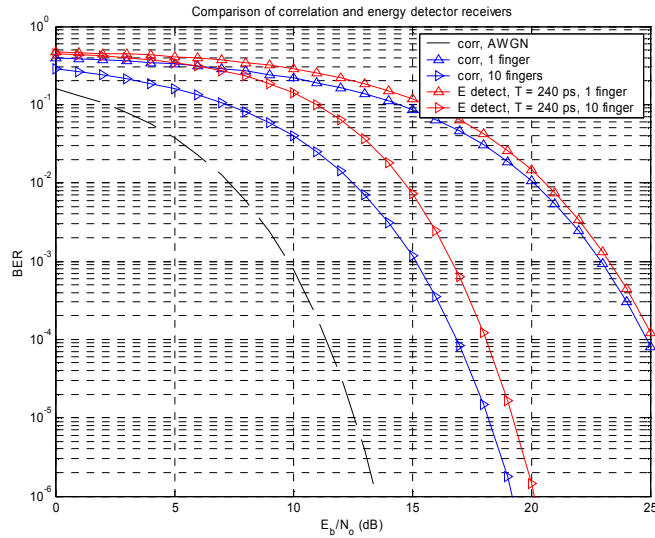


Figure 7-27. Comparison of correlation receivers and energy detectors, bicone pulse, NLOS channels

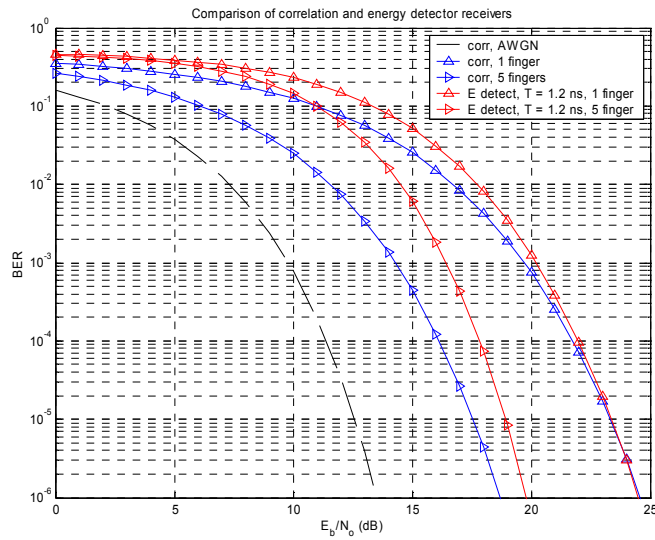


Figure 7-28. Comparison of correlation receivers and energy detectors, 6-7 GHz pulse, NLOS channels

7.3 Conclusions

In UWB channels, significant gains can be achieved by Rake receivers that capture energy from several multipath components. Modulation schemes such as PPM that can experience multipath interference even with a low pulse repetition frequency

experience some degradation in performance, but this degradation is reduced for Rake receivers with more fingers. Therefore, PPM should not be implemented with a single finger receiver, but it is reasonable for multiple finger receivers. As expected, wider bandwidth systems (the bicone pulse as compared to the 6-7 GHz pulse here) have a greater number of resolvable multipaths to be exploited by a Rake receiver. There appears to be little if any advantage for using MRC rather than EGC for UWB systems. The energy detector shows potential as a low complexity alternative to a correlator for use as a UWB receiver. The performance of energy detector receivers is suboptimal compared to correlation Rake receivers, but have less sensitive timing requirements.

8 Narrowband Interference Impact and Rejection for UWB Systems

8.1 Background

One major inherent advantage of any spread spectrum system is interference suppression. However, additional processing of the received signal can further suppress the effect of interference on the system performance and may even be necessary in the presence of strong interferers. For a signal in Gaussian noise and a sine-wave interferer, the maximum likelihood receiver has been shown to be non-linear [47]. However, other designs, though not optimal, can offer improved performance in the presence of narrowband interferers, but are reasonable to implement [47].

Two major types of narrowband interference rejection techniques that are applicable to UWB are least mean square (LMS) estimation techniques and transform domain techniques. Due to the extremely short duration of UWB pulses, purely digital techniques are not feasible. Thus, techniques that can be implemented in analog are of interest. If the interferer(s) is sufficiently narrowband, notch filtering using one of these techniques can greatly improve the performance.

The first set of techniques may use a tapped delay line to implement a one-sided prediction error (Weiner) filter or a two-sided transversal filter [47]. When a narrowband interferer is present the use of a predictive filter is helpful since the future value of that interferer can be predicted from past values whereas in a system with only Gaussian noise, a predictive filter would not help.

The second set of techniques mentioned uses a tapped delay line that acts as a real-time Fourier transformer [47]. A surface acoustic wave device (SAW) with a chirp

impulse response could potentially be used. The appropriate interfering frequency can be notched by nulling the transform response at the right time. The filtered signal can then be inverse transformed.

Both of these two types of systems can be made adaptive. Since they are both effectively tapped delay lines, they can be implemented using SAW or charge coupled device (CCD) technology. SAW devices and CCDs are analog which is important for implementation into current UWB systems because conventional analog to digital converters do not sample at high enough rates to sample UWB signals directly. Some detail about the performance and implementation of each of these techniques is given in [47].

If the interfering signal is sufficiently narrowband and sufficiently strong, a phase-locked loop circuit can be used to estimate the signal so it can be canceled out. Techniques to suppress wideband interference are also possible using circuits such as one mentioned in [47]. Another possible technique uses an A/D converter with a variable threshold to keep only the chips that retain their correct polarity in the presence of a strong interferer [47].

For CDMA systems, additional techniques have been developed to improve performance in the presence of both multiple access and narrowband interference. An in-depth tutorial of these techniques including beamforming, multiuser detection (MUD), adaptive filtering and other “code-aided” suppression techniques is given in [10].

References [4] and [8] have proposed schemes specifically for UWB communications systems to suppress narrowband interference. Reference [4] proposes a narrowband rejection system that samples the total received signal, estimates the

narrowband interfering signal in the frequency domain and then subtracts out the estimated narrowband signal. Reference [8] presents analysis of an MMSE-Rake receiver that adjusts the tap weights to achieve narrowband interference suppression.

References [45] and [35] both discuss interference suppression for UWB radar systems. In [45], the entire received signal is sampled and then narrowband interfering signals are estimated and subtracted digitally. For interfering signals at a known frequency, a least squares estimate is implemented by projecting the received signals onto a set of orthogonal basis vectors (sines and cosines). For interferers at unknown frequencies, an FFT based estimation technique is used. This method was implemented on an Army Research Laboratory synthetic aperture radar (SAR). Reference [35] proposes a parametric method to suppress the narrowband interference. The algorithm proposed is an iterative form of the RELAX algorithm which had been previously proposed for non-UWB SAR.

8.2 Impact of Narrowband Interference on a UWB signal

Over the duration of a single pulse, a narrowband interferer/jammer can be modeled as a single tone (assuming the pulse duration \ll the inverse of the bandwidth of the narrowband signal) with amplitude A_I , frequency f_I , and phase θ_I , using

$$I(t) = A_I \cos(2\pi f_I t + \theta_I) \quad (8-1)$$

and average power $P_I = A_I^2 / 2$. The UWB average power is given by

$$\bar{P}_{UWB} = \zeta E_p \quad (8-2)$$

where ζ is the average pulse repetition rate and E_p is the energy per pulse. Thus, the signal to interference ratio can be defined as

$$\text{SIR} = \frac{\bar{P}_{UWB}}{P_I} = \frac{2\zeta E_p}{A_I^2} \quad (8-3)$$

If a correlation receiver is used, the strict power ratio is a not specific enough description to determine accurate performance degradation. The correlation (or matched filter) output of a single pulse in the presence of a single tone interferer and AWGN is

$$z = \sqrt{E_p} + v_I + n \quad (8-4)$$

where v_I is the correlation of the interferer with the received pulse shape and n is a Gaussian random variable with variance equal to the noise power. The correlation of the interferer in the receiver is given by

$$v_I = \int_{-\infty}^{\infty} p(t) I(t) dt \quad (8-5)$$

where $p(t)$ is the energy normalized pulse shape. For specific pulse shapes this integral can be worked out and the impact on the correlation output can be calculated.

For example, consider a UWB system that uses Gaussian modulated sinusoidal pulses given by (1-8). Evaluating (8-5) using (1-8) gives

$$v_I = aA_I \sqrt{\frac{\pi}{4k}} \left[e^{-\frac{\pi^2(f_{c,UWB}+f_I)^2}{k}} - e^{-\frac{\pi^2(f_{c,UWB}-f_I)^2}{k}} \right] \sin(\theta_I) \quad (8-6)$$

While not elegant, (8-6) can be easily evaluated if the parameters are known. Since the UWB and narrowband signals are not expected to be synchronized, the relative phase term, θ_I , can be modeled as a uniform random variable over $[0,2\pi)$. Equation (8-6) can be rewritten in terms of the SIR given in (8-3) and the average pulse repetition rate giving

$$v_I = a \sqrt{\frac{\zeta E_p}{\text{SIR}}} \sqrt{\frac{\pi}{2k}} \left[e^{-\frac{\pi^2(f_{c,UWB}+f_I)^2}{k}} - e^{-\frac{\pi^2(f_{c,UWB}-f_I)^2}{k}} \right] \sin(\theta_I) \quad (8-7)$$

Consider a UWB system using a Gaussian modulated sinusoid that has a 10 dB bandwidth from 3.1-10.6 GHz (and thus meeting the FCC UWB spectral mask) and an average pulse repetition rate of 1 MHz in the presence of a narrowband interferer with a carrier frequency f_I . The worst case interference, $v_{I,min}$ is when $\theta_I = -\pi/2$. The resulting correlator output will increase or decrease as the narrowband interferer constructively or destructively interferes with the pulse depending on the relative phase. The worst case interference normalized by the interferer amplitude, $v_{I,min}/A_I$, as a function of frequency for the UWB pulse described is shown in Figure 8-1. As expected, this curve follows the negative of the magnitude of the spectrum of the pulse. Even over an entire band used by narrowband systems the change in the interference's impact for different frequencies is small. For example, over the ISM band from 5.725-5.875 GHz, the change in the interference's impact at the edges of the band compared to the center of the band is less than 1.4%.

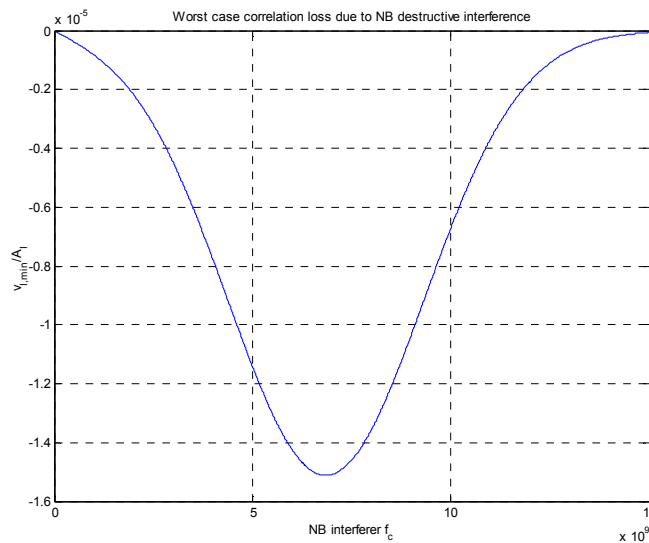


Figure 8-1. $v_{I,min}/A_I$, as a function of the narrowband interferer frequency

The worst case for $v_{I,min}/A_I$, (when $f_I = f_{c,UWB}$) is approximately -1.5×10^{-5} indicating that large processing gain is inherent for the UWB signal to reject narrowband interference and that the SIR must be very low for the narrowband interference to have a significant impact on the UWB system performance. However, such a scenario is not unlikely if the UWB system is using very low power and/or a strong narrowband transmitter is close to the UWB receiver.

8.3 Impact of UWB Interference on a Narrowband Signal

If a UWB pulse is the input to a narrowband filter (such that the bandwidth of the pulse \gg the bandwidth of the filter), the output of the filter will be very nearly the filter impulse response and the specific pulse shape is insignificant. Consider a narrowband receiver that downconverts the narrowband signal into in-phase and quadrature channels. As assumed in the above UWB analysis, the phase of the narrowband signal (the tone used to downconvert in this case) relative to the UWB pulse will be random, since this carrier will not be synchronized with the UWB pulses. The UWB input to the narrowband lowpass filter can be treated as a train of impulses with random amplitudes. The probability distribution of the amplitudes will be a function of the UWB power spectral density near the carrier frequency of the narrowband signal, and the distribution of $\sin(\theta_i)$ where θ_i is a uniform random variable over $[0, 2\pi)$ similar to the θ_i term defined above. After lowpass filtering, the UWB signal begins to be similar to low pass filtered Gaussian noise (provided the average pulse repetition rate is greater than the filter bandwidth such that the independent amplitude impulses can be treated as independent noise samples). Therefore, to a narrowband receiver, a pulsed UWB signal meeting the

above assumptions can be treated as additive Gaussian noise, which agrees with the findings of [54].

The distribution of a train of impulses with random amplitudes as described above is given by

$$x(t) = \sum_{i=-\infty}^{\infty} \delta(t - \tau_i) \sin(\theta_i) \quad (8-8)$$

where the θ_i are independent. The distribution of this signal after it has passed through a Butterworth low pass filter is shown in Figure 8-2. The Gaussian PDF of a signal with the same variance is also shown for comparison.

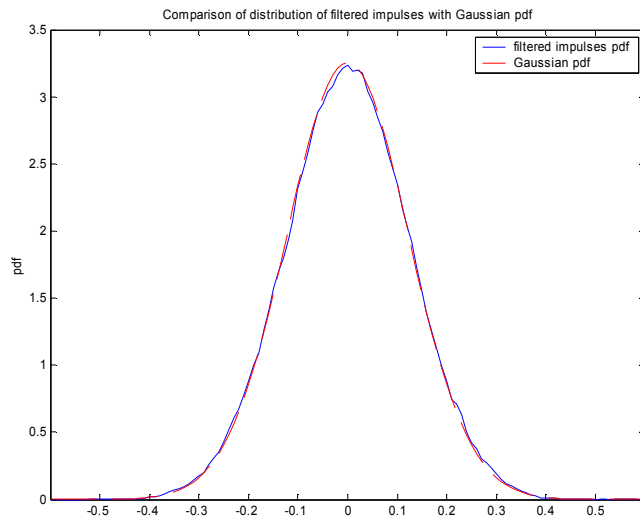


Figure 8-2. Comparison of distribution of lowpass filtered impulses and Gaussian PDF

A Gaussian approximation is pessimistic with regard to the impact of the UWB interference on narrowband system performance, because the UWB signal has a fixed power level. Therefore, the downconverted train of impulses will have amplitudes within a fixed range of possible values. The tails of the distribution of the filtered interference will not extend out to infinity as with Gaussian random variables. The error performance due to Gaussian noise tends to be dominated by the samples in the tails of the distribution,

have already been estimated. Perfect carrier estimation is assumed here, but the circuit is capable tracking the narrowband signal even if there is a small carrier offset (that is much less than the bandwidth of the narrowband signal). The received signal after narrowband cancellation is then downconverted by in-phase and quadrature forms of the narrowband carrier. Each of the I and Q channels are lowpass filtered on the order of the bandwidth of the interferer (Butterworth filters with 3 dB bandwidth of twice the baseband bandwidth of the narrowband signal were used for simulation). The low pass filtered signal is then sampled by A/D converters (at a rate very low compared to the bandwidth of the UWB signal, but greater than the Nyquist rate for the narrowband signal). This signal is the error after cancellation. The UWB signal will not be tracked by the canceller because it appears as Gaussian noise at the output of the low pass filter. Then digitally, the amplitude of the I and Q channels are tracked and estimated using an LMS algorithm. An estimate of the narrowband interferer is then recreated by multiplying the I and Q carriers by the amplitude estimates passed to D/A converters. The estimate of the interferer is subtracted from the received signal and this cancelled signal (or the error between the received signal and the estimated signal) is what is downconverted and sampled for the input to the LMS algorithm which attempts to minimize this error. The estimated narrowband signal is also subtracted from a delayed version of the received signal and the resulting signal is passed to the UWB receiver. The delay is necessary to maximize the cancellation, since the LMS algorithm tracks changes in the narrowband signal, but will do so with some delay. The error signal could instead be used by the UWB receiver but the interference would be suboptimally cancelled when the phase of the narrowband signal is changing.

The digital LMS algorithm updates the weights, w_I and w_Q by

$$w_{X,j+1} = w_{X,j} + \lambda m_{X,j}, \quad X = I, J \quad (8-9)$$

where m is the sampled error signal at the output of the low pass filter, and λ is the update weight factor that determines how quickly the algorithm can adapt to changes in the narrowband signal but also the sensitivity to the noise. λ can take values < 1 .

The downconverted I and Q channel signals are corrupted by AWGN and the effect of the UWB signal, which as discussed above appears fairly Gaussian at the output of the low pass filter. Therefore, the performance of the cancellation circuit is dependent on the characteristics of the narrowband signal and the power of the filtered noise and UWB signal, which together are modeled as Gaussian. The interference to noise ratio (INR) is defined for these specific simulation results as the ratio of the narrowband signal power to the power of the noise and the UWB signal after low pass filtering. Using the INR, the performance of the circuit can be determined independent of the specific UWB signal present or the bandwidth of the narrowband signal (where the sampling rates and filter bandwidths are relative to the narrowband bandwidth). The narrowband signal used in simulation is a QPSK signal that has RF bandwidth approximately twice the symbol rate.

The best measure of the canceller's performance is the narrowband signal's power level after cancellation. The mean of the cancelled narrowband signal power for the optimum λ (optimum in that the mean of the cancelled narrowband signal power in minimum) is plotted versus INR in Figure 8-4. As noted above, at very low INR the optimal λ may not have been accurately determined, so these rejection values (in particular for the 40 times sampling case) may be somewhat pessimistic. However, at

very low INR, the canceller on average actually adds more interference than it cancels and thus these values are somewhat irrelevant since the canceller should not be used at these INR levels. Additionally, at low INR levels (and presumably low received narrowband power levels), the impact on the UWB receiver will be negligible.

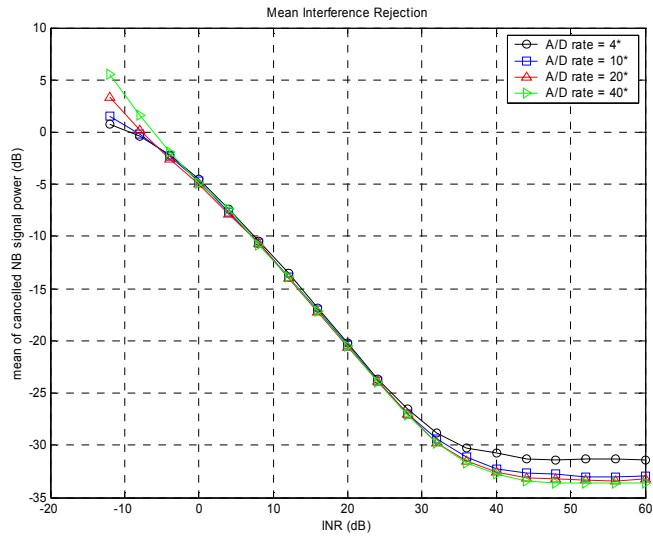


Figure 8-4. Mean narrowband interference rejection

While the mean rejection is the most significant performance measure, the variation of the rejection will also have an impact on the UWB performance. When, the narrowband signal changes (phase shift in the QPSK signal used for simulation), the LMS algorithm tracking the signal will adjust, but the error could be higher during this time, if the algorithm adapts slowly, resulting in higher narrowband power passed to the UWB receiver during this transition time. Therefore, the variance of the cancelled narrowband signal power for the optimum λ is plotted versus INR in Figure 8-5.

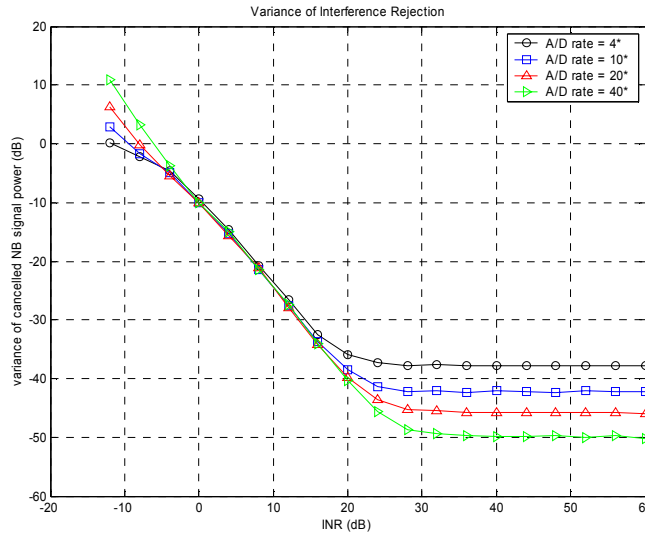


Figure 8-5. Variance of the narrowband interference rejection

The performance is found to be highly dependent on the value of λ used and the optimal value of λ changes with INR. The optimal λ (within 0.025) as a function of INR is shown in Figure 8-6. These values were found for A/D sampling rates of 4, 10, 20 and 40 times the baseband narrowband bandwidth. The mean performance as a function of λ for INR levels of 0, 8, 20, and 40 dB are shown in Figure 8-7 for the various sampling rates. At the low INR, the optimal λ is likely smaller than the smallest value (0.05) used in the simulation search. At higher INR, the fluctuation in the optimal λ , shown in Figure 8-6 (particularly noticeable for the 40 times sampling case), is because near optimal performance is achieved across a wider range of λ values and the simulation is limited in its accuracy so the true optimum value in this range cannot be determined.

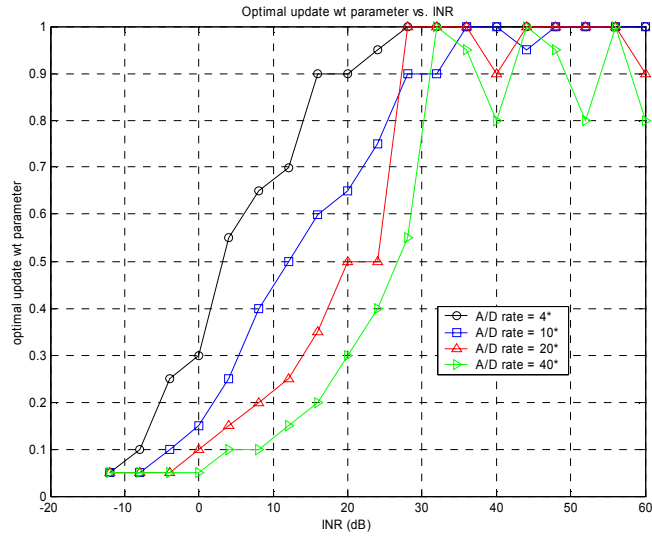
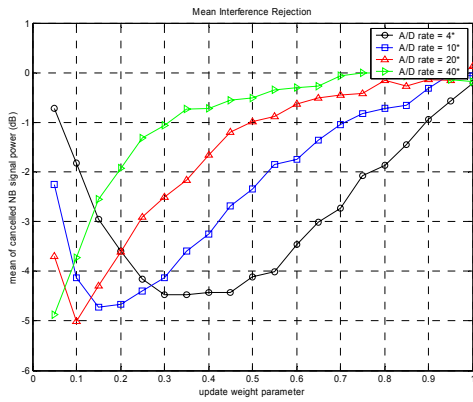
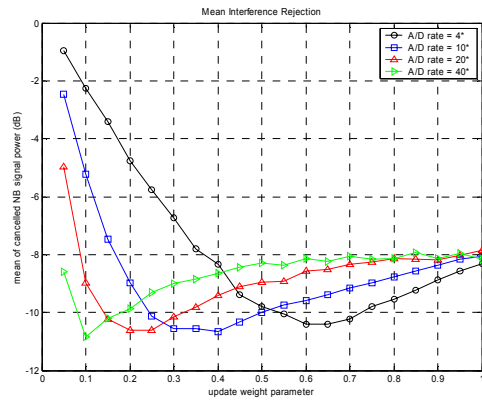


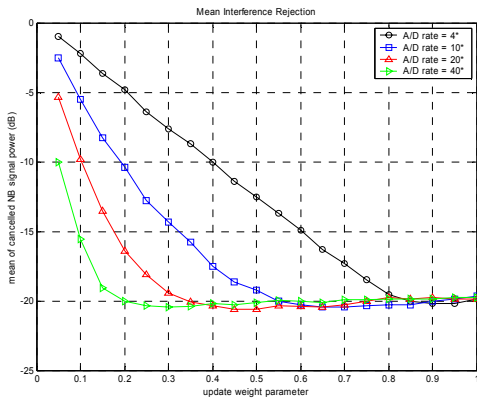
Figure 8-6. Optimal λ versus INR



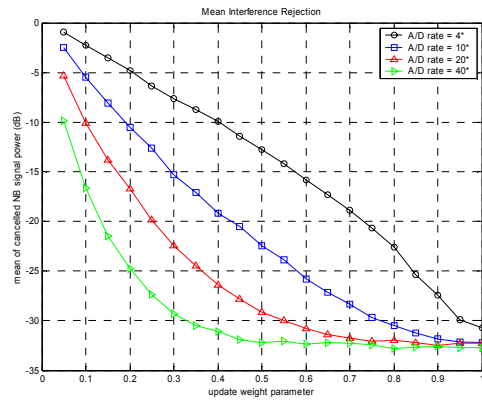
(a)



(b)



(c)



(d)

Figure 8-7. Mean narrowband interference rejection versus λ for INR = (a) 0 dB, (b) 8 dB, (c) 20 dB, and (d) 40 dB

The reason for the floor in the mean rejection and rejection variance is primarily due to noise. Noise limits how accurately the interferer can be estimated. The impact of the noise can be reduced by decreasing λ so the updates to the weights are less effected by changes in the signal due to noise, but the algorithm will track the narrowband signal more slowly as well for lower λ . It also appears to be related to the sampling frequency. It may also be partially due to the simulation resolution of the possible delay values of the received signal relative to the cancelled signal (shown in the top branch of the diagram in Figure 8-3). The simulation bandwidth is 100 times the baseband narrowband bandwidth. The optimum delay was found to be dependent on λ and the sampling rate, but independent of the INR. The optimum delay versus λ for the sampling rates considered is shown in Figure 8-8.

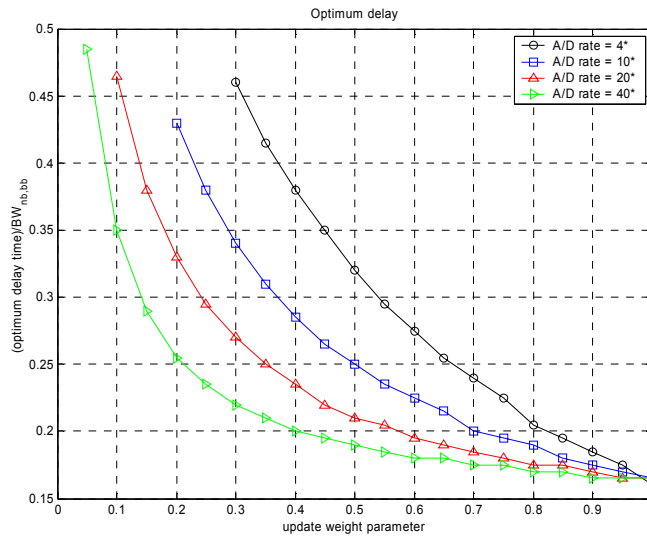


Figure 8-8. Optimum received signal delay for maximum narrowband cancellation

From the simulated performance of the narrowband canceller, and the above analysis of the impact of narrowband interference on UWB pulsed systems, the BER

performance of UWB systems can be determined. Consider a UWB system using 1 GHz bandwidth (3 dB bandwidth) Gaussian modulated sinusoidal pulses centered at 5.5 GHz (and thus overlapping with the ISM band) and an average pulse repetition rate of 10 MHz. The narrowband interferer is a QPSK signal with a carrier frequency of 5.82 GHz and a bandwidth of approximately 30 kHz. The UWB receiver is a correlation receiver with one bit per pulse and thus will be affected by the narrowband signal as described above. The UWB signal to noise ratio per bit (E_b/N_o) is set to 5, 8, and 9.5 dB. The resulting BER performance at different SIR ratios before and after cancellation is shown in Figure 8-9 (the sampling rate is taken to be 10 times the baseband narrowband bandwidth, or 150 kHz in this case, and the optimal λ is assumed). For the cases considered, the narrowband power is reduced to a nearly negligible level such that the UWB receiver is only noise limited.

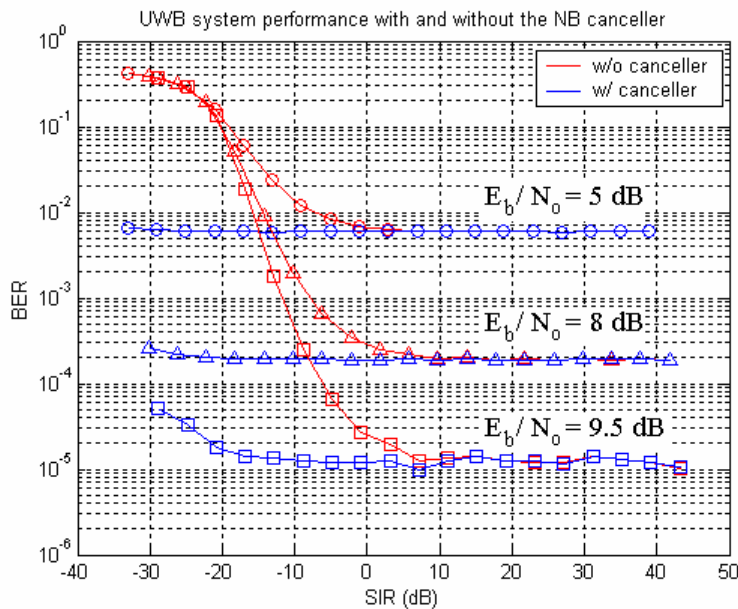


Figure 8-9. UWB BER improvement with using narrowband canceller

9 Conclusion

9.1 Summary and Future Work

This thesis has discussed a variety of topics related to ultra-wideband communications. Significant work characterizing the indoor UWB channel was presented. Based on those findings, issues in the design and performance of UWB receivers were also presented.

The frequency dependent distortion a pulse experiences when passing through various materials was discussed in Chapter 3, section 1. It was shown that for many common materials, the distortion is very small even over UWB-type frequency ranges. For materials that did cause significant distortion, the attenuation was also very high, making such signals less significant in the context of a complex multipath environment. Future work could be conducted to determine the level of pulse distortion when the signal reflects or diffracts off objects of different materials.

Numerous statistical characterizations of the indoor UWB channel, based on measurement data, were presented in Chapter 3, section 2. These statistics were based on impulse responses generated using the CLEAN algorithm deconvolution technique. Time dispersion and path arrival time statistics and the number of paths were all presented. Discussion of some traditional channel impulse response models for application to UWB was also presented. Appropriate parameters for these models were given such that key statistics of the modeled channels matched the measured channels. These analysis methods can be easily extended to future data sets, whether more indoor measurements or outdoor measurements.

It was shown in Chapter 5 that these traditional models generate channels that give significantly different performance results than the measured channels for the bicone LOS scenarios. These models do however match the limited number of available NLOS cases. A modified model with dominant early arriving paths was developed and shown to model the LOS channels much more accurately. However, it was shown that between the three traditional models considered, there is little difference in simulated performance. In future work, other types of models could also be considered, such as autoregressive modeling in the frequency domain.

Some limitations of the CLEAN algorithm were presented in Chapter 4. A more analytic approach to evaluating the CLEAN algorithm is necessary to fully understand when the results from this algorithm are unreliable and to understand how general the generated impulse responses are (for application to different bandwidths and center frequencies).

Chapter 6 discussed the significance of fractional bandwidth in the performance of UWB systems. Using the measurement channels, the fading experienced by signals of different fractional bandwidths was evaluated, and some reduced fading was observed for increasing the fractional bandwidth. Measurements at different frequencies and bandwidths would be very useful to further investigate this issue. Additionally, spatial measurements to measure fading could be conducted.

In Chapter 7, two different receiver architectures were presented: correlation receivers and energy detector receivers. Diversity schemes of each are discussed and BER performance simulation results are presented. For correlation Rake receivers, it was found that EGC has little if any performance loss compared to MRC. The energy

detector receiver shows potential for use as a receiver due to its potentially lower complexity, despite its performance degradation compared to a correlation receiver. Other architectures could also be considered in future work. A voltage threshold detector that is triggered when a threshold is exceeded by the received signal is another possible low complexity receiver type. Receivers that estimate the distorted receiver signal for use as the correlation template are also possible. This type of receiver could use the previously received symbols or pilot symbols to estimate the received profile. Further analysis and simulation of any of these receivers in the presence of interference, both narrowband and multiple access, could be conducted. Additional modulation schemes could be considered and analyzed. Analysis of multiple access schemes and comparison of different schemes would also be an important area to explore. The impact of channel coding in UWB systems, in particular with non-correlation architectures, could be examined. Synchronization for UWB, both acquisition and tracking, is another important research area that has not explored in depth. The significance of timing jitter to UWB system performance could be explored.

Finally, Chapter 8 presented some analysis of narrowband interference on UWB signals and UWB interference to narrowband signals. For both cases, specific assumptions were made and more work must be done to evaluate different and more general cases. A narrowband interference cancellation system was also presented and it was shown through simulation that significant UWB performance improvements could be achieved when in the presence of strong narrowband interferers. Possibilities for many other narrowband rejection systems, both analog and digital, exist and provide many opportunities for future research.

9.2 Contributions

This thesis has provided numerous original contributions to the state of the art in UWB technology including:

- Analysis of pulse distortion due to transmission through materials
- Statistical characterization of indoor small scale effects using VT UWB measurement data
- Analysis of limitations of the CLEAN algorithm
- Comparative analysis of three traditional channel models, shown to give nearly identical communications system performance
- New LOS model for indoor UWB channels
- Traditional channel models shown to give accurate prediction of performance in NLOS UWB channels
- Analysis of UWB fading in measured channels
- Comparison of Rake diversity combining techniques for UWB
- Energy detector proposed for use as a low complexity UWB receiver
- Analog and digital narrowband cancellation circuit for UWB communications systems proposed

References

- [1] F. J. Altman and W. Sichak, "A Simplified Diversity Communications System for Beyond-the-Horizon Links," *IRE Transactions on Communications Systems*, vol. 4, pp. 50-55, Mar. 1956.
- [2] C. R. Anderson, "Design and Implementation of an Ultrabroadband Millimeter-Wavelength Vector Sliding Correlator Channel Sounder and In-Building Multipath Measurements at 2.5 & 60 GHz," Master's Thesis, Dept. of Electrical and Computer Engineering, Virginia Tech, 2002.
- [3] A. M. Attiya and A. Safaai-Jazi, "Time Domain Characterization of Receiving TEM Horn Antennas," Accepted for presentation at the *2003 IEEE AP-S International Symposium on Antennas and Propagation and USNC/CNC/URSI North American Radio Science Meeting*, June 2003.
- [4] E. Baccarelli, M. Biagi, and L. Taglione, "A Novel Approach to In-Band Interference Mitigation in Ultra Wide Band Radio Systems," *IEEE Conference on Ultra Wideband Systems and Technologies*, 2002.
- [5] D. K. Barton, "Simple Procedures for Radar Detection Calculations," *IEEE Transactions on Aerospace and Electronic Systems*, vol. AES-5, no. 5, pp. 837-846, Sept. 1969.
- [6] N. C. Beaulieu, "An Infinite Series for the Computation of the Complementary Probability Distribution Function of a Sum of Independent Random Variables and its Application to the Sum of Rayleigh Random Variables," *IEEE Transactions on Communications*, vol. 38, no. 9, Sept. 1990.
- [7] A. Bennis and S. M. Riad, "Filtering Capabilities and Convergence of the Van-Cittert Deconvolution Technique," *IEEE Transactions on Instrumentation and Measurement*, vol. 41, no. 2, pp. 246-250, April 1992.
- [8] I. Bergel, E. Fishler, and H. Messer, "Narrow-band Interference Suppression in Time-Hopping Impulse-Radio Systems," *IEEE Conference on Ultra Wideband Systems and Technologies*, 2002.
- [9] A. Bharadwaj and J. K. Townsend, "Evaluation of the Covertness of Time-Hopping Impulse Radio using a Multi-Radiometer Detection System," *IEEE Military Communications Conference*, 2001, vol. 1, pp. 128 -134.
- [10] S. Buzzi, M. Lops, and H. V. Poor, "Code-Aided Interference Suppression for DS/CDMA Overlay Systems," *Proceedings of the IEEE*, vol. 90, no. 3, pp. 394-435, June 1988.

- [11] D. Cassioli, M Z. Win, and A. F. Molisch, "A Statistical Model for the UWB Indoor Channel". *IEEE VTS 53rd Vehicular Technology Conference*. 2001, Spring, vol. 2, pp. 1159-1163.
- [12] D. Cassioli, M Z. Win, and A. F. Molisch, "The Ultra-Wide Bandwidth Indoor Channel: From Statistical Model to Simulations," *IEEE Journal on Selected Areas in Communications*, vol. 20 issue 6, pp. 1247-1257, Aug. 2002.
- [13] R. J.-M. Cramer, R. A. Scholtz, and M. Z. Win, "Spatio-Temporal Diversity in Ultra-wideband Radio," *IEEE Wireless Communications and Networking Conference*, 1999, vol. 2, pp. 888-892.
- [14] R. J.-M. Cramer, R. A. Scholtz, and M. Z. Win, "Evaluation of an Ultra-Wide-Band Propagation Channel," *IEEE Transactions on Antennas and Propagation*, vol. 50, issue 5, pp. 561-570, May 2002.
- [15] R. J.-M. Cramer, R. A. Scholtz, and M. Z. Win, "Evaluation of an Indoor Ultra-Wideband Propagation Channel (doc.: IEEE P802.15-02/286-SG3a and IEEE P802.15-02/325-SG3a)," submitted to IEEE P802.15 Working Group for Wireless Personal Area Networks (WPANs), June 2002. Available: <http://grouper.ieee.org/groups/802/15/pub/2002/Jul02/>
- [16] H. A. David, *Order Statistics, 2nd Edition*, New York: Wiley, 1981.
- [17] R. A. Dillard, "Detectability of Spread-Spectrum Signals," *IEEE Transactions on Aerospace and Electronic Systems*, vol. AES-15, no. 4, pp. 526-537, Sept. 1969.
- [18] J. D. Edell, "Wideband, Noncoherent, Frequency-Hopped Waveforms and their Hybrids in Low-Probability of Intercept Communications," Report NRL, 8025, Naval Research Laboratory, Washington, D.C., Nov. 1976.
- [19] FCC, "Revision of Part 15 of the Commission's Rules Regarding Ultra-Wideband Transmission Systems," First Report and Order, ET Docket 98-153, Feb. 2002.
- [20] R. Fleming and C. Kushner, "Low Power, Miniature, Distributed Position Location and Communication Devices Using Ultra-Wideband, Nonsinusoidal Communication Technology," Semi-Annual Technical Report, ARPA Contract J-FBI-94-058, July 1995. Available: <http://www.aetherwire.com/> .
- [21] J. R. Foerster, "The Effects of Multipath Interference on the Performance of UWB Systems in an Indoor Wireless Channel," *IEEE VTS 53rd Vehicular Technology Conference*, Spring 2001, vol. 2, pp. 1176-1180.
- [22] J. Foerster, "The Performance of a Direct-Sequence Spread Ultra-Wideband System in the Presence of Multipath, Narrowband Interference, and Multiuser Interference," *IEEE Conference on Ultra Wideband Systems and Technology*, 2002.

- [23] J. Foerster, "Channel Modeling Sub-committee Report Final (doc.: IEEE 802-15-02/490r1-SG3a)," submitted to IEEE P802.15 Working Group for Wireless Personal Area Networks (WPANs), Feb. 2002. Available: <http://grouper.ieee.org/groups/802/15/pub/2002/Nov02/>
- [24] J. Foerster and Q. Li, "UWB Channel Modeling Contribution from Intel (doc: IEEE P802.15-02/279-SG3a)," submitted to IEEE P802.15 Working Group for Wireless Personal Area Networks (WPANs), June 2002. Available: <http://grouper.ieee.org/groups/802/15/pub/2002/Jul02/>.
- [25] C. Fowler, J. Entzminger, J. Corum, "Report: Assessment of Ultra-Wideband (UWB) Technology," OSD/DARPA Ultra-Wideband Radar Review Panel, R- 6280, 1990.
- [26] S. S. Ghassemzadeh, L. J. Greenstein, and V. Tarokh, "The Ultra-wideband Indoor Multipath Loss Model (doc: IEEE P802.15-02/282-SG3a and IEEE P802.15-02/283-SG3a)," submitted to IEEE P802.15 Working Group for Wireless Personal Area Networks (WPANs), June 2002. Available: <http://grouper.ieee.org/groups/802/15/pub/2002/Jul02/>.
- [27] S. S. Ghassemzadeh, R. Jana, C. W. Rice, W. Turin, and V. Tarokh, "A Statistical Path Loss Model for In-Home UWB Channels," *IEEE Conference on Ultra Wideband Systems and Technology*. 2002.
- [28] M. Ghavami, L. B. Michael, and R. Kohno, "Hermite Function Based Orthogonal Pulses for Ultra Wideband Communication," *4th International Symposium on Wireless Personal Multimedia Communications*, Sept. 2001, pp. 437-440.
- [29] H. Hashemi, "The Indoor Radio Propagation Channel," *Proceedings of the IEEE*, vol. 81, no. 7, pp. 943-968, July 1993.
- [30] H. Hashemi, "Impulse Response Modeling of Indoor Radio Propagation Channels," *IEEE Journal on Selected Areas in Communications*, vol. 11, no. 7, pp. 967-978, September 1993.
- [31] J. R. Hoffman, M. G. Cotton, R. J. Achatz, and R. N. Stutz, "Addendum to NTIA Report 01-384: Measurements to Determine Potential Interference to GPS Receivers from Ultrawideband Transmission Systems," *NTIA Report 01-389*, Sept. 2001.
- [32] J. R. Hoffman, M. G. Cotton, R. J. Achatz, R. N. Stutz, and R. A. Dalke, "Measurements to Determine Potential Interference to GPS Receivers from Ultrawideband Transmission Systems," *NTIA Report 01-384*. Feb. 2001.

- [33] S. J. Howard and K. Pahlavan, "Autoregressive Modeling of Wide-Band Indoor Radio Propagation," *IEEE Transactions on Communications*, vol. 40, no. 9, pp. 1540-1552, Sept. 1992.
- [34] V. Hovinen, M. Hämäläinen, and T. Pätsi, "Ultra Wideband Indoor Radio Channel Models: Preliminary Results," *IEEE Conference on Ultra Wideband Systems and Technology*. 2002.
- [35] X. Huang and D. Liang, "Gradual RELAX Algorithm for RFI Suppression in UWB-SAR," *Electronics Letters*, vol. 35, no. 22, pp. 1916-1917, March 2002.
- [36] M. G. M. Hussain, "Principles of Space-Time Array Processing for Ultrawide-Band Impulse Radar and Radio Communications," *IEEE Transactions on Vehicular Technology*, vol. 51, issue 3, pp. 393-403, May 2002.
- [37] I. Immoreev and D. Fedotov, "Ultra Wideband Radar Systems: Advantages and Disadvantages," *IEEE Conference on Ultra Wideband Systems and Technology*, 2002.
- [38] W. C. Jakes, Ed., *Microwave Mobile Communications*, New York: IEEE Press, 1993.
- [39] J. Keignart and N. Daniele, "Subnanosecond UWB Channel Sounding in Frequency and Temporal Domain," *IEEE Conference on Ultra Wideband Systems and Technology*, 2002.
- [40] J. Keignart, J. B. Pierrot, N. Daniele, and P. Rouzet, "UWB Channel Modeling Contribution from CEA-LETI and STMicroelectronics (doc: IEEE P802.15-02/444-SG3a)," submitted to IEEE P802.15 Working Group for Wireless Personal Area Networks (WPANs), Oct 2002. Available: <http://grouper.ieee.org/groups/802/15/pub/2002/Nov02/>.
- [41] W. A. Kissick (Ed.), "The Temporal and Spectral Characteristics of Ultrawideband Signals," *NTIA Report 01-383*, Jan. 2001.
- [42] J. Kunisch, and J. Pamp, "Measurement Results and Modeling Aspects for the UWB Radio Channel," *IEEE Conference on Ultra Wideband Systems and Technology*, 2002.
- [43] H. Lee, B. Han, Y. Shin, and S. Im, "Multipath Characteristics of Impulse Radio Channels," *IEEE VTS 51st Vehicular Technology Conference*. Spring 2000, vol. 3, pp. 2487-2491.
- [44] D. R. McKinstry and R. M. Buehrer, "Issues in the Performance and Covertness of UWB Communications Systems," *45th Midwest Symposium on Circuits and Systems*, 2002, vol. 3, pp. 601-604.

- [45] T. Miller, L. Porter, and J. McCorkle, "RFI Suppression for Ultra Wideband Radar," *IEEE Transactions on Aerospace and Electronic Systems*, vol. 33, no. 4, pp. 1142-1156, Oct 1997.
- [46] R. F. Mills and G. E. Prescott, "A Comparison of Various Radiometer Detection Models," *IEEE Transactions on Aerospace and Electronic Systems*, vol. 32, no. 1, Jan. 1996.
- [47] L. B. Milstein, "Interference Rejection Techniques in Spread Spectrum Communications," *Proceedings of the IEEE*, vol. 76, no. 6, pp. 657-671, June 1988.
- [48] A. H. Muqaibel, "Characterization of Ultra Wideband Communication Channels," Ph.D. Dissertation, Dept. of Electrical and Computer Engineering, Virginia Tech, 2003.
- [49] A. Muqaibel, A. Safaai-Jazi, B. Woerner, and S. Riad, "UWB Channel Impulse Response Characterization Using Deconvolution Techniques," *45th Midwest Symposium on Circuits and Systems*, 2002, vol. 3, pp. 605-608.
- [50] A. Muquibel, A. Safaai-Jazi, A. Bayram, and S. Riad, "UWB Through the Wall Propagation and Material Characterization," Accepted for presentation at the *2003 IEEE AP-S International Symposium on Antennas and Propagation and USNC/CNC/URSI North American Radio Science Meeting*, June 2003.
- [51] A. Muquibel and A. Safaai-Jazi, "A New Formulation for Evaluating Complex Permittivity of Low-Loss Materials," Accepted for presentation at the *2003 IEEE AP-S International Symposium on Antennas and Propagation and USNC/CNC/URSI North American Radio Science Meeting*, June 2003.
- [52] A. Muquibel and A. Safaai-Jazi, "A New Formulation for Characterization of Materials Based on Measured Insertion Transfer Function," Accepted for publication in the *IEEE Transactions on Microwave Theory and Techniques*.
- [53] P. Odling, O. Borjesson, T. Magesacher, and T. Nordstrom, "An Approach to Analog Mitigation of RFI," *IEEE Journal on Selected Areas in Communications*, vol. 20 issue 5, pp. 974-986, June 2002.
- [54] J. E. Padgett, J. C. Koshy, and A. A. Triolo, "Physical-Layer Modeling of UWB Interference Effects," Telcordia Technologies Report to DARPA for NETEX Program, Analysis and Simulation of UWB Interference Effects, Jan. 2003.
- [55] K. Park, "Performance Evaluation of Energy Detectors," *IEEE Transactions on Aerospace and Electronic Systems*, vol. AES-14, no. 2, pp. 237-241, Mar. 1978.

- [56] B. Parr, C. ByungLok, K. Wallace, and Zhi Ding, "A Novel Ultra-wideband Pulse Design Algorithm," *IEEE Communications Letters*, vol. 7, issue 5, pp. 219-221, May 2003.
- [57] M. Pendergrass and W. Beeler, "Emperically Based Statistical Ultra-Wideband (UWB) Channel Model (doc.: IEEE 802-15-02/240SG3a)," presented to IEEE P802.15 Working Group for Wireless Personal Area Networks (WPANs), June 2002. Available: <http://grouper.ieee.org/groups/802/15/pub/2002/Jul02/>
- [58] C. Prettie, D. Cheung, L. Rusch, and M. Ho, "Spatial Correlation of UWB Signals in a Home Environment," *IEEE Conference on Ultra Wideband Systems and Technology*. 2002.
- [59] J. G. Proakis, *Digital Communications, Fourth Edition*, Boston: McGraw Hill, 2001.
- [60] R. C. Qiu, "A Theoretical Study of the Ultra-wideband Wireless Propagation Channel Based on the Scattering Centers," *IEEE VTS 48th Vehicular Technology Conference*, 1998, vol. 1, pp. 308-312.
- [61] R. C. Qiu, "A Study of the Ultra-wideband Wireless Propagation Channel and Optimum UWB Receiver Design," *IEEE Journal on Selected Areas in Communications*, vol. 20, issue 9, pp. 1628-1637, Dec. 2002.
- [62] F. Ramirez-Mireles and R. A. Scholtz, "Wireless Multiple-Access Using SS Time-Hopping and Block Waveform Pulse Position Modulation, Part 1: Signal Design," *Proceedings ISITA Symposium*, Oct. 1998.
- [63] F. Ramirez-Mireles and R. A. Scholtz, "Wireless Multiple-Access Using SS Time-Hopping and Block Waveform Pulse Position Modulation, Part 2: Multiple-Access Performance," *Proceedings ISITA Symposium*, Oct. 1998.
- [64] F. Ramirez-Mireles and R. A. Scholtz, "Multiple-Access with Time Hopping and Block Waveform PPM Modulation," *IEEE International Conference on Communications*, 1998, vol. 2, pp. 775-779.
- [65] T. S. Rappaport, *Wireless Communications: Principles and Practice*, Upper Saddle River, NJ: Prentice Hall, 1996.
- [66] S. M. Riad, "The Deconvolution Problem, an Overview," *Proceedings of the IEEE*, vol. 74, no. 1, pp. 82-85, Jan. 1986.
- [67] A. A. Saleh and R. A. Valenzuela, "A Statistical Model for Indoor Multipath Propagation," *IEEE Journal on Selected Areas in Communications*, vol. SAC-5, no. 2, pp. 128-137, Feb. 1987.

- [68] R. Scholtz, "Multiple Access with Time-Hopping Impulse Modulation," *IEEE Military Communications Conference*, 1993, vol. 2, pp. 447-450.
- [69] R. A. Scholtz, R. J.-M. Cramer, and M. Z. Win, "Evaluation of the Propagation Characteristics of Ultra-wideband Communication Channels," *IEEE Antennas and Propagation Society International Symposium*, 1998, vol. 2, pp. 626-630.
- [70] R. A. Scholtz and M. Z. Win, "Impulse Radio," *Personal Indoor Mobile Radio Conference*, Sept. 1997.
- [71] K. Seong-Cheol, H. L. Bertoni, and M. Stern, "Pulse Propagation Characteristics at 2.4 GHz Inside Buildings," *IEEE Transactions on Vehicular Technology*, vol. 45, issue 3, pp. 576-692, Aug 1996.
- [72] V. S. Somayazulu, "Multiple Access Performance in UWB Systems Using Time Hopping vs. Direct Sequence Spreading," *IEEE Wireless Communications and Networking Conference*, Mar. 2002, vol. 2, pp. 522-525.
- [73] H. Suzuki, "A Statistical Model for Urban Radio Propagation," *IEEE Transactions on Communications*, vol. COM-25, no. 7, pp. 673-680, July 1977.
- [74] G. L. Turin, F. D. Clapp, T. L. Johnston, S. B. Fine, and D. Lavry, "A Statistical Model of Urban Multipath Propagation," *IEEE Transactions on Vehicular Technology*, vol. VT-21, pp. 1-9, Feb. 1972.
- [75] W. Turin, R. Jana, S. S. Ghassemzadeh, C. W. Rice, and V. Tarokh, "Autoregressive Modeling of an Indoor UWB Channel," *IEEE Conference on Ultra Wideband Systems and Technologies*, 2002, pp. 71-74.
- [76] R. G. Vaughan and N. L. Scott, "Super-Resolution of Pulsed Multipath Channels for Delay Spread Characterization," *IEEE Transactions on Communications*, vol. 47, no. 3, pp. 343-347, Mar. 1999.
- [77] G. D. Weeks, J. K. Townsend, and J. A. Freebersyter, "Quantifying the Covertness of Impulse Radio," *Ultra Wideband Conference*, Washington D.C., Sept. 1999.
- [78] M. L. Welborn, "System Considerations for Ultra-wideband Wireless Networks," *IEEE Radio and Wireless Conference*, 2001, pp. 5-8.
- [79] M. Welborn, and J. McCorkle, "The Importance of Fractional Bandwidth in Ultra-wideband Pulse Design," *IEEE International Conference on Communications*, 2002, vol. 2, pp. 753-757.
- [80] M. Welborn, T. Miller, J. Lynch, and J. McCorkle, "Multi-User Perspectives in UWB Communication Networks," *IEEE Conference on Ultra Wideband Systems and Technology*, 2002.

- [81] M. Z. Win, F. Ramirez-Mireles, R. A. Scholtz, and M. A. Barnes, "Ultra-wide Bandwidth (UWB) Signal Propagation for Outdoor Wireless Communications," *IEEE 47th Vehicular Technology Conference*, 1997, vol. 1, pp. 251-255.
- [82] M. Z. Win, R. A. Scholtz, and M. A. Barnes, "Ultra-wide Bandwidth Signal Propagation for Indoor Wireless Communications," *IEEE International Conference on Communications: Towards the Knowledge Millennium*. 1997, vol. 1, pp. 56-60.
- [83] P. Withington, "Comments of Time Domain Corporation, Docket 98-153," Before the Federal Communications Commission, In the Matter of Revision of Part 15 of the FCC's Rules Regarding Ultra-wideband Transmission Systems, Dec. 1998. Available: <http://www.uwb.org/files> .
- [84] P. Withington, R. Reinhardt, and R. Stanley, "Preliminary Results of an Ultra-wideband (Impulse) Scanning Receiver," *IEEE Military Communications Conference*. 1999, vol. 2, pp. 1186-1190.
- [85] S. M. Yano, "Investigating the Ultra-wideband Indoor Wireless Channel," *IEEE VTS 55th Vehicular Technology Conference*, 2002, vol. 3, pp. 1200-1204.
- [86] H. Zhang, T. Udagawa, T. Arita, and M. Nakagawa, "A Statistical Model for the Small-Scale Multipath Fading Characteristics of Ultra Wideband Indoor Channel," *IEEE Conference on Ultra Wideband Systems and Technology*, 2002.
- [87] F. Zhu, Z. Wu, and C. Nassar, "Generalized Fading Channel Model with Application to UWB," *IEEE Conference on Ultra Wideband Systems and Technology*, 2002.
- [88] R. E. Ziemer and R. L. Peterson, *Introduction to Digital Communications, Second Edition*, Upper Saddle River, NJ: Prentice Hall, 2001.

Vita

David McKinstry was born to Wayne and Shirley McKinstry on February 23, 1979. He grew up in a Christian home in Chatham, Illinois where he accepted Jesus Christ as Lord and Savior at a young age. In 1997, he graduated from Glenwood High School in Chatham. McKinstry attended the University of Missouri-Rolla having received a Master's Student Fellowship and McCourtney Scholarship. While at UMR, he was a member of Eta Kappa Nu, Tau Beta Pi, and the Baptist Student Union. He graduated summa cum laude, receiving the B.S. degree in electrical engineering in 2000. For several months after graduating, he interned with Adtran in Huntsville, Alabama. He started graduate school at Virginia Tech in the Fall of 2001, receiving a Bradley Fellowship. He joined the Mobile and Portable Radio Research Group and focused his research on ultra-wideband wireless communications. At VT, he was also involved with the Baptist Student Union. He will receive the M.S. degree also in electrical engineering in June, 2003. After graduation, McKinstry will be joining the Theater Systems Development group in the Air Defense Systems Department at the Johns Hopkins University Applied Physics Laboratory.